

Studies of The Nuclear Three-Body System with Three Dimensional Faddeev Calculations

A dissertation presented to
the faculty of
the College of Arts and Sciences

In partial fulfillment
of the requirements for the degree
Doctor of Philosophy

Hang Liu
August 2005

© 2005
Hang Liu
All rights reserved

This dissertation entitled

STUDIES OF THE NUCLEAR THREE-BODY SYSTEM
WITH THREE DIMENSIONAL FADDEEV CALCULATIONS

BY
HANG LIU

has been approved for
the Department of Physics and Astronomy
and the College of Arts and Sciences by

Charlotte Elster
Professor of Physics

Benjamin M. Ogles
Interim Dean, College of Arts and Sciences

LIU, HANG. Ph.D. August 2005. Department of Physics and Astronomy

**Studies of The Nuclear Three-Body System
with Three Dimensional Faddeev Calculations** (216pp.)

Director of dissertation: Charlotte Elster

A three-body system consists of either a bound state of three particles with definite binding energy or a beam of single particles scattered from a target where two of the particles are bound. Of the particles are nucleons, the interactions between them are strong and short ranged. A theoretical framework for studying the dynamics of a nuclear three-body system is the Faddeev scheme. In this work the equation for three-body scattering and the bound state are formulated in momentum space, and directly solved in terms of vector variables. For three identical bosons the Faddeev equation for scattering is a three-dimensional inhomogeneous integral equation in five variables, and is solved by Padé summation. The equation for the bound state is a homogeneous one in three variables, and is solved by a Lanczos' type method. The corresponding algorithms are presented, and their numerical feasibility is demonstrated. Elastic as well as inelastic scattering processes in the intermediate energy regime up to 1 GeV incident energy are studied for the first within a Faddeev scheme. The two-body force employed is of Malfliet-Tjon type. Specific emphasis is placed on studying the convergence of the multiple scattering series given by the Faddeev equations. For the bound state, a three-body force of Fujita-Miyazawa type is incorporated in addition to the two-body force. The effects of this three-body force on the bound state properties are investigated.

Approved: Charlotte Elster
Professor of Physics

*To my wife and daughter, Zongqin Ruan and Qingshan Liu
and my parents, Shifa Liu and Chengxun Gao*

Acknowledgments

I would like to express my thanks and appreciation to all people who helped me throughout my academic career.

I would sincerely thank my advisor, Dr. Charlotte Elster, for her warmth, guidance and perseverance. It is her continual instruction and inspiration that make this work possible. I am indebted to Dr. Walter Glökle for his collaboration. Special thanks to Dr. Daniel Phillips for his teaching and discussion regarding various physics questions which greatly extend my horizon.

I wish to thank our Department of Physics and Astronomy at Ohio University, especially the nuclear physics group, where I received so much help from faculty and staff. Specially I would like to acknowledge Dr. Louis Wright, Dr. Allena Opper, Dr. Kenneth Hicks and Dr. Anders Gardestig for their advices. I received many useful comments from my graduate student peers in nuclear theory group, Deepshikha Choudhury and Ting Lin. I also benefitted from stimulating discussions with Dr. Andreas Nogga and Dr. Imam Fachruddin when they visited here.

I am fortunate to have my parents, Shifa Liu and Chengxun Gao, to whom I owe everything. Their inspiration and support are the major source for me to pursue my goals. Most of all, I would like to thank my wife and daughter, Zongqin Ruan and Qingshan Liu, for their love and support throughout this endeavor. We share the happiness of family and the burden of life together. They are colors of my life.

My friends, Xiaodong Zhang, Lu Tong, Hong Chen, Yin Zhou and Haiyang Tao, deserve my hearty appreciation for their invaluable helps on almost everything in past years.

This work was performed in part under the auspices of the U. S. Department of Energy under contract No. DE-FG02-93ER40756 with Ohio University. The computational supports of the Ohio Supercomputer Center (OSC) for the use of their facilities under Grant No. PHS206, the Neumann Institute for Computing (NIC) under project JIKP01 and the National Energy Research Scientific Computing Center (NERSC) are acknowledged.

Table of Contents

Abstract	4
Dedication	5
Acknowledgments	6
Table of Contents	8
List of Figures	10
List of Tables	16
1 Introduction	22
2 Description of Three Particle Systems with Faddeev Scheme	27
2.1 The Hamiltonian of Three-Body System	27
2.2 The Faddeev Equation for Three-Body Bound State	28
2.3 Faddeev Equations for Three-Body Scattering Operators	31
2.4 The Unitarity Relation of Scattering Operators	36
3 The Scattering of Three Identical Bosons	43
3.1 The Jacobi Coordinate System	44
3.2 Equations for The Scattering Operators	46
3.2.1 The Two-Body t -Matrix	46
3.2.2 Explicit Equations with Invariant Variables	47
3.2.3 Structure and Treatment of The Moving Singularities	62
3.3 Cross Sections and Optical Theorem	71
3.4 The Explicit Calculation of the Scattering Operator	76
3.5 Accuracy and Self-Consistency Analysis	78
3.6 The Study of The Reaction Mechanisms in Three-Body Scattering . .	89
3.6.1 The Elastic Scattering	91
3.6.2 The Semi-Exclusive Breakup Process	96
3.6.3 The Exclusive Breakup Process	112

3.7	Summary	118
4	The Bound State of Three Bosons	120
4.1	The Explicit Equation for Bound State	121
4.2	Models of Two-Body and Three-Body Forces	129
4.3	The Accuracy Analysis of Three-Body Force Calculation	132
4.4	Three-Body Bound State Properties	140
4.5	Model Studies of Three-Body Forces	147
4.5.1	The Meson-Nucleon Amplitude	147
4.5.2	The Exchanged Meson Mass	151
4.5.3	The Momentum Cut-off Parameter	155
4.6	The Three-Body Force with Repulsive Core	158
4.7	The Bound State with Three-Body Force Only	162
4.8	The Interplay Between Two-Body and Three-Body Forces	167
4.9	Summary	170
5	Analytical and Numerical Techniques	171
5.1	Spline Based Interpolation and Integration	171
5.1.1	The Cubic Splines Interpolation	171
5.1.2	The Integration with Logarithmic Singularity	174
5.2	Padé Method and The Solution of The Inhomogeneous Equation for Scattering Operator	186
5.3	Iterated Ortho-normalized Vector Method and the Solution of The Homogeneous Equation for a Three-Body Bound State	193
6	Summary and Outlook	197
A	High Performance Computing and Its Application to The Faddeev Calculations for The Nuclear Three-Body System	201
A.1	The Overview of Parallel High Performance Computing	202
A.1.1	The Parallel Processing	202
A.1.2	The High Performance Execution	203
A.1.3	Performance Tuning Techniques.	204
A.2	The Application of HPC in Faddeev Calculation for Three-Body System	206
A.2.1	Load Balanced Domain Decomposition and Data Distribution	207
A.2.2	The Scalable Multi-Leveled Computing Model for Three-Body Scattering Calculation	209
A.2.3	The High Performance Demonstration of Three-Body Force Calculation	210
	Bibliography	212

List of Figures

- 3.1 The geometry of three vectors \mathbf{q}_0 , \mathbf{q} , and \mathbf{p} relevant in the three-body scattering problem. The independent angle variables x_q , x_p , and $x_{pq}^{q_0}$ as defined in text are indicated. The dashed arrows represent the normal vectors $(\mathbf{q}_0 \times \mathbf{q})$ and $(\mathbf{p} \times \mathbf{q}_0)$ 52
- 3.2 The region of singularities of the free three-particle propagator as function of the momenta q and q'' . The shaded area in the $q - q''$ plane indicates the region where $|x_0| \leq 1$, i.e. the region where a pole in the x'' -integration occurs. This region is enclosed by the bounding curves q_+ and q_- , which contain the logarithmic singularities as functions of q'' 64
- 3.3 The percent error of optical theorem as a function of points on q and q'' grid at selected energies: $E_{lab} = 0.01$ GeV (upper panel), $E_{lab} = 0.1$ GeV (middle panel) and $E_{lab} = 0.5$ GeV (lower panel). 86
- 3.4 The total elastic cross section σ_{el} (dashed line), the total break-up cross section σ_{br} (dash-dotted line) and the total cross section evaluated by the optical theorem σ_{opt} (solid line) given as function of the projectile laboratory energy. At selected energies where the calculations have been carried out the sum of the calculated total elastic and break-up cross section, $\sigma_{tot} = \sigma_{el} + \sigma_{br}$, is indicated by the open diamond. The open diamonds coincide with the solid line according to the optical theorem, Eq. (3.141), and the numerical values are given in Table 3.6. 90
- 3.5 The elastic differential cross section (c.m.) at $E_{lab} = 3.0$ MeV and $E_{lab} = 10.0$ MeV very low projectile energies (upper panel) and $E_{lab} = 0.2$ GeV, $E_{lab} = 0.5$ GeV, $E_{lab} = 0.8$ GeV and $E_{lab} = 1.0$ GeV intermediate projectile energies (lower panel) as function of the scattering angle $\theta_{c.m.}$. All calculations are solutions of full Faddeev Equation. . . 92

- 3.6 The elastic differential cross section at $E_{lab} = 0.2$ GeV, $E_{lab} = 0.5$ GeV, $E_{lab} = 0.8$ GeV and $E_{lab} = 1.0$ GeV projectile energies as function of the scattering angle $\theta_{c.m.}$. The result of the full Faddeev calculation is given by the solid line and compared with calculations based on the first order, 2nd order, 3rd order and 4th order in t as indicated in the legend. 94
- 3.7 The elastic cross section (c.m.) at different angles $\theta_{c.m.} = 45^\circ, 90^\circ, 135^\circ, 180^\circ$ as function of the projectile laboratory energy. The result of the full Faddeev calculation is given by the solid line and compared with calculations based on the first order, 2nd order, 3rd order and 4th order in t as indicated in the legend. 95
- 3.8 The semi-exclusive cross section at 495 MeV laboratory incident energy and at 18° angle of the emitted particle. The upper panel displays the first order results obtained from the realistic potentials AV18 [13] (long dashed line) and Bonn-B [50] (dashed-dotted line) together with our calculation based on the scalar MT potential of Eq. (3.164) (dashed line). The lower panel displays again our first order calculation from the upper panel (dashed line), together with a successive addition of the next three rescattering terms. The exact solution of the Faddeev equation is given by the solid line. 99
- 3.9 The semi-exclusive cross section at 0.2 GeV laboratory incident energy and at 24° emission angle of the emitted particle. The upper panel displays the entire energy range of the emitted particle, whereas the two lower panels show only the lowest and highest energies in a linear scale. The full solution of the Faddeev equation is given by the solid line in all panels. The contribution of the lowest orders of the multiple scattering series added up successively is given by the other curves as indicated in the legend of the lower left panel. 102
- 3.10 Same as Fig. 3.9 but for an angle of 39° of the emitted particle. . . . 103

- 3.11 The semi-exclusive cross section at 0.5 GeV laboratory incident energy and at 24° angle of the emitted particle. The upper panel displays the entire energy range of the emitted particle, whereas the two lower panels show only the lowest and highest energies in a linear scale. The full solution of the Faddeev equation is given by the solid line in all panels. The contribution of the lowest orders of the multiple scattering series added up successively is given by the other curves as indicated in the legend of the lower left panel. 105
- 3.12 Same as Fig. 3.11 but for an angle of 36° of the emitted particle. . . 106
- 3.13 The semi-exclusive cross section at 1 GeV laboratory incident energy and at 18° angle of the emitted particle. The upper panel displays the entire energy range of the emitted particle, whereas the two lower panels show only the lowest and highest energies in a linear scale. The full solution of the Faddeev equation is given by the solid line in all panels. The contribution of the lowest orders of the multiple scattering series added up successively is given by the other curves as indicated in the legend of the lower left panel. 107
- 3.14 Same as Fig. 3.13 but for an angle of 30° of the emitted particle. . . 108
- 3.15 The cross section (c.m.) for the semi-exclusive break-up reaction in which two particles emerge in forward direction with a relative energy between 0 and 3 MeV, and one particle is detected at backward angle as function of the projectile laboratory energy. The result of the full Faddeev calculation is given by the solid line and compared with calculations based on the first order, 2nd order, 3rd order and 4th order in t as indicated in the legend. 111
- 3.16 The exclusive cross section at $E_{lab} = 1.0\text{GeV}$ and $x_p = 1$, $\phi_{pq} = 0^\circ$, $x_q = 1$ (upper panel) and at $E_{lab} = 1.0\text{GeV}$ and $x_p = 0$, $\phi_{pq} = 90^\circ$, $x_q = 1$ (lower panel). The full solution of the Faddeev equation is given by the solid line. The contributions of the lowest orders of the multiple scattering series added up successively are given by the other curves as indicated in the legend. 114

- 3.17 The exclusive differential cross section at $E_{lab} = 1.0\text{GeV}$ and $x_p = 1$, $\phi_{pq} = 0^\circ$, $x_q = -1$ (upper panel) and at $E_{lab} = 1.0\text{GeV}$ and $x_p = 0$, $\phi_{pq} = 0^\circ$, $x_q = -1$ (lower panel). The full solution of the Faddeev equation is given by the solid line. The contributions of the lowest orders of the multiple scattering series added up successively are given by the other curves as indicated in the legend. 115
- 3.18 The exclusive differential cross section at $E_{lab} = 1.0\text{GeV}$ and $x_p = 0$, $\phi_{pq} = 90^\circ$, $x_q = 0$ (upper panel) and at $E_{lab} = 1.0\text{GeV}$ and $x_p = \sqrt{2}/2$, $\phi_{pq} = 0^\circ$, $x_q = -\sqrt{2}/2$ (lower panel). The full solution of the Faddeev equation is given by the solid line. The contributions of the lowest orders of the multiple scattering series added up successively are given by the other curves as indicated in the legend. 117
- 4.1 The diagrammatic representation of the three-body force $V_4^{(1)}$. The particle 1 is singled out by the meson-nucleon amplitude described by the blob. The three-body force of this type is then given according to Eq. (4.7). 123
- 4.2 The calculated single particle momentum distribution $n(q)$ (upper panel) and two-body correlation function $c(r)$ (lower panel) for MT2-II two-body potential only, MT2-II+MT3-I two-body and three-body potential and MT2-II+MT3-II two-body and three-body potential. 145
- 4.3 The contour slice when the calculated $\Psi(p, q, x = 1)$ is equal to 1.0, 10^{-1} , 10^{-2} and 10^{-3} in unit of fm^3 for MT2-II two-body potential only, and MT2-II+MT3-I two-body and three-body potential. 146
- 4.4 The calculated single particle momentum distribution $n(q)$ (upper panel) and two-body correlation function $c(r)$ (lower panel) as functions of the different meson-nucleon coupling strength a_α of the three-body force MT3-I with $a_\alpha = 1.73$ 149
- 4.5 The calculated total wave function of three-body bound state $|\Psi(p, q, x)|$ in unit $[\text{fm}^3]$ at $x = 1$ as a function of the different meson-nucleon coupling strength a_α of the three-body force MT3-I. The upper left: $2a_\alpha$, the upper right: $4a_\alpha$, the lower left: $6a_\alpha$, the lower right: $8a_\alpha$ 150

- 4.6 The calculated single particle momentum distribution $n(q)$ (upper panel) and two-body correlation function $c(r)$ (lower panel) as functions of the exchanged meson mass m_α of the three-body force MT3-I with $m_\alpha = 305.8593$ MeV and $\frac{a_\alpha}{m_\alpha} = \frac{-1.73}{305.8593}$ unchanged. 153
- 4.7 The The calculated single particle momentum distribution $n(q)$ (upper panel) and two-body correlation function $c(r)$ (lower panel) corresponding the cases of $\frac{1}{3}a_\alpha$ in Table 4.17 and $m_\alpha + 100 \approx 400$ MeV in Table 4.16. 154
- 4.8 The calculated single particle momentum distribution $n(q)$ (upper panel) and two-body correlation function $c(r)$ (lower panel) as functions of the momentum cut-off parapeter Λ_α of the three-body force MT3-I with $\Lambda_\alpha = 1000$ MeV. 157
- 4.9 The calculated single particle momentum distribution $n(q)$ (upper panel) and two-body correlation function $c(r)$ (lower panel) as functions of the both attractive and repulsive coupling strength a_α and $a_{\alpha\rho}$ of the three-body force MT3-II with $a_\alpha = -2.69$ and $a_{\alpha\rho} = 2.40$ 160
- 4.10 The calculated total wave function of three-body bound state $|\Psi(p, q, x)|$ in unit $[\text{fm}^3]$ at $x = 1$ as a function of the different meson-nucleon coupling strength a_α of the three-body force MT3-II. The upper left: $2a_\alpha, 2a_{\alpha\rho}$, the upper right: $4a_\alpha, 4a_{\alpha\rho}$, the lower left: $8a_\alpha, 8a_{\alpha\rho}$, the lower right: $16a_\alpha, 16a_{\alpha\rho}$ 161
- 4.11 The calculated single particle momentum distribution $n(q)$ (upper panel) and two-body correlation function $c(r)$ (lower panel) as functions of different force models. 165
- 4.12 The calculated total wave function of three-body bound state $|\Psi(p, q, x)|$ in unit $[\text{fm}^3]$ at $x = 1$ as a function of the different force models. 166
- 4.13 The calculated single particle momentum distribution $n(q)$ (upper panel) and two-body correlation function $c(r)$ (lower panel) as functions of different force models: MT2-I and MMT3-I. 169

A.1	The microprocessor architecture of SP CPU on Seaborg.	208
-----	---	-----

List of Tables

3.1	The parameters and deuteron binding energy for the Malfliet-Tjon type potential of our calculation. As conversion factor We use units such that $\hbar c = 197.3286 \text{ MeV fm} = 1$	76
3.2	The elastic differential cross sections at different energies for selected scattering angles. The cross section labeled by T results from the converged solution of the integral equation Eq. (3.69) by Padé summation. The column labeled T' is calculated by reinserting the original solution into the Faddeev equation Eq. (3.143).	79
3.3	The elastic differential cross section at selected angles with energy $E_{lab} = 0.01 \text{ GeV}$ as function of the grid points. The double prime quantities represent the integration variables.	81
3.4	The elastic differential cross section at selected angles energy $E_{lab} = 0.5 \text{ GeV}$ as function of the grid points. The double prime quantities represent the integration variables.	82
3.5	The total elastic and break-up cross sections together with the total cross section extracted via the optical theorem at two selected energies (0.01 and 0.5 GeV) as function of the grid points. The double prime quantities are the integration variables.	83
3.6	The total elastic cross section, total breakup cross section and total cross section extracted via the optical theorem calculated in different coordinate systems at selected energies. The choice of coordinate system, i.e. which vector is aligned parallel to the z-axis, is indicated by the superscripts q_0 , q and p	84

3.7	The total elastic cross sections at $E_{lab} = 3.0$ MeV calculated for different values of the angle φ_{q_0} in Eq. (3.70) with the + sign of $\sin(\varphi_p - \varphi_{q_0})$. The calculations are carried out in two different coordinate systems, characterized by the superscripts q_0 and q , which indicate, which vector is chosen to be parallel to the z-axis.	88
3.8	The total elastic cross sections at $E_{lab} = 3.0$ MeV calculated for different sign of $\sin(\varphi_p - \varphi_{q_0})$ where $\varphi_{q_0} = 0$. The meaning of the superscripts is the same as in Table 3.7.	88
4.1	The parameters of the purely attractive two-body force MT2-I. . . .	130
4.2	The parameters of two-body force MT2-II.	130
4.3	The parameters of three-body force MT3-I.	131
4.4	The parameters of the three-body force MT3-II.	131
4.5	The calculated eigenvalue E from the the solution of the Faddeev equation and the expectation values of the kinetic energy $\langle H_0 \rangle$, the two-body potential $\langle V_{II} \rangle$, the three-body potential energy $\langle V_{III} \rangle$ and the total Hamiltonian $\langle H \rangle$ as functions of the number of grid points NPHIINT for the ϕ'' grid with the other grid sizes fixed as NP = 44, NQ = 44 and NX = 20. The calculations are based on the two-body and three-body forces of MT2-II+MT3-I.	135
4.6	The calculated eigenvalue E from the the solution of the Faddeev equation and the expectation values of the kinetic energy $\langle H_0 \rangle$, the two-body potential $\langle V_{II} \rangle$, the three-body potential energy $\langle V_{III} \rangle$ and the total Hamiltonian $\langle H \rangle$ as functions of the number of grid points NX for the x and x'' grid with the other grid sizes fixed as NP = 44, NQ = 44 and NPHIINT = 20. The calculations are based on the two-body and three-body forces of MT2-II+MT3-I.	135

- 4.7 The calculated eigenvalue E from the the solution of the Faddeev equation and the expectation values of the kinetic energy $\langle H_0 \rangle$, the two-body potential $\langle V_{II} \rangle$, the three-body potential energy $\langle V_{III} \rangle$ and the total Hamiltonian $\langle H \rangle$ as functions of the number of grid points NP for the p and p'' grid with the other grid sizes fixed as NQ = 44, NX = 42, and NPHIINT = 20. The calculations are based on the two-body and three-body forces of MT2-II+MT3-I. 136
- 4.8 The calculated eigenvalue E from the the solution of the Faddeev equation and the expectation values of the kinetic energy $\langle H_0 \rangle$, the two-body potential $\langle V_{II} \rangle$, the three-body potential energy $\langle V_{III} \rangle$ and the total Hamiltonian $\langle H \rangle$ as functions of the number of grid points NPHIINT for the ϕ'' grid with the other grid sizes fixed as NP = 74, NX = 42, and NPHIINT = 20. The calculations are based on the two-body and three-body forces of MT2-II+MT3-I. 136
- 4.9 The calculated eigenvalue E from the the solution of the Faddeev equation and the expectation values of the kinetic energy $\langle H_0 \rangle$, the two-body potential $\langle V_{II} \rangle$, the three-body potential energy $\langle V_{III} \rangle$ and the total Hamiltonian $\langle H \rangle$ as functions of the number of grid points NP=NQ for the $p - q$ grid with NX = 42 NPHIINT = 20. The calculations are based on the two-body and three-body forces of MFT2NF-II+MFT3NF-I. 137
- 4.10 The results of average relative error $\overline{\Delta}$ calculated on different (p, q) region with different grid sizes. 138
- 4.11 The same as Table 4.9 but calculations are based on MT2-II two-body force alone. 138
- 4.12 The same as Table 4.10 but calculations are based on MT2-II two-body force alone. 138
- 4.13 The same as Table 4.9 but the calculations are based on the MT2-II + MT3-II. 140

- 4.14 The binding energy E , the expectation values $\langle r \rangle$, $\langle R \rangle$ and deviation δ characterizes the deviation from the shape of an equilateral triangle and is defined in Eq. (4.56) calculated with the MT2-II two-body force alone and with the addition of the two different three-body forces. 143
- 4.15 The calculated expectation values of the kinetic energy $\langle H_0 \rangle$, the two-body potential $\langle V_{II} \rangle$, the three-body potential energy $\langle V_{III} \rangle$ and the total Hamiltonian $\langle H \rangle$ as functions of the different meson-nucleon coupling strength a_α of the three-body force MT3-I. 148
- 4.16 The calculated expectation values of the kinetic energy $\langle H_0 \rangle$, the two-body potential $\langle V_{II} \rangle$, the three-body potential energy $\langle V_{III} \rangle$ and the total Hamiltonian $\langle H \rangle$ as functions of the exchanged meson mass m_α of the three-body force MT3-I with $m_\alpha = 305.8593$ MeV and ratio $\frac{a_\alpha}{m_\alpha}$ kept constant. 152
- 4.17 The same as Table 4.15 but with the meson-nucleon coupling strength a_α changed to $\frac{1}{5}a_\alpha$ and $\frac{1}{3}a_\alpha$ 155
- 4.18 The calculated expectation values of the kinetic energy $\langle H_0 \rangle$, the two-body potential $\langle V_{II} \rangle$, the three-body potential energy $\langle V_{III} \rangle$ and the total hamiltonian $\langle H \rangle$ as functions of the momentum cut-off parameter Λ_α of the three-body force MT3-I with $\Lambda_\alpha = 1000$ MeV. 156
- 4.19 The calculated expectation values of the kinetic energy $\langle H_0 \rangle$, the two-body potential $\langle V_{II} \rangle$, the three-body potential energy $\langle V_{III} \rangle$ and the total hamiltonian $\langle H \rangle$ as functions of both the attractive and repulsive coupling strength a_α and $a_{\alpha\rho}$ of the three-body force MT3-II with $a_\alpha = -2.69$ and $a_{\alpha\rho} = 2.40$ 158
- 4.20 The MT3M-I parameters. 162
- 4.21 The MT3M-II parameters. 162

4.22	The calculated expectation values of the kinetic energy $\langle H_0 \rangle$, the two-body potential $\langle V_{II} \rangle$, the three-body potential energy $\langle V_{III} \rangle$, the total hamiltonian $\langle H \rangle$ and the binding energy E as functions of different models.	162
4.23	The parameters of the purely attractive three-body force MMT3-I. .	167
4.24	The calculated eigenvalue E from the the solution of the Faddeev equation, the expectation values of the kinetic energy $\langle H_0 \rangle$, and the potential energy $\langle V \rangle$ for the two-body force MT2-I and the three-body force MMT3-I. Both forces give similar binding energies. The expectation values of $\langle R \rangle$ and $\langle r \rangle$ are also given for both cases.	167
5.1	The percentage error of Gaussian quadrature and spline based method for the integration $\int_b^a f(x) \ln x - q dx$ when $f(x) = \sqrt{x}$ at different number of grid points. The calculations of spline based method are performed on both the Gaussian grid and usual equal spacing grid. .	185
5.2	The percentage error of Gaussian quadrature and spline based method for the integration $\int_b^a f(x) \ln x - q dx$ when $f(x) = x^2$ at different number of grid points. The calculations of spline based method are performed on both the Gaussian grid and usual equal spacing grid. .	185
5.3	The percentage error of Gaussian quadrature and spline based method for the integration $\int_b^a f(x) \ln x - q dx$ when $f(x) = x^4$ at different number of grid points. The calculations of spline based method are performed on both the Gaussian grid and usual equal spacing grid. .	185
5.4	Convergence property of Padé approximation and direct sum of Neumann series at different orders for the solution of T . The results are based on the calculation at $E_{lab} = 10$ MeV.	192
5.5	Convergence property of Padé approximation and direct sum of Neumann series at different orders for the solution of T . The results are based on the calculation at $E_{lab} = 500$ MeV.	192

5.6	The sequence of the trial energy E and the corresponding largest eigenvalue $\lambda(E)$ in IOV method. The results is based on the real calculation of three-body bound state according to Eq. (4.3).	196
A.1	The run time of one Padé iteration with the different number of threads on each node.	210
A.2	Performance Counting of direct and permutation methods for calculating three-body force.	211

Chapter 1

Introduction

The wish to understand the forces between fundamental constituents is a basic goal in physics. An enormous amount of efforts has been made to understand and model nuclear forces. Especially during the last years considerable progress has been made towards this goal. The time has now come to apply those models in an environment where three or four nucleons interact with each other and thoroughly test underlying assumptions of nuclear physics.

The vast majority of information about the nuclear (or strong) interaction has been and is still obtained with scattering experiments. Because of the short range of the nuclear interaction and thus the small distances involved, scattering experiments testing the short-range part of the strong force should be carried out at higher energies, e.g. with the proton beam from the RCNP Ring Cyclotron at Osaka University with an energy up to 400 MeV and the polarized proton beam in the COoler SYnchrotron (COSY) at the Forschungszentrum Jülich with an energy up to 2.5 GeV.

Since scattering is a process in three space dimensions, ideally one should solve the Schrödinger equation exactly in all three dimensions at once. Since the 1950s, solutions for three-body scattering have been obtained using a partial wave approximation. The main reason for this have been computer limitations. The technique of partial wave approximation consists of solving a large number of one-dimensional equations and summing the results to obtain the final solution, which then describes the experimental data in three dimensions. In principle, this summation involves an

infinite number of terms. Of course, one can not solve the equation an infinite number of times, so convergence with respect to the number of terms must be shown for each application when using the partial wave based method.

The aim of this work is to abandon these traditional partial wave based methods used in three-nucleon scattering calculations, and formulate, develop and implement new conceptual techniques and computational algorithms to obtain solutions for few-body systems directly in three dimensions. This pioneering work will abolish the necessity for partial wave approximations altogether. We believe that our work will open the road to new types and applications of exact few-body calculations in nuclear physics. We would also like to emphasize that our numerical technique is not restricted to nuclear physics, but is generally applicable to physical situations which have many angular momentum contributions, e.g. in atomic and molecular physics through the weak and long range Coulomb force.

Pioneering work in the theoretical foundation of the three-body problem was carried out by Faddeev [1, 2, 3]. After some important reformulation by Alt, Grassberger and Sandhas [4], and Glöckle [5], the kernel of Faddeev equation is compact, which guarantees the convergence and the uniqueness of the solution. The Faddeev formalism takes advantage of the fact that hadronic forces are strong and short ranged, it sums all pair interactions as a two-body t -matrix by Lippmann-Schwinger equation [6]. The first calculation based on the Faddeev scheme were carried out in [7, 8] using separable spin-dependent s -wave Yamaguchi forces [9] and in [10] using a general local force. After this, a huge body of work by different groups followed. With realistic nuclear two-body forces, e.g. Nijmegen [11], CD-Bonn [12] and AV18 [13], the three-body system has been calculated within the Faddeev formalism through various techniques. Some recent examples for three-body scattering are given in [14, 15, 16, 17], or the bound states in [18, 19, 20, 21, 22, 23, 24, 25]. A summary of those achievements is given in [26, 27, 28, 30].

The present available realistic nuclear forces are constructed and fitted at the energy scale below $E_{lab} = 350$ MeV. Their structure and properties at short range below 1 fm are not clear. In order to probe the strong interaction in nuclear systems at shorter distances, experimental facilities all over the world are upgraded to per-

form three-body scattering experiments with the incident projectile energy from few hundred MeV to the GeV scale.

The traditional Faddeev calculations carried out in a partial wave basis have problems in describing nucleon-deuteron (Nd) scattering at energies higher than 250 MeV. The partial wave decomposition works in a truncated angular momentum basis where the continuous angular variables are replaced by a finite number of discrete angular momentum quantum numbers. This approach reduces the number of continuous variables to be discretized in numerical calculations. For low projectile energies, the validity of the partial wave decomposition is justified by arguments related to the centrifugal barrier and the short range of the nuclear force. If one considers three-body scattering at a few hundred MeV projectile energy, the number of partial waves needed to achieve convergence proliferates, and limitations with respect to computational feasibility and accuracy are reached. Thus it appears natural to avoid a partial wave representation completely and work directly with vector variables. Indeed this is common practice in bound state calculations based on variational [31] and Green's Function Monte Carlo (GFMC) methods [32, 33, 34, 35], which are carried out in coordinate space.

An approach directly based on momentum vectors was pioneered for a three-body system of identical bosons. In Ref. [36], by using the two-body force of Malfliet-Tjon type [10], the Lippmann-Schwinger equation for two-body t -matrix was solved in momentum space and the two-body t -matrix was obtained as a function of momentum vectors. In Refs. [37, 38], the Faddeev equations for three-body bound state as well as the three-body scattering below the breakup threshold were solved straightforwardly with high numerical efficiency and accuracy. These works indicate that the formulation of Faddeev equations in terms of momentum vectors for identical bosons is very feasible and transparent. For fermions, the coupling of spin (and isospin) will lead only to a finite number of equations. Thus for both, bosons and fermions, a momentum vector based approach to solve Faddeev equations for the three-body system is relatively easy. In this spirit, the two-body t -matrix based on realistic force has been formulated in [39], and the proton-deuteron breakup process has been successfully studied up to 500 MeV projectile energy based on the first order approximation

of the three-body transition operator in a Faddeev equation using realistic nuclear two-body forces [40].

In this work the full Faddeev equation for three-boson scattering at higher energies is solved in momentum space with momentum vectors using two-body forces of Malfliet-Tjon type, i.e. Yukawa potentials describing the intermediate range attraction and short range repulsion of the nuclear force. The purpose of this is to obtain the solution of the full three-body transition operator as a function of momentum vectors, which accounts for all rescattering effects in terms of a two-body t -matrix. The full solution of the Faddeev equation needs to treat the three-body breakup singularities inherent in the free three-body propagator. As an extension of the work in Ref. [37], we will also solve the Faddeev equation for the three-body bound state with the inclusion of a three-body force. The purpose for this is to develop an efficient way to calculate three-body forces in the momentum vector approach, which can also be applied to three-body scattering.

The dissertation is organized as follows. Chapter 2 gives the Hamiltonian governing the three-body dynamics. The derivation of the Faddeev equations for the total wave function of the three-body bound state and the three-body scattering amplitudes is briefly reviewed. These equations are the theoretical foundations of this work.

In Chapter 3 we show that the three-body scattering equation can be solved in a straightforward manner when employing momentum vector variables, i.e. magnitudes of momenta and angles between the momentum vectors. We first review the Jacobi coordinates in momentum space for three-body system. Using these Jacobi coordinates, we establish the explicit Faddeev equation for the three-body transition operator and the operators for elastic scattering and breakup processes in terms of the selected variables. The numerical method to solve the Faddeev equation for the three-body transition operator is described. Results showing the accuracy of this technique as well as a demonstration of its self-consistency are given. Then we study in detail reaction mechanisms in three-body scattering driven by a two-body force, including the elastic scattering, semi-exclusive and exclusive breakup processes in the intermediate energy regime from projectile energy $E_{lab} = 0.2$ GeV to $E_{lab} = 1.0$ GeV.

Our focus here is to explore the importance of rescattering terms as a function of the projectile energy and the reaction considered.

In Chapter 4 we study the system of three bosons bound with two- and three-body forces. First we explicitly set up the bound state Faddeev equation in Jacobi momentum coordinates. Then we implement a three-dimensional approach for calculating the three-body forces based on their permutation symmetry. The equation is solved and the total wave function of the three-body bound state is obtained as a function of momentum vector variables. We further analyze the accuracy of the calculation. Using our now well established procedure to treat three-body forces, we investigate the three-body bound state properties as functions thereof. We also do an excursion into a playground with forces by changing the three-body force parameters, and study how the three-body systems bound by only three-body force behaves, and investigate the interplay between two- and three-body forces in this scenario.

In Chapter 5 the necessary analytical and numerical techniques used in this work are described in detail. The cubic spline based method for multi-dimensional interpolations is briefly reviewed. The spline based integration methods are introduced, especially the one for calculating an integral with logarithmic singularities. The Padé summation for solving the inhomogeneous equation of the three-body scattering amplitude and an iterative method of the Lanczos' type for solving the homogeneous eigenvalue equation of the three-body bound state are presented. We summarize in Chapter. 6

In Appendix A, we give an overview about the parallel high performance computing techniques applied in our Faddeev calculations for a three-body system.

Chapter 2

Description of Three Particle Systems with Faddeev Scheme

In this chapter a generic total Hamiltonian governing three-body dynamics is introduced. Without losing the generality of the three-body Hamiltonian structure, one widely applied two-body and three-body force decomposition approach having nice features with respect to the Faddeev scheme is described. The derivation of the Faddeev equations for the total wave function of three-body bound state and the three-body scattering amplitudes is briefly reviewed. These equations are the theoretical foundations of this work.

2.1 The Hamiltonian of Three-Body System

The total Hamiltonian of a three-body system in general is given as

$$H = H_0 + V_{II} + V_{III}. \quad (2.1)$$

Here the H_0 is the total kinetic energy, V_{II} is the two-body force and V_{III} is the three-body force. Suppose that three particles are labeled as i, j, k respectively, then V_{II} can be written into three different pieces by using the “odd-man-out” notation as

$$V_{II} = \sum_{i=1}^3 V_i \quad (2.2)$$

where the V_i is the pair force between particles j and k with ($j \neq i \neq k$). Obviously V_i is symmetric under the permutation of particles j and k . Similarly any three-body force V_{III} can also be decomposed into three pieces as

$$V_{III} = \sum_{i=1}^3 V_4^{(i)}. \quad (2.3)$$

such that the $V_4^{(i)}$ is symmetric under the permutation of particles j and k . The decomposition suggested in Eq. (2.3) is motivated by Tucson-Melbourne [41] and Fujita-Miyazawa [42] three-body forces which are based on 2π -exchange mechanism and constitute the basis of widely used three-body force models in nuclear physics. For example, when considering 2π -exchange three-body forces, the $V_4^{(i)}$ is the part where the nucleon i undergoes the $\pi - N$ off-mass-shell scattering. Following the decomposition scheme in Eqs. (2.2) and (2.3), the total Hamiltonian in Eq. (2.1) becomes

$$H = H_0 + \sum_{i=1}^3 \left(V_i + V_4^{(i)} \right). \quad (2.4)$$

It is obvious that this decomposition allows the treatment of both two-body and three-body forces on equal footing.

2.2 The Faddeev Equation for Three-Body Bound State

For sake of the simplicity and clarity and to show the basic idea of the Faddeev scheme, we consider a three-body bound state at first [19]. The Schrödinger equation for the total wave function Ψ of a three-body bound state described by the Hamiltonian in Eq. (2.4) is

$$\left(H_0 + \sum_{i=1}^3 \left(V_i + V_4^{(i)} \right) \right) |\Psi\rangle = E|\Psi\rangle. \quad (2.5)$$

This Schrödinger equation can be cast into an integral form as

$$|\Psi\rangle = G_0 \sum_{i=1}^3 \left(V_i + V_4^{(i)} \right) |\Psi\rangle. \quad (2.6)$$

where $G_0 = (E - H_0)^{-1}$ is the free three-body propagator. This defines the Faddeev decomposition

$$|\Psi\rangle = \sum_{i=1}^3 |\psi_i\rangle \quad (2.7)$$

where each Faddeev component $|\psi_i\rangle$ fulfills

$$|\psi_i\rangle = G_0 \left(V_i + V_4^{(i)} \right) |\Psi\rangle = G_0 \left(V_i + V_4^{(i)} \right) |\psi_i\rangle + G_0 \left(V_i + V_4^{(i)} \right) \sum_{j \neq i} |\psi_j\rangle, \quad (2.8)$$

one has

$$\begin{aligned} (1 - G_0 V_i) |\psi_i\rangle &= G_0 V_4^{(i)} |\psi_i\rangle + G_0 V_i \sum_{j \neq i} |\psi_j\rangle + G_0 V_4^{(i)} \sum_{j \neq i} |\psi_j\rangle \\ &= G_0 V_i \sum_{j \neq i} |\psi_j\rangle + G_0 V_4^{(i)} \sum_j |\psi_j\rangle \end{aligned} \quad (2.9)$$

and thus

$$|\psi_i\rangle = (1 - G_0 V_i)^{-1} G_0 V_i \sum_{j \neq i} |\psi_j\rangle + (1 - G_0 V_i)^{-1} G_0 V_4^{(i)} \sum_j |\psi_j\rangle. \quad (2.10)$$

According to the Lippmann-Schwinger equation for two-body t -matrix

$$t_i = V_i + V_i G_0 t_i, \quad (2.11)$$

the two-body force V_i in Eq. (2.10) can be summed up separately as

$$\begin{aligned} (1 - G_0 V_i)^{-1} &= 1 + G_0 V_i + G_0 V_i G_0 V_i + G_0 V_i G_0 V_i \cdots \\ &= 1 + G_0 \underbrace{(V_i + V_i G_0 V_i + V_i G_0 V_i G_0 V_i + \cdots)}_{t_i} \\ &= 1 + G_0 t_i \end{aligned} \quad (2.12)$$

and

$$\begin{aligned} (1 - G_0 V_i)^{-1} G_0 V_i &= G_0 V_i + G_0 V_i G_0 V_i + G_0 V_i G_0 V_i G_0 V_i + \cdots \\ &= G_0 \underbrace{(V_i + V_i G_0 V_i + V_i G_0 V_i G_0 V_i + \cdots)}_{t_i} \\ &= G_0 t_i. \end{aligned} \quad (2.13)$$

Substituting Eqs. (2.12) and (2.13) into Eq. (2.10), one gets a set of three coupled equations

$$\begin{aligned} |\psi_i\rangle &= G_0 t_i \sum_{j \neq i} |\psi_j\rangle + (1 + G_0 t_i) G_0 V_4^{(i)} \sum_j |\psi_j\rangle \\ &= G_0 \left(t_i \sum_{j \neq i} |\psi_j\rangle + (1 + t_i G_0) V_4^{(i)} \sum_j |\psi_j\rangle \right). \end{aligned} \quad (2.14)$$

These are the homogeneous Faddeev equations for a three-body bound state. For three identical particles, all Faddeev components $|\psi_i\rangle$ take identical functional form and only particles permute. Thus $|\psi_j\rangle$ and $|\psi_k\rangle$ can be expressed in terms of $|\psi_i\rangle$ with the help of permutation operators. For example,

$$\begin{aligned} |\psi_2\rangle &= P_{12} P_{23} |\psi_1\rangle \\ |\psi_3\rangle &= P_{13} P_{23} |\psi_1\rangle \end{aligned} \quad (2.15)$$

where P_{ij} is the permutation operator of particle i and j . The $P_{12} P_{23}$ is cyclic, the $P_{13} P_{23}$ is anti-cyclic, and together with the identity, they furnish a complete irreducible representation of the permutation group $S(3)$. So without losing generality, the pair indices can be dropped and the coupled Faddeev equations in Eq. (2.14) for three identical particles become a single one, i.e.

$$|\psi\rangle = G_0 t P |\psi\rangle + G_0 (1 + t G_0) V_4^{(1)} (1 + P) |\psi\rangle \quad (2.16)$$

where $P = P_{12} P_{23} + P_{13} P_{23}$ and $|\psi\rangle$ means $|\psi_1\rangle$. When the three-body force $V_4^{(1)}$ is ignored, one ends up with

$$|\psi\rangle = G_0 t P |\psi\rangle. \quad (2.17)$$

The total wave function in Eq. (2.7) then is given as

$$|\Psi\rangle = (1 + P) |\psi\rangle. \quad (2.18)$$

Summarizing, the two-body and three-body forces are treated on an equal footing based on the decomposition in Eq. (2.4) in the Faddeev scheme for a three-body system. The main advantage of the Faddeev scheme is that the two-body interactions

can be summed up to infinite order into the two-body t -matrix separately by using the Lippmann-Schwinger equation in Eq. (2.11). In the case of identical particles, the three coupled Faddeev equations for Faddeev components in Eq. (2.14) are reduced to a single one in Eq. (2.16) with the application of permutation operators.

2.3 Faddeev Equations for Three-Body Scattering Operators

In an experiment, a three-body scattering process is usually initiated by a particle incident on a two-body bound pair. This initial channel state is given by

$$|\phi_i\rangle = |\varphi_d \mathbf{q}_0\rangle_i \quad (2.19)$$

where the $|\mathbf{q}_0\rangle$ is the momentum eigenstate of the projectile particle i coming with experimentally controlled momentum \mathbf{q}_0 and the $|\varphi_d\rangle$ is the two-body bound state composed of particles j and k . After the scattering the final channel states for the three particles can be categorized into two types. One is the elastic channel where a bound pair is still there. The elastic channel state has the same form as that of the initial channel state in Eq. (2.19) but with different momentum \mathbf{q} carried by the free particle i , i.e.

$$|\phi'_i\rangle = |\varphi_d \mathbf{q}\rangle_i. \quad (2.20)$$

The other one is the breakup channel where all three particles are free. The channel state $|\phi_0\rangle$ is given by

$$|\phi_0\rangle = |\mathbf{p} \mathbf{q}\rangle \quad (2.21)$$

where $|\mathbf{p}\rangle$ is the relative momentum of a nucleon j and k pair and \mathbf{q} is the relative momentum between the nucleon i and the nucleon j and k pair. (Here we use the Jacobi coordinates as variables in momentum space \mathbf{p} and \mathbf{q} for three particles. A detailed discussion of the Jacobi coordinates will be given in Section 3.1.) The elastic channel states in Eqs. (2.20) and the initial channel state in (2.19) are governed by

the channel Hamiltonian

$$H_i = H_0 + V_i \quad (2.22)$$

in which the H_0 is the operator of kinetic energy and V_i is the pair interaction which supports the bound state. Each elastic channel state fulfills its corresponding channel Hamilton equation

$$\begin{aligned} H_i |\phi_i\rangle &= \left(E_d + \frac{3}{4m} q_0^2 \right) |\phi_i\rangle, \\ H_i |\phi'_i\rangle &= \left(E_d + \frac{3}{4m} q^2 \right) |\phi'_i\rangle. \end{aligned} \quad (2.23)$$

Here E_d is the binding energy of the pair and m is the particle mass. The breakup channel state in Eq. (2.21) which describes the free motion of three particle is thus the eigenstate of H_0 :

$$H_0 |\mathbf{p}\mathbf{q}\rangle = \left(\frac{p^2}{m} + \frac{3}{4m} q^2 \right) |\mathbf{p}\mathbf{q}\rangle. \quad (2.24)$$

The scattering state $|\Psi\rangle^{(+)}$ initiated by $|\phi_i\rangle$ is governed by the total Hamiltonian in Eq. (2.4) and its Schrödinger equation in the integral form is

$$|\Psi\rangle^{(+)} = G_0 \sum_{i=1}^3 \left(V_i + V_4^{(i)} \right) |\Psi\rangle^{(+)}. \quad (2.25)$$

Like the three-body bound state case in Eq. (2.6), the scattering state in Eq. (2.25) can also be used to define the Faddeev decomposition for $|\Psi\rangle^{(+)}$ as

$$|\Psi\rangle^{(+)} = \sum_{i=1}^3 |\psi_i\rangle^{(+)} \quad (2.26)$$

with

$$|\psi_i\rangle^{(+)} = G_0 \left(V_i + V_4^{(i)} \right) |\Psi\rangle^{(+)}. \quad (2.27)$$

As illustrated in Eqs. (2.6) and (2.25), (2.7) and (2.26), (2.8) and (2.27), there is formal equivalence between the bound state and scattering state in their corresponding Schrödinger equations, Faddeev decompositions and components [43]. Then the resulting Faddeev equation for the Faddeev component $|\psi_1\rangle^{(+)}$ of scattering state $|\Psi\rangle^{(+)}$ is given by

$$|\psi\rangle^{(+)} = |\phi\rangle + G_0 t P |\psi\rangle^{(+)} + G_0 (1 + t G_0) V_4^{(1)} (1 + P) |\psi\rangle^{(+)}. \quad (2.28)$$

where the boundary condition of initial channel state $|\phi_1\rangle$ is naturally incorporated by noting that $(1 - G_0 V_1)|\phi_1\rangle = 0$ according to Eq. (2.23). The homogeneous version thereof is the same one as that for three-body bound state in Eq. (2.16). Without losing generality for the scattering of three identical particles, here we already assume (1) is the incoming free nucleon and (23) is the bound pair in the deuteron. So we drop the index 1, and always refer to this particular choice $|\phi_1\rangle \equiv |\phi\rangle$ and $|\psi\rangle^{(+)} \equiv |\psi_1\rangle^{(+)}$. However, the observables in a scattering experiment are not the scattering states, but the elastic and breakup cross sections σ_{el} and σ_{br} , which are proportional to the square of the magnitudes of their transition amplitudes, i.e.

$$\begin{aligned}\sigma_{el} &\propto |\langle\phi|\Psi\rangle^{(+)}|^2 = |\langle\phi'|U|\phi\rangle|^2, \\ \sigma_{br} &\propto |\langle\phi_0|\Psi\rangle^{(+)}|^2 = |\langle\phi_0|U_0|\phi\rangle|^2.\end{aligned}\quad (2.29)$$

Eqs. (2.29) defines the operator U for the elastic scattering and the operator U_0 for the breakup process. The central task in a scattering problem is to find the solutions of U and U_0 . The transition operator T accompanying the Faddeev component $|\psi\rangle^{(+)}$ in Eq. (2.28) can be defined by

$$|\psi\rangle^{(+)} = |\phi\rangle + G_0 T |\phi\rangle. \quad (2.30)$$

Then comparing Eq. (2.28) and Eq. (2.30), one has

$$T|\phi\rangle = tP|\psi\rangle^{(+)} + (1 + tG_0)V_4^{(1)}(1 + P)|\psi\rangle^{(+)}. \quad (2.31)$$

Substituting Eq. (2.30) back to Eq. (2.31) yields the Faddeev like equation for the operator T as

$$\begin{aligned}T|\phi\rangle &= tP|\phi\rangle + tPG_0 T|\phi\rangle \\ &+ (1 + tG_0)V_4^{(1)}(1 + P)|\phi\rangle + (1 + tG_0)V_4^{(1)}(1 + P)G_0 T|\phi\rangle.\end{aligned}\quad (2.32)$$

Since Eq. (2.28) incorporates all boundary conditions, the associated transition operator T in above equation contains all aspects of the scattering dynamics driven by both two-body and three-body forces. Thus the elastic scattering operator U and the breakup operator U_0 can be constructed from T with their specific channel conditions. In the breakup channel, all three particles are outgoing and asymptotically free with

the propagator G_0 . Therefore the breakup operator U_0 should be the infinite sum of all two-body and three-body interactions. Since there are three Faddeev components, the full breakup operator U_0 is straightforwardly constructed by using T and the permutation operator P

$$U_0|\phi\rangle = (1 + P)T|\phi\rangle. \quad (2.33)$$

In the elastic channel, there is a free particle plus a bound pair with the channel propagator G . The sum of two-body interactions between this bound pair should not occur in U , i.e only the sum associated with the projectile-target interactions are allowed. In order to explicitly extract the asymptotic behavior of elastic channel provided in Eq. (2.28), we first notice that

$$\begin{aligned} G_0 t &= G_0(V + VG_0V + VG_0VG_0V + \cdots) \\ &= (G_0 + G_0VG_0 + G_0VG_0VG_0 + \cdots)V \\ &= GV \end{aligned} \quad (2.34)$$

and

$$\begin{aligned} (1 + G_0 t)G_0 &= G_0 + G_0 t G_0 \\ &= G_0 + G_0(V + VG_0V + VG_0VG_0V + \cdots)G_0 \\ &= G_0 + G_0VG_0 + G_0VG_0VG_0 + \cdots \\ &= G, \end{aligned} \quad (2.35)$$

where we apply the Lippmann-Schwinger equation in Eq. (2.11) and the resolvent identity $G = G_0 + G_0VG$. Here $G \equiv G_1$, $t \equiv t_1$ and $V \equiv V_1$ if the scattering is initiated by $|\phi_1\rangle$. Then Eq. (2.28) can be rewritten in the following form

$$|\psi\rangle^{(+)} = |\phi\rangle + GVP|\psi\rangle^{(+)} + GV_4^{(1)}(1 + P)|\psi\rangle^{(+)} \quad (2.36)$$

where the elastic channel condition with channel propagator G is explicit. The elastic operator can be defined as

$$|\psi\rangle^{(+)} = |\phi\rangle + GU|\phi\rangle \quad (2.37)$$

Comparing Eqs. (2.36) and (2.37), the elastic operator U is identified as

$$U|\phi\rangle = VP|\psi\rangle^{(+)} + V_4^{(1)}(1+P)|\psi\rangle^{(+)}. \quad (2.38)$$

According to Eq. (2.23), one has $\langle\phi|V = \langle\phi|G_0^{-1}$ which means that in elastic channel the V can be replaced by G_0^{-1} . The U can then be written as

$$U|\phi\rangle = G_0^{-1}P|\psi\rangle^{(+)} + V_4^{(1)}(1+P)|\psi\rangle^{(+)}. \quad (2.39)$$

Again, substituting Eq. (2.30) into Eq. (2.39) yields the equation for U in terms of T and $V_4^{(1)}$ as

$$U|\phi\rangle = PG_0^{-1}|\phi\rangle + PT|\phi\rangle + V_4^{(1)}(1+P)(1+G_0T)|\phi\rangle. \quad (2.40)$$

Eq. (2.32) for the three-body transition operator T , Eq. (2.33) for the breakup process operator U_0 and Eq. (2.40) for the elastic scattering operator U are the basic dynamical equations to describe the elastic and breakup processes in three-body scattering. When only a two-body force is considered, Eq. (2.32) for the transition operator T is reduced to

$$T|\phi\rangle = tP|\phi\rangle + tPG_0T|\phi\rangle, \quad (2.41)$$

and the Eqs. (2.33) and (2.40) for physical breakup and elastic operators become

$$U_0|\phi\rangle = (1+P)T|\phi\rangle \quad (2.42)$$

and

$$U|\phi\rangle = PG_0^{-1}|\phi\rangle + PT|\phi\rangle. \quad (2.43)$$

The closed form of the Faddeev equation is given by Eq. (2.41). If it is explicitly written out as

$$T = tP + tPG_0tP + tPG_0tPG_0tP + \cdots, \quad (2.44)$$

it generates the multiple scattering series for three-body scattering in terms of the two-body t -matrix. An inspection of the operators may yield transparent physical insight

into the reaction mechanism of three-body elastic and breakup processes. The first term tP in Eq. (2.41) can be clearly interpreted as the scattering contribution of the projectile particle from each component in the bound pair. It should be emphasized that all pair interactions have already been summed up into the two-body t -matrix because of the application of Faddeev scheme. This is important because the two-body interactions in hadronic physics are strong and thus non-perturbative. The next term tPG_0tP contains the rescattering effects next to that of the initial ones. The permutation operator P guarantees that the scattering never occurs subsequently in the same pair, which is self consistent since all pair interactions are already in the two-body t -matrix. It has been well established in [26] that at energies below $E_{lab} = 300$ MeV, the multiple rescattering series converges very slowly, thus the full solution of T in Eq. (2.32) has to be obtained. Nevertheless, at higher energies the approximation up to first and second order in the multiple rescattering series are favored [44]. With two-body interaction only, the convergence of the multiple scattering series as a function of scattering energy will be studied in detail in this work.

2.4 The Unitarity Relation of Scattering Operators

The operators U and U_0 define the transition amplitude from channel state to outgoing scattering state ($t \rightarrow +\infty$). Correspondingly their conjugate operators define the transition amplitudes from channel state to incoming scattering state ($t \rightarrow -\infty$). The outgoing states generated by the action of U and U_0 on the channel state span a complete Hilbert space for a three particle system, so do those of the incoming ones. Thus there is a unitarity relation between operators U and U_0 which basically means that the incoming probability should be equal to the outgoing probability. Here we will show this unitary relation of U and U_0 in the case of only two-body force considered.

We know that all transition operators, including t , T , U and U_0 are analytic functions of $z^\pm = E \pm i\epsilon$, and their outgoing and incoming characters are specified

by the Green functions, namely

$$\begin{aligned} G_0(z^\pm) &= \frac{1}{z^\pm - H_0}, \\ G_i(z^\pm) &= \frac{1}{z^\pm - H_0 - V_i} \end{aligned} \quad (2.45)$$

For simplicity we denote channel Green function $G_i \equiv G$. The sign of the $\pm i\epsilon$ dictates the outgoing or incoming character. The z^+ suggests the outgoing and the z^- suggests the incoming. Thus the unitary relation can be derived from $[U(z^-) - U(z^+)]$. Substituting Eq. (2.37) into Eq. (2.38) and ignoring three-body force, one has

$$U|\phi\rangle = PV|\phi\rangle + PVGU|\phi\rangle. \quad (2.46)$$

This is true for the cases when U and G contain both, z^+ and z^- . Now we consider the unitary relation of U , $\langle\phi'|[U(z^-) - U(z^+)]|\phi\rangle$. One has

$$\begin{aligned} & [U(z^-) - U(z^+)]|\phi\rangle \\ &= [PVG(z^-)U(z^+) - PVG(z^+)U(z^+)]|\phi\rangle \\ &= [PVG(z^-)U(z^-) - PVG(z^+)U(z^+)]|\phi\rangle \\ &+ [PVG(z^-)U(z^+) - PVG(z^-)U(z^+)]|\phi\rangle \\ &= PVG(z^-)[U(z^-) - U(z^+)]|\phi\rangle + PV[G(z^-) - G(z^+)]U(z^+)|\phi\rangle, \end{aligned} \quad (2.47)$$

and thus

$$\langle\phi'|[U(z^-) - U(z^+)]|\phi\rangle = [1 - PVG(z^-)]^{-1}PV[G(z^-) - G(z^+)]U(z^+)|\phi\rangle. \quad (2.48)$$

Now we need to consider $[G(z^-) - G(z^+)]$. For the two-body subsystem in the given channel $|\phi\rangle$, one has the completeness relation [45]

$$|\varphi_d\rangle\langle\varphi_d| + \int d^3p |\mathbf{p}\rangle^{(+)} \langle\mathbf{p}| = 1. \quad (2.49)$$

Here we assume the two-body force just gives one bound state. Let the $|\mathbf{q}\rangle$ the momentum state describing the free motion of the third particle relative to the pair and normalize it as

$$\int d^3q |\mathbf{q}\rangle\langle\mathbf{q}| = 1. \quad (2.50)$$

Define the states

$$\begin{aligned} |\phi_q\rangle &= |\varphi_d\rangle|\mathbf{q}\rangle, \\ |\phi_{pq}\rangle &= |\mathbf{p}\rangle^{(+)}|\mathbf{q}\rangle, \end{aligned} \quad (2.51)$$

which satisfy

$$\begin{aligned} H|\phi_q\rangle &= \left(E_d + \frac{3}{4m}q^2\right)|\phi_q\rangle = E_q|\phi_q\rangle, \\ H|\phi_{pq}\rangle &= \left(\frac{p^2}{m} + \frac{3}{4m}q^2\right)|\phi_{pq}\rangle = E_{pq}|\phi_{pq}\rangle. \end{aligned} \quad (2.52)$$

Here the $H \equiv H_i$ is one of the channel Hamiltonian given in Eq. (2.22) corresponding the states in Eq. (2.49). Then we have following completeness relation

$$\int d^3q |\phi_q\rangle\langle\phi_q| + \int d^3p d^3q |\phi_{pq}\rangle\langle\phi_{pq}| = 1, \quad (2.53)$$

which is suitable to do the spectral expansion of channel propagator $G_i \equiv G$ in Eq (2.45). Inserting the complete set in Eq. (2.53) into the $G_i \equiv G$ in Eq. (2.45) and using Eq. (2.52), the spectral expansion of $G_i \equiv G$ is

$$G(z^\pm) = \int d^3q |\phi_q\rangle \frac{1}{z^\pm - E_q} \langle\phi_q| + \int d^3p d^3q |\phi_{pq}\rangle \frac{1}{z^\pm - E_{pq}} \langle\phi_{pq}| = 1. \quad (2.54)$$

According to the principal value identity

$$\lim_{\epsilon \rightarrow 0} \frac{1}{E \pm i\epsilon - E'} = \frac{P}{E - E'} \mp i\pi\delta(E - E'), \quad (2.55)$$

the expansion of $[G(z^-) - G(z^+)]$ is given as

$$\begin{aligned} &[G(z^-) - G(z^+)] \\ &= \int d^3q |\phi_q\rangle 2\pi i \delta(E - E_q) \langle\phi_q| \\ &+ \int d^3p d^3q |\phi_{pq}\rangle 2\pi i \delta(E - E_{pq}) \langle\phi_{pq}|. \end{aligned} \quad (2.56)$$

In order to derive the unitarity relation in Eq. (2.48), we substitute Eq. (2.56) back to Eq. (2.48) and have following matrix elements which need to be worked out,

$$\begin{aligned} &\langle\phi'| (1 - PVG(z^-))^{-1} PV |\phi_q\rangle, \\ &\langle\phi'| (1 - PVG(z^-))^{-1} PV |\phi_{pq}\rangle, \\ &\langle\phi_{pq}| U(z^+) |\phi\rangle. \end{aligned} \quad (2.57)$$

These matrix elements need to be rewritten in such a form so that the operators are in terms of U and U_0 with argument z^+ , and the bra and ket vectors are the channel states $|\phi\rangle$, $|\phi'\rangle$ and $|\phi_0\rangle$ given in Eqs. (2.19), (2.20) and (2.21) respectively. Since the $|\phi_q\rangle$ and $|\phi_{pq}\rangle$ have different asymptotic behavior as shown in Eq. (2.51), they have different behavior when V acts from left. Together with Eq. (2.52), one has

$$\begin{aligned} V|\phi_q\rangle &= G_0^{-1}|\phi_q\rangle \\ V|\phi_{pq}\rangle &= t|\phi_0\rangle \\ |\phi_{pq}\rangle &= (1 + tG_0)|\phi_0\rangle. \end{aligned} \quad (2.58)$$

For $\langle\phi'|(1 - PVG(z^-))^{-1}PV|\phi_q\rangle$, we use the identity $VG = tG_0$, and have

$$\begin{aligned} &\langle\phi'|(1 - PVG(z^-))^{-1}PV|\phi_q\rangle \\ &= \langle\phi'|[(1 - PtG_0(z^-))^{-1}PG^{-1}(z^-)]|\phi_q\rangle \\ &= \langle\phi'|[(1 + PtG_0(z^-) + PtG_0(z^-)PtG_0(z^-) + \cdots)PG^{-1}(z^-)]|\phi_q\rangle \\ &= \langle\phi'|[PG_0^{-1}(z^-) + P(tP + tPG_0(z^-)tP + \cdots)]|\phi_q\rangle \\ &= \langle\phi'|[PG_0^{-1}(z^-) + PT(z^-)]|\phi_q\rangle \\ &= \langle\phi'|U(z^-)|\phi_q\rangle = \langle\phi_q|U(z^+)|\phi'\rangle^* \end{aligned} \quad (2.59)$$

For $\langle\phi'|(1 - PVG(z^-))^{-1}PV|\phi_{pq}\rangle$, one obtains in a similar fashion

$$\begin{aligned} &\langle\phi'|(1 - PVG(z^-))^{-1}PV|\phi_{pq}\rangle \\ &= \langle\phi'|(1 - t(z^-)PG_0)^{-1}(z^-)Pt(z^-)|\phi_0\rangle \\ &= \langle\phi'|[1 + t(z^-)PG_0(z^-) + t(z^-)PG_0(z^-)t(z^-)PG_0(z^-) + \cdots]t(z^-)P|\phi_0\rangle \\ &= \langle\phi'|[t(z^-)P + t(z^-)PG_0(z^-)T(z^-)]|\phi_0\rangle \\ &= \langle\phi'|T(z^-)|\phi_0\rangle = \langle\phi_0|T(z^+)|\phi'\rangle^* \end{aligned} \quad (2.60)$$

For $\langle\phi_{pq}|U(z^+)|\phi\rangle$,

$$\begin{aligned} \langle\phi_{pq}|U|\phi\rangle &= \langle\phi_0|(1 + tG_0)U|\phi\rangle \\ &= \langle\phi_0|[1 + t(z^+)G_0(z^+)](G_0^{-1}(z^+)P + PT(z^+))|\phi\rangle \\ &= \langle\phi_0|[PG_0^{-1}(z^+) + PT(z^+) + t(z^+)P + t(z^+)G_0P(z^+)T(z^+)]|\phi\rangle \\ &= \langle\phi_0|[PG_0^{-1}(z^+) + PT(z^+) + T(z^+)]|\phi\rangle \\ &= \langle\phi_0|[PG_0^{-1}(z^+) + U_0(z^+)]|\phi\rangle \end{aligned} \quad (2.61)$$

If one considers on-shell matrix elements, $\langle \phi_0 | (PG_0^{-1}(z^+)) | \phi \rangle = 0$. One has

$$\langle \phi_{pq} | U(z^+) | \phi \rangle = \langle \phi_0 | U_0(z^+) | \phi \rangle \quad (2.62)$$

Now we stay in the outgoing case specified by z^+ argument, and take the usual convention

$$\begin{aligned} \langle \phi_q | U(z^+) | \phi' \rangle^* &= \langle \phi_q | U | \phi' \rangle^* \\ \langle \phi_0 | T(z^+) | \phi' \rangle^* &= \langle \phi_0 | T | \phi' \rangle^* \\ \langle \phi_0 | U_0(z^+) | \phi \rangle &= \langle \phi_0 | U_0 | \phi \rangle, \end{aligned} \quad (2.63)$$

which drops the z^+ argument for simplicity. Then the unitarity relation in Eq. (2.48) can be written as

$$\begin{aligned} \langle \phi | U | \phi' \rangle^* - \langle \phi' | U | \phi \rangle &= \int d^3q \langle \phi_q | U | \phi' \rangle^* 2\pi i \delta(E - E_q) \langle \phi_q | U | \phi \rangle \\ &+ \int d^3p d^3q \langle \phi_0 | T | \phi' \rangle^* 2\pi i \delta(E - E_{pq}) \langle \phi_0 | U_0 | \phi \rangle \end{aligned} \quad (2.64)$$

Up to this step, only the term $\langle \phi_0 | T | \phi' \rangle^*$ needs to be determined. Because of the permutation operator identity

$$P_{12}P_{23}(1+P) = P_{13}P_{23}(1+P) = (1+P), \quad (2.65)$$

The matrix element of operator $\langle \phi_0 | U_0 | \phi \rangle$ has following permutation symmetry

$$\langle \phi_0 | U_0 | \phi \rangle = \langle \phi_0 | (1+P)T | \phi \rangle = \langle \phi_0 | P_{12}P_{23}U_0 | \phi \rangle = \langle \phi_0 | P_{13}P_{23}U_0 | \phi \rangle. \quad (2.66)$$

In considering $\int d^3p d^3q \langle \phi_0 | P_{12}P_{23}T | \phi' \rangle^* 2\pi i \delta(E - E_{pq}) \langle \phi_0 | U_0 | \phi \rangle$, one has

$$\begin{aligned} &\int d^3p d^3q \langle \phi_0 | P_{12}P_{23}T | \phi' \rangle^* 2\pi i \delta(E - E_{pq}) \langle \phi_0 | U_0 | \phi \rangle \\ &= \int d^3p d^3q \langle \phi_0 | P_{12}P_{23}T | \phi' \rangle^* 2\pi i \delta(E - E_{pq}) \langle \phi_0 | P_{12}P_{23}U_0 | \phi \rangle \\ &= \int d^3p d^3q {}_2\langle \phi_0 | T | \phi' \rangle^* 2\pi i \delta(E - E_{pq}) {}_2\langle \phi_0 | U_0 | \phi \rangle, \end{aligned} \quad (2.67)$$

where the subscript 2 in above equation means that the matrix element are evaluated in the type 2 Jacobi coordinate. (For the definition of Jacobi coordinates, see

Section 3.1). The integral volume $\int d^3p d^3q$ in type 1 coordinate can also be written in terms of type 2 coordinate as

$$\int d^3p d^3q = \int d^3p_2 d^3q_2 \frac{\partial(\mathbf{p}_1, \mathbf{q}_1)}{\partial(\mathbf{p}_2, \mathbf{q}_2)}. \quad (2.68)$$

The linear transformation between the type 1 and type 2 coordinates has unit Jacobian, $\frac{\partial(\mathbf{p}_1, \mathbf{q}_1)}{\partial(\mathbf{p}_2, \mathbf{q}_2)} = 1$. One has

$$\begin{aligned} & \int d^3p d^3q \langle \phi_0 | P_{12} P_{23} T | \phi' \rangle^* 2\pi i \delta(E - E_{pq}) \langle \phi_0 | U_0 | \phi \rangle \\ &= \int d^3p_2 d^3q_2 \langle \phi_0 | T | \phi' \rangle^* 2\pi i \delta(E - E_{pq}) \langle \phi_0 | U_0 | \phi \rangle. \\ &= \int d^3p d^3q \langle \phi_0 | T | \phi' \rangle^* 2\pi i \delta(E - E_{pq}) \langle \phi_0 | U_0 | \phi \rangle. \end{aligned} \quad (2.69)$$

Similarly,

$$\begin{aligned} & \int d^3p d^3q \langle \phi_0 | P_{13} P_{23} T | \phi' \rangle^* 2\pi i \delta(E - E_{pq}) \langle \phi_0 | U_0 | \phi \rangle \\ &= \int d^3p d^3q \langle \phi_0 | T | \phi' \rangle^* 2\pi i \delta(E - E_{pq}) \langle \phi_0 | U_0 | \phi \rangle. \end{aligned} \quad (2.70)$$

For $U_0 = (1 + P)T$, one has

$$\begin{aligned} & \int d^3p d^3q \langle \phi_0 | U_0 | \phi' \rangle^* 2\pi i \delta(E - E_{pq}) \langle \phi_0 | U_0 | \phi \rangle \\ &= \int d^3p d^3q \langle \phi_0 | (1 + P)T | \phi' \rangle^* 2\pi i \delta(E - E_{pq}) \langle \phi_0 | U_0 | \phi \rangle \\ &= 3 \int d^3p d^3q \langle \phi_0 | T | \phi' \rangle^* 2\pi i \delta(E - E_{pq}) \langle \phi_0 | U_0 | \phi \rangle. \end{aligned} \quad (2.71)$$

Then the unitary relation of scattering operators U and U_0 for identical particles in Eq. (2.64) is rewritten as

$$\begin{aligned} \langle \phi | U | \phi' \rangle^* - \langle \phi' | U | \phi \rangle &= \int d^3q \langle \phi_q | U | \phi' \rangle^* 2\pi i \delta(E - E_q) \langle \phi_q | U | \phi \rangle \\ &+ \frac{1}{3} \int d^3p d^3q \langle \phi_0 | U_0 | \phi' \rangle^* 2\pi i \delta(E - E_{pq}) \langle \phi_0 | U_0 | \phi \rangle. \end{aligned} \quad (2.72)$$

This equation shows the unitary relation between the operator U and the operator U_0 for arbitrary $|\phi\rangle$ and $|\phi'\rangle$. If we take $|\phi'\rangle = |\phi\rangle$, the δ functions at the r.h.s are the on-the-energy-shell conditions for elastic scattering and breakup process. We shall

see later that this makes the r.h.s of Eq. (2.72) proportional to the sum of elastic and breakup cross sections, i.e. total cross section, and the l.h.s is the imaginary part of elastic scattering amplitude. This is the so called optical theorem for three-body scattering of identical particles. We would like to point out that in the derivation of this relation in Ref. [26], the $\frac{1}{3}$ factor in the second term of Eq. (2.72) at r.h.s is missing.

Chapter 3

The Scattering of Three Identical Bosons

Below about 300 MeV projectile energy the Faddeev equations for three-body scattering have been solved with high accuracy for most modern two-body and three-body realistic forces using a traditional partial wave decomposition approach. If one considers three-body scattering at intermediate energies from few hundred MeV up to the GeV scale, the algebraic and algorithmic steps in the approach based on partial wave decomposition are very involved and reach limitations with respect to computational feasibility and accuracy. In this chapter we want to show that the full solution of the three-body scattering equations as laid out in chapter 2 can be obtained in a straightforward manner when directly employing vector variables, i.e. magnitudes of momenta and angles between the momenta. As a simplification we neglect spin and iso-spin degrees of freedom and treat three-boson scattering. The two-body interaction employed is of Malfliet-Tjon type [10]. The transition operator and the operators for elastic scattering and breakup process for three identical bosons are solved exactly as the functions of momentum vectors.

First we introduce the Jacobi coordinates in momentum space. Using Jacobi coordinate vectors in momentum space, we establish the explicit Faddeev equations for the three-body transition operator and operators for elastic scattering and breakup process in terms of the selected variables. In solving these Faddeev equations, the

major concern is the treatment of the singularities in the free three-body propagator. We describe the numerical algorithms and steps with the corresponding accuracy and self-consistency tests. This demonstrates the applicability of our newly developed vector based approach at intermediate projectile energies up to the GeV scale. We also explicitly work out the basic equations for calculating the scattering observables and the optical theorem. We investigate the reaction mechanisms in three-body scattering driven by the two-body forces in detail, including elastic scattering, semi-exclusive and exclusive breakup process at the intermediate energy regime from $E_{lab} = 0.2$ GeV to $E_{lab} = 1.0$ GeV. We focus on the importance of rescattering effects in terms of the two-body t -matrix as a function of the projectile energy and the reaction considered.

3.1 The Jacobi Coordinate System

For a three-body system, the Jacobi momentum coordinates are defined as the relative momentum \mathbf{p} between two particles in the two-body subsystem and the relative momentum \mathbf{q} between the third one and the center-of-mass of the two-body subsystem [45]. There are three choices corresponding to the three two-body subsystems.

$$\begin{cases} \mathbf{p}_1 &= \frac{1}{2} (\mathbf{k}_2 - \mathbf{k}_3) \\ \mathbf{q}_1 &= \frac{2}{3} (\mathbf{k}_1 - \frac{1}{2} (\mathbf{k}_2 + \mathbf{k}_3)) \end{cases} \quad (3.1)$$

$$\begin{cases} \mathbf{p}_2 &= \frac{1}{2} (\mathbf{k}_3 - \mathbf{k}_1) \\ \mathbf{q}_2 &= \frac{2}{3} (\mathbf{k}_2 - \frac{1}{2} (\mathbf{k}_3 + \mathbf{k}_1)) \end{cases} \quad (3.2)$$

$$\begin{cases} \mathbf{p}_3 &= \frac{1}{2} (\mathbf{k}_1 - \mathbf{k}_2) \\ \mathbf{q}_3 &= \frac{2}{3} (\mathbf{k}_3 - \frac{1}{2} (\mathbf{k}_1 + \mathbf{k}_2)) \end{cases} \quad (3.3)$$

where $\mathbf{k}_1, \mathbf{k}_2, \mathbf{k}_3$ are momenta of particle 1, 2, 3 respectively. The $(\mathbf{p}_1, \mathbf{q}_1)$, $(\mathbf{p}_2, \mathbf{q}_2)$ and $(\mathbf{p}_3, \mathbf{q}_3)$ called type 1, type 2 and type 3 coordinate systems and can be transformed linearly into each other. Explicitly, in terms of $(\mathbf{p}_1, \mathbf{q}_1)$, one has

$$\begin{aligned} \mathbf{p}_2 &= -\frac{1}{2}\mathbf{p}_1 - \frac{3}{4}\mathbf{q}_1 & \mathbf{p}_3 &= -\frac{1}{2}\mathbf{p}_1 + \frac{3}{4}\mathbf{q}_1 \\ \mathbf{q}_2 &= +\mathbf{p}_1 - \frac{1}{2}\mathbf{q}_1 & \mathbf{q}_3 &= -\mathbf{p}_1 - \frac{1}{2}\mathbf{q}_1 \end{aligned} \quad (3.4)$$

in terms of $(\mathbf{p}_2, \mathbf{q}_2)$,

$$\begin{aligned} \mathbf{p}_1 &= -\frac{1}{2}\mathbf{p}_2 + \frac{3}{4}\mathbf{q}_2 & \mathbf{p}_3 &= -\frac{1}{2}\mathbf{p}_2 - \frac{3}{4}\mathbf{q}_2 \\ \mathbf{q}_1 &= -\mathbf{p}_2 - \frac{1}{2}\mathbf{q}_2 & \mathbf{q}_3 &= +\mathbf{p}_2 - \frac{1}{2}\mathbf{q}_2 \end{aligned} \quad (3.5)$$

and in terms of $(\mathbf{p}_3, \mathbf{q}_3)$,

$$\begin{aligned} \mathbf{p}_1 &= -\frac{1}{2}\mathbf{p}_3 - \frac{3}{4}\mathbf{q}_3 & \mathbf{p}_2 &= -\frac{1}{2}\mathbf{p}_3 - \frac{3}{4}\mathbf{q}_3 \\ \mathbf{q}_1 &= +\mathbf{p}_3 - \frac{1}{2}\mathbf{q}_3 & \mathbf{q}_2 &= -\mathbf{p}_3 - \frac{1}{2}\mathbf{q}_3 \end{aligned} \quad (3.6)$$

The Jacobian for all the above transformations is equal to one. With the three types of Jacobi coordinates, there are three types of momentum states that can be introduced as

$$|\mathbf{p}\mathbf{q}\rangle_i = |\mathbf{p}_i\rangle|\mathbf{q}_i\rangle \quad (3.7)$$

with normalization

$${}_i\langle\mathbf{p}'\mathbf{q}'|\mathbf{p}\mathbf{q}\rangle_i = \delta(\mathbf{p}'_i - \mathbf{p}_i)\delta(\mathbf{q}'_i - \mathbf{q}_i). \quad (3.8)$$

When the cyclic and anti-cyclic permutation operators from Eq. (2.15) are applied, one gets

$$\begin{aligned} P_{12}P_{23}|\mathbf{p}\mathbf{q}\rangle_1 &= P_{12}P_{23}(1, 23) = (2, 31) = |\mathbf{p}\mathbf{q}\rangle_2, \\ P_{13}P_{23}|\mathbf{p}\mathbf{q}\rangle_1 &= P_{13}P_{23}(1, 23) = (3, 12) = |\mathbf{p}\mathbf{q}\rangle_3. \end{aligned} \quad (3.9)$$

The permutation operator $P = P_{12}P_{23} + P_{13}P_{23}$ occurs in the Faddeev equations for three-body scattering, namely Eq. (2.41) for the three-body transition operator T , Eq. (2.42) for the breakup process operator U_0 and Eq. (2.43) for the elastic scattering operator. Using Eq. (3.4), one can write the permutation operator P explicitly in type 1 coordinates as

$$\begin{aligned} \langle\mathbf{p}'\mathbf{q}'|P|\mathbf{p}\mathbf{q}\rangle &= \delta\left(\mathbf{p}' - \frac{1}{2}\mathbf{q}' - \mathbf{q}\right)\delta\left(\mathbf{q}' + \mathbf{p} + \frac{1}{2}\mathbf{q}\right) \\ &+ \delta\left(\mathbf{p}' + \frac{1}{2}\mathbf{q}' + \mathbf{q}\right)\delta\left(\mathbf{q}' - \mathbf{p} + \frac{1}{2}\mathbf{q}\right) \end{aligned} \quad (3.10)$$

The δ functions in the matrix element of P indicate the important fact that the operators which contain P undergo a coordinate transformation. Since all types of Jacobi coordinates are equivalent, we choose without losing generality the coordinates of type 1 as the principal system and drop the index 1 from now on.

3.2 Equations for The Scattering Operators

In this section we establish the equations for three-body scattering transition operator T , elastic scattering operator U and breakup operator U_0 in the explicit momentum vector variables which are selected invariant under coordinate rotation. The treatment of the singularities in the free three-body propagator is described in detail.

3.2.1 The Two-Body t -Matrix

As described in Chapter 2, the Faddeev equation for a three-body bound state in Eq. (2.16) and that for three-body scattering in Eq. (2.41) require the two-body t -matrix as input. With a given two-body potential V the two-body t -matrix is obtained by solving the Lippmann-Schwinger equation as shown in Eq. (2.11)

$$t = V + VG_0t \quad (3.11)$$

where $G_0 = (z - H_0)^{-1}$ is the free two-body propagator. In momentum space with Jacobi variables, the t -matrix acting in the pair and evaluated by the relative momentum variable \mathbf{p} is given as

$$\langle \mathbf{p}'\mathbf{q}'|t(z)|\mathbf{p}\mathbf{q}\rangle = \langle \mathbf{p}'|t(z)|\mathbf{p}\rangle\delta(\mathbf{q}' - \mathbf{q}), \quad (3.12)$$

where $z = E - \frac{3}{4m}q^2 + i\epsilon$. It obeys the following integral equation

$$\langle \mathbf{p}'|t(z)|\mathbf{p}\rangle \equiv t(\mathbf{p}', \mathbf{p}, z) = V(\mathbf{p}', \mathbf{p}) + \int d^3p'' V(\mathbf{p}', \mathbf{p}'') \frac{1}{z - \frac{p''^2}{m}} t(\mathbf{p}'', \mathbf{p}, z). \quad (3.13)$$

For the case of identical scalar particles, the $V(\mathbf{p}', \mathbf{p})$ and $t(\mathbf{p}', \mathbf{p}, z)$ are scalar functions, i.e.

$$V(\mathbf{p}', \mathbf{p}) = V(p', p, \hat{\mathbf{p}}' \cdot \hat{\mathbf{p}}) \quad (3.14)$$

and

$$t(\mathbf{p}', \mathbf{p}, z) = t(p', p, \hat{\mathbf{p}}' \cdot \hat{\mathbf{p}}, z). \quad (3.15)$$

Here $\hat{\mathbf{p}}$ is the unit vector of \mathbf{p} . Similarly all other hat vectors are defined. In the coordinate system in which \mathbf{p} is parallel to the z -axis, the explicit form of the Lippmann-Schwinger equation in momentum space can be written as

$$t(p', p, x') = V(p', p, x') + \int_0^\infty dp'' p''^2 \int_{-1}^{+1} dx'' \int_0^{2\pi} d\varphi'' V(p', p'', y) \frac{1}{z - \frac{p''^2}{m}} t(p'', p, x'') \quad (3.16)$$

with

$$\begin{aligned} p &= |\mathbf{p}|, \\ p' &= |\mathbf{p}'|, \\ p'' &= |\mathbf{p}''|, \\ x' &= \hat{\mathbf{p}}' \cdot \hat{\mathbf{p}}, \\ x'' &= \hat{\mathbf{p}}'' \cdot \hat{\mathbf{p}}, \\ y &= x' x'' + \sqrt{1 - x'^2} \sqrt{1 - x''^2} \cos(\varphi'' - \varphi'). \end{aligned} \quad (3.17)$$

The azimuthal angle φ' of \mathbf{p}' is arbitrary and can be taken as zero. It is convenient to define the matrix element of V as

$$v(p', p, x', x) = \int_0^{2\pi} d\varphi V(p', p, x x' + \sqrt{1 - x'^2} \sqrt{1 - x^2} \cos \varphi) \quad (3.18)$$

where φ is the azimuthal angle of \mathbf{p} . The Eq. (3.16) becomes

$$\begin{aligned} t(p', p, x') &= \frac{1}{2\pi} v(p', p, x', 1) \\ &+ \int_0^\infty dp'' p''^2 \int_{-1}^{+1} dx'' v(p', p'', x', x'') \frac{1}{z - \frac{p''^2}{m}} t(p'', p, x''). \end{aligned} \quad (3.19)$$

This is a two-dimensional integral equation for the off-shell t -matrix. The numerical solution of Eq. (3.19) and the properties of fully off-shell t -matrix are investigated in detail in Ref. [36]

3.2.2 Explicit Equations with Invariant Variables

Now we derive an explicit equation for the three-body scattering operator T . As far as only two-body forces are concerned, the equation for the three-body scattering

amplitude T is

$$T|\phi\rangle = tP|\phi\rangle + tPG_0T|\phi\rangle, \quad (3.20)$$

as shown in Eq.(2.41). The scattering is initiated by the channel state $|\phi\rangle = |\varphi_d\rangle|\mathbf{q}_0\rangle$. The state $|\varphi_d\rangle$ is the two-body bound state wave function and the $|\mathbf{q}_0\rangle$ is the momentum eigenstate of the incident particle. The explicit representation of Eq.(3.20) is obtained by representing each term in Jacobi coordinates. The first term can be written as

$$\begin{aligned} & \langle \mathbf{p}\mathbf{q}|t(z)P|\varphi_d\mathbf{q}_0\rangle \\ &= \int d^3p' d^3q' d^3p'' d^3q'' \langle \mathbf{p}\mathbf{q}|t(z)|\mathbf{p}'\mathbf{q}'\rangle \langle \mathbf{p}'\mathbf{q}'|P|\mathbf{p}''\mathbf{q}''\rangle \langle \mathbf{p}''\mathbf{q}''|\varphi_d\mathbf{q}_0\rangle, \end{aligned} \quad (3.21)$$

where a complete set of momentum state is inserted between $t(z)$, P and $|\varphi_d\mathbf{q}_0\rangle$ respectively. As shown in the Hamiltonian equation for channel states in Eqs. (2.23) and (2.24), the energy carried by a two-body subsystem in a three-body system is $z = E - \frac{3}{4m}q^2$. One has

$$\begin{aligned} \langle \mathbf{p}\mathbf{q}|t(z)|\mathbf{p}'\mathbf{q}'\rangle &= \delta(\mathbf{q} - \mathbf{q}')t(\mathbf{p}, \mathbf{p}', E - \frac{3}{4m}q^2), \\ \langle \mathbf{p}''\mathbf{q}''|\varphi_d\mathbf{q}_0\rangle &= \delta(\mathbf{q}'' - \mathbf{q}_0)\varphi(\mathbf{p}''). \end{aligned} \quad (3.22)$$

Substituting the matrix element of permutation operator P of Eq. (3.10) and Eq. (3.22) into Eq. (3.21), one get the first term of Eq. (3.20) as

$$\begin{aligned} & \langle \mathbf{p}\mathbf{q}|t(z)P|\varphi_d\mathbf{q}_0\rangle \\ &= \int d^3p' d^3p'' t(\mathbf{p}, \mathbf{p}', E - \frac{3}{4m}q^2) \varphi_d(\mathbf{p}'') \\ & \quad \times [\delta(\mathbf{p}' - (\frac{1}{2}\mathbf{q} + \mathbf{q}_0))\delta(\mathbf{p}'' - (-\mathbf{q} - \frac{1}{2}\mathbf{q}_0)) \\ & \quad + \delta(\mathbf{p}' - (-\frac{1}{2}\mathbf{q} - \mathbf{q}_0))\delta(\mathbf{p}'' - (\mathbf{q} + \frac{1}{2}\mathbf{q}_0))] \\ &= \varphi_d(-\mathbf{q} - \frac{1}{2}\mathbf{q}_0)t(\mathbf{p}, \frac{1}{2}\mathbf{q} + \mathbf{q}_0, E - \frac{3}{4m}q^2) \\ & \quad + \varphi_d(\mathbf{q} + \frac{1}{2}\mathbf{q}_0)t(\mathbf{p}, -\frac{1}{2}\mathbf{q} - \mathbf{q}_0, E - \frac{3}{4m}q^2) \\ &= \varphi_d\left(\mathbf{q} + \frac{1}{2}\mathbf{q}_0\right) t_s\left(\mathbf{p}, \frac{1}{2}\mathbf{q} + \mathbf{q}_0, E - \frac{3}{4m}q^2\right) \end{aligned} \quad (3.23)$$

Here the symmetric property of two-body bound state $\varphi_d(\mathbf{p}) = \varphi_d(-\mathbf{p})$ is applied, and t_s is the symmetrized two-body t -matrix which is defined as

$$t_s(\mathbf{p}, \mathbf{p}') = t(\mathbf{p}, \mathbf{p}') + t(\mathbf{p}, -\mathbf{p}'). \quad (3.24)$$

The second term in Eq. (3.20) can be obtained in a similar way as

$$\begin{aligned} & \langle \mathbf{p}\mathbf{q} | t(z) P G_0 T | \varphi_d \mathbf{q}_0 \rangle \\ &= \int d^3 p' d^3 q' d^3 p'' d^3 q'' \langle \mathbf{p}\mathbf{q} | t(E) | \mathbf{p}' \mathbf{q}' \rangle \langle \mathbf{p}' \mathbf{q}' | P | \mathbf{p}'' \mathbf{q}'' \rangle \langle \mathbf{p}'' \mathbf{q}'' | G_0 T | \varphi_d \mathbf{q}_0 \rangle. \end{aligned}$$

By inserting complete sets of momentum state between $t(z)$, P and G_0 and with the explicit form of P in Eq. (3.23), one has

$$\begin{aligned} & \langle \mathbf{p}\mathbf{q} | t(E) P G_0 T | \varphi_d \mathbf{q}_0 \rangle \\ &= \int d^3 p' d^3 p'' d^3 q'' t(\mathbf{p}, \mathbf{p}', E - \frac{3}{4m} q^2) \frac{\langle \mathbf{p}'' \mathbf{q}'' | T | \varphi_d \mathbf{q}_0 \rangle}{E - \frac{p'^2}{m} - \frac{3}{4m} q''^2 + i\varepsilon} \\ & \quad \times [\delta(\mathbf{p}' - (\frac{1}{2}\mathbf{q} + \mathbf{q}'')) \delta(\mathbf{p}'' - (-\mathbf{q} - \frac{1}{2}\mathbf{q}'')) \\ & \quad + \delta(\mathbf{p}' - (-\frac{1}{2}\mathbf{q} - \mathbf{q}'')) \delta(\mathbf{p}'' - (\mathbf{q} + \frac{1}{2}\mathbf{q}''))] \\ &= \int d^3 q'' t_s\left(\mathbf{p}, \frac{1}{2}\mathbf{q} + \mathbf{q}'', E - \frac{3}{4m} q^2\right) \frac{\langle \mathbf{q} \frac{1}{2}\mathbf{q}'', \mathbf{q}'' | T | \varphi_d \mathbf{q}_0 \rangle}{E - \frac{1}{m}(-\mathbf{q} - \frac{1}{2}\mathbf{q}'')^2 - \frac{3}{4m} q''^2 + i\varepsilon}. \end{aligned} \quad (3.25)$$

Thus, the Faddeev equation for T from Eq. (3.20) is explicitly written as

$$\begin{aligned} \langle \mathbf{p}\mathbf{q} | T | \varphi_d \mathbf{q}_0 \rangle &= \varphi_d(\mathbf{q} + \frac{1}{2}\mathbf{q}_0) t_s\left(\mathbf{p}, \frac{1}{2}\mathbf{q} + \mathbf{q}_0, E - \frac{3}{4m} q^2\right) \\ &+ \int d^3 \mathbf{q}'' t_s(\mathbf{p}, \frac{1}{2}\mathbf{q} + \mathbf{q}'', E - \frac{3}{4m} q^2) \frac{\langle \mathbf{q} + \frac{1}{2}\mathbf{q}'', \mathbf{q}'' | T | \varphi_d \mathbf{q}_0 \rangle}{E - \frac{1}{m}(q^2 + q''^2 + \mathbf{q} \cdot \mathbf{q}'') + i\varepsilon} \end{aligned} \quad (3.26)$$

Since Eq. (3.26) is an integral equation, one needs to know T for all values of \mathbf{p} and \mathbf{q} . This means that in the kernel $t_s(\mathbf{p}, \frac{1}{2}\mathbf{q} + \mathbf{q}'', E - \frac{3}{4m} q^2)$ has to be evaluated for all values of $q^2 \in (0, \infty)$, especially for negative values of the energy argument $z = E - \frac{3}{4m} q^2$. We know that the two-body interaction supports a bound state, which is characterized by a pole in the two-body t -matrix at the two-body binding energy

E_d , thus we need to consider this pole, which is located at $E - \frac{3}{4m}q^2 = E_d$. The residue at the pole can be explicitly extracted by defining

$$\hat{t}_s(\mathbf{p}, \mathbf{p}', E) = (E - E_d)t_s(\mathbf{p}, \mathbf{p}', E). \quad (3.27)$$

When $E = E_d$, one has

$$\lim_{E \rightarrow E_d} (E - E_d)t_s = V|\varphi_d\rangle\langle\varphi_d|V. \quad (3.28)$$

And explicitly in Jacobi coordinate, it is

$$\begin{aligned} & \lim_{E \rightarrow E_d} (E - E_d)\hat{t}_s(\mathbf{p}, \mathbf{p}', E) \\ &= \left(\int d^3p'' V(\mathbf{p}, \mathbf{p}'')\varphi_d(\mathbf{p}'') \right) \left(\int d^3p'' V(\mathbf{p}', \mathbf{p}'')\varphi_d(\mathbf{p}'') \right) \end{aligned} \quad (3.29)$$

Since the pole of t_s will be present in T , we define

$$\hat{T} = (E - E_d)T, \quad (3.30)$$

and formulate the Faddeev equation for \hat{T} as

$$\begin{aligned} \langle \mathbf{p}\mathbf{q}|\hat{T}|\varphi_d\mathbf{q}_0\rangle &= \varphi_d(\mathbf{q} + \frac{1}{2}\mathbf{q}_0)\hat{t}_s(\mathbf{p}, \frac{1}{2}\mathbf{q} + \mathbf{q}_0, E - \frac{3}{4m}q^2) \\ &+ \int d^3\mathbf{q}'' \frac{\hat{t}_s(\mathbf{p}, \frac{1}{2}\mathbf{q} + \mathbf{q}'', E - \frac{3}{4m}q^2)}{E - \frac{1}{m}(q^2 + q''^2 + \mathbf{q} \cdot \mathbf{q}'') + i\varepsilon} \frac{\langle \mathbf{q} + \frac{1}{2}\mathbf{q}'', \mathbf{q}''|\hat{T}|\varphi_d\mathbf{q}_0\rangle}{E - \frac{3}{4m}q''^2 - E_d + i\varepsilon}. \end{aligned} \quad (3.31)$$

Similar to the derivation of T in Jacobi coordinate, we proceed now to the explicit form of U and U_0 . By inserting a complete set of momentum state and substituting the explicit form of permutation operator P , one obtains the equation for elastic operator $U = PG_0^{-1} + PT$ as

$$\begin{aligned} & \langle \mathbf{q}\varphi_d|U|\mathbf{q}_0\varphi_d\rangle \\ &= 2\varphi_d\left(\frac{1}{2}\mathbf{q} + \mathbf{q}_0\right) \left(E - \frac{1}{m}(q^2 + \mathbf{q} \cdot \mathbf{q}_0 + q_0^2)\right) \varphi_d\left(\mathbf{q} + \frac{1}{2}\mathbf{q}_0\right) \\ &+ 2 \int d\mathbf{q}'' \varphi_d\left(\frac{1}{2}\mathbf{q} + \mathbf{q}''\right) \langle \mathbf{q} + \frac{1}{2}\mathbf{q}'', \mathbf{q}''|T|\mathbf{q}_0\varphi_d\rangle \\ &= 2\varphi_d\left(\frac{1}{2}\mathbf{q} + \mathbf{q}_0\right) \left(E - \frac{1}{m}(q^2 + \mathbf{q} \cdot \mathbf{q}_0 + q_0^2)\right) \varphi_d\left(\mathbf{q} + \frac{1}{2}\mathbf{q}_0\right) \\ &+ 2 \int d\mathbf{q}'' \varphi_d\left(\frac{1}{2}\mathbf{q} + \mathbf{q}''\right) \frac{\langle \mathbf{q} + \frac{1}{2}\mathbf{q}'', \mathbf{q}''|\hat{T}|\mathbf{q}_0\varphi_d\rangle}{E - \frac{3}{4m}q''^2 - E_d + i\varepsilon}. \end{aligned} \quad (3.32)$$

By using the different types of coordinates of Eq. (3.4), one obtains the breakup operator $U_0 = (1 + P)T$

$$\begin{aligned}
& \langle \mathbf{p}\mathbf{q}|U_0|\mathbf{q}_0\varphi_d\rangle \\
&= \langle \mathbf{p}\mathbf{q}|T|\mathbf{q}_0\varphi_d\rangle \\
&\quad + \langle -\frac{1}{2}\mathbf{p} + \frac{3}{4}\mathbf{q}, -\mathbf{p} - \frac{1}{2}\mathbf{q}|T|\mathbf{q}_0\varphi_d\rangle + \langle -\frac{1}{2}\mathbf{p} - \frac{3}{4}\mathbf{q}, +\mathbf{p} - \frac{1}{2}\mathbf{q}|T|\mathbf{q}_0\varphi_d\rangle \\
&= \frac{\langle \mathbf{p}\mathbf{q}|\hat{T}|\mathbf{q}_0\varphi_d\rangle}{E - \frac{3}{4m}\mathbf{q}^2 - E_d} \\
&\quad + \frac{\langle -\frac{1}{2}\mathbf{p} + \frac{3}{4}\mathbf{q}, -\mathbf{p} - \frac{1}{2}\mathbf{q}|\hat{T}|\mathbf{q}_0\varphi_d\rangle}{E - \frac{3}{4m}(-\mathbf{p} - \frac{1}{2}\mathbf{q})^2 - E_d} + \frac{\langle -\frac{1}{2}\mathbf{p} - \frac{3}{4}\mathbf{q}, +\mathbf{p} - \frac{1}{2}\mathbf{q}|\hat{T}|\mathbf{q}_0\varphi_d\rangle}{E - \frac{3}{4m}(+\mathbf{p} - \frac{1}{2}\mathbf{q})^2 - E_d}
\end{aligned} \tag{3.33}$$

Eqs. (3.31), (3.32) and (3.33) are the equations for scattering operators in Jacobi coordinate and are the underlying equations for our scattering calculations.

First we need to select appropriate variables for representing \hat{T} defined in vectors \mathbf{p} , \mathbf{q} and \mathbf{q}_0 . Because we ignore the spin and isospin degrees of freedom, \hat{T} is a scalar function of the vectors \mathbf{p} , \mathbf{q} and \mathbf{q}_0 . The magnitude of \mathbf{q}_0 is fixed by incident energy due to energy conservation, so we need five variables to uniquely specify the geometry of the vectors \mathbf{p} , \mathbf{q} and \mathbf{q}_0 in an arbitrary coordinate system. Since \hat{T} is a scalar function, it should be invariant under rotation of the coordinate system. This means that the five independent variables selected for representing \hat{T} should be invariant under rotation of the coordinate system. One can select four variables as follows

$$p = |\mathbf{p}|, \quad q = |\mathbf{q}|, \quad x_p = \hat{\mathbf{p}} \cdot \hat{\mathbf{q}}_0, \quad x_q = \hat{\mathbf{q}} \cdot \hat{\mathbf{q}}_0, \tag{3.34}$$

which are all defined by a scalar dot product, and thus invariant under rotation. The quantities p and q specify the magnitude of vectors \mathbf{p} and \mathbf{q} , x_p specifies the relative angles between \mathbf{p} and \mathbf{q}_0 , and x_q specifies the relative angle between \mathbf{q} and \mathbf{q}_0 . We need to find another angular variable to specify the relative angle between \mathbf{p} and \mathbf{q} . Geometrically, when \mathbf{p} , \mathbf{q} , and \mathbf{q}_0 are given, as shown in Fig. 3.1, two planes can be defined. One is spanned by \mathbf{p} and \mathbf{q}_0 with the normal unit vector $(\widehat{\mathbf{q}_0 \times \mathbf{p}})$, the other is spanned by \mathbf{q} and \mathbf{q}_0 with the normal unit vector $(\widehat{\mathbf{q}_0 \times \mathbf{q}})$. These two planes

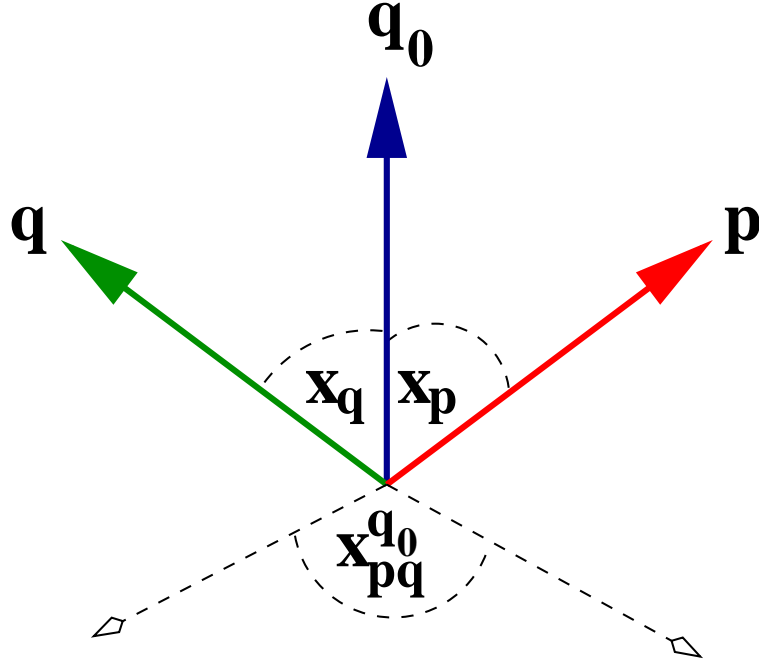


Figure 3.1: The geometry of three vectors \mathbf{q}_0 , \mathbf{q} , and \mathbf{p} relevant in the three-body scattering problem. The independent angle variables x_q , x_p , and $x_{pq}^{q_0}$ as defined in text are indicated. The dashed arrows represent the normal vectors $(\mathbf{q}_0 \times \mathbf{q})$ and $(\mathbf{p} \times \mathbf{q}_0)$.

intersect along the line on \mathbf{q}_0 . There is an angle between these two planes with cosine function value $x_{pq}^{q_0}$. Algebraically, one has

$$x_{pq}^{q_0} = (\widehat{\mathbf{q}_0 \times \mathbf{q}}) \cdot (\widehat{\mathbf{q}_0 \times \mathbf{p}}).. \quad (3.35)$$

Because of

$$\begin{aligned} (\widehat{\mathbf{q}_0 \times \mathbf{p}}) &= \frac{\hat{\mathbf{q}}_0 \times \hat{\mathbf{p}}}{\sqrt{1 - (\hat{\mathbf{q}}_0 \cdot \hat{\mathbf{p}})^2}}, \\ (\widehat{\mathbf{q}_0 \times \mathbf{q}}) &= \frac{\hat{\mathbf{q}}_0 \times \hat{\mathbf{q}}}{\sqrt{1 - (\hat{\mathbf{q}}_0 \cdot \hat{\mathbf{q}})^2}}, \end{aligned} \quad (3.36)$$

and the identity

$$(\mathbf{A} \times \mathbf{B}) \cdot (\mathbf{C} \times \mathbf{D}) = (\mathbf{A} \cdot \mathbf{C})(\mathbf{B} \cdot \mathbf{D}) - (\mathbf{A} \cdot \mathbf{D})(\mathbf{B} \cdot \mathbf{C}), \quad (3.37)$$

one has

$$\begin{aligned} x_{pq}^{q_0} &= \frac{\hat{\mathbf{p}} \cdot \hat{\mathbf{q}} - (\hat{\mathbf{q}}_0 \cdot \hat{\mathbf{p}})(\hat{\mathbf{q}}_0 \cdot \hat{\mathbf{q}})}{\sqrt{1 - (\hat{\mathbf{q}}_0 \cdot \hat{\mathbf{p}})^2} \sqrt{1 - (\hat{\mathbf{q}}_0 \cdot \hat{\mathbf{q}})^2}} \\ &= \frac{y_{pq} - x_p x_q}{\sqrt{1 - x_p^2} \sqrt{1 - x_q^2}}. \end{aligned} \quad (3.38)$$

where $y_{pq} = \hat{\mathbf{p}} \cdot \hat{\mathbf{q}}$. It is obvious that x_p , x_q and $x_{pq}^{q_0}$ can uniquely specify the angular geometry of vectors \mathbf{p} , \mathbf{q} and \mathbf{q}_0 . Thus the scalar function \hat{T} defined in \mathbf{p} , \mathbf{q} and \mathbf{q}_0 can be properly represented as

$$\langle \mathbf{p} \mathbf{q} | \hat{T} | \varphi_d \mathbf{q}_0 \rangle = \hat{T}(p, x_p, x_{pq}^{q_0}, x_q, q). \quad (3.39)$$

By using this set of variables, we have the freedom to choose the coordinate system according to the convenience in a numerical calculation.

Here we would like to point out that even though y_{pq} is invariant under rotation, it is not a suitable variable for representing \hat{T} . We notice that if x_p and x_q in Eq. (3.34) are given, the domain of y_{pq} is bound by following inequality

$$x_p x_q - \sqrt{1 - x_p^2} \sqrt{1 - x_q^2} \leq y_{pq} \leq x_p x_q + \sqrt{1 - x_p^2} \sqrt{1 - x_q^2}. \quad (3.40)$$

This means that when x_p and x_q are defined on the interval $[-1, 1]$, the y_{pq} can not be independently defined on the interval $[-1, 1]$. Thus y_{pq} is not independent. However y_{pq} can be evaluated in terms of x_p , x_q and $x_{pq}^{q_0}$ as

$$y_{pq} = x_p x_q + \sqrt{1 - x_p^2} \sqrt{1 - x_q^2} x_{pq}^{q_0}. \quad (3.41)$$

If one works in an arbitrary selected coordinate system, one can express y_{pq} as

$$y_{pq} = x_p x_q + \sqrt{1 - x_p^2} \sqrt{1 - x_q^2} \cos \varphi_{pq}. \quad (3.42)$$

where φ_{pq} is the azimuthal angle difference between vectors \mathbf{p} and \mathbf{q} measured in the selected coordinate system. It should be emphasized that Eq. (3.41) and Eq. (3.42) both are valid to evaluate y_{pq} , but they have distinct geometric meaning. The first one defined in $x_{pq}^{q_0}$ is in an invariant form and fully independent to the selection of coordinate system, whereas the later one requires a selected coordinate system to

measure φ_{pq} . Eq. (3.42) implies an alternative way to evaluate $\cos \varphi_{pq}$ in terms of invariant variables as

$$\cos \varphi_{pq} = \frac{y_{pq} - x_p x_q}{\sqrt{1 - x_p^2} \sqrt{1 - x_q^2}}. \quad (3.43)$$

We will use the relation in Eq. (3.43) later to determine the angular relations uniquely when considering the integration over \mathbf{q}'' .

Now we need to determine an appropriate coordinate system in which the singularity in the free three-body propagator has its simplest form. From Eq. (3.31) we find that the form of the singularities in the free three-body propagator is given in the denominator of G_0 as

$$G_0 = \frac{1}{E - \frac{1}{m}(q^2 + q''^2 + \mathbf{q} \cdot \mathbf{q}'') + i\varepsilon}. \quad (3.44)$$

The position of the singularities is a function of the vector \mathbf{q}'' if \mathbf{q} is fixed, namely they depend on the magnitude q'' and the relative angle between vectors \mathbf{q} and \mathbf{q}'' . Thus these singularities are usually called moving singularities and cause a major complication in calculations. We want to set up the equation of \hat{T} in such a way that these moving singularities have their simplest form. This can be done by selecting an appropriate coordinate system. The unit vector of the integration variable \mathbf{q}'' can be written as

$$\hat{\mathbf{q}}'' = \begin{pmatrix} \sqrt{1 - x''^2} \cos \varphi'' \\ \sqrt{1 - x''^2} \sin \varphi'' \\ x'' \end{pmatrix}, \quad (3.45)$$

in any selected coordinate system. If we choose the z -axis parallel to \mathbf{q} , then

$$\hat{\mathbf{q}} = \begin{pmatrix} 0 \\ 0 \\ 1 \end{pmatrix}, \quad (3.46)$$

and $\mathbf{q} \cdot \mathbf{q}'' = qq''x''$. With this choice the free three-body propagator takes its simplest form. We call this system the q -system and use it for setting up the equation for \hat{T} .

Now we need to work out Eq. (3.31) for \hat{T} in the q -system term by term using the variables $p, q, x_p, x_q, x_{pq}^{q_0}, q'', x''$ and φ'' . The first term in Eq. (3.31) is given as

$$\begin{aligned} & \varphi_d(\mathbf{q} + \frac{1}{2}\mathbf{q}_0)\hat{t}_s(\mathbf{p}, \frac{1}{2}\mathbf{q} + \mathbf{q}_0, E - \frac{3}{4m}q^2) \\ = & \varphi_d\left(\sqrt{q^2 + \frac{1}{4}q_0^2 + qq_0x_q}\right) \\ \times & \hat{t}_s\left(p, \sqrt{\frac{1}{4}q^2 + q_0^2 + qq_0x_q}, \frac{\frac{1}{2}qy_{pq} + q_0x_p}{\sqrt{\frac{1}{4}q^2 + q_0^2 + qq_0x_q}}; E - \frac{3}{4m}q^2\right). \end{aligned} \quad (3.47)$$

with

$$\begin{aligned} p &= |\mathbf{p}|, \\ q &= |\mathbf{q}|, \\ x_p &= \hat{\mathbf{q}}_0 \cdot \hat{\mathbf{p}}, \\ x_q &= \hat{\mathbf{q}}_0 \cdot \hat{\mathbf{q}}, \\ y_{pq} &= x_px_q + \sqrt{1 - x_p^2}\sqrt{1 - x_q^2}x_{pq}^{q_0}. \end{aligned} \quad (3.48)$$

The integration part is more complicated. The free three-body propagator is

$$E - \frac{1}{m}(q^2 + q''^2 + \mathbf{q} \cdot \mathbf{q}'') = E - \frac{1}{m}(q^2 + q''^2 + qq''x''). \quad (3.49)$$

with

$$x'' = \hat{\mathbf{q}} \cdot \hat{\mathbf{q}}''. \quad (3.50)$$

The \hat{t}_s matrix part is

$$\begin{aligned} & \hat{t}_s(\mathbf{p}, \frac{1}{2}\mathbf{q} + \mathbf{q}'', E - \frac{3}{4m}q^2) \\ = & \hat{t}_s\left(p, \sqrt{\frac{1}{4}q^2 + q''^2 + qq''x''}, \frac{\frac{1}{2}qy_{pq} + q''y_{pq}''}{\sqrt{\frac{1}{4}q^2 + q''^2 + qq''x''}}, E - \frac{3}{4m}q^2\right) \end{aligned} \quad (3.51)$$

with

$$y_{pq}'' = \hat{\mathbf{p}} \cdot \hat{\mathbf{q}}'' = y_{pq}x'' + \sqrt{1 - x''^2}\sqrt{1 - y_{pq}^2}\cos(\varphi_p - \varphi''). \quad (3.52)$$

where the φ_p is the azimuthal angle of the vector \mathbf{p} . This is obtained by using the relation in Eq. (3.43),

$$\cos(\varphi_p - \varphi'') = \frac{\hat{\mathbf{p}} \cdot \hat{\mathbf{q}}'' - (\hat{\mathbf{q}} \cdot \hat{\mathbf{p}})(\hat{\mathbf{q}} \cdot \hat{\mathbf{q}}'')}{\sqrt{1 - (\hat{\mathbf{q}} \cdot \hat{\mathbf{p}})^2} \sqrt{1 - (\hat{\mathbf{q}} \cdot \hat{\mathbf{q}}'')^2}} = \frac{y_{pq''} - y_{pq}x''}{\sqrt{1 - y_{pq}^2} \sqrt{1 - x''^2}}. \quad (3.53)$$

The variable φ_p is unknown and needs to be determined. The quantity \hat{T} in the integral part is

$$\langle \mathbf{q} + \frac{1}{2}\mathbf{q}'', \mathbf{q}'' | \hat{T} | \mathbf{q}_0 \varphi_d \rangle. \quad (3.54)$$

For convenience, we define

$$\Pi_p = \mathbf{q} + \frac{1}{2}\mathbf{q}'', \quad \Pi_q = \mathbf{q}'', \quad (3.55)$$

then we get

$$\begin{aligned} \pi_p &= |\Pi_p| = \sqrt{q^2 + \frac{1}{4}q''^2 + qq''x''}, \\ \pi_q &= |\Pi_q| = q'', \\ x_{\pi_p} &= \hat{\Pi}_p \cdot \hat{\mathbf{q}}_0 = \frac{qx_q + \frac{1}{2}q''y_{q_0q''}}{\sqrt{q^2 + \frac{1}{4}q''^2 + qq''x''}}, \\ x_{\pi_q} &= \hat{\Pi}_q \cdot \hat{\mathbf{q}}_0 = y_{q_0q''}, \\ x_{\pi_p \pi_q}^{q_0} &= \frac{\hat{\Pi}_p \cdot \hat{\Pi}_q - (\hat{\Pi}_p \cdot \hat{\mathbf{q}}_0)(\hat{\Pi}_q \cdot \hat{\mathbf{q}}_0)}{\sqrt{1 - (\hat{\Pi}_p \cdot \hat{\mathbf{q}}_0)^2} \sqrt{1 - (\hat{\Pi}_q \cdot \hat{\mathbf{q}}_0)^2}} = \frac{\frac{qx'' + \frac{1}{2}q''}{\sqrt{q^2 + \frac{1}{4}q''^2 + qq''x''}} - x_{\pi_p}x_{\pi_q}}{\sqrt{1 - x_{\pi_p}^2} \sqrt{1 - x_{\pi_q}^2}} \end{aligned} \quad (3.56)$$

with

$$y_{q_0q''} = \hat{\mathbf{q}}_0 \cdot \hat{\mathbf{q}}'' = x_q x'' + \sqrt{1 - x_q^2} \sqrt{1 - x''^2} \cos(\varphi_{q_0} - \varphi''). \quad (3.57)$$

where φ_{q_0} is the azimuthal angle of vector \mathbf{q}_0 . This is obtained by using the relation in Eq. (3.43),

$$\cos(\varphi_{q_0} - \varphi'') = \frac{\hat{\mathbf{q}}_0 \cdot \hat{\mathbf{q}}'' - (\hat{\mathbf{q}} \cdot \hat{\mathbf{q}}_0)(\hat{\mathbf{q}} \cdot \hat{\mathbf{q}}'')}{\sqrt{1 - (\hat{\mathbf{q}} \cdot \hat{\mathbf{q}}_0)^2} \sqrt{1 - (\hat{\mathbf{q}} \cdot \hat{\mathbf{q}}'')^2}} = \frac{y_{q_0q''} - x_q x''}{\sqrt{1 - x_q^2} \sqrt{1 - x''^2}}. \quad (3.58)$$

The variable φ_{q_0} is also unknown and needs to be determined.

Up to now, everything is properly defined except the angle φ_p in Eq. (3.53) and the angle φ_{q_0} in Eq. (3.58). In these two equations we notice that the φ_p and φ_{q_0}

only occur in the φ'' integration. Here we will show that these two angles only occur as $\sin(\varphi_p - \varphi_{q_0})$ and $\cos(\varphi_p - \varphi_{q_0})$ in the φ'' integration. Furthermore we will prove that φ_{q_0} can be arbitrarily selected, and $\sin \varphi_p$, $\cos \varphi_p$ are well defined. With fixed p , q , x_p , x_q , $x_{pq}^{q_0}$, q'' and x'' , the φ'' integration in Eq. (3.31) can be written as

$$I(\varphi_{q_0}, \varphi_p) = \int_0^{2\pi} F[\cos(\varphi'' - \varphi_{q_0})] G[\cos(\varphi'' - \varphi_p)] d\varphi''. \quad (3.59)$$

where the F and G are known functions determined by \hat{t}_s and \hat{T} . Let $\varphi' = \varphi'' - \varphi_{q_0}$, so that

$$\begin{aligned} I(\varphi_{q_0}, \varphi_p) &= \int_{-\varphi_{q_0}}^{2\pi - \varphi_{q_0}} F[\cos \varphi'] G[\cos(\varphi' - (\varphi_p - \varphi_{q_0}))] d\varphi' \\ &= \left\{ \int_{-\varphi_{q_0}}^0 + \int_0^{2\pi} + \int_{2\pi}^{2\pi - \varphi_{q_0}} \right\} F[\cos \varphi'] G[\cos(\varphi' - (\varphi_p - \varphi_{q_0}))] d\varphi' \\ &= \int_0^{2\pi} F[\cos \varphi'] G[\cos(\varphi' - (\varphi_p - \varphi_{q_0}))] d\varphi' \\ &= I(\varphi_{q_0} - \varphi_p) \end{aligned} \quad (3.60)$$

Thus one finds that only the difference $(\varphi_{q_0} - \varphi_p)$ is needed. According to the relation in Eq. (3.43), one has

$$\cos(\varphi_p - \varphi_{q_0}) = \frac{\hat{\mathbf{q}}_0 \cdot \hat{\mathbf{p}} - (\hat{\mathbf{q}} \cdot \hat{\mathbf{q}}_0)(\hat{\mathbf{q}} \cdot \hat{\mathbf{p}})}{\sqrt{1 - (\hat{\mathbf{q}} \cdot \hat{\mathbf{q}}_0)^2} \sqrt{1 - (\hat{\mathbf{p}} \cdot \hat{\mathbf{q}})^2}} = \frac{x_p - y_{pq} x_q}{\sqrt{1 - y_{pq}^2} \sqrt{1 - x_q^2}}. \quad (3.61)$$

In evaluating $\sin(\varphi_p - \varphi_{q_0})$, one has

$$\sin(\varphi_p - \varphi_{q_0}) = +\sqrt{1 - \cos^2(\varphi_p - \varphi_{q_0})} \quad (3.62)$$

for $(\varphi_p - \varphi_{q_0}) \in [0, \pi]$ and

$$\sin(\varphi_p - \varphi_{q_0}) = -\sqrt{1 - \cos^2(\varphi_p - \varphi_{q_0})} \quad (3.63)$$

for $(\varphi_p - \varphi_{q_0}) \in [\pi, 2\pi]$. In order to determine which sign for $\sin(\varphi_p - \varphi_{q_0})$ should be taken, we consider the φ'' integration further. The $I(\varphi_p - \varphi_{q_0})$ can be decomposed as

$$\begin{aligned} I(\varphi_p - \varphi_{q_0}) &= \int_0^\pi F[\cos \phi''] G[\cos((\varphi_p - \varphi_{q_0}) - \phi'')] d\phi'' \\ &+ \int_\pi^{2\pi} F[\cos \phi'''] G[\cos((\varphi_p - \varphi_{q_0}) - \phi''')] d\phi''' \end{aligned} \quad (3.64)$$

Let $\varphi'''' = 2\pi - \varphi'''$, one has

$$\begin{aligned} & \int_{\pi}^{2\pi} F[\cos \phi'''] G[\cos((\varphi_p - \varphi_{q_0}) - \varphi''')] d\varphi''' \\ &= \int_0^{\pi} F[\cos \phi'''''] G[\cos((\varphi_p - \varphi_{q_0}) + \varphi''''')] d\varphi'''''. \end{aligned} \quad (3.65)$$

Then the $I(\varphi_p - \varphi_{q_0})$ can be rewritten as

$$\begin{aligned} I(\varphi_p - \varphi_{q_0}) &= \int_0^{\pi} F[\cos \phi''] G[\cos((\varphi_p - \varphi_{q_0}) - \varphi'')] d\varphi'' \\ &+ \int_0^{\pi} F[\cos \phi''] G[\cos((\varphi_p - \varphi_{q_0}) + \varphi'')] d\varphi''. \end{aligned} \quad (3.66)$$

Now consider $I(2\pi - (\varphi_p - \varphi_{q_0}))$, which is

$$\begin{aligned} I(2\pi - (\varphi_p - \varphi_{q_0})) &= \int_0^{\pi} F[\cos \phi''] G[\cos((\varphi_p - \varphi_{q_0}) + \varphi'')] d\varphi'' \\ &+ \int_0^{\pi} F[\cos \phi''] G[\cos((\varphi_p - \varphi_{q_0}) - \varphi'')] d\varphi''. \end{aligned} \quad (3.67)$$

Comparing Eqs. (3.66) and (3.67), one has $I(\varphi_p - \varphi_{q_0}) = I(2\pi - (\varphi_p - \varphi_{q_0}))$. This suggests that we can consider either the case of $(\varphi_p - \varphi_{q_0}) \in [0, \pi]$ or the case of $(\varphi_p - \varphi_{q_0}) \in [\pi, 2\pi]$, and these two cases give the same result for $I(\varphi_p - \varphi_{q_0})$. So, there is no ambiguity about the sign of $\sin(\varphi_p - \varphi_{q_0})$, we can take either $+$ or $-$. Since the q -system only defines the z -axis without a specification of the corresponding $x-z$ plane, we still need to set one of the azimuthal angles, φ_p or φ_{q_0} . It is clear that one of the two values can be arbitrarily chosen due to the invariance under the rotation. Without losing generality, we assume that the φ_{q_0} is arbitrarily chosen to determine the $x-z$ plane of the q -system. Then $\cos(\varphi_p - \varphi_{q_0})$ given by Eq. (3.61) and $\sin(\varphi_p - \varphi_{q_0})$ given by Eq. (3.62) or Eq. (3.63) as well as the selected φ_{q_0} can determine $\cos \varphi_p$ and $\sin \varphi_p$ uniquely as

$$\begin{aligned} \cos \varphi_p &= \cos \varphi_{q_0} \cos(\varphi_p - \varphi_{q_0}) - \sin \varphi_{q_0} \sin(\varphi_p - \varphi_{q_0}), \\ \sin \varphi_p &= \sin \varphi_{q_0} \cos(\varphi_p - \varphi_{q_0}) + \cos \varphi_{q_0} \sin(\varphi_p - \varphi_{q_0}). \end{aligned} \quad (3.68)$$

If we take different values of φ_{q_0} or the different signs of $\sin(\varphi_p - \varphi_{q_0})$, we should get the same result for \hat{T} . This freedom of selection can be used to test the self-consistency of our numerical calculation.

Now every variable in Eq. (3.31) for \hat{T} is well defined. When $p, q, x_p, x_q, x_{pq}^{q_0}, q'', x'', \varphi''$ are given together with the arbitrarily selected value of φ_{q_0} and sign of $\sin(\varphi_p - \varphi_{q_0})$, the complete equation of \hat{T} in the q -system is

$$\begin{aligned}
& \langle p, x_p, x_{pq}^{q_0}, x_q, q | \hat{T} | q_0 \varphi_d \rangle \\
&= \varphi_d \left(\sqrt{q^2 + \frac{1}{4}q_0^2 + qq_0x_q} \right) \\
&\times \hat{t}_s \left(p, \sqrt{\frac{1}{4}q^2 + q_0^2 + qq_0x_q}, \frac{\frac{1}{2}qy_{pq} + q_0x_p}{\sqrt{\frac{1}{4}q^2 + q_0^2 + qq_0x_q}}; E - \frac{3}{4m}q^2 \right) \\
&+ \int_0^\infty dq'' q''^2 \int_{-1}^{+1} dx'' \int_0^{2\pi} d\varphi'' \frac{1}{E - \frac{1}{m}(q^2 + qq''x'' + q''^2) + i\varepsilon} \\
&\times \hat{t}_s \left(p, \sqrt{\frac{1}{4}q^2 + q''^2 + qq''x''}, \frac{\frac{1}{2}qy_{pq} + q''y_{pq''}}{\sqrt{\frac{1}{4}q^2 + q''^2 + qq''x''}}; E - \frac{3}{4m}q^2 \right) \\
&\times \frac{\left\langle \sqrt{q^2 + \frac{1}{4}q''^2 + qq''x''}, \frac{qx_q + \frac{1}{2}q''y_{q_0q''}}{\sqrt{q^2 + \frac{1}{4}q''^2 + qq''x''}}, \frac{\frac{qx'' + \frac{1}{2}q''}{\sqrt{q^2 + \frac{1}{4}q''^2 + qq''x''}} - x_{\pi p}x_{\pi q}}{\sqrt{1-x_{\pi p}^2}\sqrt{1-x_{\pi q}^2}}, y_{q_0q''}, q'' | \hat{T} | q_0 \varphi_d \right\rangle}{E - \frac{3}{4m}q''^2 - E_d + i\varepsilon}
\end{aligned} \tag{3.69}$$

with

$$\begin{aligned}
p &= |\mathbf{p}|, \\
q &= |\mathbf{q}|, \\
q'' &= |\mathbf{q}''|, \\
x_p &= \hat{\mathbf{p}} \cdot \hat{\mathbf{q}}_0, \\
x_q &= \hat{\mathbf{q}} \cdot \hat{\mathbf{q}}_0, \\
x_{pq}^{q_0} &= (\widehat{\mathbf{q}_0 \times \mathbf{q}}) \cdot (\widehat{\mathbf{q}_0 \times \mathbf{p}}), \\
y_{pq} &= \hat{\mathbf{p}} \cdot \hat{\mathbf{q}} = x_p x_q + \sqrt{1-x_p^2} \sqrt{1-x_q^2} x_{pq}^{q_0}, \\
y_{qq''} &= \hat{\mathbf{q}} \cdot \hat{\mathbf{q}}'' = x'', \\
\varphi_{q_0} &= \text{arbitrarily selected value}, \\
\cos(\varphi_p - \varphi_{q_0}) &= \frac{x_p - y_{pq}x_q}{\sqrt{1-y_{pq}^2}\sqrt{1-x_q^2}}, \\
\sin(\varphi_p - \varphi_{q_0}) &= \sqrt{1 - \cos^2(\varphi_p - \varphi_{q_0})} \text{ or } -\sqrt{1 - \cos^2(\varphi_p - \varphi_{q_0})},
\end{aligned}$$

$$\begin{aligned}
\cos \varphi_p &= \cos \varphi_{q_0} \cos(\varphi_p - \varphi_{q_0}) - \sin \varphi_{q_0} \sin(\varphi_p - \varphi_{q_0}), \\
\sin \varphi_p &= \sin \varphi_{q_0} \cos(\varphi_p - \varphi_{q_0}) + \cos \varphi_{q_0} \sin(\varphi_p - \varphi_{q_0}), \\
y_{q_0 q''} &= \hat{\mathbf{q}}_0 \cdot \mathbf{q}'' = x_q x'' + \sqrt{1 - x_q^2} \sqrt{1 - x''^2} \cos(\varphi_{q_0} - \varphi''), \\
y_{pq''} &= \hat{\mathbf{p}} \cdot \mathbf{q}'' = y_{pq} x'' + \sqrt{1 - x''^2} \sqrt{1 - y_{pq}^2} \cos(\varphi_p - \varphi''), \\
x_{\pi_p} &= \hat{\Pi}_p \cdot \hat{\mathbf{q}}_0 = \frac{qx_q + \frac{1}{2}q''y_{q_0 q''}}{\sqrt{q^2 + \frac{1}{4}q''^2 + qq''x''}}, \\
x_{\pi_q} &= \hat{\Pi}_q \cdot \hat{\mathbf{q}}_0 = y_{q_0 q''}.
\end{aligned} \tag{3.70}$$

This is a three-dimensional integral equation in five variables. It should be emphasized that even though the explicit equation for \hat{T} in Eq. (3.69) is solved in the q -system, the solution of \hat{T} in terms of p , x_p , $x_{pq}^{q_0}$, x_q and q are rotationally invariant.

After the solution of \hat{T} is obtained, the operator U for elastic scattering in Eq. (3.32) is given using the same coordinate as

$$\begin{aligned}
&\langle \mathbf{q}\varphi_d | U | \mathbf{q}_0\varphi_d \rangle = \langle q_0 x \varphi_d | U | q_0 \varphi_d \rangle \\
&= 2\varphi_d^2 \left(q_0 \sqrt{\frac{5}{4} + x} \right) \left(E - \frac{q_0^2}{m} (2 + x) \right) \\
&+ 2 \int_0^\infty dq'' q''^2 \int_{-1}^{+1} dx'' \int_0^{2\pi} d\varphi'' \varphi_d \left(\sqrt{\frac{1}{4}q_0^2 + q''^2 + q_0 q'' x''} \right) \\
&\times \frac{\left\langle \sqrt{q''^2 + \frac{1}{4}q''^2 + qq''y_{qq''}}, \frac{q_0 x + \frac{1}{2}q''y_{q_0 q''}}{\sqrt{q''^2 + \frac{1}{4}q''^2 + qq''y_{qq''}}}, \frac{\frac{q_0 y_{qq''} + \frac{1}{2}q''}{\sqrt{q_0^2 + \frac{1}{4}q''^2 + q_0 q''y_{q_0 q''}}} - x_{\pi_p} x_{\pi_q}}{\sqrt{1 - x_{\pi_p}^2} \sqrt{1 - x_{\pi_q}^2}}, y_{q_0 q'', q''} | \hat{T} | q_0 \varphi_d \right\rangle}{E - \frac{3}{4m}q''^2 - E_d + i\varepsilon}
\end{aligned} \tag{3.71}$$

with

$$\begin{aligned}
x &= \hat{\mathbf{q}} \cdot \hat{\mathbf{q}}_0 \\
y_{q_0 q''} &= \hat{\mathbf{q}}_0 \cdot \mathbf{q}'' \\
y_{qq''} &= \hat{\mathbf{q}} \cdot \mathbf{q}'', \\
x_{\pi_p} &= \frac{q_0 x + \frac{1}{2}q''y_{q_0 q''}}{\sqrt{q_0^2 + \frac{1}{4}q''^2 + q_0 q''y_{qq''}}}, \\
x_{\pi_q} &= y_{q_0 q''}.
\end{aligned} \tag{3.72}$$

The angle $x = \hat{\mathbf{q}} \cdot \hat{\mathbf{q}}_0$ is rotationally invariant, so we need to fix the coordinate system to specify $y_{q_0 q''}$ and $y_{qq''}$. If we choose the z -axis parallel to the vector \mathbf{q}_0 , called q_0 -system, one has

$$\begin{aligned} y_{q_0 q''} &= x'' \\ y_{qq''} &= xx'' + \sqrt{1-x^2}\sqrt{1-x''^2}\cos(\varphi'' - \varphi_q). \end{aligned} \quad (3.73)$$

where the angle φ_q can be taken as zero. In q -system, similarly one has

$$\begin{aligned} y_{q_0 q''} &= xx'' + \sqrt{1-x^2}\sqrt{1-x''^2}\cos(\varphi'' - \varphi_{q_0}), \\ y_{qq''} &= x''. \end{aligned} \quad (3.74)$$

where the angle φ_{q_0} can be taken as zero. Due to invariance under rotation, the U calculated via Eq. (3.73) and Eq. (3.74) should be the same. This invariance can also be used to check numerical self-consistency and accuracy.

The breakup operator U_0 in Eq. (3.33) can be evaluated straightforwardly as

$$\begin{aligned} \langle \mathbf{p}\mathbf{q} | U_0 | \mathbf{q}_0 \varphi_d \rangle &= \langle p, x_p, x_{pq}^{q_0}, x_q, q | U_0 | \mathbf{q}_0 \varphi_d \rangle \\ &= \frac{\langle p, x_p, x_{pq}^{q_0}, x_q, q | \hat{T} | \mathbf{q}_0 \varphi_d \rangle}{E - \frac{3}{4m}q^2 - E_d} + \frac{\langle p_2, x_{p_2}, x_{p_2 q_2}^{q_0}, x_{q_2}, q_2 | \hat{T} | q_0 \varphi_d \rangle}{E - \frac{3}{4m}q_2^2 - E_d} \\ &+ \frac{\langle p_3, x_{p_3}, x_{p_3 q_3}^{q_0}, x_{q_3}, q_3 | \hat{T} | q_0 \varphi_d \rangle}{E - \frac{3}{4m}q_3^2 - E_d} \end{aligned} \quad (3.75)$$

with

$$\begin{aligned} y_{pq} &= x_p x_q + \sqrt{1-x_p^2}\sqrt{1-x_q^2}x_{pq}^{q_0} \\ p_2 &= \left| -\frac{1}{2}\mathbf{p} + \frac{3}{4}\mathbf{q} \right| = \frac{1}{2}\sqrt{p^2 + \frac{9}{4}q^2 - 3pqy_{pq}} \\ q_2 &= \left| -\mathbf{p} - \frac{1}{2}\mathbf{q} \right| = \sqrt{p^2 + \frac{1}{4}q^2 + pqy_{pq}} \\ p_3 &= \left| -\frac{1}{2}\mathbf{p} - \frac{3}{4}\mathbf{q} \right| = \frac{1}{2}\sqrt{p^2 + \frac{9}{4}q^2 + 3pqy_{pq}} \\ q_3 &= \left| +\mathbf{p} - \frac{1}{2}\mathbf{q} \right| = \sqrt{p^2 + \frac{1}{4}q^2 - pqy_{pq}} \\ x_{p_2} &= \hat{\mathbf{p}}_2 \cdot \hat{\mathbf{q}}_0 = \frac{-\frac{1}{2}px_p + \frac{3}{4}qx_q}{p_2} \end{aligned}$$

$$\begin{aligned}
x_{q_2} &= \hat{\mathbf{q}}_2 \cdot \hat{\mathbf{q}}_0 = \frac{-px_p - \frac{1}{2}qx_q}{q_2} \\
x_{p_3} &= \hat{\mathbf{p}}_3 \cdot \hat{\mathbf{q}}_0 = \frac{-\frac{1}{2}px_p - \frac{3}{4}qx_q}{p_3} \\
x_{q_3} &= \hat{\mathbf{q}}_3 \cdot \hat{\mathbf{q}}_0 = \frac{+px_p - \frac{1}{2}qx_q}{q_3} \\
x_{p_2q_2}^{q_0} &= (\widehat{\mathbf{q}_0 \times \mathbf{p}_2}) \cdot (\widehat{\mathbf{q}_0 \times \mathbf{q}_2}) = \frac{\frac{1}{2}p^2 - \frac{3}{8}q^2 - \frac{1}{2}pqy_{pq} - x_{p_2}x_{q_2}}{p_2q_2} \\
x_{p_3q_3}^{q_0} &= (\widehat{\mathbf{q}_0 \times \mathbf{p}_3}) \cdot (\widehat{\mathbf{q}_0 \times \mathbf{q}_3}) = \frac{-\frac{1}{2}p^2 + \frac{3}{8}q^2 - \frac{1}{2}pqy_{pq} - x_{p_3}x_{q_3}}{p_3q_3} \cdot \frac{1}{\sqrt{1-x_{p_2}^2}\sqrt{1-x_{q_2}^2}}. \quad (3.76)
\end{aligned}$$

The Eqs. (3.69), (3.71) and (3.75) are the starting points for the numerical calculation of three-body scattering operators.

3.2.3 Structure and Treatment of The Moving Singularities

In three-body scattering observed in center of mass frame, a particle with mass m and momentum \mathbf{q}_0 heads on a two-body bound state target with mass $2m$ and momentum $-\mathbf{q}_0$. The total energy E is given by

$$E = E_d + \frac{q_0^2}{2m} + \frac{q_0^2}{4m} = E_d + \frac{3q_0^2}{4m}. \quad (3.77)$$

where $E_d = -|E_d|$ is the binding energy of the two-body bound state. For the case of $E < 0$, the total energy is not enough to have three free particles in final state and only elastic scattering is allowed. This case is called below breakup threshold. The free three-body propagator can then be written as

$$G_0 = \frac{1}{E - \frac{1}{m}(q^2 + \mathbf{q} \cdot \mathbf{q}'' + q''^2)}. \quad (3.78)$$

For the case of $E > 0$, three free particles in the final state are allowed. So this case is called above breakup threshold. The free propagator must be written as

$$G_0 = \frac{1}{E - \frac{1}{m}(q^2 + \mathbf{q} \cdot \mathbf{q}'' + q''^2) + i\varepsilon}. \quad (3.79)$$

It has singularities and the $i\varepsilon$ prescription is introduced to fix the asymptotic boundary condition. In the q -system, G_0 can be written as

$$G_0 = \frac{1}{E - \frac{1}{m}(q^2 + \mathbf{q} \cdot \mathbf{q}'' + q''^2) + i\varepsilon} = \frac{m}{(mE - q^2 - q''^2) - qq''x'' + i\varepsilon}$$

$$= \frac{\frac{m}{qq''}}{x_0 - x'' + i\varepsilon} \quad (3.80)$$

with

$$x_0 = \frac{mE - q^2 - q''^2}{qq''}. \quad (3.81)$$

This means the singularities in the free propagator are functions of q , q'' and x'' [26]. The integration variable x'' is defined on the interval $[-1, +1]$, so singularities occur when $|x_0| \leq 1$. In order to treat them, we need to locate the singularities at first. The boundaries of the singular region is specified by $|x_0| = 1$, i.e.

$$\left| \frac{mE - q^2 - q''^2}{qq''} \right| = 1. \quad (3.82)$$

The solutions of above equation define the curves

$$q'' = \pm \frac{q}{2} \pm \sqrt{mE - \frac{3}{4}q^2}. \quad (3.83)$$

Because q'' should be real and positive, it is convenient to define

$$\begin{aligned} q_+ &= \frac{q}{2} + \sqrt{Q_0^2 - \frac{3}{4}q^2}, \\ q_- &= \left| \frac{q}{2} - \sqrt{Q_0^2 - \frac{3}{4}q^2} \right| \end{aligned} \quad (3.84)$$

where $Q_0 = \sqrt{mE}$. More explicitly for q_- , one has

$$q_- = \begin{cases} -\frac{q}{2} + \sqrt{Q_0^2 - \frac{3}{4}q^2} & q < Q_0, \\ +\frac{q}{2} - \sqrt{Q_0^2 - \frac{3}{4}q^2} & q > Q_0. \end{cases} \quad (3.85)$$

The singular region is enclosed by the q_+ and q_- curves in the $q-q''$ plane corresponding to $|x_0| \leq 1$, as shown in Fig 3.2. It is not difficult to show that the maximum value of q'' is q_{max} on the top of q_+ curve when $q = \frac{q_{max}}{2}$ where q_{max} is given as

$$q_{max} = \sqrt{\frac{4m}{3}}E. \quad (3.86)$$

Furthermore, one finds that $x_0 < -1$ when $q > q_{max}$. So the singular region in x'' integration is bound within a box with length q_{max} .

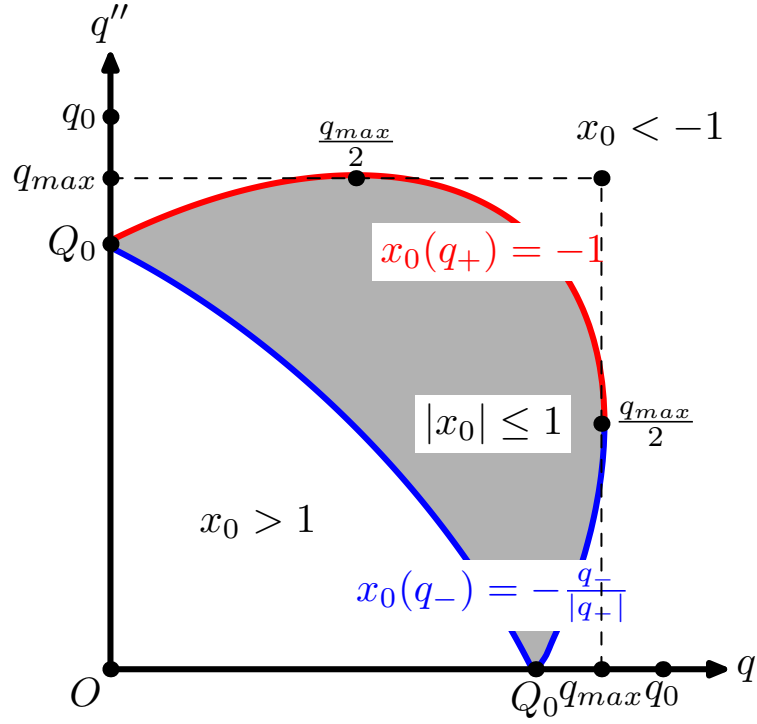


Figure 3.2: The region of singularities of the free three-particle propagator as function of the momenta q and q'' . The shaded area in the $q - q''$ plane indicates the region where $|x_0| \leq 1$, i.e. the region where a pole in the x'' -integration occurs. This region is enclosed by the bounding curves q_+ and q_- , which contain the logarithmic singularities as functions of q'' .¹

There is another special value of q , namely

$$q_0 = \sqrt{\frac{4m}{3}(E - E_d)}. \quad (3.87)$$

When $q = q_0$, the residue of $t_s(z)$ at $z = E - \frac{3}{4m}q^2 = E_d$ should be explicitly treated as shown in Eq. (3.29). Comparing Eq. (3.86) and Eq. (3.87) indicates that $q_{max} < q_0$. Thus the isolated pole at $q'' = q_0$ and the moving singularity in the “half-moon” region shown in Fig. 3.2 can be treated separately in the integration part of Eq. (3.69) by dividing the domain of q into pieces.

In order to carry out the different integration parts in Eq. (3.69) for \hat{T} , we need to find a way to treat the singularities. Since the free propagator does not depend on φ'' , we can carry out the integration over φ'' separately. With fixed values of p , x_p , $x_{pq}^{q_0}$, x_q and q , we define for clarity a function $G(q'', x'')$ by

$$G(q'', x'') = \int_0^{2\pi} d\varphi'' \hat{t}_s \left(p, \sqrt{\frac{1}{4}q^2 + q''^2 + qq''x''}, \frac{\frac{1}{2}qy_{pq} + q''y_{pq''}}{\sqrt{\frac{1}{4}q^2 + q''^2 + qq''x''}}; E - \frac{3}{4m}q^2 \right) \\ \left\langle \sqrt{q^2 + \frac{1}{4}q''^2 + qq''x''}, \frac{qx_q + \frac{1}{2}q''y_{q_0q''}}{\sqrt{q^2 + \frac{1}{4}q''^2 + qq''x''}}, \frac{\frac{qx'' + \frac{1}{2}q''}{\sqrt{q^2 + \frac{1}{4}q''^2 + qq''x''}} - x_{\pi_p}x_{\pi_q}}{\sqrt{1 - x_{\pi_p}^2}\sqrt{1 - x_{\pi_q}^2}}, y_{q_0q''}, q''|\hat{T}|q_0\varphi_d \right\rangle$$

The definitions for the variables in above equation can be found in Eq. (3.70). The integration part of Eq. (3.69) for \hat{T} can then be written as

$$I = \int_0^{\bar{q}} dq'' q''^2 \int_{-1}^{+1} dx'' \frac{G(q'', x'')}{\left(E - \frac{1}{m}(q^2 + q''^2 + qq''x'') + i\varepsilon\right) \left(E - E_d - \frac{3}{4m}q''^2 + i\varepsilon\right)}, \quad (3.88)$$

where \bar{q} is the cutoff of q'' integration. The integral I is a function of p , x_p , $x_{pq}^{q_0}$, x_q and q . In order to carry out this integral, we decompose the q -domain into intervals as $0 \cup (0, q_{max}) \cup q_{max} \cup (q_{max}, \bar{q})$.

- $q = 0$:

When $q = 0$, x_0 is not defined. The three-body propagator is reduced as

$$\frac{1}{E - \frac{1}{m}(q^2 + q''^2 + qq''x'') + i\varepsilon} = \frac{m}{Q_0^2 - q''^2}, \quad (3.89)$$

which does not depend on x'' . Then the integration in Eq. (3.88) is simplified as

$$I_1 = \int_0^{\bar{q}} dq'' F_x(q'') \left[\frac{1}{Q_0^2 - q''^2 + i\varepsilon} - \frac{1}{q_0^2 - q''^2 + i\varepsilon} \right], \quad (3.90)$$

where

$$F_x(q'') = \frac{4m^2}{3(q_0^2 - Q_0^2)} \int_{-1}^{+1} dx'' G(q'', x''). \quad (3.91)$$

The two isolated singularities in Eq. (3.90) can be treated by the subtraction method. As given in Ref. [46], for any general k_{min} and k_{max} where $k_{min} < k < k_{max}$ and $k_{max} \neq \infty$, one has

$$\begin{aligned} \int_{k_{min}}^{k_{max}} dq'' \frac{F(k'')}{k^2 - k''^2 + i\varepsilon} &= \text{P} \int_{k_{min}}^{k_{max}} dq'' \frac{F(k'') - F(k)}{k^2 - k''^2} \\ &+ \frac{F(k)}{2k} \left[\ln \left(\frac{k - k_{min}}{k + k_{min}} \frac{k_{max} + k}{k_{max} - k} \right) - i\pi \right]. \end{aligned} \quad (3.92)$$

Then the integration in Eq. (3.90) is calculated as

$$\begin{aligned} I_1 &= \left(\text{P} \int_0^{\bar{q}} dq'' \frac{F_x(q'') - F_x(Q_0)}{Q_0^2 - q''^2} + \frac{F_x(Q_0)}{2Q_0} \left[\ln \left(\frac{\bar{q} + Q_0}{\bar{q} - Q_0} \right) - i\pi \right] \right) \\ &- \left(\text{P} \int_0^{\bar{q}} dq'' \frac{F_x(q'') - F_x(q_0)}{q_0^2 - q''^2} + \frac{F_x(q_0)}{2q_0} \left[\ln \left(\frac{\bar{q} + q_0}{\bar{q} - q_0} \right) - i\pi \right] \right) \end{aligned} \quad (3.93)$$

- $0 < q < q_{max}$:

When $0 < q < q_{max}$, the moving singularity in the half-moon region has to be treated explicitly. We decompose the q'' -domain into $(0, q_{max}) \cup (q_{max}, \bar{q})$. The integration in Eq. (3.88) then can be written as

$$\begin{aligned} I_2 &= \underbrace{\int_0^{q_{max}} dq'' \int_{-1}^{+1} dx'' \frac{F(q'', x'')}{(q_0^2 - q''^2)(x_0 - x'' + i\varepsilon)}}_{I_{21}} \\ &+ \underbrace{\int_{q_{max}}^{\bar{q}} dq'' \int_{-1}^{+1} dx'' \frac{F(q'', x'')}{(q_0^2 - q''^2 + i\varepsilon)(x_0 - x'')}}_{I_{22}} \end{aligned} \quad (3.94)$$

with

$$F(q'', x'') = \frac{4m^2}{3qq''} G(q'', x''). \quad (3.95)$$

Only the integral I_{21} contains the moving singularities in the half-moon region, and the integral I_{22} contains the isolated pole at $q'' = q_0$. Considering the moving singularities in integral I_{21} , one has

$$I_{21} = \int_0^{q_{max}} dq'' \int_{-1}^{+1} dx'' \frac{F_{q''}(q'', x'')}{x_0 - x'' + i\varepsilon} \quad (3.96)$$

where

$$F_{q''}(q'', x'') = \frac{F(q'', x'')}{q_0^2 - q''^2}. \quad (3.97)$$

The singularities in the x'' integration are treated by the subtraction method. We define the subtracted integrand as

$$\hat{F}_{q''}(q'', x_0) = \begin{cases} F_{q''}(q'', x_0) : & |x_0| \leq 1 \\ F_{q''}(q'', \frac{x_0}{|x_0|}) : & |x_0| > 1. \end{cases} \quad (3.98)$$

The subtraction is performed not only on the region of $|x_0| \leq 1$, but also for $|x_0| > 1$. The reason for such subtraction over extended region is that we need to make the subtracted integrand as least continuous at $|x_0| = 1$ because the integrand is given by splines in our numerical calculations. We will discuss this in detail later. For $|x_0| \leq 1$, the integral gives

$$\int_{-1}^{+1} dx'' \frac{1}{x_0 - x'' + i\varepsilon} = P \int_{-1}^{+1} dx'' \frac{1}{x_0 - x''} - i\pi\delta(x_0 - x'') \quad (3.99)$$

where P indicates the principal value. For $|x_0| > 1$ one has

$$\int_{-1}^{+1} dx'' \frac{1}{x_0 - x'' + i\varepsilon} = \int_{-1}^{+1} dx'' \frac{1}{x_0 - x''}. \quad (3.100)$$

Then the integral I_{21} is evaluated as

$$\begin{aligned} I_{21} &= \int_0^{q_{max}} dq'' \int_{-1}^{+1} dx'' \frac{F_{q''}(q'', x'')}{x_0 - x'' + i\varepsilon} \\ &= \int_0^{q_{max}} dq'' \int_{-1}^{+1} dx'' \frac{F_{q''}(q'', x'') - \hat{F}_{q''}(q'', x_0)}{x_0 - x''} \\ &\quad + \int_0^{q_{max}} dq'' \hat{F}_{q''}(q'', x_0) P \int_{-1}^{+1} dx'' \frac{1}{x_0 - x''} \\ &\quad - i\pi \int_0^{q_{max}} dq'' \Theta(1 - |x_0|) \hat{F}_{q''}(q'', x_0) \end{aligned}$$

$$\begin{aligned}
&= \int_0^{q_{max}} dq'' \int_{-1}^{+1} dx'' \frac{F_{q''}(q'', x'') - \hat{F}_{q''}(q'', x_0)}{x_0 - x''} \\
&+ \int_0^{q_{max}} dq'' \hat{F}_{q''}(q'', x_0) \ln \left| \frac{1+x_0}{1-x_0} \right| \\
&- i\pi \int_0^{q_{max}} dq'' \Theta(1 - |x_0|) \hat{F}_{q''}(q'', x_0). \tag{3.101}
\end{aligned}$$

With this the x'' integration is regularized, but there is still a logarithmic singularity left in the q'' integration when $|x_0| = \pm 1$. Considering $q_- = \frac{q}{2} - \sqrt{Q_0^2 - \frac{3}{4}q^2}$, one has

$$\begin{aligned}
\ln \left| \frac{1+x_0}{1-x_0} \right| &= \left(-\frac{q_-}{|q_-|} \ln |q'' + |q_-|| - \ln |q'' + q_+| \right) \\
&+ \left(+\frac{q_-}{|q_-|} \ln |q'' - |q_-|| + \ln |q'' - q_+| \right), \tag{3.102}
\end{aligned}$$

which is singular for $q'' = |q_-|$ or $q'' = q_+$ in the q'' integration. The integration over this logarithmic singularity can be decomposed as

$$\begin{aligned}
&\int_0^{q_{max}} dq'' \hat{F}_{q''}(q'', x_0) \ln \left| \frac{1+x_0}{1-x_0} \right| \\
&= \int_0^{q_{max}} dq'' \hat{F}_{q''}(q'', x_0) \left(-\frac{q_-}{|q_-|} \ln |q'' + |q_-|| - \ln |q'' + q_+| \right) \\
&+ \int_0^{q_{max}} dq'' \hat{F}_{q''}(q'', x_0) \left(+\frac{q_-}{|q_-|} \ln |q'' - |q_-|| + \ln |q'' - q_+| \right). \tag{3.103}
\end{aligned}$$

where only the second term in Eq. (3.103) is logarithmically singular. Instead of performing a further subtraction which is possible, we use a different method to evaluate Eq. (3.103), namely the cubic spline-based integration method described in Section 5.1.2. Because the cubic spline functions are polynomials up to third order, the integration with the logarithmic singularity can be carried out quasi analytically as integral over ln-function with a polynomial. This is the main advantage of the spline-based integration method. This is why we do the subtraction over an extended region as shown in Eq. (3.98), which guarantees that the subtracted integrand $\hat{F}_{q''}(q'', x_0)$ for q'' integration is at least continuous at $x_0 = \pm 1$. This continuity is necessary for the application of spline functions when the integrating over q'' across $x_0 = \pm 1$.

We consider now the second integral in Eq. (3.94) where $q'' > q_{max}$. Let

$$F_x(q'') = \int_{-1}^{+1} dx'' \frac{F(q'', x'')}{x_0 - x''}, \tag{3.104}$$

then

$$\begin{aligned}
I_{22} &= \int_{q_{max}}^{\bar{q}} dq'' \frac{F_x(q'', x'')}{q_0^2 - q''^2 + i\varepsilon} \\
&= \int_{q_{max}}^{\bar{q}} dq'' \frac{F_x(q'') - F_x(q_0)}{q_0^2 - q''^2} + \frac{F_x(q_0)}{2q_0} \left[\ln \left(\frac{q_0 - q_{max} \bar{q} + q_0}{q_0 + q_{max} \bar{q} - q_0} \right) - i\pi \right]
\end{aligned} \tag{3.105}$$

- $q = q_{max}$:

This case is just a special situation when $0 < q'' < q_{max}$. One can formally define the integration in Eq. (3.88) as

$$\begin{aligned}
I_3 &= \underbrace{\int_0^{q_{max}} dq'' \int_{-1}^{+1} dx'' \frac{F(q'', x'')}{(q_0^2 - q''^2)(x_0 - x'' + i\varepsilon)}}_{I_{31}} \\
&+ \underbrace{\int_{q_{max}}^{\bar{q}} dq'' \int_{-1}^{+1} dx'' \frac{F(q'', x'')}{(q_0^2 - q''^2 + i\varepsilon)(x_0 - x'')}}_{I_{32}}
\end{aligned} \tag{3.106}$$

with

$$F(q'', x'') = \frac{4m^2}{3q_{max}q''} G(q'', x''). \tag{3.107}$$

From Fig. 3.2, we see that when $q = q_{max}$, $q_+ = q_- = \frac{q_{max}}{2}$. Also, when $q'' = q_{max}$, $x_0 = -1$. So similar to the integral I_{21} in Eq. (3.101), the integral I_{31} is written as

$$\begin{aligned}
I_{31} &= \int_0^{q_{max}} dq'' \int_{-1}^{+1} dx'' \frac{F_{q''}(q'', x'')}{x_0 - x'' + i\varepsilon} \\
&= \int_0^{q_{max}} dq'' \int_{-1}^{+1} dx'' \frac{F_{q''}(q'', x'') - F_{q''}(q'', -1)}{x_0 - x''} \\
&+ \int_0^{q_{max}} dq'' F_{q''}(q'', -1) \text{P} \int_{-1}^{+1} dx'' \frac{1}{x_0 - x''} \\
&- i\pi \int_0^{q_{max}} dq'' \Theta(1 - |x_0|) F_{q''}(q'', x_0 = -1) \\
&= \int_0^{q_{max}} dq'' \int_{-1}^{+1} dx'' \frac{F_{q''}(q'', x'') - F_{q''}(q'', -1)}{x_0 - x''} \\
&+ \int_0^{q_{max}} dq'' F_{q''}(q'', -1) \ln \left| \frac{1 + x_0}{1 - x_0} \right| - i\pi F_{q''}\left(\frac{q_{max}}{2}, -1\right).
\end{aligned} \tag{3.108}$$

When $q = q_{max}$, $\frac{q_-}{|q_-|} = -1$, and one has

$$\begin{aligned} \ln \left| \frac{1+x_0}{1-x_0} \right| &= (-\ln |q'' + |q_-|| - \ln |q'' + q_+|) + (\ln |q'' - |q_-|| + \ln |q'' - q_+|) \\ &= -2 \ln \left| q'' + \frac{q_{max}}{2} \right| + 2 \ln \left| q'' - \frac{q_{max}}{2} \right| \end{aligned} \quad (3.109)$$

where only the second term is logarithmically singular. Again, this integral will also be evaluated by spline based integration. The I_{32} has exactly the same form as I_{22} in Eq. (3.105).

- $q_{max} < q < \bar{q}$:

For this case, there is no singularity with respect to the x'' integration, and one can define

$$F_x(q'') = \int_{-1}^{+1} dx'' \frac{F(q'', x'')}{x_0 - x''}. \quad (3.110)$$

The isolated pole in the q'' integration at $q'' = q_0$ is treated by the subtraction method shown in Eq. (3.92). Then the integration in Eq. (3.88) is evaluated as

$$I_4 = \int_0^{\bar{q}} dq'' \frac{F_x(q'')}{q_0^2 - q''^2} = \int_0^{\bar{q}} dq'' \frac{F_x(q'') - F_x(q_0)}{q_0^2 - q''^2} + \frac{F_x(q_0)}{2q_0} \left(\ln \left(\frac{\bar{q} + q_0}{\bar{q} - q_0} \right) - i\pi \right). \quad (3.111)$$

Up to now, the integration in Eq. (3.69) above breakup threshold is regularized and can be carried out.

Below the breakup threshold, there is no singularity in free propagator G_0 . The only one isolated pole is at $q'' = q_0$ in the q'' integration, and can be treated by the standard subtraction method as shown in Eq (3.92). Explicitly one can carry out the x'' integration as

$$F_x(q'') = \int_{-1}^{+1} dx'' \frac{F(q'', x'')}{x_0 - x''}, \quad (3.112)$$

with

$$F(q'', x'') = \frac{4m^2}{3qq''} G(q'', x'') \quad (3.113)$$

and then evaluate the integration in Eq. (3.88) as

$$I = \int_0^{\bar{q}} dq'' \frac{F_x(q'')}{q_0^2 - q''^2 + i\varepsilon} = \int_0^{\bar{q}} dq'' \frac{F_x(q'') - F_x(q_0)}{q_0^2 - q''^2} + \frac{F_x(q_0)}{2q_0} \left(\ln \left(\frac{\bar{q} + q_0}{\bar{q} - q_0} \right) - i\pi \right) \quad (3.114)$$

We are now in a situation where all integrations in Eq. (3.69) can be carried out numerically for both above and below the breakup threshold cases.

3.3 Cross Sections and Optical Theorem

The observables in three-body scattering process involving scalar particles are various kinds of cross sections, including elastic cross sections and breakup cross sections. One can calculate the cross sections once the elastic scattering operator U and the breakup process operator U_0 are obtained. If one considers a reaction of the type

$$\mathbf{A} + \mathbf{B} \rightarrow \mathbf{C}_1 + \mathbf{C}_2 + \cdots \mathbf{C}_n \quad (3.115)$$

in which there are n distinct particles in the final state with wave vectors $\mathbf{k}_1, \mathbf{k}_2, \dots, \mathbf{k}_n$, internal quantum numbers $\alpha_1, \alpha_2, \dots, \alpha_n$ and energies E_1, E_2, \dots, E_n . The cross section of this final state can be written as

$$\sigma = \sum_{\alpha_1, \alpha_2, \dots, \alpha_n} \int d^3k_1 d^3k_2 \cdots d^3k_n \delta(E_f - E_i) \delta(\mathbf{P}_f - \mathbf{P}_i) \frac{(2\pi)^4}{|\mathbf{v}_A - \mathbf{v}_B|} |T_{fi}|^2 \quad (3.116)$$

The dynamics is entirely contained in the square of transition matrix element T_{fi} while the phase space factors are of purely kinematic nature [47] .

In the elastic channel of three-body scattering, the kinematics is quite simple. There is the relative motion between the single particle and the bound state pair. In center of mass frame (c.m.) the single particle and the two-body bound pair are incoming toward each other with relative momentum \mathbf{q}_0 and outgoing with relative momentum \mathbf{q} . The momentum conservation has been automatically considered by working in center of mass frame. The energy conservation is

$$E_i = E_d + \frac{3}{4m} q_0^2 = E_f = E_d + \frac{3}{4m} q^2 \quad (3.117)$$

where m is the mass of each particle and E_d is the binding energy of two-body bound state. The cross section is

$$\sigma_{el} = \int d^3q \delta(E_f - E_i) \frac{(2\pi)^4}{|\mathbf{v}_A - \mathbf{v}_B|} |T_{fi}|^2 \quad (3.118)$$

Considering the phase factor alone, one has

$$\begin{aligned} & \int d^3q \delta(E_f - E_i) \frac{(2\pi)^4}{|\mathbf{v}_A - \mathbf{v}_B|} \\ &= \int d\Omega_q dq q^2 \delta\left(\frac{3}{4m}q^2 - \frac{3}{4m}q_0^2\right) \frac{(2\pi)^4}{|\mathbf{v}_A - \mathbf{v}_B|} \end{aligned}$$

The δ function is evaluated as,

$$\delta(f(x)) = \sum_{k=1}^n \left| \frac{1}{\frac{df}{dx}|_{x=x_0^k}} \right| \delta(x - x_0^k), \quad (3.119)$$

where the x_0^k are the simple zeros of $f(x)$. Because q is positive, the only zero is $q = q_0$. Thus we have

$$\delta\left(\frac{3q^2}{4m} - \frac{3q_0^2}{4m}\right) = \frac{2m}{3q_0} \delta(q - q_0). \quad (3.120)$$

The relative velocity in the initial channel is

$$|\mathbf{v}_A - \mathbf{v}_B| = \left| \frac{\mathbf{q}_0}{m} - \frac{-\mathbf{q}_0}{2m} \right| = \frac{3q_0}{2m} \quad (3.121)$$

Since $q = q_0$, the elastic transition operator can be written as

$$T_{el} = \langle q_0 x \varphi_d | U_{el} | \mathbf{q}_0 \varphi_d \rangle. \quad (3.122)$$

Now we need to identify the U_{el} . Here we consider the scattering initiated by a particle heading on a two-body bound pair in target. Due to the symmetrization of identical bosons, we have no way to distinguish the initial channel $|\phi_\alpha\rangle$ with index $\alpha = 1, 2, 3$. So the initial state is constructed by the averaging over these three possible rearrangements as

$$|\phi\rangle = \frac{1}{\sqrt{3}} \sum_{\alpha=1}^3 |\phi_\alpha\rangle. \quad (3.123)$$

Meanwhile the contributions from all possible elastic final states needs to be summed up. There are three possible elastic final states $|\phi'_\beta\rangle$ with index $\beta = 1, 2, 3$, so the total elastic amplitude is

$$\langle q_0 x \varphi_d | U_{el} | \mathbf{q}_0 \varphi_d \rangle^2 = \frac{1}{3} \sum_{\beta}^3 \left| \sum_{\alpha}^3 \langle \phi'_\beta | U_{\beta\alpha} | \phi_\alpha \rangle \right|^2 \quad (3.124)$$

where the $U_{\beta\alpha}$ is elastic operator for the transition from initial α to final β elastic channels. According to the definition of U in Eq. (2.40),

$$\frac{1}{3} \sum_{\beta}^3 \left| \sum_{\alpha}^3 \langle \phi'_\beta | U_{\beta\alpha} | \phi_\alpha \rangle \right|^2 = |\langle \phi' | U | \phi \rangle|^2. \quad (3.125)$$

Thus the differential elastic cross section for three-body scattering expressed in terms of U is

$$\frac{d\sigma^{el}}{d\Omega} = \left(\frac{2m}{3} \right)^2 (2\pi)^4 |\langle q_0 x \varphi_d | U | \mathbf{q}_0 \varphi_d \rangle|^2 \quad (3.126)$$

and the total elastic cross section is

$$\sigma_{el} = \int d\Omega \frac{d\sigma^{el}}{d\Omega} = \left(\frac{2m}{3} \right)^2 (2\pi)^5 \int_{-1}^{+1} dx |\langle q_0 x \varphi_d | U | \mathbf{q}_0 \varphi_d \rangle|^2. \quad (3.127)$$

For the breakup process, the phase factor in the center of mass frame can be written as

$$\int d^3p \, d^3q \delta(E_f - E_i) \frac{(2\pi)^4}{|\mathbf{v}_A - \mathbf{v}_B|} = \int d^3p \, d^3q \delta \left(E - \frac{p^2}{m} - \frac{3q^2}{4m} \right) \frac{(2\pi)^4}{\frac{q_0}{\frac{2}{3}m}}. \quad (3.128)$$

Carrying out the p integration, we have

$$\int_0^{\sqrt{\frac{4mE}{3}}} dq \int d\Omega_p d\Omega_q \frac{(2\pi)^4 m^2}{3q_0} q^2 \sqrt{mE - \frac{3}{4}q^2} \quad (3.129)$$

The initial channel for breakup case is the same as that for elastic expressed in Eq. (3.123) but the final state in the breakup channel state is $|\phi_0\rangle = |\mathbf{p}\mathbf{q}\rangle$. According to the definition of U_0 in Eq. (2.33), one has

$$\left| \frac{1}{\sqrt{3}} \sum_{\alpha=1}^3 \langle \phi_0 | U_{0\alpha} | \phi_\alpha \rangle \right|^2 = \frac{1}{3} |\langle \phi_0 | U_0 | \phi \rangle|^2 \quad (3.130)$$

where $U_{0\alpha}$ is the breakup operator for the transition from initial channel $|\phi_\alpha\rangle$ to final breakup channel $|\phi_0\rangle$. Thus the five fold differential cross section is

$$\frac{d^5\sigma_{br}}{d\Omega_p d\Omega_q dq} = \frac{1}{3} \frac{(2\pi)^4 m^2}{3q_0} q^2 \sqrt{mE - \frac{3}{4}q^2} |\langle\phi_0|U_0|\phi\rangle|^2. \quad (3.131)$$

After the U_0 is obtained as $U_0(p, x_p, x_{pq}^{q_0}, x_q, q)$ by Eq. (3.75), in calculating total breakup cross sections, we have at least three different ways to carry out the angular integration due to the rotational invariance of the U_0 .

- If the integration is carried out in q_0 -system, then the integral volume is

$$\int d\Omega_p d\Omega_q = 2\pi \int_{-1}^{+1} dx_p'' \int_{-1}^{+1} dx_q'' \int_0^{2\pi} d\varphi_{pq}''. \quad (3.132)$$

with

$$\begin{aligned} x_p &\rightarrow x_p'', \\ x_q &\rightarrow x_q'', \\ x_{pq}^{q_0} &\rightarrow \cos \varphi_{pq}''. \end{aligned} \quad (3.133)$$

Here the \rightarrow means the arguments of U_0 in Eq. (3.75) at the left hand side are replaced by the integral variables at right hand side when the angular integration is evaluated.

- If the integration is carried out in q -system, then the integral volume is

$$\int d\Omega_p d\Omega_q = 2\pi \int_{-1}^{+1} dx_q'' \int_{-1}^{+1} dy_{pq}'' \int_0^{2\pi} d\varphi_{pq_0}''. \quad (3.134)$$

with

$$\begin{aligned} x_p &\rightarrow x_q'' y_{pq}'' + \sqrt{1 - x_q''^2} \sqrt{1 - y_{pq}''^2} \cos \varphi_{pq_0}'', \\ x_q &\rightarrow x_q'', \\ x_{pq}^{q_0} &\rightarrow \frac{y_{pq}'' - (x_q'' y_{pq}'' + \sqrt{1 - x_q''^2} \sqrt{1 - y_{pq}''^2} \cos \varphi_{pq_0}'') x_q''}{\sqrt{1 - (x_q'' y_{pq}'' + \sqrt{1 - x_q''^2} \sqrt{1 - y_{pq}''^2} \cos \varphi_{pq_0}'')^2} \sqrt{1 - x_q''^2}}. \end{aligned} \quad (3.135)$$

- If the integration is carried out in p -system, in which the z -axis is parallel to \mathbf{p} , then the integral volume is

$$\int d\Omega_p d\Omega_q = 2\pi \int_{-1}^{+1} dx_p'' \int_{-1}^{+1} dy_{pq}'' \int_0^{2\pi} d\varphi_{qq_0}''. \quad (3.136)$$

with

$$\begin{aligned} x_p &\rightarrow x_p'', \\ x_q &\rightarrow x_p'' y_{pq}'' + \sqrt{1 - x_p''^2} \sqrt{1 - y_{pq}''^2} \cos \varphi_{qq_0}'', \\ x_{pq}^{q_0} &\rightarrow \frac{y_{pq}'' - (x_p'' y_{pq}'' + \sqrt{1 - x_p''^2} \sqrt{1 - y_{pq}''^2} \cos \varphi_{qq_0}'') x_p''}{\sqrt{1 - (x_p'' y_{pq}'' + \sqrt{1 - x_p''^2} \sqrt{1 - y_{pq}''^2} \cos \varphi_{qq_0}'')^2} \sqrt{1 - x_p''^2}}. \end{aligned} \quad (3.137)$$

The total breakup cross section resulted from these three ways should be the same. After the angular integration carried out, one has

$$F(p, q) = \int d\Omega_p d\Omega_q |\langle \phi_0 | U_0 | \phi \rangle|^2 \quad (3.138)$$

and

$$\frac{d\sigma_{br}}{dq} = \frac{1}{3} \frac{(2\pi)^4 m^2}{3q_0} q^2 \sqrt{mE - \frac{3}{4}q^2} F\left(\sqrt{mE - \frac{3}{4}q^2}, q\right). \quad (3.139)$$

With this the total breakup cross section can be calculated as

$$\sigma_{br} = \frac{1}{3} \frac{(2\pi)^4 m^2}{3q_0} \int_0^{\sqrt{\frac{4mE}{3}}} dq q^2 \sqrt{mE - \frac{3}{4}q^2} F\left(\sqrt{mE - \frac{3}{4}q^2}, q\right). \quad (3.140)$$

For the unitary relation between U and U_0 in Eq. (2.72), multiplying the factor $\frac{(2\pi)^3 2m}{3}$ on both side, one gets the so called optical theorem

$$\begin{aligned} \sigma_{opt} &= -\frac{(2\pi)^3 4m}{3q_0} \text{Im} \langle \phi | U | \phi \rangle \\ &= \sigma_{el} + \sigma_{br}. \end{aligned} \quad (3.141)$$

where the σ_{opt} is total cross section evaluated by optical theorem.

V_A [MeV fm]	μ_A [fm ⁻¹]	V_R [MeV fm]	μ_R [fm ⁻¹]	E_d [MeV]
-626.8932	1.550	1438.7228	3.11	-2.2307

Table 3.1: The parameters and deuteron binding energy for the Malfliet-Tjon type potential of our calculation. As conversion factor We use units such that $\hbar c = 197.3286$ MeV fm = 1.

3.4 The Explicit Calculation of the Scattering Operator

As model two-body interaction in our three-body scattering study, we choose a potential of Malfliet-Tjon type [10] which is a superposition of two Yukawa interactions,

$$V(\mathbf{p}', \mathbf{p}) = \frac{1}{2\pi^2} \left(\frac{V_R}{(\mathbf{p}' - \mathbf{p})^2 + \mu_R^2} - \frac{V_A}{(\mathbf{p}' - \mathbf{p})^2 + \mu_A^2} \right). \quad (3.142)$$

The parameters are given in Table 3.1, and fitted such that the potential supports a two-body bound state with binding energy $E_d = -2.23$ MeV. The fully off-shell two-body t -matrix $t(\mathbf{p}', \mathbf{p}, z)$ is solved directly from the Lippmann-Schwinger equation with the explicit form in Eq. (3.19) at the off-shell energies $E - \frac{3}{4m}q^2$ as required by Eq. (3.69). The function $t(p', p, x, E - \frac{3}{4m}q^2)$ is obtained for each fixed q on a symmetric momentum grid with 60 p (p') points and 40 x (x') points by solving Eq. (3.19). Since the momentum region which contributes to a solution of the two-body t -matrix is quite different from the region of importance in a three-body calculation, we map our solution for t onto the momentum grid relevant for the three-body transition amplitude. This is done by applying the Lippmann-Schwinger equation in Eq. (3.19) repeatedly. The symmetrized operator t_s is constructed via Eq. (3.24). With the solved two-body symmetric t -matrix t_s and the treatment of moving singularity, the integration kernel of the integral equation in Eq. (3.69) can be prepared. The singularities present in G_0 and the pole in t_s are handled as described in the previous section. The integrations in the kernel of \hat{T} are carried out by Gaussian quadrature, except those with the logarithmic singularities which are treated by a spline-based

integration. The p grid is defined from 0 to 30 fm^{-1} , the q and q'' grids are defined from 0 to 20 fm^{-1} , the angular grids for x_p , $x_{pq}^{q_0}$, x_q and x'' are defined on the interval $[-1, 1]$, and the angular grid for φ'' is defined on the interval $[0, 2\pi]$. As prescriptions for treating singularities in G_0 , we show in Eqs. (3.94) and (3.106) that the q and q'' grids are decomposed as $0 \cup (0, q_{max}) \cup q_{max} \cup (q_{max}, \bar{q})$, where $q_{max} = \sqrt{\frac{4m}{3}E}$ and $\bar{q} = 20 \text{ fm}^{-1}$.

The integral equation for \hat{T} in Eq. (3.69) can be written in a form

$$\hat{T} = \hat{T}^{(0)} + K\hat{T} \quad (3.143)$$

where the K is the integration kernel. Since Eq. (3.69) is a three-dimensional integral equation with five variables, the kernel K needs to be represented on an eight dimensional grid, with size up to $50 \times 20 \times 20 \times 20 \times 50 \times 50 \times 20 \times 20$. It is impossible to directly solve the linear equation of the form

$$[1 - K]\hat{T} = \hat{T}^{(0)} \quad (3.144)$$

with such high dimensionality. Instead we generate the Neumann series up to a certain finite order by the successive application of kernel K on $\hat{T}^{(0)}$, i.e.

$$\hat{T} = \hat{T}^{(0)} + K\hat{T}^{(0)} + K^2\hat{T}^{(0)} + K^3\hat{T}^{(0)} + \dots \quad (3.145)$$

The terms of consecutive order are generated recursively as

$$T^{(n)} = KT^{(n-1)}, \quad (n \geq 1). \quad (3.146)$$

The infinite sum of the Neumann series

$$\sum_{i=0}^{\infty} \hat{T}^{(i)} \quad (3.147)$$

diverges in the channel that has the same J^Π quantum number of three-body bound state. For the case we consider, there are three identical scalar boson interacting with two-body force, and this two-body force supports a two-body bound state with binding energy E_d . This two-body force also supports a three-body bound state, therefore in our case the infinite sum of the Neumann series diverges when the total

energy E is low enough and close to E . At higher energies, the infinite sum of the Neumann series might converge but very slowly. So it is necessary to use a method which can get the full solution of \hat{T} from a finite terms. This can be done by a Padé summation described in Section 5.2. As we show there, the Padé summation gives a convergent solution of \hat{T} whereas the sum of Neumann series diverges when the scattering energy $E_{lab} = 0.01$ GeV. At $E_{lab} = 0.5$ GeV, it turns out that the sum of Neumann series converges slowly, but Padé summation displays much faster convergence.

Since the converged results obtained by Padé summation sometimes fail to give the physical results we want [48], we need to test if the Padé solution of T is indeed the solution satisfying the Faddeev equation in Eq. (3.143). This can be done by reinserting the solution \hat{T} obtained via Padé summation back into the r.h.s of Eq. (3.143) and obtaining \hat{T}' , i.e.

$$\hat{T}' = \hat{T}^{(0)} + K\hat{T}. \quad (3.148)$$

One should have $\hat{T}' = \hat{T}$. Since \hat{T} and \hat{T}' are in the form of five dimensional matrix element, it is not easy to check their equality. To do this, we compare the observables, e.g. the elastic differential cross sections. We show the results in Table 3.2 at selected angles for energies $E_{lab} = 0.01$ GeV, $E_{lab} = 0.2$ GeV, $E_{lab} = 0.5$ GeV and $E_{lab} = 1.0$ GeV. The table shows excellent agreement of the two values of the cross section. It can be concluded that \hat{T} obtained by Padé summation is the solution of the Faddeev equation. In order to ensure the $\hat{T} = \hat{T}'$, we enforce this reinsertion check in every calculation of \hat{T} that we do.

3.5 Accuracy and Self-Consistency Analysis

After we obtain the solution of \hat{T} in Eq. (3.69) by Padé summation, we should check the self-consistency and accuracy of the calculation because of the high complexity of the numerics involved. We have a variety of ways to do this through the convergence against the number of Gaussian grid points, the built-in invariance under coordinate rotation and the unitary relation between the scattering operators. Before

E_{lab} [GeV]	$\theta_{c.m.}$ [deg]	$\frac{d\sigma^{el}}{d\Omega_{c.m.}} _T$ [mb]	$\frac{d\sigma^{el}}{d\Omega_{c.m.}} _{T'}$ [mb]
0.01	0.0	537.536	537.536
	21.8	420.036	420.036
	62.1	70.726	70.725
	93.4	38.289	38.289
	151.5	227.899	227.899
0.2	0.0	676.821	676.821
	21.8	148.880	148.880
	62.1	0.363	0.363
	93.4	0.223	0.223
	151.5	0.010	0.010
0.5	0.0	519.389	519.389
	21.8	16.209	16.209
	26.3	4.430	4.430
	62.1	0.088	0.088
	93.4	0.005	0.005
	151.5	0.004	0.004
1.0	0.0	$3.903 \times 10^{+2}$	$3.903 \times 10^{+2}$
	21.8	5.325×10^{-1}	5.325×10^{-1}
	62.1	4.072×10^{-4}	4.072×10^{-4}
	93.4	2.678×10^{-3}	2.678×10^{-3}
	151.5	3.705×10^{-4}	3.703×10^{-4}

Table 3.2: The elastic differential cross sections at different energies for selected scattering angles. The cross section labeled by T results from the converged solution of the integral equation Eq. (3.69) by Padé summation. The column labeled T' is calculated by reinserting the original solution into the Faddeev equation Eq. (3.143).

carrying on, we want to explain the meaning of the symbols in the following tables. After \hat{T} of Eq. (3.69) is solved in the q -system, the operator U for elastic scattering can be constructed in the q_0 -system by Eq (3.73), and in the q -system by equation by Eq. (3.74). The elastic cross sections evaluated correspondingly are denoted as $\sigma_{el}^{q_0}$ and σ_{el}^q . The total breakup cross section can be calculated in the q_0 -system, the q -system and the p -system via Eq. (3.133), Eq. (3.135) and Eq. (3.137). The corresponding total breakup cross sections are denoted as $\sigma_{br}^{q_0}$, σ_{br}^q , and σ_{br}^p . According to the built in invariance of our approach, we should have $\sigma_{el}^{q_0} = \sigma_{el}^q$ and $\sigma_{br}^{q_0} = \sigma_{br}^q = \sigma_{br}^p$. The total cross section is $\sigma_{el} + \sigma_{br}$. It should be equal to σ_{opt} which is evaluated by the optical theorem in Eq. (3.141).

In Tables 3.3 and 3.4 the differential elastic cross section at selected angles for two energies $E_{lab} = 0.01$ GeV and $E_{lab} = 0.5$ GeV are shown together with various grid points used in the calculation. In Table 3.5 the total elastic, the total breakup as well as the total cross section evaluated according to Eq. (3.141) via the optical theorem are given as function of various sets of grid points. The momentum grids for p and q are discretized with 49 points each. The integration variable q'' plays the same role as q , and is therefore also discretized with 49 points. For the q and q'' grid, there are 30 points in $(0, q_{max})$ interval and 19 points in (q_{max}, \bar{q}) interval, for a better accuracy in the treatment of singularities in G_0 . Both tables show that the angular dependence at the low energy, 0.01 GeV, is very weak, and in principle 12 grid points are sufficient for all angles. This is quite different at 0.5 GeV, where 16 angle points are clearly insufficient for x_p , x_q , and x'' . Only $x_{pq}^{q_0}$ and φ'' exhibit a weaker angular dependence, and 13 to 18 grid points are enough. It turns out that with 20 points for x_p and 24 points for x_q and x'' we achieve a converged calculations when considering the differential cross section at selected angles in Tables 3.3 and 3.4 and the total cross sections in Table 3.5. The calculations at higher energies presented here, are based on the grids given in the last 2 rows of Table 3.5. This grid allows sufficiently accurate calculations over a wide energy range.

E_{lab}	p	x_p	$x_{pq}^{q_0}$	x_q	q, q''	x''	φ''	$\theta_{c.m.}$ [deg]	$\frac{d\sigma_{el}}{d\Omega}$ [mb]
0.01	49	4	4	4	49	4	4	0.0	498.57
								46.4	177.68
								90.1	51.01
								135.8	144.96
								180.0	834.18
0.01	49	8	8	8	49	8	8	0.0	556.69
								46.4	173.82
								90.1	69.05
								135.8	165.08
								180.0	631.95
0.01	49	12	12	12	49	12	12	0.0	539.24
								46.4	182.08
								90.1	40.16
								135.8	179.09
								180.0	764.95
0.01	49	16	16	16	49	16	16	0.0	537.53
								46.4	179.59
								90.1	46.27
								135.8	183.49
								180.0	766.87

Table 3.3: The elastic differential cross section at selected angles with energy $E_{lab} = 0.01$ GeV as function of the grid points. The double prime quantities represent the integration variables.

E_{lab}	p	x_p	x_{pq}^{g0}	x_q	q, q''	x''	φ''	θ_{cm} [deg]	$\frac{d\sigma_{el}}{d\Omega}$ [mb]
0.5	49	16	16	16	49	16	16	0.0	487.02
								21.8	9.0338
								62.1	0.0776
								93.4	0.0039
								151.5	0.0031
0.5	49	20	20	16	49	16	20	0.0	509.09
								21.8	10.128
								62.1	0.0806
								93.4	0.0041
								151.5	0.0032
0.5	49	20	16	20	49	20	16	0.0	516.43
								21.8	14.628
								62.1	0.0798
								93.4	0.0041
								151.5	0.0047
0.5	49	20	20	20	49	20	20	0.0	515.98
								21.8	15.019
								62.1	0.0856
								93.4	0.0045
								151.5	0.0040
0.5	49	24	20	20	49	20	20	0.0	517.33
								21.8	15.301
								62.1	0.0858
								93.4	0.0045
								151.5	0.0040
0.5	49	20	20	24	49	24	20	0.0	519.42
								21.8	16.374
								62.1	0.0888
								93.4	0.0046
								151.5	0.0044
0.5	49	23	23	24	49	24	20	0.0	519.39
								21.8	16.209
								62.1	0.0883
								93.4	0.0045
								151.5	0.0041

Table 3.4: The elastic differential cross section at selected angles energy $E_{lab} = 0.5$ GeV as function of the grid points. The double prime quantities represent the integration variables.

$E_{lab}[GeV]$	p	x_p	x_{pq}^{q0}	x_q	q, q''	x''	φ''	σ_{opt} [mb]	σ_{el} [mb]	σ_{br} [mb]
0.01	49	4	4	4	49	4	4	1913.48	1799.08	67.81
	49	8	8	8	49	8	8	1886.84	1807.50	70.14
	49	12	12	12	49	12	12	1904.99	1820.77	73.75
	49	16	16	16	49	16	16	1903.22	1820.46	73.20
0.5	49	12	12	12	49	12	12	92.41	51.35	81.99
	49	16	16	16	49	16	16	100.67	53.71	38.79
	49	20	20	16	49	16	20	100.76	55.77	38.62
	49	20	16	20	49	20	16	107.85	63.11	37.50
	49	20	20	20	49	20	20	107.25	63.40	37.89
	49	24	20	20	49	20	20	107.71	63.32	37.88
	49	20	20	24	49	24	20	108.50	63.84	38.40
	49	23	23	24	49	24	20	108.69	63.22	38.09

Table 3.5: The total elastic and break-up cross sections together with the total cross section extracted via the optical theorem at two selected energies (0.01 and 0.5 GeV) as function of the grid points. The double prime quantities are the integration variables.

E_{lab} [GeV]	$\sigma_{el}^{q_0}$ [mb]	σ_{el}^q [mb]	$\sigma_{br}^{q_0}$ [mb]	σ_{br}^q [mb]	σ_{br}^p [mb]	$\sigma_{opt}^{q_0}$ [mb]	σ_{opt}^q [mb]
0.003	2561.74	2561.14	0.0	0.0	0.0	2562.65	2562.65
0.01	1820.71	1820.51	73.69	73.55	73.13	1902.63	1902.56
0.2	204.30	204.30	53.92	53.93	53.93	245.57	245.57
0.5	63.22	63.23	38.09	38.11	38.17	108.69	108.69
0.8	30.73	30.74	27.59	27.60	27.63	66.70	66.70
1.0	21.90	21.90	23.44	23.46	23.40	49.59	49.59

Table 3.6: The total elastic cross section, total breakup cross section and total cross section extracted via the optical theorem calculated in different coordinate systems at selected energies. The choice of coordinate system, i.e. which vector is aligned parallel to the z -axis, is indicated by the superscripts q_0 , q and p .

A nontrivial test for the quality and accuracy of our calculation is the numerical verification of the optical theorem Eq. (3.141). Our results are given for selected energies in Table 3.6. Here we show two sets of cross sections, distinguished by the superscripts q_0 and q . The superscripts indicate that the calculation is carried out by choosing the z -axis either parallel to $\hat{\mathbf{q}}_0$ or to $\hat{\mathbf{q}}$. Performing the calculation with two different choices of the z -axis is a nontrivial test for our choice of independent variables as well as for the entire calculation. The calculations are based on the standard grid given above and show an excellent agreement of the results obtained in the two different coordinate systems, indicating the numerical rotational invariance of our calculations.

It should be highlighted that for the q and q'' grid, the number and the distribution of the grid points in $(0, q_{max})$ interval are decisive to the accuracy and self-consistency of optical theorem. As we mentioned before, for treating the singularities in G_0 , the q and q'' grids are decomposed in intervals $0 \cup (0, q_{max}) \cup q_{max} \cup (q_{max}, \bar{q})$ with $q_{max} = \sqrt{\frac{4m}{3}E}$ and $\bar{q} = 20 \text{ fm}^{-1}$. The interval $(0, q_{max})$ on the q and q'' grids is the region where the singularities in G_0 are located. In Fig 3.3 we show the relative error of optical theorem at selected energies as a function of the average distance between the points in $(0, q_{max})$ interval on the q and q'' grid. The the relative error of optical

theorem is defined as

$$\delta_{opt} = \frac{|\sigma_{opt} - \sigma_{el} - \sigma_{br}|}{\sigma_{opt}} \times 100, \quad (3.149)$$

and used as the quality measure in the fulfillment of the optical theorem. The average distance between the points in $(0, q_{max})$ interval on the q and q'' grid is defined as

$$\Delta_q = \frac{q_{max}}{\text{number of grid points in } (0, q_{max}) \text{ interval}}. \quad (3.150)$$

At $E_{lab} = 0.01$ GeV, one has $q_{max} = 74.5$ MeV. As shown in the top panel in Fig 3.3, for $\Delta_q = 7.45$ MeV one has $\delta_{opt} = 1.27$ when 10 points in the interval $(0, q_{max})$ on the q and q'' grid. With increasing grid points from 10 to 30 by an increment of 4, Δ_q linearly drops down to 2.48 MeV, and δ_{opt} also drops linearly at first and eventually saturates at 0.064%. The optical theorem is very accurately reproduced. In this calculation the number of grid points for all angular grids is 12.

At $E_{lab} = 0.1$ GeV, one has $q_{max} = 284.02$ MeV. We first do the similar calculation by using 12 grid points for all angular grids as in the case of $E_{lab} = 0.01$ MeV. As shown at middle panel of Fig 3.3, for $\Delta_q = 28.40$ MeV one gets $\delta_{opt} = 21.67$ when 10 points in the interval $(0, q_{max})$ on the q and q'' grid. With increasing grid points from 10 to 22 by an increment of 4, Δ_q drops linearly down to 12.91 MeV, and δ_{opt} also drops linearly to 0.05%. However, δ_{opt} is increased from 0.05% to 2.23% when the number of grid points in the interval $(0, q_{max})$ increases further from 22 to 30 and Δ_q decreases from 12.91 MeV to 9.47 MeV. This means that the more refined grids of q and q'' do not help to improve the accuracy in this case. In order to find the reason for this purely accidental 0.05% accuracy, we repeat the calculation at $E_{lab} = 0.1$ GeV by increasing the number of grid points for all angular grids from 12 to 24. The results are also shown at middle panel of Fig 3.3 and is indicated by the solid open square symbol. We find that the unreasonable increasing error with a more refined grid for $(0, q_{max})$ interval disappears, the δ_{opt} steadily drops down and approaches saturation with increased number of grid points in the $(0, q_{max})$ interval. This example indicates that the overall accuracy of the entire multi-dimensional calculation is determined by the balanced accuracy in each dimension. More and more refined grids in one individual dimension does not help, and possibly even makes it worse.

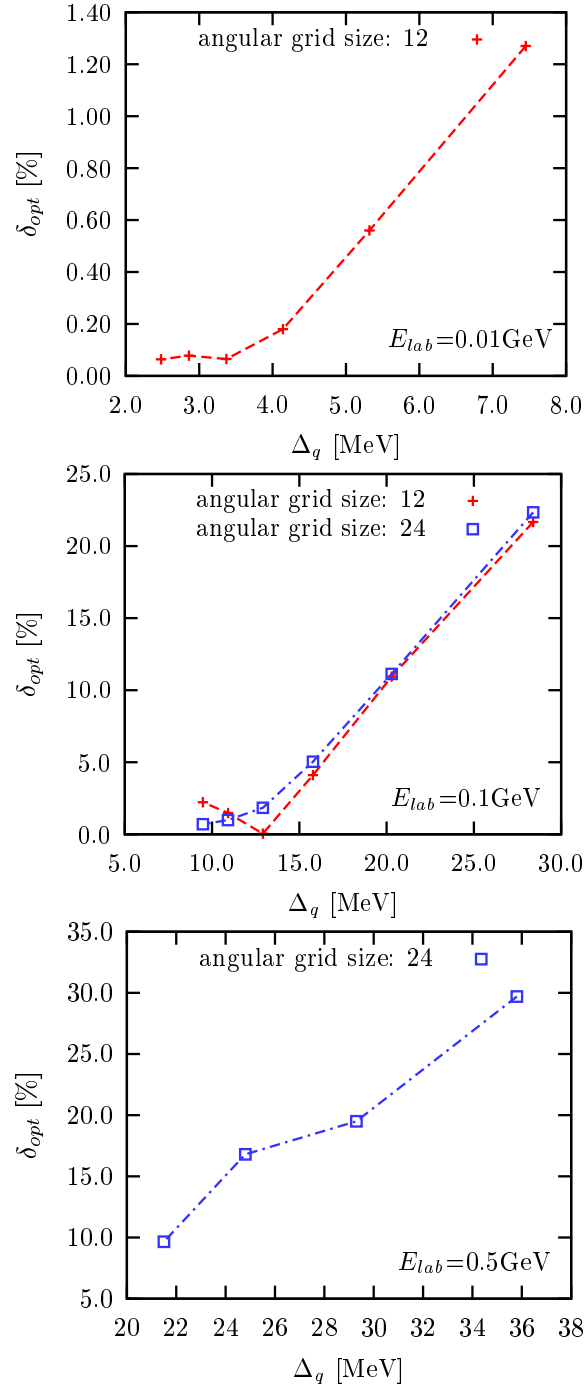


Figure 3.3: The percent error of optical theorem as a function of points on q and q'' grid at selected energies: $E_{lab} = 0.01$ GeV (upper panel), $E_{lab} = 0.1$ GeV (middle panel) and $E_{lab} = 0.5$ GeV (lower panel).

At $E_{lab} = 0.5$ GeV, we do a similar test and show the results in the bottom panel of Fig 3.3. We use 24 grid points for all angular grids because of the stronger angular dependence at this energy as shown in Table 3.5. For this case one has $q_{max} = 643.82$ MeV. When the number of grid points in $(0, q_{max})$ interval is increased from 18 to 30 and the Δ_q is decreased from 35.8 MeV to 21.5 MeV, the δ_{opt} drops from 29.7% to 9.56% as we expected.

If combining the cases for three energies together, we can find the systematics as follows. For the cases of $E_{lab} = 0.01$ GeV and $E_{lab} = 0.1$ GeV, at $\Delta_q = 7.45$ MeV and $\Delta_q = 9.47$ MeV respectively, their corresponding relative error of optical theorem are $\delta_{opt} = 1.27\%$ and $\delta_{opt} = 0.85\%$, which are close to each other. Similarly For the cases of $E_{lab} = 0.1$ GeV and $E_{lab} = 0.5$ GeV, at $\Delta_q = 20.29$ MeV and $\Delta_q = 21.5$ MeV respectively, their corresponding relative error of optical theorem are $\delta_{opt} = 11.13\%$ and $\delta_{opt} = 9.56\%$, which are also close to each other. This quantitatively indicates that for all these energies, the relative error of optical theorem δ_{opt} is a function of Δ_q , i.e. essential grid points in $(0, q_{max})$ interval is crucial to the accuracy of optical theorem. Considerable number of grid points on angular grids are also necessary if the accuracy $\delta_{opt} < 1\%$ is preferred at higher energies.

φ_{q_0} [rad]	$\sigma_{el}^{q_0}$ [mb]	σ_{el}^q [mb]	$\sigma_{opt}^{q_0}$ [mb]	σ_{opt}^q [mb]
0.0	2561.736	2561.138	2562.649	2562.649
$\frac{\pi}{2}$	2560.885	2560.729	2562.496	2562.496
π	2561.550	2561.206	2562.091	2562.091

Table 3.7: The total elastic cross sections at $E_{lab} = 3.0$ MeV calculated for different values of the angle φ_{q_0} in Eq. (3.70) with the + sign of $\sin(\varphi_p - \varphi_{q_0})$. The calculations are carried out in two different coordinate systems, characterized by the superscripts q_0 and q , which indicate, which vector is chosen to be parallel to the z-axis.

$\text{sign}[\sin(\varphi_p - \varphi_{q_0})]$	$\sigma_{el}^{q_0}$ [mb]	σ_{el}^q [mb]	$\sigma_{opt}^{q_0}$ [mb]	σ_{opt}^q [mb]
+	2561.736	2561.138	2562.649	2562.649
-	2559.674	2559.536	2560.091	2560.091

Table 3.8: The total elastic cross sections at $E_{lab} = 3.0$ MeV calculated for different sign of $\sin(\varphi_p - \varphi_{q_0})$ where $\varphi_{q_0} = 0$. The meaning of the superscripts is the same as in Table 3.7.

Finally, another highly nontrivial test of our calculation is the independence of the cross sections from the arbitrary angle φ_{q_0} and the sign of $\sin(\varphi_p - \varphi_{q_0})$. This is documented in Tables 3.7 and 3.8 for the energy $E_{lab} = 3$ MeV. In order to check the rotational invariance numerically, the calculations are carried out in two different coordinate systems, one where \mathbf{q}_0 is parallel the z -axis, and one where \mathbf{q} is parallel to z . Both tables show excellent agreement for the cross sections, and thus we conclude that our choice of variables is correct.

3.6 The Study of The Reaction Mechanisms in Three-Body Scattering

Since we can solve the Faddeev equation via completely three-dimensional fashion with sufficient accuracy, we are not restricted to any specific region of the projectile energy [26]. Though we neglect spin and iso-spin degrees of freedom and stay in a strictly non-relativistic framework, we nevertheless can provide first qualitative insights for various cross sections in three-body scattering in the intermediate energy regime which we define from $E_{lab} = 0.2$ GeV to $E_{lab} = 1.0$ GeV projectile energy. The primary focus of our investigations will be the question of the convergence of the multiple scattering series given by the Faddeev equation. Naive expectation suggests that if the energy is high enough, the Born approximation will be sufficient for a reasonable prediction of three-body scattering observables. We are now in a position to study such an assumption in more detail. It is interesting to see how the rescattering effects contribute to an observable up to a certain order of the two-body t -matrix, and how those contributions depend on the projectile energy E_{lab} and the specific kinematic configurations of the observables. By comparing to the exact calculation, we can have important insight about the validity of those approximations. At a more detailed level, we can argue how the validity of those approximations is associated with an observable at a specific kinematic configuration.

As first observable, we show in Fig. 3.4 the total cross section together with the total elastic and total break-up cross section as function of the laboratory projectile energy. In addition, the total cross section is also evaluated via the optical theorem as a test of our numerics. This duplicates the information already given in Table 3.6. We see that the optical theorem is quite well fulfilled. The figure shows that all the total cross sections decrease with the increase of projectile energy. At roughly $E_{lab} = 1.0$ GeV the total elastic and total break-up cross section become equal in magnitude in our model.

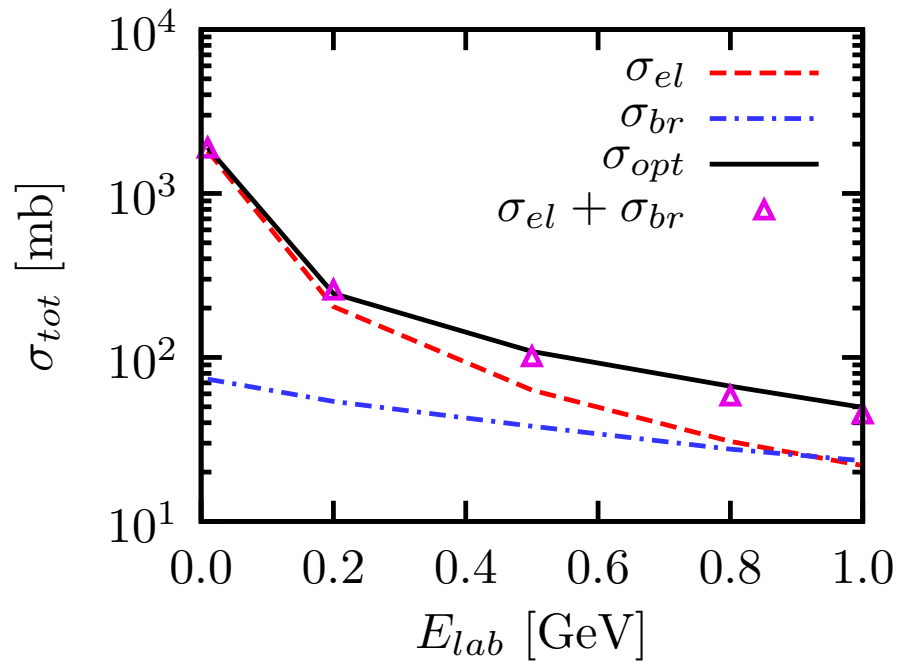


Figure 3.4: The total elastic cross section σ_{el} (dashed line), the total break-up cross section σ_{br} (dash-dotted line) and the total cross section evaluated by the optical theorem σ_{opt} (solid line) given as function of the projectile laboratory energy. At selected energies where the calculations have been carried out the sum of the calculated total elastic and break-up cross section, $\sigma_{tot} = \sigma_{el} + \sigma_{br}$, is indicated by the open diamond. The open diamonds coincide with the solid line according to the optical theorem, Eq. (3.141), and the numerical values are given in Table 3.6.

3.6.1 The Elastic Scattering

Next we consider the elastic differential cross section. First we show in the top panel of Fig 3.5 the elastic differential cross section at very low projectile energies, $E_{lab} = 3.0$ MeV and $E_{lab} = 10.0$ MeV. As the consequence of the particle identity, the cross sections at such low energies show an approximate symmetry around the scattering angle $\theta_{c.m.} = 90^\circ$. Therefore there is a characteristic minimum around scattering angle at $\theta_{c.m.} = 90^\circ$. For elastic scattering at intermediate projectile energies, we show the elastic differential cross section for projectile energies at $E_{lab} = 0.2$ GeV, $E_{lab} = 0.5$ GeV, $E_{lab} = 0.8$ GeV and $E_{lab} = 1.0$ GeV in the bottom panel of Fig. 3.5. First we notice that with increasing energy the cross section in forward direction dominant. In forward direction, $\theta_{c.m.} \leq 40^\circ$, the value of the cross section decreases with increasing energy. Around $\theta_{c.m.} = 90^\circ$, the characteristic minimum shown in the low energy elastic scattering disappears. At backward direction, around $\theta_{c.m.} = 180^\circ$, the rising tail due to particle identity gets lower and lower with the increasing energy.

Looking at the dominant forward direction in detail, we show in Fig. 3.6 the angular distribution in elastic scattering for selected energies in a linear scale. In addition to the exact Faddeev result, the cross sections are evaluated in first order in the two-body t -matrix, second order in t , third order in t , and fourth order in t and displayed. Furthermore, for all energies shown, the first rescattering (2nd order in t) always increases the cross section, and subsequent rescatterings lower it again. As expected, for the lowest energy, $E_{lab} = 0.2$ GeV, rescattering terms of higher order are important, and even the 4th order is not yet close to the full result. The same is true for $E_{lab} = 0.8$ GeV. We notice, that even at $E_{lab} = 1.0$ GeV two rescattering terms (3rd order in t) are necessary to come into the vicinity of the final result. The same is true for $E_{lab} = 0.5$ GeV. In view of the standard ‘ t - ρ ’ impulse approximation for the optical potential in nucleon-nucleus scattering employed at intermediate energies [49], it is interesting to notice that the first order result in t in our model study is quite insufficient. Even at energies larger than $E_{lab} = 0.5$ GeV rescattering corrections up to the 3rd order are required to come close to the exact result for small scattering angles. Therefore it seems likely that the first order impulse approximation in nucleon-nucleus scattering at forward direction is insufficient at energies below $E_{lab} = 1.0$ GeV.

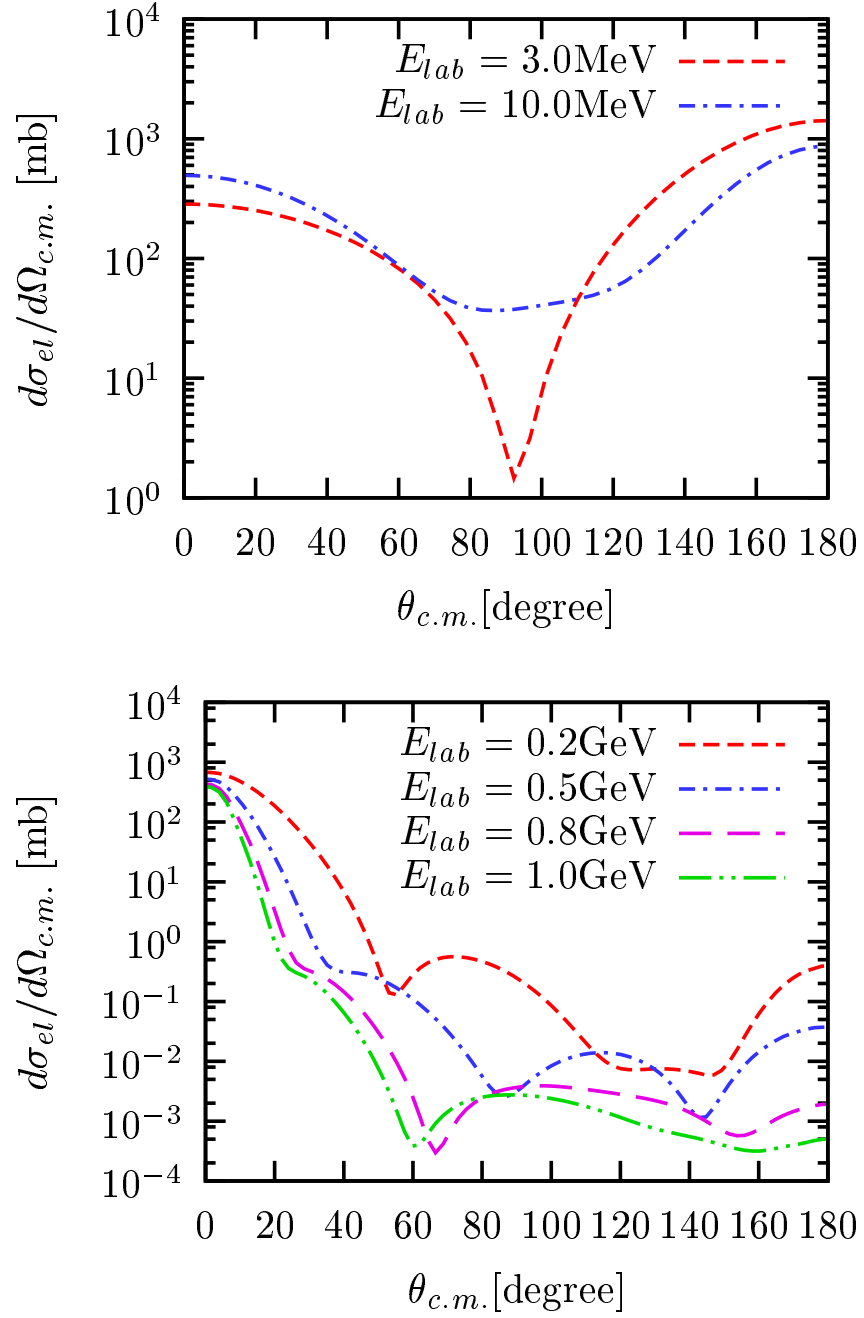


Figure 3.5: The elastic differential cross section (c.m.) at $E_{lab} = 3.0 \text{ MeV}$ and $E_{lab} = 10.0 \text{ MeV}$ very low projectile energies (upper panel) and $E_{lab} = 0.2 \text{ GeV}$, $E_{lab} = 0.5 \text{ GeV}$, $E_{lab} = 0.8 \text{ GeV}$ and $E_{lab} = 1.0 \text{ GeV}$ intermediate projectile energies (lower panel) as function of the scattering angle $\theta_{c.m.}$. All calculations are solutions of full Faddeev Equation.

Apart from the dominant forward direction, we also look at the rescattering effects in elastic scattering at other angles. In Fig 3.7 we show the elastic cross section at several large angles $\theta_{c.m.} = 45^\circ$, $\theta_{c.m.} = 90^\circ$, $\theta_{c.m.} = 135^\circ$ and $\theta_{c.m.} = 180^\circ$ as function of projectile energy. In addition to the exact Faddeev result, the cross sections are evaluated in first order in the two-body t -matrix, second order in t , third order in t , and 4th order in t , and displayed. In general cross section values corresponding the rescattering terms up to a certain order in two-body t -matrix decreases with increasing energy, as the exact result does. We notice that the rescattering contributing to different orders of the two-body t -matrix have a different energy dependence for the selected angles. At lower energies, below $E_{lab} = 0.4$ GeV, the aggregated rescattering terms increase and lower the cross section alternatively, as we see in forward direction at lower energies in Fig 3.7. At the energies between $E_{lab} = 0.4$ GeV and $E_{lab} = 0.6$ GeV, the rescattering terms at different order of the two-body t -matrix cross and gradually lead to a regular pattern at backward direction as the energy increases. We find that at backward direction $\theta_{c.m.} \geq 90^\circ$ with energy up to $E_{lab} = 0.8$ GeV, rescattering terms beyond the first order in the two-body t -matrix are good approximations of the exact solution. It can be concluded that for elastic scattering in our model, the first order approximation of T in the two-body t -matrix is insufficient, approximations up to second, third and forth order in the two-body t -matrix can be a good approximation to the exact result at energies higher than $E_{lab} = 0.5$ GeV, especially at backward angles. A measurement of the extreme backward scattering elastic pd cross section has been investigated in [44]. This situation corresponds to elastic scattering from a deuteron at backward angle, as is shown for $\theta_{c.m.} = 180^\circ$ case in Fig 3.7. It shows that the first order calculation is insufficient over the entire energy regime considered, except of course for the crossing point around 0.5 GeV. The first rescattering contribution (2nd order calculation), though close at 0.2 GeV, is insufficient below roughly 0.9 GeV. The figure also shows that at about 0.9 GeV the relative magnitude of contributions from the second and higher rescattering become small. Thus, we conclude that at 1 GeV one needs at least one rescattering to be in the vicinity of the full result for the elastic cross section at the backward angle.

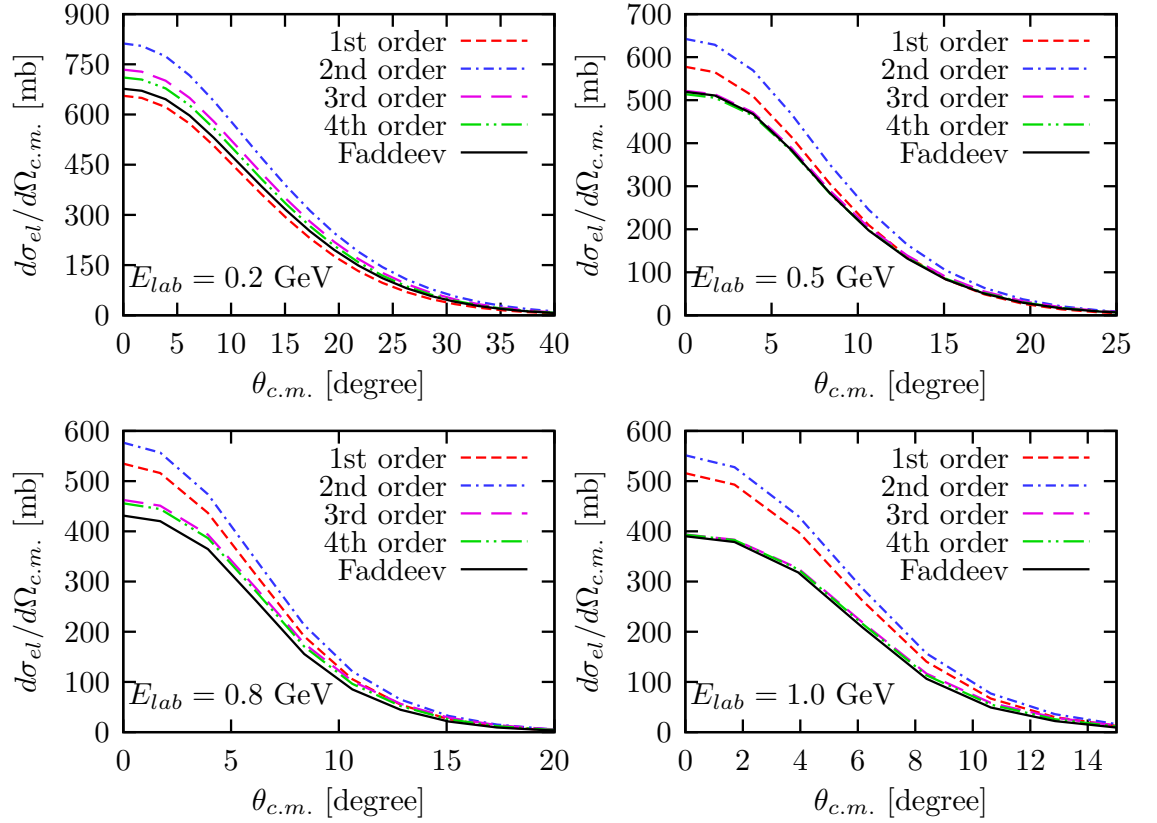


Figure 3.6: The elastic differential cross section at $E_{lab} = 0.2$ GeV, $E_{lab} = 0.5$ GeV, $E_{lab} = 0.8$ GeV and $E_{lab} = 1.0$ GeV projectile energies as function of the scattering angle $\theta_{c.m.}$. The result of the full Faddeev calculation is given by the solid line and compared with calculations based on the first order, 2nd order, 3rd order and 4th order in t as indicated in the legend.

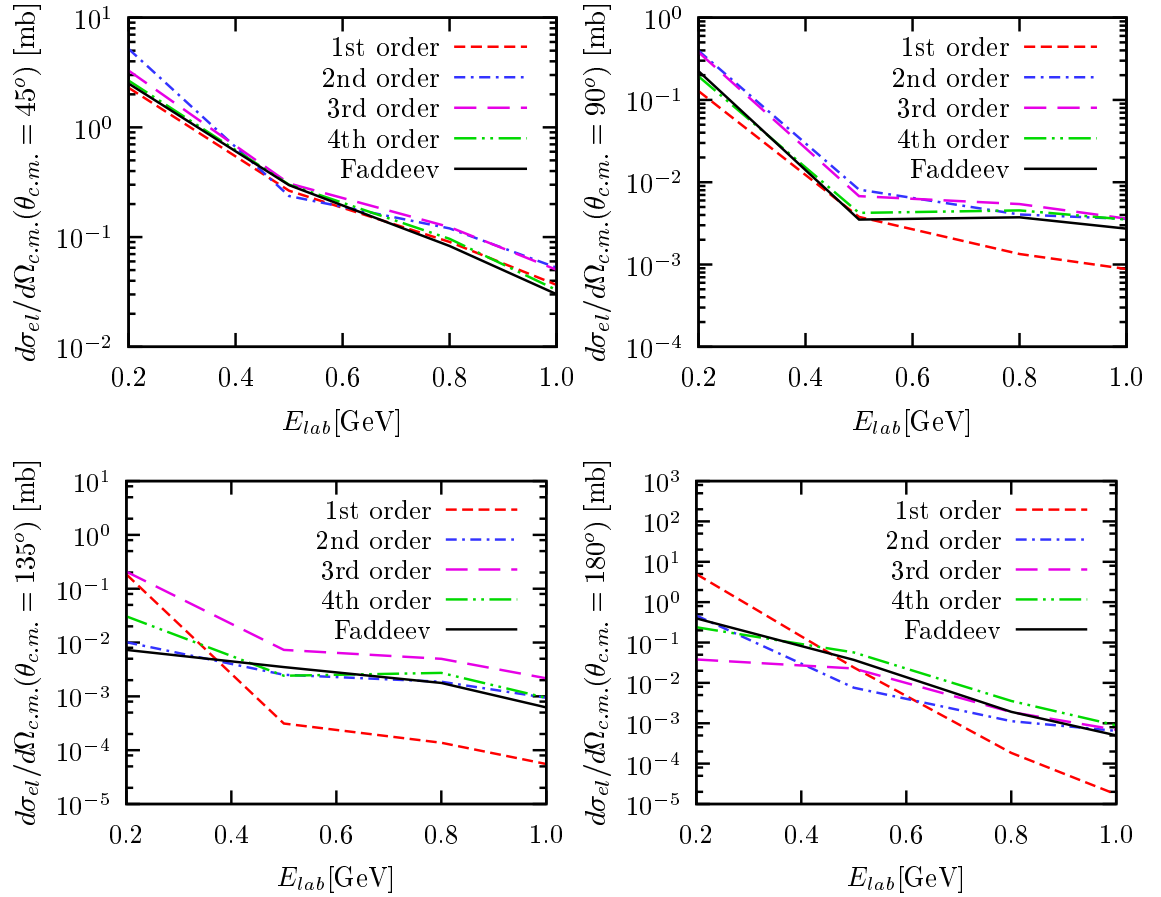


Figure 3.7: The elastic cross section (c.m.) at different angles $\theta_{c.m.} = 45^\circ, 90^\circ, 135^\circ, 180^\circ$ as function of the projectile laboratory energy. The result of the full Faddeev calculation is given by the solid line and compared with calculations based on the first order, 2nd order, 3rd order and 4th order in t as indicated in the legend.

3.6.2 The Semi-Exclusive Breakup Process

Let us now consider the breakup process. We first regard the semi-exclusive reaction where only one particle is detected. Only one particle measured means that one particle with certain energy is detected at a specific solid angle. When using Jacobi variables \mathbf{p} and \mathbf{q} , the one particle cross sections can be obtained by integrating out the two particle variable \mathbf{p} . Since the angular integration measure of the five fold breakup cross section in q_0 -system (see Eq. (3.132)) is

$$d\Omega_p d\Omega_q = 2\pi \int_{-1}^{+1} dx_q \int_{-1}^{+1} dx_p \int_0^{2\pi} d\phi_{pq}, \quad (3.151)$$

the one particle cross section in the center of mass frame can be calculated by following integration over five fold breakup cross section as

$$\left. \frac{d^3\sigma}{d\Omega_q dq} \right|_{1PT}^{c.m.} = \int_{-1}^{+1} dx_p \int_0^{2\pi} d\phi_{pq} \frac{d^5\sigma}{d\Omega_p d\Omega_q dq}. \quad (3.152)$$

Usually experiments measure the energy of the detected particle rather than its momentum. So we need to define the cross section in terms of energy and angle as $\left. \frac{d^3\sigma}{d\Omega_q dE_q} \right|_{1PT}^{c.m.}$. The energy of that measured single particle in terms of \mathbf{q} is

$$E_q = \frac{3}{4m} q^2, \quad (3.153)$$

so that Eq. (3.152)

$$\left. \frac{d^3\sigma}{d\Omega_q dq} \right|_{1PT}^{c.m.} = \sqrt{\frac{3E_q}{m}} \left. \frac{d^3\sigma}{d\Omega_q dE_q} \right|_{1PT}^{c.m.}. \quad (3.154)$$

The semi-exclusive cross section for one measured particle in laboratory frame can be denoted as $\left. \frac{d^3\sigma}{d\Omega_1 dE_1} \right|_{1PT}^{lab}$ with

$$\begin{aligned} E_1 &= \frac{k_1^2}{2m}, \\ x_1 &= \hat{\mathbf{k}}_1 \cdot \hat{\mathbf{k}}_{lab}. \end{aligned} \quad (3.155)$$

Now we need to work out the transformation between $\left. \frac{d^3\sigma}{d\Omega_1 dE_1} \right|_{1PT}^{lab}$ and $\left. \frac{d^3\sigma}{d\Omega_{p_1} dE_{p_1}} \right|_{1PT}^{c.m.}$. Because of

$$\mathbf{q} = \frac{2}{3} \left(\mathbf{k}_1 - \frac{1}{2} (\mathbf{k}_2 + \mathbf{k}_3) \right) = \mathbf{k}_1 - \frac{1}{3} \mathbf{k}_{lab}, \quad (3.156)$$

one has

$$\begin{aligned} E_q &= \frac{3}{2} \left(E_1 + \frac{1}{9} E_{lab} - \frac{2}{3} \sqrt{E_1 E_{lab}} x_1 \right), \\ x_q &= \frac{\sqrt{E_1} x_1 - \frac{1}{3} \sqrt{E_{lab}}}{\left[E_1 + \frac{1}{9} E_{lab} - \frac{2}{3} \sqrt{E_1 E_{lab}} x_1 \right]^{\frac{1}{2}}}. \end{aligned} \quad (3.157)$$

Conversely,

$$\begin{aligned} E_1 &= \frac{2}{3} E_q + \frac{1}{9} E_{lab} + \frac{2}{3} \sqrt{\frac{2}{3} E_q E_{lab} x_q}, \\ x_1 &= \frac{\sqrt{\frac{2}{3} E_q x_q} + \frac{1}{3} \sqrt{E_{lab}}}{\left[\frac{2}{3} E_q + \frac{1}{9} E_{lab} + \frac{2}{3} \sqrt{\frac{2}{3} E_q E_{lab} x_q} \right]^{\frac{1}{2}}}. \end{aligned} \quad (3.158)$$

With this the semi-exclusive cross section in laboratory frame then can be written as

$$\left. \frac{d^3 \sigma}{d\Omega_1 dE_1} \right|_{1PT}^{lab} = \frac{\partial(E_q, x_q)}{\partial(E_1, x_1)} \left. \frac{d^3 \sigma}{d\Omega_q dE_q} \right|_{1PT}^{cm} \quad (3.159)$$

where

$$\frac{\partial(E_q, x_q)}{\partial(E_1, x_1)} = \frac{3}{2} \sqrt{\frac{E_1}{E_1 + \frac{1}{9} E_{lab} - \frac{2}{3} \sqrt{E_1 E_{lab}} x_1}}. \quad (3.160)$$

Since the maximum value of E_q is E , the angle $\theta_1 = \cos^{-1}(x_1)$ is restricted by the following relations

$$\begin{aligned} \sqrt{\frac{2}{3}} E > \frac{1}{3} \sqrt{E_{lab}} &\Rightarrow \theta_1 \in [0, 180], \\ \sqrt{\frac{2}{3}} E \leq \frac{1}{3} \sqrt{E_{lab}} &\Rightarrow \theta_1 \in \left[0, \sin^{-1} \left(\frac{\sqrt{\frac{2}{3}} E}{\frac{1}{3} \sqrt{E_{lab}}} \right) \right] \end{aligned} \quad (3.161)$$

Indeed the energy window for θ_1 is very narrow. Since the energy threshold for the breakup process is $E_{lab} > -\frac{3}{2} E_d$, the condition $\sqrt{\frac{2}{3}} E > \frac{1}{3} \sqrt{E_{lab}}$ means that $E_{lab} > -3E_d$. The restriction on the angle of the measured particle only occurs when E_{lab} is smaller than $-3E_d$. After the angle x_1 is fixed, with the definitions

$$\begin{aligned} a &= \frac{1}{3} \sqrt{E_{lab}} x_1, \\ b &= \left[\frac{2}{3} E - \left(\frac{1}{3} \sqrt{E_{lab}} \sqrt{1 - x_1^2} \right)^2 \right]^{\frac{1}{2}}, \end{aligned} \quad (3.162)$$

one has the following relations for the maximum and minimum value of the energy E_1

$$\begin{aligned} E_1^{max} &= (a + b)^2, \\ E_1^{min} &= (a - b)^2, \quad a > b, \\ E_1^{min} &= 0, \quad a < b. \end{aligned} \tag{3.163}$$

It is found that $a < b$ is equivalent to $E_{lab} > -3E_d$. So the kinematics of the semi-exclusive process in the laboratory frame can be classified into two cases:

- $E_{lab} < -3E_d$, $\theta_1 \in \left[0, \sin^{-1} \left(\frac{\sqrt{\frac{2}{3}E}}{\frac{1}{3}\sqrt{E_{lab}}} \right) \right]$, $E_1 \in [(a - b)^2, (a + b)^2]$;
- $E_{lab} > -3E_d$, $\theta_1 \in [0, 180]$, $E_1 \in [0, (a + b)^2]$.

Now we can set up the algorithm to calculate the semi-exclusive breakup cross section via the five-fold differential cross section of Eq. (3.131):

- Calculate $\left. \frac{d^3\sigma}{d\Omega_q dp} \right|_{1PT}^{c.m.}$ from Eq. (3.152), and get $\left. \frac{d^3\sigma}{d\Omega_p dE_q} \right|_{1PT}^{c.m.}$ from Eq. (3.154).
- Calculate the range of x_1 and E_1 from Eqs. (3.161) and (3.163).
- With given angle x_1 and a set of E_1 , calculate the corresponding x_q and E_q from Eq. (3.157), then obtain $\left. \frac{d^3\sigma}{d\Omega_1 dE_1} \right|_{1PT}^{lab}$ from Eq. (3.159).

We work out the semi-exclusive cross section expressed in the laboratory frame in Eq. (3.159), here we can make a first contact to calculations based on realistic nucleon-nucleon (NN) forces. In [40] the semi-exclusive process $d(p, n)$ has been determined in first order in t based on the NN potentials AV18 [13] and Bonn-B [50]. In the upper panel of Fig. 3.8 we compare our first order calculation at projectile laboratory energy 495 MeV and 18° emission angle with the first order calculations from [40] based on the two realistic potentials. The position of the peak is solely determined by kinematics, thus the peak position coincides for all three calculations. Though our model calculation refers to bosons and the potential contains only the crude features of a central short range repulsion and intermediate range attraction, the magnitudes of the cross sections differ only by roughly 20%. In the lower panel we show the

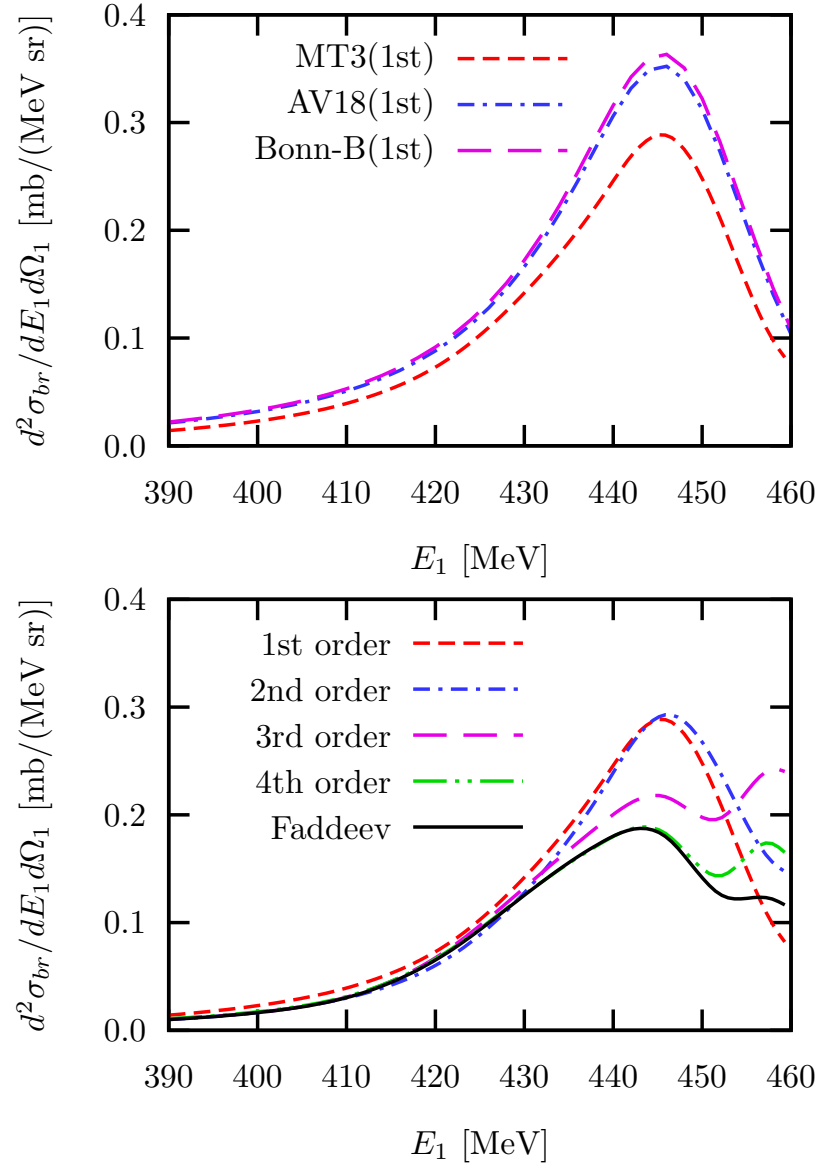


Figure 3.8: The semi-exclusive cross section at 495 MeV laboratory incident energy and at 18° angle of the emitted particle. The upper panel displays the first order results obtained from the realistic potentials AV18 [13] (long dashed line) and Bonn-B [50] (dashed-dotted line) together with our calculation based on the scalar MT potential of Eq. (3.164) (dashed line). The lower panel displays again our first order calculation from the upper panel (dashed line), together with a successive addition of the next three rescattering terms. The exact solution of the Faddeev equation is given by the solid line.

contributions of the first orders of the multiple scattering series successively summed up together with the exact solution of the Faddeev equation for our model. At this angle and energy the contribution of the first rescattering (2nd-order in the multiple scattering series) is quite weak, the contributions of the next two orders are large and lower the size of the peak. At the very high energies of the emitted particle, the 4th order in the multiple scattering series is still not yet close to the exact result. Therefore we conjecture that at this energy calculations with realistic forces will also require higher order rescattering contributions.

In the three-body breakup process, there are two configurations special since they are believed to have a simple two-body interaction mechanism and have been treated by rough approximations [26]. One is the so called quasi free scattering (QFS) process, where in the final state there is one particle at rest in the laboratory system. The simple assumed picture in QFS process is that the projectile only interacts with one of the two particles in the two-body bound state in target and the other is a spectator. Another configuration is called final state interaction (FSI) process where in the final state there are two particles leaving reaction region with equal momentum. The physics picture behind the FSI process is that the relative energy between the two particles is small. If the interaction is attractive, the process is strongly enhanced. In our model we will study the QFS and FSI mechanism in the semi-exclusive process. We choose three different laboratory energies, $E_{lab} = 0.2$ GeV, $E_{lab} = 0.5$ GeV and $E_{lab} = 1.0$ GeV and show the inclusive cross section as a few selected angles for the detected nucleon. The results are shown in Figs. 3.9 through 3.14.

At $E_{lab} = 0.2$ GeV the semi-exclusive cross section is given in Fig. 3.9 for the emission angle 24° and in Fig. 3.10 for the emission angle 39° . Both figures show in the upper panel the entire energy range of the emitted particle. Since the cross section varies by two orders of magnitude, we display it in a logarithmic scale. In order to better flesh out the peak structures, the two lower panels show the high and low energies of the emitted particle in a linear scale. Together with the full solution of the Faddeev equation (solid line) we display the sums of the lowest orders of the multiple scattering series as indicated in the figure. The peak at the highest energy of the emitted particle is the so called final state interaction (FSI) peak, which only

develops when rescattering terms are taken into account. This peak is a general feature of semi-exclusive scattering and is present for all energies. The next peak is the quasi-free (QFS) peak, and one sees that at both angles one needs at least rescattering of 4th order to come close to the full result. However, in contrast to the smaller angle, at the larger angle, 39° in Fig. 3.10, the first order result for the larger energies is surprisingly close to the full solution, though the multiple scattering series is by no means converged, as the following higher orders indicate. We also observe that the QFS peak moves to lower energies of the emitted particle with increasing emission angle. At both angles the very low energies of the emitted particle exhibit a strong peak in first order, which is considerably lowered by the first rescattering. Here the calculation up to 3rd order in the multiple scattering series seems already sufficient.

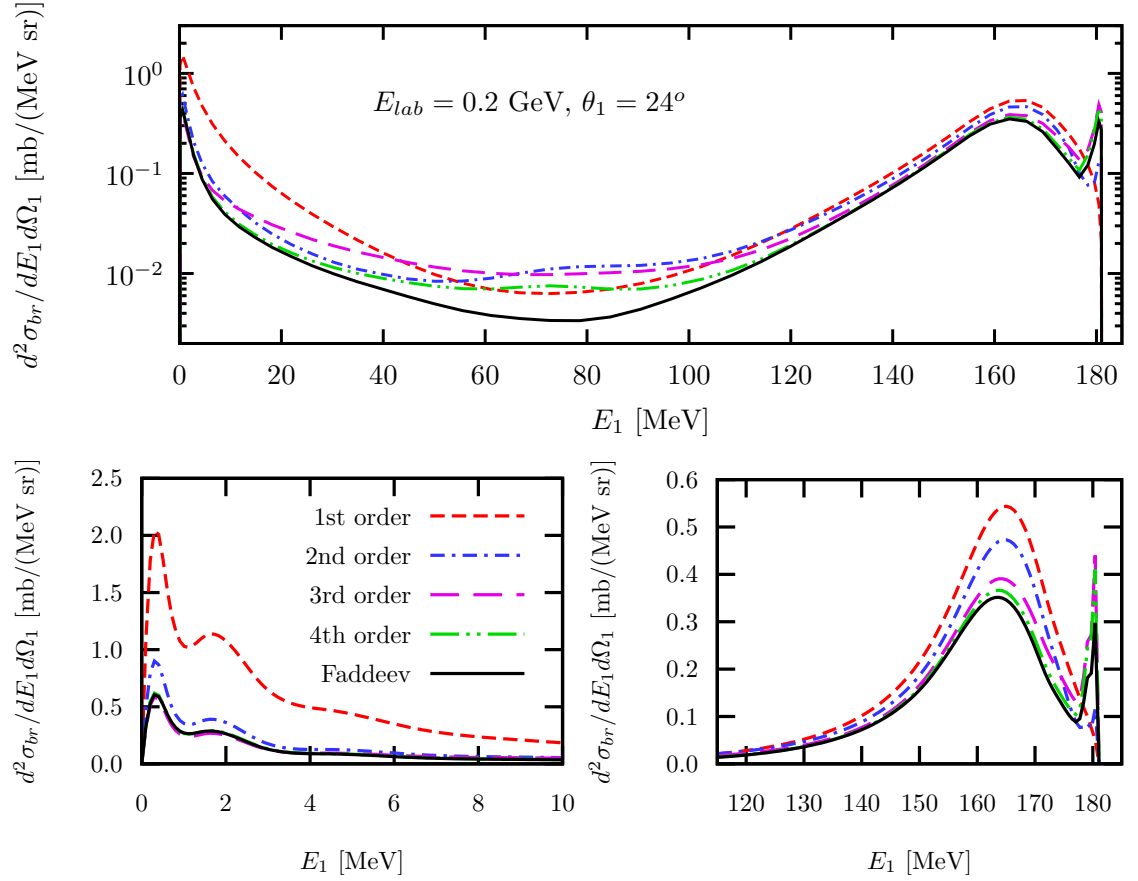


Figure 3.9: The semi-exclusive cross section at 0.2 GeV laboratory incident energy and at 24° emission angle of the emitted particle. The upper panel displays the entire energy range of the emitted particle, whereas the two lower panels show only the lowest and highest energies in a linear scale. The full solution of the Faddeev equation is given by the solid line in all panels. The contribution of the lowest orders of the multiple scattering series added up successively is given by the other curves as indicated in the legend of the lower left panel.

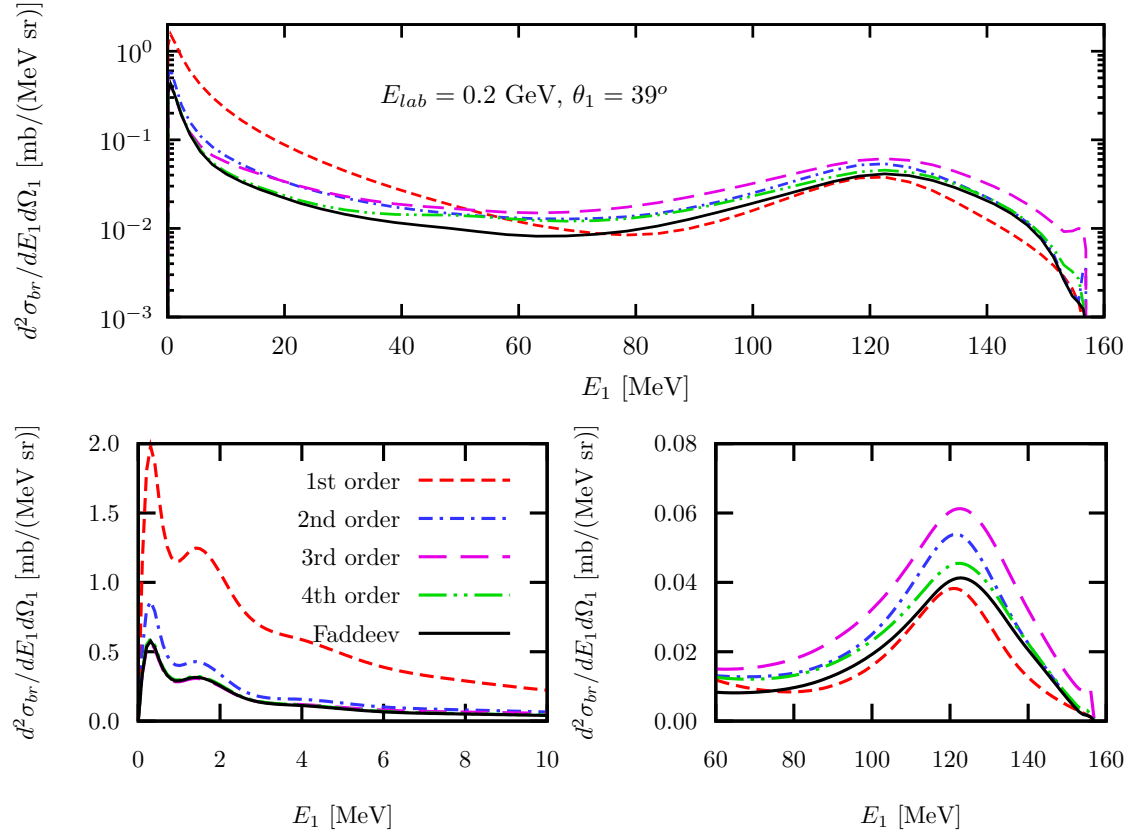


Figure 3.10: Same as Fig. 3.9 but for an angle of 39° of the emitted particle.

For $E_{lab} = 0.5$ GeV incident energy the semi-exclusive cross section is given in Fig. 3.11 for the emission angle 24° and in Fig. 3.12 for the emission angle 36° . We again see three peaks along the energy axis of the detected nucleon, the FSI and QFS peaks as well as the peak at the extreme low energy of the emitted particle. Again we see that the results based on first and second order in t alone are quite insufficient and higher order rescatterings can not be neglected. It is also interesting to observe that at 24° , Fig. 3.11, the third and higher order rescattering terms shift the peak to higher energies, whereas at the larger angle of 36° the peak positions of the various orders coincide more or less and agree with the peak position of the full calculation. Again, for the peak for the very low energies of the emitted particle, the 3rd order calculation agrees already quite well with the full result.

At $E_{lab} = 1.0$ GeV the situation is similar. As examples we have selected two angles, 18° displayed in Fig. 3.13 and 30° displayed in Fig. 3.14. For the small emission angle the second rescattering shifts the QFS peak towards higher energies, at the larger angle this is not the case. It seems that at the larger angle (Fig. 3.14) the multiple scattering series converges a little faster with respect to the higher orders compared to the smaller angle (Fig. 3.13). The final result for the peak at the very low energy of the emitted particle is as before reached with two rescattering contributions. It is remarkable that for the energies between about 200 and 500 MeV of the emitted particle the first rescattering contributes almost an order of magnitude to the cross section.

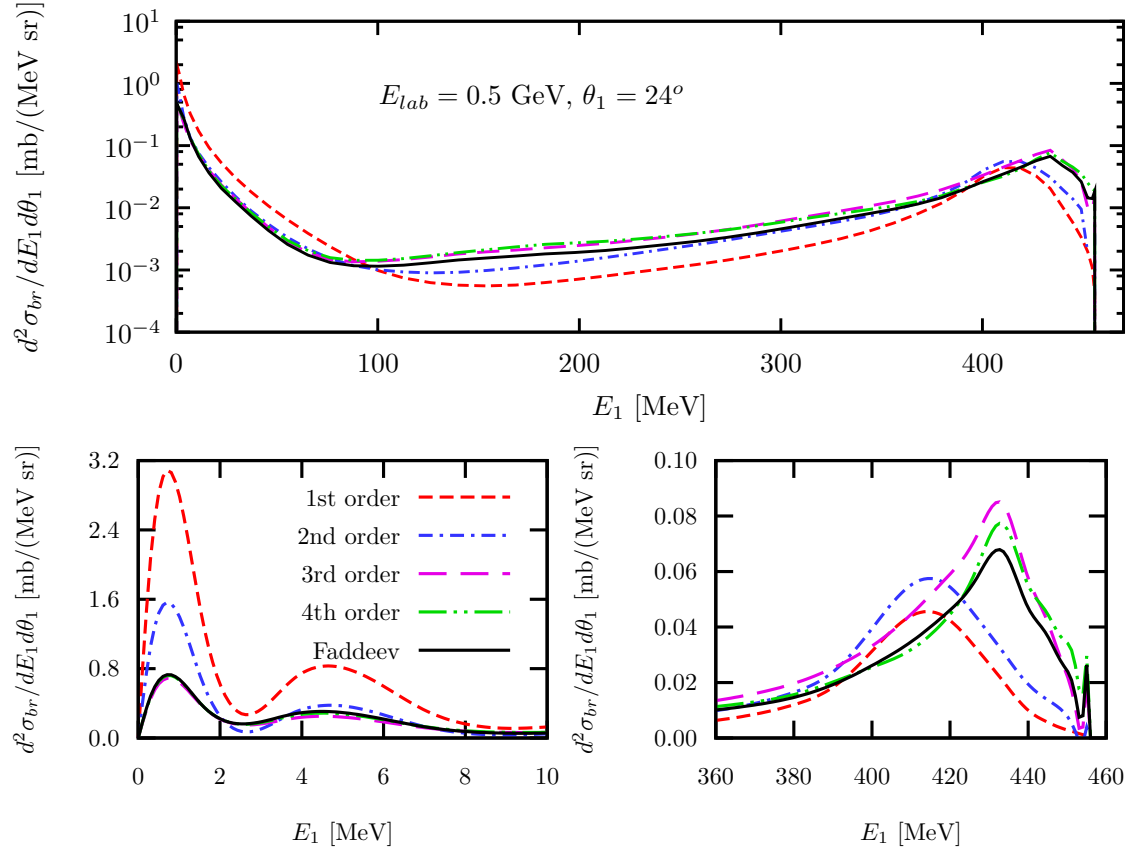


Figure 3.11: The semi-exclusive cross section at 0.5 GeV laboratory incident energy and at 24° angle of the emitted particle. The upper panel displays the entire energy range of the emitted particle, whereas the two lower panels show only the lowest and highest energies in a linear scale. The full solution of the Faddeev equation is given by the solid line in all panels. The contribution of the lowest orders of the multiple scattering series added up successively is given by the other curves as indicated in the legend of the lower left panel.

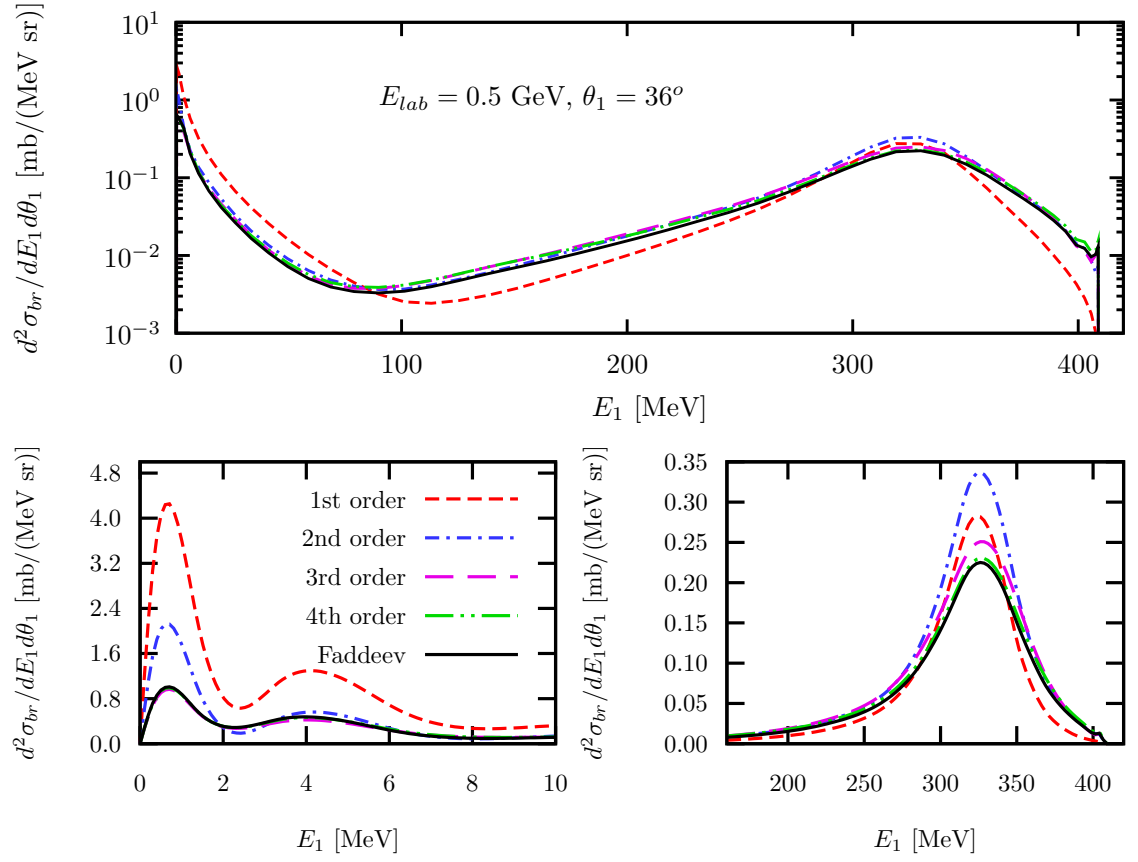


Figure 3.12: Same as Fig. 3.11 but for an angle of 36° of the emitted particle.

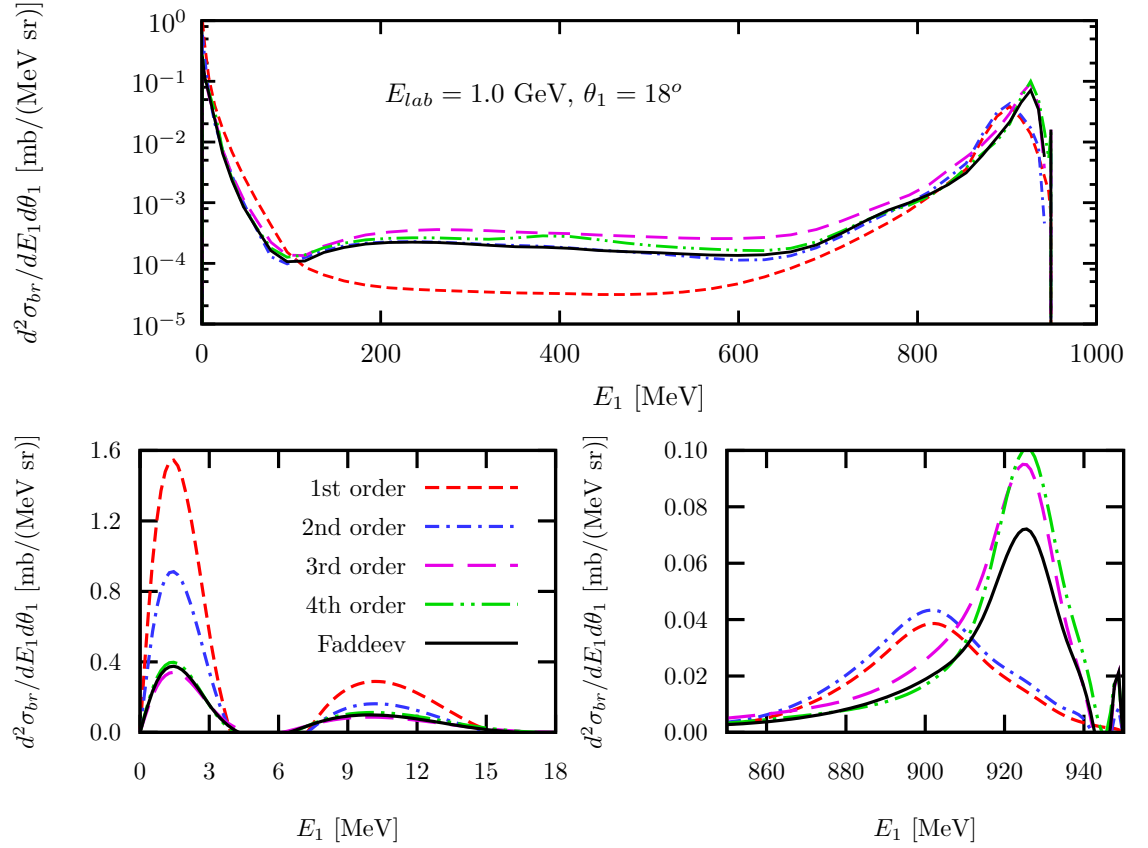


Figure 3.13: The semi-exclusive cross section at 1 GeV laboratory incident energy and at 18° angle of the emitted particle. The upper panel displays the entire energy range of the emitted particle, whereas the two lower panels show only the lowest and highest energies in a linear scale. The full solution of the Faddeev equation is given by the solid line in all panels. The contribution of the lowest orders of the multiple scattering series added up successively is given by the other curves as indicated in the legend of the lower left panel.

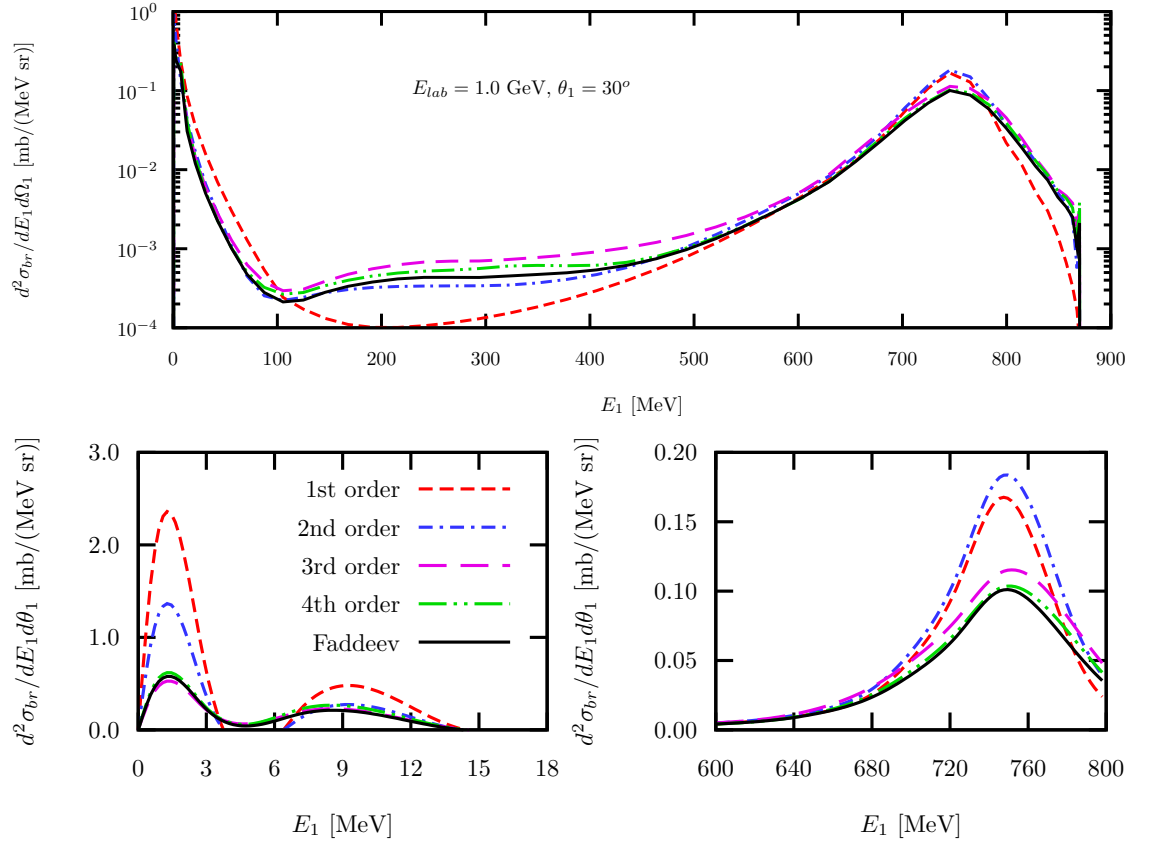


Figure 3.14: Same as Fig. 3.13 but for an angle of 30° of the emitted particle.

As we show in previous analysis, there are FSI peaks developed at the large E_1 energy region in which an interference between the FSI and QFS occurs and shifts the peak position when the emission angle θ_1 is small. If the emission angle θ_1 is large enough, the FSI is suppressed and there is no shift of the peak positions. We find that there exists a critical maximum energy E_1^{max} for such interference to occur. For $E_{lab} = 0.2$ GeV, this happens when $E_1^{max} = 0.16$ GeV; For $E_{lab} = 0.5$ GeV, this happens when $E_1^{max} = 0.44$ GeV; And for $E_{lab} = 1.0$ GeV, this happens when $E_1^{max} = 0.88$ GeV. For all the energies, this reaction mechanism change occurs at $\frac{E_1^{max}}{E_{lab}} \approx 0.8$. If this ratio is larger than 0.8, the QFS process interferes with the FSI process and the peak is shifted by rescattering at higher orders. If this ratio is smaller than 0.8, the FSI process is suppressed and the peak of QFS process in the higher orders coincide more or less and agree with the peak position of the full calculation. This suggest that the approximation of \hat{T} up to a finite order in two-body t -matrix might be reasonable when the emission angle is larger than the critical value of θ_1 corresponding the $\frac{E_1^{max}}{E_{lab}} \approx 0.8$.

Finally we comment on a recently measured and analyzed reaction $pd \rightarrow (pp)n$ at high momentum transfer [51, 44]. In this experiment the breakup configuration has been chosen such that the neutron is ejected at extreme backward angles, and the two protons at extreme forward angles. The measurement was carried out at GeV laboratory energies. The experimental data [51] have been analyzed in Ref.[44] using first and second order processes in the NN t -matrix including a Δ -isobar mechanism. Within our nonrelativistic toy model for three bosons we are of course unable to analyze the data. However, we can give a clear answer whether higher order rescattering processes are essential in this reaction. In [51, 44] the data are integrated over a small interval of the relative pp energy between 0 and 3 MeV, and averaged over the neutron c.m. angle in the interval between 172° and 180° . In our qualitative study we fix the c.m. angle of one particle at 180° , but integrate over the relative energy $E_{pp} = p^2/m$ of the two other particles between 0 and 3 MeV. Thus, we evaluate the cross section

$$\frac{d\sigma}{d\Omega_q} = (2\pi)^4 \left(\frac{2}{3}\right)^2 \frac{m^2}{q_0} \int_0^{\sqrt{mE_{pp}}} dp \, p^2 \, q \int d\hat{p} |U_0(p, x_p, x_{pq}^{q_0}, x_q = -1, q, q_0)|^2. \quad (3.164)$$

Since we choose the z-axis parallel to $\hat{\mathbf{q}}_0$, and $\hat{\mathbf{q}}$ is antiparallel to $\hat{\mathbf{q}}_0$, the φ_p dependence is directly given by $x_{pq}^{q_0} = \cos \varphi_p$. Our calculations are carried out for projectile laboratory energies between 0.2 and 1 GeV, and are displayed in Fig. 3.15. Here we compare different low orders in the two-body t -matrix with the full solution of the Faddeev equation. We notice that all our calculations exhibit a smooth fall-off as a function of the projectile energy. This behavior is present in the data of Ref. [51]. None of our calculations shows a dip structure around 0.7 GeV as indicated for some of the calculations in Ref. [44]. The reason may be that our calculation is carried out in three dimension, i.e. all partial waves are included exactly, where as in Ref. [44] only the lowest partial waves are considered. At low projectile energies rescattering terms of higher order still give considerable contributions to the cross section. At 1 GeV the first order calculation is an order of magnitude smaller than the result of the full calculation. It is interesting to notice that at 1 GeV the contribution from the first rescattering is relatively small, and one needs to go to the 3rd order in t to come close to the full result for this particular break-up configuration.

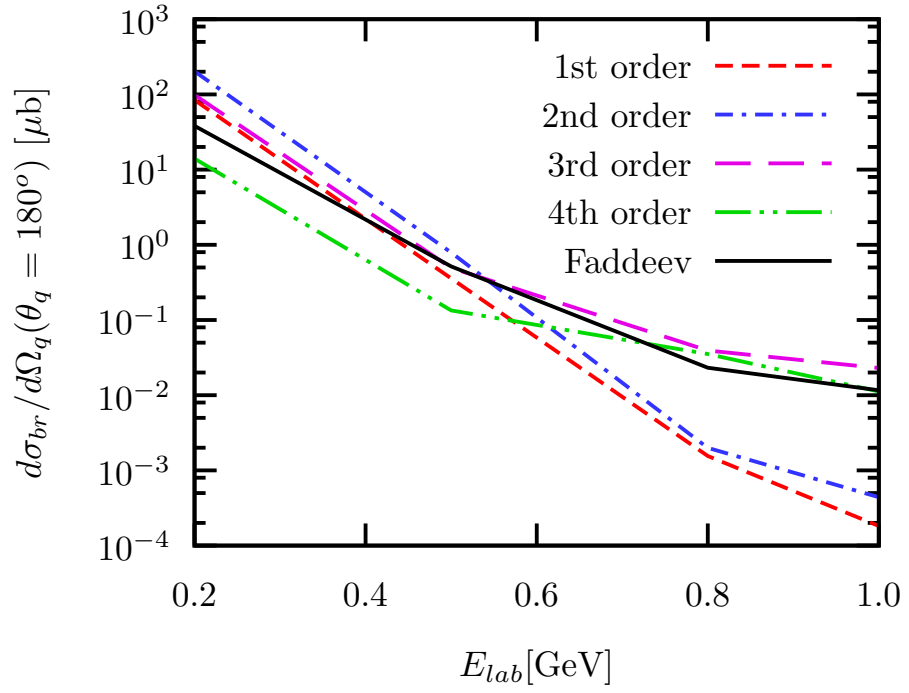


Figure 3.15: The cross section (c.m.) for the semi-exclusive break-up reaction in which two particles emerge in forward direction with a relative energy between 0 and 3 MeV, and one particle is detected at backward angle as function of the projectile laboratory energy. The result of the full Faddeev calculation is given by the solid line and compared with calculations based on the first order, 2nd order, 3rd order and 4th order in t as indicated in the legend.

3.6.3 The Exclusive Breakup Process

In the exclusive breakup process, two particles are measured in coincidence. According to the five-fold breakup cross section in Eq. (3.131), with all angles fixed, only the energy of one of the two detected particles needs to be measured. However, because the energy conservation is expressed in a quadratic form with respect to the momentum which allows two solutions, one has to measure the energies of both particles. Since here we just do a very brief model study of the exclusive breakup process at $E_{lab} = 1.0$ GeV, for sake of simplicity, we consider in the following the exclusive breakup cross section in the center of mass frame

$$\frac{d^5\sigma_{br}}{d\Omega_p d\Omega_q dE_q} \quad (3.165)$$

which is a five fold breakup differential cross section in terms of angles and energy $E_q = \frac{3}{4m}q^2$ of the outgoing particle. According to the E_q definition, one has

$$\frac{d^5\sigma_{br}}{d\Omega_p d\Omega_q dq} = \sqrt{\frac{3E_q}{m}} \frac{d^5\sigma_{br}}{d\Omega_p d\Omega_q dE_q}. \quad (3.166)$$

where the r.h.s of Eq. (3.166) is the five fold breakup cross section of Eq. (3.131). At $E_{lab} = 1.0$ GeV, the maximum value of E_q is $\frac{2}{3}E_{lab} + E_d \approx 664$ MeV.

First we consider a special case that one particle is scattered out along the beam direction, i.e. $x_q = 1$. We show in Fig. 3.16 two sets of configurations with $x_q = 1$. One configuration is $x_p = 1$, $\phi_{pq} = 0^\circ$ and $x_q = 1$ displayed in the top panel of Fig. 3.16. The other is $x_p = 0$, $\phi_{pq} = 90^\circ$ and $x_q = 1$ displayed in the bottom panel of Fig 3.16. For both cases, the first order approximation in two-body t -matrix dramatically overestimates the peak value at E_q between 660 to 664 MeV. At this E_q energy region, the single particle carries all kinetic energy in the center of mass frame, so the other two particles are at rest in the center of mass, with almost zero relative momentum. Therefore the final state rescattering effect is enhanced and lowers the peaks. The rescattering terms up to the fourth order in two-body t -matrix are required in order to get close to the exact solution. The major difference between these two configurations is that the one at $x_p = 1$, $\phi_{pq} = 0^\circ$ and $x_q = 1$ fulfils collinearity, where all three particles exit on one line, but the one at $x_p = 0$,

$\phi_{pq} = 90^\circ$ and $x_q = 1$ is off collinearity. In the past [52] there arose interest whether or not any special effects occur under collinearity conditions. Recent investigations about this in Ref. [53, 54] at low energies around $E_{lab} = 10$ MeV indicate that both the data and theory show no peculiarity at all at and around the point of collinearity. Our calculation at $E_{lab} = 1.0$ GeV in Fig 3.16 also shows that with and without the collinearity does not make much difference in the FSI region we considered.

We show two QFS configurations with (at top) and without (at bottom) collinearity in Fig 3.17. The QFS condition assumes one particle is at rest in laboratory, for example $\mathbf{k}_1 = 0$. This is equivalent to $\mathbf{q} = -\frac{1}{2}\mathbf{q}_0$. So the two configurations are all at $x_q = -1$. The energy E_q corresponding the QFS configuration is approximately one quarter of the total energy if we ignore the small binding energy of the target. The peaks in Fig 3.17 are exactly located at $E_q = \frac{667}{4} = 168$ MeV. In these two QFS configurations we find a large impact of collinearity condition. For the collinear case shown in the top panel of Fig 3.17, the second rescattering lowers the QFS peak at large scale and the consecutive rescattering up to fourth order in two-body t -matrix converges to the exact solution. The magnitude of the QFS peak is about 1.7 mb. For the non-collinear case shown in the bottom panel of Fig 3.17, the scatterings in first and second order in two-body t -matrix give the same result, the rescatterings up to third order in two-body t -matrix coincide with the full solution. The magnitude of the QFS peak is just 0.04 mb, which is much smaller than that for the collinear case. Therefore the QFS configurations we consider is not really free in the sense that the rest particle is not a spectator, because the three-body configuration strongly influence the QFS mechanism we considered. The sensitivity to collinearity in the reaction we consider can be understood through the dominant forward scattering at higher energies. At low energies ($E_{lab} = 0.01$ GeV), S -wave mainly contributes. Thus the orientation makes no difference. At higher energies, all particles are most likely scattered into forward direction. Therefore orientation along and perpendicular to the beam direction shows a big difference as we see in Fig 3.17.

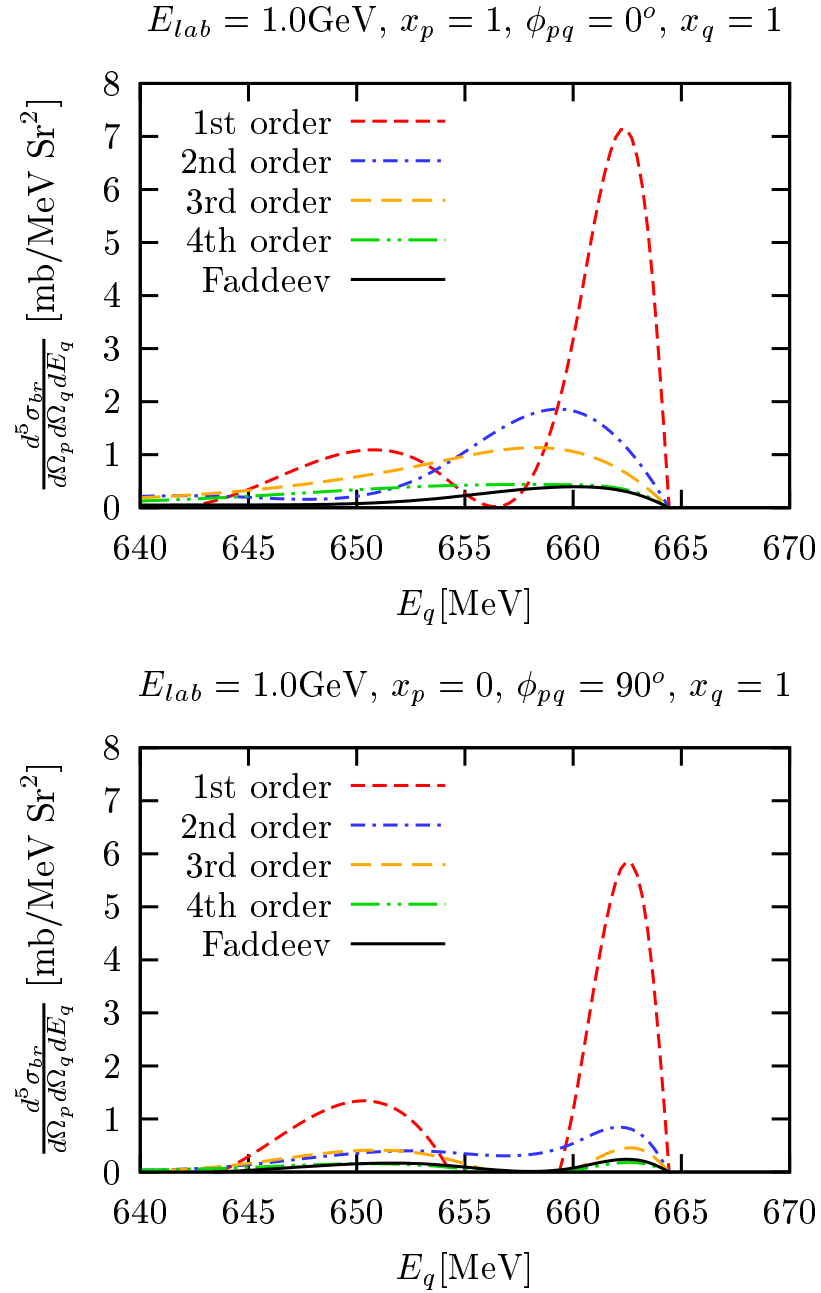


Figure 3.16: The exclusive cross section at $E_{lab} = 1.0\text{GeV}$ and $x_p = 1, \phi_{pq} = 0^\circ, x_q = 1$ (upper panel) and at $E_{lab} = 1.0\text{GeV}$ and $x_p = 0, \phi_{pq} = 90^\circ, x_q = 1$ (lower panel). The full solution of the Faddeev equation is given by the solid line. The contributions of the lowest orders of the multiple scattering series added up successively are given by the other curves as indicated in the legend.

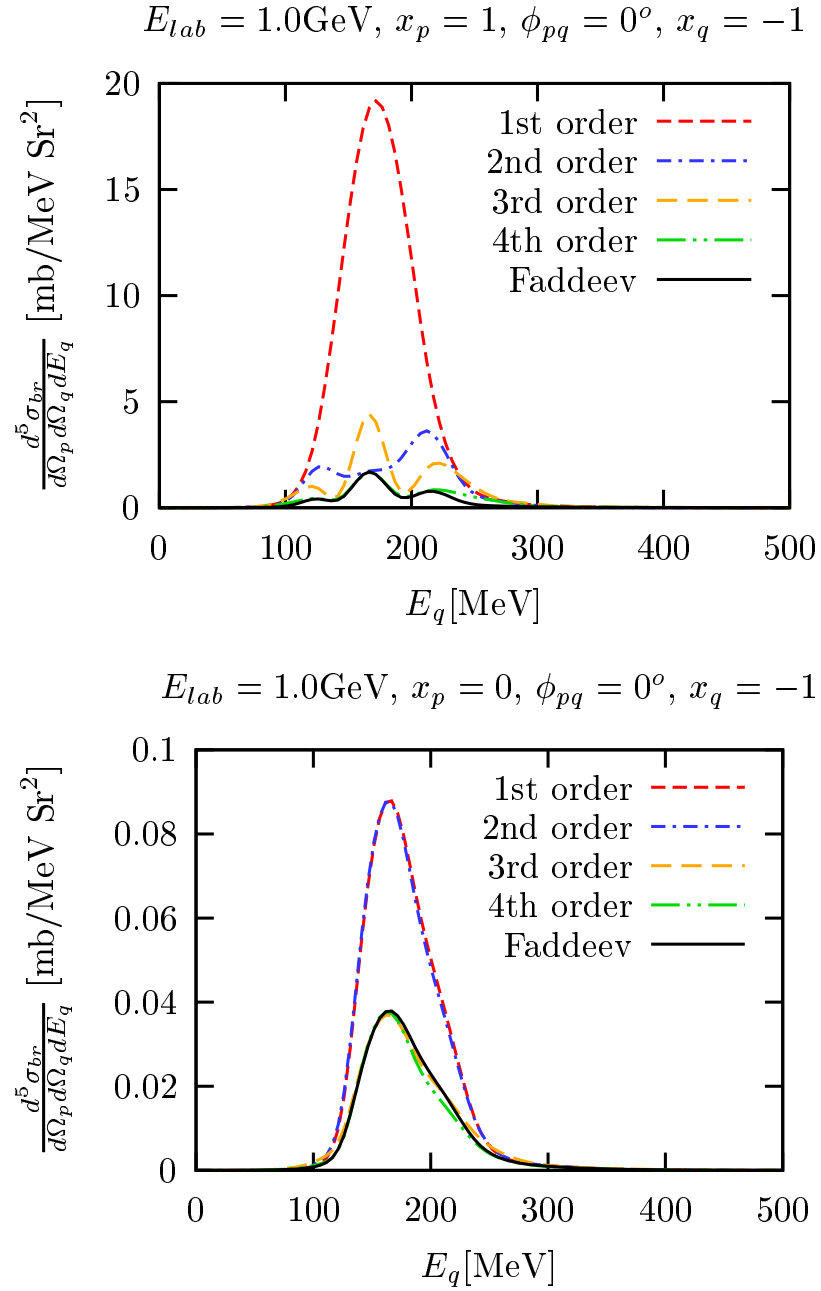


Figure 3.17: The exclusive differential cross section at $E_{lab} = 1.0\text{GeV}$ and $x_p = 1$, $\phi_{pq} = 0^\circ$, $x_q = -1$ (upper panel) and at $E_{lab} = 1.0\text{GeV}$ and $x_p = 0$, $\phi_{pq} = 0^\circ$, $x_q = -1$ (lower panel). The full solution of the Faddeev equation is given by the solid line. The contributions of the lowest orders of the multiple scattering series added up successively are given by the other curves as indicated in the legend.

Finally we consider another configuration, the so called star configuration, where three particles have equal energies and interparticle angles of 120° in the center of mass system. The plane spanned by the three particles can have any orientation with respect to the beam direction. If it is orthogonal to the beam direction, it is called space star; if the beam direction lies in the plane, it is called coplanar star. The space star was expected to be a good candidate to see effects of three-body forces [55]. In the center of mass frame, the energy relation of star configuration is very simple. Assume the three particles in the star configuration have momentum with magnitude k , then one has according to the definition of Jacobi variables,

$$\begin{aligned} p &= \frac{\sqrt{3}}{2}k, \\ q &= k. \end{aligned} \tag{3.167}$$

The total energy is $E = \frac{3}{2m}k^2$, the single particle energy $E_q = \frac{3}{4m}k^2$. So the position of star configuration on E_q is approximately at $(\frac{2}{3}E_{lab} + E_d)/2 = 332$ MeV. We show in Fig 3.18 a space star configuration at top with $x_p = 0$, $\phi_{pq} = 90^\circ$, $x_q = 0$ and a coplanar star at the bottom with $x_p = \sqrt{2}/2$, $\phi_{pq} = 0^\circ$, $x_q = -\sqrt{2}/2$. We find that at $E_{lab} = 1.0$ GeV, the cross section for star configuration is very small, just 10^{-5} mb. One important feature for both star configurations considered is that the first order contribution is essentially zero and the peak around $E_q = 330$ MeV is totally developed by rescattering effects. In the space star configuration we considered, where the rescattering effects order by order increase the peak values, whereas the exact solution lowers it down. This indicates that the fully converged result is needed. In the coplanar star configuration we find that there is a peak developed by rescattering order by order in two-body t -matrix at maximum value of E_q , which indicates the enhanced FSI. This marks the major difference between the space star and coplanar star configurations. In the coplanar star configurations we considered, there are rescattering effects and enhanced FSI in terms of two-body t -matrix. The contribution order by order oscillates around the full solution and is not converged. This indicates that any approximation based on the finite order in two-body t -matrix does not work, the full solution of \hat{T} is necessary.

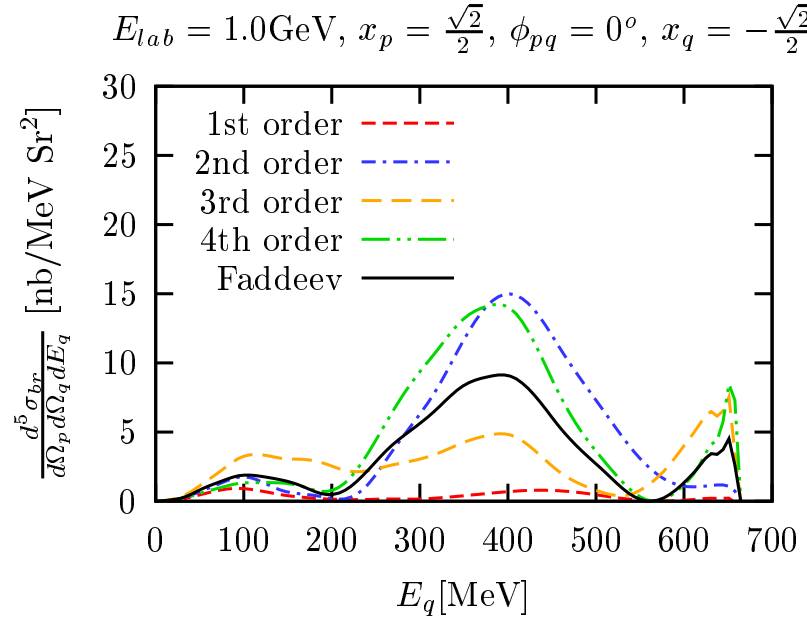
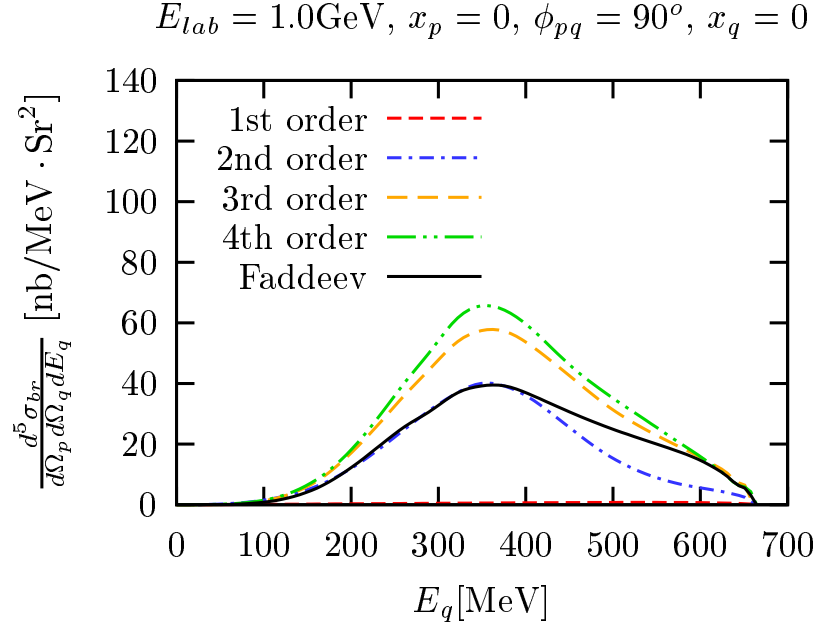


Figure 3.18: The exclusive differential cross section at $E_{lab} = 1.0\text{GeV}$ and $x_p = 0$, $\phi_{pq} = 90^\circ$, $x_q = 0$ (upper panel) and at $E_{lab} = 1.0\text{GeV}$ and $x_p = \sqrt{2}/2$, $\phi_{pq} = 0^\circ$, $x_q = -\sqrt{2}/2$ (lower panel). The full solution of the Faddeev equation is given by the solid line. The contributions of the lowest orders of the multiple scattering series added up successively are given by the other curves as indicated in the legend.

3.7 Summary

In our study of three-body scattering, we perform fully converged Faddeev calculations for three identical bosons interacting by local forces in the intermediate energy range between about $E_{lab} = 0.2$ GeV to $E_{lab} = 1.0$ GeV. To the best of our knowledge these are the first calculations of this kind. The key point is to neglect the partial wave decomposition generally used at low energies and to work directly with momentum vectors. Thus all partial waves are exactly included. A suitable choice of variables is important. Besides the magnitudes of the two relative Jacobi momenta \mathbf{p} and \mathbf{q} we choose the angles between the vectors \mathbf{p} and \mathbf{q}_0 and between \mathbf{q} and \mathbf{q}_0 , where \mathbf{q}_0 is the projectile momentum. The fifth variable is the angle between the two planes spanned by \mathbf{p} , \mathbf{q}_0 and \mathbf{q} , \mathbf{q}_0 . In the technical piece of this work we introduce a spline-based integration of the moving logarithmic singularities, which is a very valuable alternative to procedures used so far. The numerical results are well converged and self-consistent as demonstrated. We show elastic and breakup cross sections in the above mentioned intermediate energy range. We focus on the question how many orders of rescattering beyond the often used first order calculation in the two-body t -matrix are needed to come close to the full Faddeev result. We find that in nearly all cases studied processes of at least 2nd and 3rd order rescattering are required. Whether this will be also required in performing calculations with realistic dynamical inputs has to be seen in the future.

In one case we can make first contact to a result based on the NN forces AV18 and Bonn B, which are considered to be realistic in the sense that they describe all NN data below 350 MeV extremely well. This was the semi-exclusive cross section at 495 MeV evaluated in first order in the NN t -matrix. Of course, at that energy AV18 and Bonn-B are at the upper limit of their applicability. Despite our simple two-body model force, a superposition of two Yukawa interactions, one attractive the other repulsive, our results turn out to be within about 20% to the calculation based on the realistic models. This shows that our investigations might allow some conclusions about results based on present and future models with more dynamical inputs.

As a first example for considering data in the light of our toy model we study the extreme backward elastic dN scattering over the energy range from $E_{lab} = 0.2$ GeV to $E_{lab} = 1.0$ GeV. We find that first order results in the two-body t -matrix are totally insufficient and even around $E_{lab} = 1.0$ GeV the first order rescattering is needed to comes close to the full result. Parallel to those data in elastic scattering in [51, 44] the complete break up process d(p,n)pp has also been investigated. Here the neutron was ejected antiparallel to the beam direction and the two protons at extreme forward angles with a very small relative energy. Again we study the significance of rescattering processes, and find that for this particular breakup configuration two rescatterings are necessary to get close to the result of the full Faddeev calculation.

We have a very brief study of exclusive breakup process in the center of mass frame, and address the possible impact of the collinearity and coplanarity condition on the reaction mechanism of the breakup process, such as quasi-free, final state interaction and star configurations. Further studies scanning the complete three-body phase space in laboratory for the total breakup are underway. This may be important in order to shed light on previous theoretical analysis of p(d,ppn) reactions which relied on low order reaction mechanisms.

In conclusion we can say that the three-body Faddeev equations can be exactly solved at intermediate energies directly using momentum vectors. Calculations based on partial wave decomposition would hardly be feasible at these energies.

Chapter 4

The Bound State of Three Bosons

Calculations of nuclear three-body systems based on presently available nuclear two-body force models achieve partial success in describing nuclear three-body data. All realistic nuclear two-body force models fail to provide the experimental value of the triton binding energy, which clearly indicates that further physics insight is necessary. One suggested further step is the study of the three-body system with the inclusion of the three-body forces [56, 57, 58, 59]. For this purpose, the two-body and the three-body forces should be investigated together on equal footing. This is also true for an atomic three-body system, such as the three-body force contribution to the Ar-trimer binding energy discussed in Ref. [60]. The calculations of three-body system with three-body forces have been carried out successfully by partial wave decomposition scheme for three-body bound state and scattering at low energies ($E_{lab} \leq 250$ MeV). Because of the short-range character of the three-body forces, a more detailed study about the three-body force properties can be carried through in higher energy scattering processes. However, the calculations of three-body force at high energies (≥ 300 MeV) are not carried out yet, because of the limitation posed by a partial wave decomposition. This situation calls for the development of new computational techniques for three-body force calculation directly based on vectors without partial wave decomposition.

In this chapter we study the bound state of three bosons with two-body and three-body forces. We set up the bound state Faddeev equation in Jacobi momentum

variables explicitly at first, followed by introducing a three-dimensional implementation of the three-body force calculation [61]. The equation is a typical eigenvalue equation and solved by an iterative method. Then we analyze the accuracy and some issues related to our three-body force calculation. By using this procedure, we investigate the three-body bound state properties as functions of the three-body force. We also do an excursion into a playground with forces by changing the three-body force parameters from its original values, and study how the three-body bound state with three-body force only behaves and how the two-body and three-body force interplay in this scenario.

4.1 The Explicit Equation for Bound State

For clarity, we write the Faddeev equation for a three-body bound state with three-body force (c.f. Eq. (2.16)) again,

$$|\psi\rangle = G_0 t P |\psi\rangle + G_0 (1 + t G_0) V_4^{(1)} (1 + P) |\psi\rangle. \quad (4.1)$$

The three-body free propagator for bound state equation is given as

$$G_0 = \frac{1}{E - \frac{p^2}{m} - \frac{3q^2}{4m}}. \quad (4.2)$$

where the m is the boson mass. Since the total energy E of three boson bound state is negative, the free propagator G_0 has no singularities. By using the definition of the symmetrized two-body t -matrix t_s introduced in Eq. (3.24) and explicitly working out the permutation operator P , the Faddeev equation for the three-body bound state with both two-body and three-body forces in Eq. (2.16) is given as

$$\begin{aligned} \langle \mathbf{p} \mathbf{q} | \psi \rangle &= \frac{1}{E - \frac{p^2}{m} - \frac{3q^2}{4m}} \left[\int d^3 q' t_s \left(\mathbf{p}, \frac{1}{2} \mathbf{q} + \mathbf{q}'; E - \frac{3}{4m} q^2 \right) \langle \mathbf{q} + \frac{1}{2} \mathbf{q}', \mathbf{q}' | \psi \rangle \right. \\ &\quad \left. + \langle \mathbf{p} \mathbf{q} | V_4^{(1)} (1 + P) | \psi \rangle + \frac{1}{2} \int d^3 \tilde{p} \frac{t_s \left(\mathbf{p}, \tilde{\mathbf{p}}; E - \frac{3}{4m} q^2 \right)}{E - \frac{\tilde{p}^2}{m} - \frac{3}{4m} q^2} \langle \tilde{\mathbf{p}} \mathbf{q} | V_4^{(1)} (1 + P) | \psi \rangle \right]. \end{aligned} \quad (4.3)$$

The equation for the three-body bound state with two-body forces alone (c.f. Eq. (2.17)) is given as

$$\langle \mathbf{p}\mathbf{q}|\psi\rangle = \frac{1}{E - \frac{p^2}{m} - \frac{3q^2}{4m}} \left[\int d^3q' t_s \left(\mathbf{p}, \frac{1}{2}\mathbf{q} + \mathbf{q}'; E - \frac{3}{4m}q^2 \right) \langle \mathbf{q} + \frac{1}{2}\mathbf{q}', \mathbf{q}'|\psi\rangle \right]. \quad (4.4)$$

Since an unpolarized bound state has no preferred direction, we choose the coordinate system in such a way that the vector \mathbf{q} is parallel to the z -axis and the vector \mathbf{p} is in $x - z$ plane. In this coordinate system Eq. (4.4) becomes

$$\begin{aligned} \psi(p, q, x) &= \frac{1}{E - \frac{p^2}{m} - \frac{3}{4m}q^2} \int_0^\infty dq' q'^2 \int_{-1}^{+1} dx' \int_0^{2\pi} d\phi' \\ &\quad t_s \left(p, \sqrt{\frac{1}{4}q^2 + q'^2 + qq'x'}, \frac{\frac{1}{2}qx + q'y}{|\frac{1}{2}\mathbf{q} + \mathbf{q}'|}, E - \frac{3}{4m}q^2 \right) \\ &\quad \times \psi \left(\sqrt{q^2 + \frac{1}{4}q'^2 + qq'x'}, q', \frac{\frac{1}{2}q' + qx'}{|\frac{1}{2}\mathbf{q}' + \mathbf{q}|} \right) \end{aligned} \quad (4.5)$$

with

$$\begin{aligned} p &= |\mathbf{p}|, \\ q &= |\mathbf{q}|, \\ x &= \hat{\mathbf{p}} \cdot \hat{\mathbf{q}}, \\ q' &= |\mathbf{q}'|, \\ x' &= \hat{\mathbf{q}}' \cdot \hat{\mathbf{q}}, \\ y &= \hat{\mathbf{p}} \cdot \hat{\mathbf{q}}' = xx' + \sqrt{1-x^2}\sqrt{1-x'^2}\cos\phi', \\ \left| \frac{1}{2}\mathbf{q} + \mathbf{q}' \right| &= \sqrt{\frac{1}{4}q^2 + q'^2 + qq'x'}, \\ \left| \frac{1}{2}\mathbf{q}' + \mathbf{q} \right| &= \sqrt{q^2 + \frac{1}{4}q'^2 + qq'x'}. \end{aligned} \quad (4.6)$$

where the ϕ' is the azimuthal angle of \mathbf{p}' . The numerical solution of Eq. (4.5) has already been well established and proven to be very accurate in Ref. [37].

In order to solve Eq. (4.3) with the inclusion of a three-body force, the matrix elements of three-body force $\langle \mathbf{p}\mathbf{q}|V_4^{(1)}(1+P)|\psi\rangle$ needs to be calculated. As typical structure of a three-body force $V_4^{(1)}$ we consider a three-body force of Fujita-Miyazawa

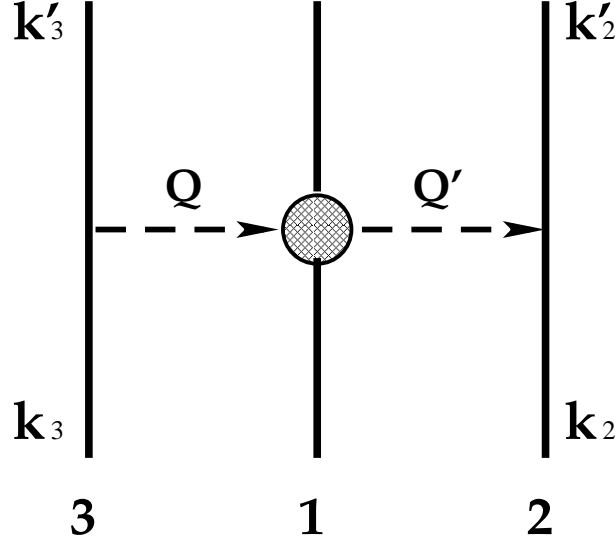


Figure 4.1: The diagrammatic representation of the three-body force $V_4^{(1)}$. The particle 1 is singled out by the meson-nucleon amplitude described by the blob. The three-body force of this type is then given according to Eq. (4.7).

type [42], which is specified by a sequence of meson exchanges in the subsystem (12), called for convenience subsystem 3, and subsystem (31), called 2. Particle 1 is singled out by the meson-nucleon scattering, as indicated in Fig. 4.1. The functional form of the three-body force with two scalar meson exchange and a constant meson-nucleon amplitude can be written as

$$V_4^{(1)} \propto \frac{F(Q^2)}{Q^2 + m_s^2} \frac{F(Q'^2)}{Q'^2 + m_s^2} \quad (4.7)$$

with the momentum cutoff function

$$F(Q^2) = \left(\frac{\Lambda^2 - m_s^2}{\Lambda^2 + Q^2} \right)^2. \quad (4.8)$$

Here m_s is the mass of the exchanged meson and the Λ is the momentum cutoff parameter. The momentum transfers are

$$\begin{aligned} \mathbf{Q} &= \mathbf{k}_2 - \mathbf{k}'_2 \\ \mathbf{Q}' &= \mathbf{k}'_3 - \mathbf{k}_3. \end{aligned} \quad (4.9)$$

In Jacobi momenta of coordinate system 1 they are

$$\begin{aligned}\mathbf{Q} &= \mathbf{k}_2 - \mathbf{k}'_2 = \mathbf{p}_1 - \mathbf{p}'_1 + \frac{1}{2}(\mathbf{q}_1 - \mathbf{q}'_1) \\ \mathbf{Q}' &= \mathbf{k}'_3 - \mathbf{k}_3 = \mathbf{p}_1 - \mathbf{p}'_1 - \frac{1}{2}(\mathbf{q}_1 - \mathbf{q}'_1).\end{aligned}\quad (4.10)$$

The momentum transfers in the meson propagators contain linear combinations of three or four momentum vectors and thus a direct integrations for evaluating the matrix element of the three-body force would involve magnitudes of vectors and angles between all of them, which can be very complicated and involved.

However, since the structure of the three-body force we consider is specified by two momentum transfers of consecutive meson exchanges, it is convenient to insert a complete set of states of the type 3 between $V_4^{(1)}$ and $(1+P)|\psi\rangle$ and another complete set of states of type 2 between the two meson exchanges. Then the matrix element of $V_4^{(1)}$ is rewritten as

$$\begin{aligned}{}_1\langle\mathbf{p}\mathbf{q}|V_4^{(1)}|\Psi\rangle &\propto \int d^3p'_3 d^3q'_3 d^3p'_2 d^3q'_2 d^3p''_3 d^3q''_3 d^3p''_2 d^3q''_2 \\ &{}_1\langle\mathbf{p}\mathbf{q}|\mathbf{p}'\mathbf{q}'\rangle_2 \\ &{}_2\langle\mathbf{p}'\mathbf{q}'|\frac{F(Q^2)}{Q^2+m_\alpha^2}|\mathbf{p}''\mathbf{q}''\rangle_2 \\ &{}_2\langle\mathbf{p}''\mathbf{q}''|\mathbf{p}'\mathbf{q}'\rangle_3 \\ &{}_3\langle\mathbf{p}'\mathbf{q}'|\frac{F(Q'^2)}{Q'^2+m_\alpha^2}|\mathbf{p}''\mathbf{q}''\rangle_3 {}_3\langle\mathbf{p}''\mathbf{q}''|\Psi\rangle.\end{aligned}\quad (4.11)$$

The subscripts $i = 1, 2, 3$ of the bra and ket vectors in above equation indicate that the momentum variables are in the coordinate system of i -th type. It is observed that both meson-exchange propagators in this three-body force term only depend on the momentum transfer in a two-body subsystem, i.e.

$$\begin{aligned}{}_2\langle\mathbf{p}'\mathbf{q}'|\frac{F(Q^2)}{Q^2+m_\alpha^2}|\mathbf{p}''\mathbf{q}''\rangle_2 &= \delta(\mathbf{q}'_2 - \mathbf{q}''_2) \frac{F((p'_2 - p''_2)^2)}{(p'_2 - p''_2)^2 + m_\alpha^2} \\ {}_3\langle\mathbf{p}'\mathbf{q}'|\frac{F(Q'^2)}{Q'^2+m_\alpha^2}|\mathbf{p}''\mathbf{q}''\rangle_3 &= \delta(\mathbf{q}'_3 - \mathbf{q}''_3) \frac{F((p'_3 - p''_3)^2)}{(p'_3 - p''_3)^2 + m_\alpha^2}.\end{aligned}\quad (4.12)$$

Now the momentum transfer in meson propagators become easy to compute. Using Eq. (4.12), one can rewrite Eq. (4.11) as

$${}_1\langle\mathbf{p}\mathbf{q}|V_4(1+P)|\psi\rangle = \int d^3p' d^3q' {}_1\langle\mathbf{p}\mathbf{q}|\mathbf{p}'\mathbf{q}'\rangle_2$$

$$\begin{aligned}
& \times \int d^3 p'' \frac{F((\mathbf{p}' - \mathbf{p}'')^2)}{(\mathbf{p}' - \mathbf{p}'')^2 + m_\alpha^2} \\
& \times \int d^3 p''' d^3 q''' {}_2\langle \mathbf{p}'' \mathbf{q}' | \mathbf{p}''' \mathbf{q}''' \rangle_3 \\
& \times \int d^3 p'''' \frac{F((\mathbf{p}''' - \mathbf{p}'''')^2)}{(\mathbf{p}''' - \mathbf{p}'''')^2 + m_\alpha^2} {}_3\langle \mathbf{p}'''' \mathbf{q}''' | \Psi \rangle. \quad (4.13)
\end{aligned}$$

Explicitly evaluating the coordinate transformations ${}_1\langle \mathbf{p} \mathbf{q} | \mathbf{p}' \mathbf{q}' \rangle_2$ and ${}_2\langle \mathbf{p} \mathbf{q} | \mathbf{p}' \mathbf{q}' \rangle_3$ in Eq. (4.13) gives

$$\begin{aligned}
\langle \mathbf{p} \mathbf{q} | V_4^{(1)}(1 + P) | \psi \rangle &= \int d^3 q' \frac{F((- \mathbf{p} - \frac{1}{2} \mathbf{q} - \mathbf{q}')^2)}{(- \mathbf{p} - \frac{1}{2} \mathbf{q} - \mathbf{q}')^2 + m_s^2} \\
&\times \int d^3 p' \frac{F((- \mathbf{p} + \frac{1}{2} \mathbf{q} - \frac{1}{2} \mathbf{q}' - \mathbf{p}')^2)}{(- \mathbf{p} + \frac{1}{2} \mathbf{q} - \frac{1}{2} \mathbf{q}' - \mathbf{p}')^2 + m_s^2} \langle \mathbf{p}' \mathbf{q}' | (1 + P) | \psi \rangle. \quad (4.14)
\end{aligned}$$

The key point of the method proposed in Ref. [61] is not to carry out the coordinate transformations analytically. Instead, we define an auxiliary function

$$F_3(\mathbf{p}''', \mathbf{q}''') = \int d^3 p'''' \frac{F((\mathbf{p}''' - \mathbf{p}'''')^2)}{(\mathbf{p}''' - \mathbf{p}'''')^2 + m_\alpha^2} {}_3\langle \mathbf{p}'''' \mathbf{q}''' | \Psi \rangle. \quad (4.15)$$

The integration of the meson exchange between particles 2 and 1 in Eq. (4.15) is carried out completely in the coordinate system of type 3. Once $F_3(\mathbf{p}''', \mathbf{q}''')$ is obtained, it needs to be expressed in terms of momenta in a coordinate system of type 2 in order to carry out the integration over the remaining meson exchange. This transformation, labeled $F_{32}(\mathbf{p}'', \mathbf{q}')$, is explicitly given as

$$\begin{aligned}
F_{32}(\mathbf{p}'', \mathbf{q}') &= \int d^3 p''' d^3 q''' {}_2\langle \mathbf{p}'' \mathbf{q}' | \mathbf{p}''' \mathbf{q}''' \rangle_3 F_3(\mathbf{p}''', \mathbf{q}''') \\
&= F_3 \left(\left| -\frac{1}{2} \mathbf{p}'' - \frac{3}{4} \mathbf{q}' \right|, \left| \mathbf{p}'' - \frac{1}{2} \mathbf{q}' \right|, \frac{(-\frac{1}{2} \mathbf{p}'' - \frac{3}{4} \mathbf{q}') \cdot (\mathbf{p}'' - \frac{1}{2} \mathbf{q}')}{|-\frac{1}{2} \mathbf{p}'' - \frac{3}{4} \mathbf{q}'| |\mathbf{p}'' - \frac{1}{2} \mathbf{q}'|} \right). \quad (4.16)
\end{aligned}$$

In our vector based method, this transformation is effectively a three dimensional interpolation on F_3 in Eq. (4.15), which can be handled by the cubic spline interpolation described in [61] and Section 5.1.1. The integration over the second meson exchange between particle 1 and 3 in the coordinate system of type 2 is now given by

$$F_2(\mathbf{p}', \mathbf{q}') = \int d^3 p'' \frac{F((\mathbf{p}' - \mathbf{p}'')^2)}{(\mathbf{p}' - \mathbf{p}'')^2 + m_\alpha^2} F_{32}(\mathbf{p}'', \mathbf{q}'). \quad (4.17)$$

The matrix element $\langle \mathbf{p}\mathbf{q}|V_4(1+P)|\psi\rangle$ is finally obtained by integrating $F_2(\mathbf{p}', \mathbf{q}')$ over \mathbf{p}' and \mathbf{q}' , i.e. carrying out the final coordinate transformation from the system of type 2 back to the one of type 1,

$$\begin{aligned}\langle \mathbf{p}\mathbf{q}|V_4(1+P)|\psi\rangle &= \int d^3p' d^3q' \langle \mathbf{p}\mathbf{q}|\mathbf{p}'\mathbf{q}'\rangle_2 F_2(\mathbf{p}', \mathbf{q}') \\ &= F_2\left(\left|-\frac{1}{2}\mathbf{p} + \frac{3}{4}\mathbf{q}\right|, \left|-\mathbf{p} - \frac{1}{2}\mathbf{q}\right|, \frac{(-\frac{1}{2}\mathbf{p} + \frac{3}{4}\mathbf{q}) \cdot (-\mathbf{p} - \frac{1}{2}\mathbf{q})}{\left|-\frac{1}{2}\mathbf{p} + \frac{3}{4}\mathbf{q}\right| \left|-\mathbf{p} - \frac{1}{2}\mathbf{q}\right|}\right).\end{aligned}\quad (4.18)$$

The integrations over the meson propagators in Eq. (4.13) are carried out in separate steps from Eq. (4.15) to Eq. (4.18). Thus they contain only one integration over one vector variable at a time. This approach avoids the complexity of a direct evaluation of the meson propagators as given in Eq. (4.14), where many vectors are involved simultaneously. Our three-dimensional vector based method reveals a remarkable advantage over partial wave based approach. When the coordinate transformations in Eqs. (4.16) and (4.18) are performed via a partial wave decomposition approach, there is a complicated angular momentum recoupling algebra involved, whereas in a three dimensional scheme the evaluation of the permutation are simple three dimensional interpolations.

For the numerical calculation of the matrix elements of Eq. (4.13), we start by first calculating $F_3(\mathbf{p}''', \mathbf{q}''')$ by Eq. (4.15). We can choose \mathbf{q}''' parallel to the z -axis and \mathbf{p}''' in $x - z$ plane. This leads to the simplification of the azimuthal angles. The explicit expression is

$$\begin{aligned}F_3(p''', q''', x''') &= \\ &\int_0^\infty dp'''' p''''^2 \int_{-1}^{+1} dx'''' \int_0^{2\pi} d\phi'''' \frac{\left(\frac{\Lambda^2 - m_\alpha^2}{\Lambda^2 + (p'''^2 + p''''^2 - 2p'''p''''y''')^2}\right)^2}{(p'''^2 + p''''^2 - 2p'''p''''y''')^2 + m_\alpha^2} \Psi(p''''', q''''', x''''').\end{aligned}\quad (4.19)$$

with

$$\begin{aligned}p''' &= |\mathbf{p}'''|, \\ q''' &= |\mathbf{q}'''|,\end{aligned}$$

$$\begin{aligned}
x''' &= \hat{\mathbf{p}}''' \cdot \hat{\mathbf{q}}''', \\
p''' &= |\mathbf{p}''|, \\
x'''' &= \hat{\mathbf{p}}'''' \cdot \hat{\mathbf{q}}''', \\
y'''' &= x'''x'''' + \sqrt{1-x'''^2}\sqrt{1-x''''^2}\cos\phi''''
\end{aligned} \tag{4.20}$$

where ϕ'''' is the azimuthal angle of \mathbf{p}'''' . After obtaining $F_3(p''', q'', x''')$, the evaluation of $F_{32}(\mathbf{p}'', \mathbf{q}')$ in Eq. (4.16) by a three dimensional interpolation is explicitly given as

$$\begin{aligned}
F_{32}(p'', q', x'') &= \\
F_3 \left(\frac{1}{2}\sqrt{\frac{9}{4}q'^2 + p''^2 + 3p''q'x''}, \sqrt{\frac{1}{4}q'^2 + p''^2 - p''q'x''}, \frac{\frac{3}{8}q'^2 - \frac{1}{2}p''^2 - \frac{1}{2}p''q'x''}{\left|-\frac{3}{4}\mathbf{q}' - \frac{1}{2}\mathbf{p}''\right|\left|+\mathbf{p}'' - \frac{1}{2}\mathbf{q}'\right|} \right).
\end{aligned} \tag{4.21}$$

with

$$\begin{aligned}
\left|-\frac{3}{4}\mathbf{q}' - \frac{1}{2}\mathbf{p}''\right| &= \frac{1}{2}\sqrt{\frac{9}{4}q'^2 + p''^2 + 3p''q'x''} \\
\left|+\mathbf{p}'' - \frac{1}{2}\mathbf{q}'\right| &= \sqrt{\frac{1}{4}q'^2 + p''^2 - p''q'x''}.
\end{aligned} \tag{4.22}$$

The integration over the second meson exchange, i.e. the calculation of $F_2(\mathbf{p}', \mathbf{q}')$ in Eq. (4.17) has functionally the same form as shown in Eq. (4.19). We choose the variable \mathbf{q}' parallel to the z -axis and \mathbf{p}' in the $x-z$ plane. Thus we have the same expression as Eq. (4.19) with p', q', x', p'', x'' and ϕ'' instead of $p''', q''', x''', p''''', x''''$ and ϕ'''' . Finally, the matrix element $\langle \mathbf{p}\mathbf{q}|V_4^{(1)}|\Psi\rangle$ is explicitly obtained by a second interpolation

$$\langle \mathbf{p}\mathbf{q}|V_4^{(1)}|\Psi\rangle = F_2 \left(\frac{1}{2}\sqrt{\frac{9}{4}q^2 + p^2 - 3pqx}, \sqrt{\frac{1}{4}q^2 + p^2 + pqx}, \frac{-\frac{3}{8}q^2 + \frac{1}{2}p^2 - \frac{1}{2}pqx}{\left|+\frac{3}{4}\mathbf{q} - \frac{1}{2}\mathbf{p}\right|\left|-\mathbf{p} - \frac{1}{2}\mathbf{q}\right|} \right) \tag{4.23}$$

with

$$\begin{aligned}
\left|+\frac{3}{4}\mathbf{q} - \frac{1}{2}\mathbf{p}\right| &= \frac{1}{2}\sqrt{\frac{9}{4}q^2 + p^2 - 3pqx} \\
\left|-\mathbf{p} - \frac{1}{2}\mathbf{q}\right| &= \sqrt{\frac{1}{4}q^2 + p^2 + pqx}.
\end{aligned} \tag{4.24}$$

The last term in Eq. (4.3) requires an additional integration of the matrix element $\langle \mathbf{p}\mathbf{q}|V_4(1+P)|\psi\rangle$ and the half shell two-body t -matrix. Again, by choosing \mathbf{q} parallel to the z -axis, and \mathbf{p} and \mathbf{q} are in $x-z$ plane and one has

$$\begin{aligned} & \frac{1}{2} \int d^3\tilde{p} \frac{t_s(\mathbf{p}, \tilde{\mathbf{p}}; E - \frac{3}{4m}q^2)}{E - \frac{\tilde{p}^2}{m} - \frac{3}{4m}q^2} \langle \tilde{\mathbf{p}}\mathbf{q}|V_4^1(1+P)|\psi\rangle \\ &= \frac{1}{2} \int_0^\infty d\tilde{p} \tilde{p}^2 \int_1^{+1} d\tilde{x} \int_0^{2\pi} d\tilde{\phi} \frac{t_s(p, \tilde{p}, \tilde{y}_p; E - \frac{3}{4m}q^2)}{E - \frac{\tilde{p}^2}{m} - \frac{3}{4m}q^2} V_4^{(1)} \Psi(\tilde{p}, q, \tilde{x}) \end{aligned} \quad (4.25)$$

with

$$\begin{aligned} \tilde{x} &= \hat{\tilde{\mathbf{p}}} \cdot \hat{\mathbf{q}} \\ \tilde{y}_p &= \hat{\tilde{\mathbf{p}}} \cdot \hat{\mathbf{p}} = x\tilde{x} + \sqrt{1-x^2}\sqrt{1-\tilde{x}^2}\cos\tilde{\phi}. \end{aligned} \quad (4.26)$$

Here the $\tilde{\phi}$ is the azimuthal angle of $\tilde{\mathbf{p}}$. The total wave function $|\Psi\rangle = (1+P)|\psi\rangle$, which directly appears in Eqs. (4.14) and (4.25), is constructed as

$$\begin{aligned} & \langle \mathbf{p}\mathbf{q}|(1+P)|\psi\rangle = \Psi(\mathbf{p}, \mathbf{q}) \\ &= \psi(\mathbf{p}, \mathbf{q}) + \psi\left(-\frac{3}{4}\mathbf{q} - \frac{1}{2}\mathbf{p}, \mathbf{p} - \frac{1}{2}\mathbf{q}\right) + \psi\left(\frac{3}{4}\mathbf{q} - \frac{1}{2}\mathbf{p}, -\mathbf{p} - \frac{1}{2}\mathbf{q}\right), \end{aligned} \quad (4.27)$$

and explicitly given by

$$\begin{aligned} & \Psi(\mathbf{p}, \mathbf{q}) = \Psi(p, q, x) \\ &= \psi(p, q, x) \\ &+ \psi\left(\frac{1}{2}\sqrt{\frac{9}{4}q^2 + p^2 + 3pqx}, \sqrt{\frac{1}{4}q^2 + p^2 - pqx}, \frac{\frac{3}{8}q^2 - \frac{1}{2}p^2 - \frac{1}{2}pqx}{|-\frac{3}{4}\mathbf{q} - \frac{1}{2}\mathbf{p}||\mathbf{p} - \frac{1}{2}\mathbf{q}|}\right) \\ &+ \psi\left(\frac{1}{2}\sqrt{\frac{9}{4}q^2 + p^2 - 3pqx}, \sqrt{\frac{1}{4}q^2 + p^2 + pqx}, \frac{\frac{3}{8}q^2 + \frac{1}{2}p^2 - \frac{1}{2}pqx}{|-\frac{3}{4}\mathbf{q} - \frac{1}{2}\mathbf{p}||-\mathbf{p} - \frac{1}{2}\mathbf{q}|}\right) \end{aligned} \quad (4.28)$$

with

$$\begin{aligned} \left|-\frac{3}{4}\mathbf{q} - \frac{1}{2}\mathbf{p}\right| &= \frac{1}{2}\sqrt{\frac{9}{4}q^2 + p^2 + 3pqx} \\ \left|+\mathbf{p} - \frac{1}{2}\mathbf{q}\right| &= \sqrt{\frac{1}{4}q^2 + p^2 - pqx} \end{aligned}$$

$$\begin{aligned}
\left| -\frac{3}{4}\mathbf{q} - \frac{1}{2}\mathbf{p} \right| &= \frac{1}{2} \sqrt{\frac{9}{4}q^2 + p^2 - 3pqx} \\
\left| -\mathbf{p} - \frac{1}{2}\mathbf{q} \right| &= \sqrt{\frac{1}{4}q^2 + p^2 + pqx}.
\end{aligned} \tag{4.29}$$

The wave function is normalized according to

$$\int d^3p d^3q \Psi^2(\mathbf{p}, \mathbf{q}) = 1. \tag{4.30}$$

After all terms in Eq. (4.3) are prepared, this equation can be solved as an eigenvalue problem of $|\psi\rangle = K(E)|\psi\rangle$ type by the Iterated Orthonormalized Vector method described in Section 5.3.

In summary, the permutation-based method in Eq. (4.13) suggests a more efficient approach with great advantages, though theoretically it is equivalent to Eq. (4.14). First, at each point on the grid (p, q, x) , the permutation based method just needs two three-dimensional integrations plus two three-dimensional interpolations, whereas the method in Eq. (4.14) needs a six-dimensional integration. Second, based on the reduced dimension, the permutation-based method is more easily implemented with the required features for high performance computing. The permutation-based method exhibits much better computing performance as demonstrated in Appendix A.2.3.

4.2 Models of Two-Body and Three-Body Forces

In our model studies of three-body bound state we choose a two-body force of the modified Malfliet-Tjon types with dipole cut-off function

$$\begin{aligned}
V(\mathbf{p}, \mathbf{p}') = & - \frac{g_A^2}{(2\pi)^3} \frac{1}{(\mathbf{p} - \mathbf{p}')^2 + m_A^2} \left(\frac{\Lambda_A^2 - m_A^2}{(\mathbf{p} - \mathbf{p}')^2 + \Lambda_A^2} \right)^2 \\
& + \frac{g_R^2}{(2\pi)^3} \frac{1}{(\mathbf{p} - \mathbf{p}')^2 + m_R^2} \left(\frac{\Lambda_R^2 - m_R^2}{(\mathbf{p} - \mathbf{p}')^2 + \Lambda_R^2} \right)^2.
\end{aligned} \tag{4.31}$$

We consider here two different forces, a purely attractive one (MT2-I) and one with repulsive core (MT2-II). The indices A and R in the coupling constant g , exchanged meson mass m and momentum cutoff parameter Λ refer to attractive and repulsive pieces. The exchanged masses m_A and m_R are those from the original Malfliet-Tjon model [10]. The cutoff masses Λ have values typical for one-boson-exchange

$g_A^2/4\pi$	$m_A[\text{MeV}]$	$\Lambda_A[\text{MeV}]$
-0.7210	330.2104	1500.0

Table 4.1: The parameters of the purely attractive two-body force MT2-I.

$g_A^2/4\pi$	$m_A[\text{MeV}]$	$\Lambda_A[\text{MeV}]$	$g_R^2/4\pi$	$m_R[\text{MeV}]$	$\Lambda_R[\text{MeV}]$
-3.5775	330.2104	1500.0	9.4086	612.4801	1500.0

Table 4.2: The parameters of two-body force MT2-II.

models [62]. The coupling constants are chosen so that the two-body force gives a binding of the three-body system which is slightly smaller than the experimental value of the triton binding energy, which is 8.48 MeV. The two-body force MT2-I has parameters in Table 4.1 and gives the calculated binding energy of three-body bound state $E = 7.6986$ MeV. The two-body force MT2-II has parameters in Table 4.2 and gives calculated binding energy of three-body bound state $E = 7.5801$ MeV. One three-body force model applied in our calculation with the structure in Fig 4.1 is

$$V_4^{(1)} = \frac{1}{(2\pi)^6} \frac{a_\alpha}{m_\alpha} g_\alpha^2 \frac{F(Q^2)}{Q^2 + m_\alpha^2} \frac{F(Q'^2)}{Q_3'^2 + m_\alpha^2}, \quad (4.32)$$

which is called MT3-I. The constant g_α^2 is the coupling strength due to the two meson exchanges with mass m_α . The constant meson-nucleon amplitude a_α is tuned to be a negative constant that gives a small attractive contribution to the three-body binding energy when it is applied together with the two-body force MT2-II, so that we end up in the neighborhood of the measured triton binding energy $E_d = -8.48$ MeV. With the parameters of MT3-I in Table 4.3, we obtain three-body binding energy $E = 8.8732$ MeV when using MT2-II + MT3-I as the two-body and three-body force combinations.

$g_\alpha^2/4\pi$	$m_\alpha[\text{MeV}]$	$\Lambda_\alpha[\text{MeV}]$	a_α
5.0	305.8593	1000.0	-1.73

Table 4.3: The parameters of three-body force MT3-I.

$g_\alpha^2/4\pi$	$m_\alpha[\text{MeV}]$	$\Lambda_\alpha[\text{MeV}]$	a_α	$g_\rho^2/4\pi$	$m_\rho[\text{MeV}]$	$\Lambda_\rho[\text{MeV}]$	$a_{\alpha\rho}$
5.0	305.8593	1000.0	-2.69	9.0	650.0000	1900.0	2.40

Table 4.4: The parameters of the three-body force MT3-II.

The three-body force can also be a superposition of one attractive part and one repulsive part. The functional form is

$$\begin{aligned}
V_4^{(1)} = & \frac{1}{(2\pi)^6} \frac{a_\alpha}{m_\alpha} g_\alpha^2 \frac{F(Q^2)}{Q^2 + m_\alpha^2} \frac{F(Q'^2)}{Q_3'^2 + m_\alpha^2} \\
& + \frac{1}{(2\pi)^6} \frac{a_{\alpha\rho}}{\sqrt{m_\alpha m_\rho}} g_\alpha g_\rho \left(\frac{F(Q^2)}{Q^2 + m_\alpha^2} \frac{F(Q'^2)}{Q_3'^2 + m_\rho^2} + \frac{F(Q^2)}{Q^2 + m_\rho^2} \frac{F(Q'^2)}{Q_3'^2 + m_\alpha^2} \right).
\end{aligned} \tag{4.33}$$

Here g_α and $g_{\alpha\rho}$ are coupling strength due to the meson exchanges with different meson masses m_α and m_ρ respectively. The second part in Eq. (4.33) is formulated in such a way that this $V_4^{(1)}$ is symmetric under the exchange of nucleon 2 and 3. This type of three-body is called MT3-II. The constant meson-nucleon amplitudes a_α for attractive part and $a_{\alpha\rho}$ for repulsive part are tuned so that it gives a small attractive contribution to the three-body binding energy when it is applied together with the two-body force MT2-II. With parameters listed in Table 4.4, we obtain a three-body binding energy $E = 8.6478$ MeV when using MT2-II + MT3-II as the two-body and three-body force combination.

4.3 The Accuracy Analysis of Three-Body Force Calculation

We use Gaussian quadrature to carry out all the integrations, which means that the variable p , q , and x in the Faddeev component $\psi(p, q, x)$ as well as all integral variables are discretized by Gaussian grids. As indicated in the permutation based method for three-body calculation suggested in Eq. (4.13), the integrations over the meson exchange contributions of the three-body force require grids similar in range to the one used to calculate the two-body t -matrix. So the momentum magnitude and angle grids for the integrations in Eqs.(4.25) and (4.19) have the same size and structure as those used in Eq. (4.4) for the t_s . The p grid is defined between 0 and 60 fm^{-1} and the q -grid is defined between 0 and 40 fm^{-1} . For the accuracy and convergence analysis we considered, we use MT2-II and MF3-I as the two-body and three-body force combination.

Since we use a Gaussian grid to discretize the continuous momentum variables, all the calculated values of observables and expectation values of operators are functions of Gaussian grid size. So we will use these calculated values to check the convergence with respect to the grid size. We calculate the binding energy E directly from the IOV iteration as described in Section 5.3, the expectation values of the kinetic energy operator $\langle H_0 \rangle$, two-body and three-body potential energies $\langle V_{II} \rangle$ and $\langle V_{III} \rangle$. The total energy can be obtained by calculating the expectation value of total hamiltonian $\langle H \rangle$. Based on their convergence properties with respect to the Gaussian grid size, we can determine the essential grid size for getting these results converged up to 5th digit in order to match the experimental accuracy. Using the total wave function Ψ in Eq. (4.28) and the Faddeev component ψ therein, the expectation value of total energy is

$$\langle H \rangle = \langle \Psi | H | \Psi \rangle = \langle \Psi | H_0 | \Psi \rangle + \langle \Psi | V_{II} | \Psi \rangle + \langle \Psi | V_{III} | \Psi \rangle, \quad (4.34)$$

where the expectation value of kinetic energy is

$$\langle H_0 \rangle \equiv \langle \Psi | H_0 | \Psi \rangle = 3 \langle \psi | H_0 | \Psi \rangle$$

$$\begin{aligned}
&= 3 \cdot 8\pi^2 \int_0^\infty p^2 dp \int_0^\infty q^2 dq \left(\frac{p^2}{m} + \frac{3q^2}{4m} \right) \int_{-1}^{+1} dx \psi(p, q, x) \Psi(p, q, x), \\
&\quad (4.35)
\end{aligned}$$

the expectation value of the two-body potential energy is

$$\begin{aligned}
\langle V_{II} \rangle &\equiv \langle \Psi | V_{II} | \Psi \rangle = 3 \langle \Psi | V^1 | \Psi \rangle \\
&= 3 \cdot 8\pi^2 \int_0^\infty p^2 dp \int_0^\infty q^2 dq \int_{-1}^{+1} dx \int_0^\infty p'^2 dp' \int_{-1}^{+1} dx' \\
&\times \Psi(p, q, x) v_1(p, p', x, x') \Psi(p', q, x') \\
&\quad (4.36)
\end{aligned}$$

with

$$v_1(p, p', x, x') = \int_0^{2\pi} d\phi V^1(p, p', xx' + \sqrt{1-x^2}\sqrt{1-x'^2} \cos \phi), \quad (4.37)$$

and the expectation value of the three-body potential energy is

$$\begin{aligned}
\langle V_{III} \rangle &\equiv \langle \Psi | V_{III} | \Psi \rangle = 3 \langle \Psi | V_4^{(1)} | \Psi \rangle \\
&= 3 \cdot 8\pi^2 \int_0^\infty p^2 dp \int_0^\infty q^2 dq \int_{-1}^{+1} dx \Psi(p, q, x) V_4^{(1)} \Psi(p, q, x). \\
&\quad (4.38)
\end{aligned}$$

The number of Gaussian points for the p and p'' integration are the same and is denoted as NP, the number of Gaussian points for the q and q'' integration are denoted as NQ, and the number of Gaussian points for x and x'' are denoted as NX. We also need to check convergence with respect to the number of Gaussian points for all the azimuthal angle integral variables, and its number is denoted as NPHIINT.

The results for the NPHIINT dependence are listed in the Table 4.5. It is found that using only 10 points for ϕ'' grid is enough to archive convergence. This is due to the fact that we only need to put Gaussian points in $[0, \pi]$ for the azimuthal angle integration over $[0, 2\pi]$ because

$$\begin{aligned}
\int_0^{2\pi} F[\cos(\phi'')] d\phi'' &= \left(\int_0^\pi + \int_\pi^{2\pi} \right) F[\cos(\phi'')] d\phi'' \\
&= \int_0^\pi F[\cos(\phi'')] d\phi'' - \int_\pi^0 F[\cos(2\pi - \phi')] d\phi' \\
&= 2 \int_0^\pi F[\cos(\phi'')] d\phi''. \\
&\quad (4.39)
\end{aligned}$$

In Table 4.6 we show that when the number of x and x'' Gaussian points N_X is greater than 30, the energy results converge to the 5-th digit. The results in Tables 4.5 and 4.6 indicate that the angular dependence of the iterated state in the calculation is weak. For checking the convergence with respect to the grid of p and p'' , the number of Gaussian points are separately distributed in the low p region ($0.0 \text{ fm}^{-1}, 10.0 \text{ fm}^{-1}$) with M points and in high p region ($10.0 \text{ fm}^{-1}, 60.0 \text{ fm}^{-1}$) with N points, so the total number is $M + N$ and are listed at the first column from left in Table 4.7. It shows that the energy results are the same up to 5-th digit when the number of points in high p region is up to $N = 20$ with the fixed number of points in low p region $M = 32$. Then we put $N = 20$ points in such high p region and increase the number of points in low p region from 44 to 64, we find that the energy results slightly change and finally converge at the 5-th digit. For the q and q'' grid, we do the same and list the results in Table 4.8. Increasing the number of Gaussian points at high q region within ($10.0 \text{ fm}^{-1}, 40.0 \text{ fm}^{-1}$) from 12 to 28, we find that the results are the same up to the 5-th digit and 20 points is sufficient for the high q region. By increasing the number of points in the low q region ($0.0 \text{ fm}^{-1}, 10.0 \text{ fm}^{-1}$) from 44 to 64, we find that the energies converge to the 4-th digit. From the convergence test of p - and q -grid, we find that the contributions from the high p, q region is small and more grid points should be put in low p, q region. In order to archive the overall convergence on the 5-th digit, we need to increase the p - and q -grid size further. The results are listed in Table 4.9, where we put the same points in both p and q grid and find a convergence of the energy eigenvalue and the expectation values within 5 digits at the grid size of p, q, x for $97 \times 97 \times 42$. This size is taken as the typical size in the following calculations.

NPHIINT	$\langle H_0 \rangle$ (MeV)	$\langle V_{II} \rangle$ (MeV)	$\langle V_{III} \rangle$ (MeV)	$\langle H \rangle$ (MeV)	E (MeV)
5	31.8839	-39.4071	-1.3392	-8.8624	-8.8715
10	31.8838	-39.4069	-1.3392	-8.8623	-8.8715
20	31.8838	-39.4069	-1.3392	-8.8623	-8.8715

Table 4.5: The calculated eigenvalue E from the the solution of the Faddeev equation and the expectation values of the kinetic energy $\langle H_0 \rangle$, the two-body potential $\langle V_{II} \rangle$, the three-body potential energy $\langle V_{III} \rangle$ and the total Hamiltonian $\langle H \rangle$ as functions of the number of grid points NPHIINT for the ϕ'' grid with the other grid sizes fixed as NP = 44, NQ = 44 and NX = 20. The calculations are based on the two-body and three-body forces of MT2-II+MT3-I.

NX	$\langle H_0 \rangle$ (MeV)	$\langle V_{II} \rangle$ (MeV)	$\langle V_{III} \rangle$ (MeV)	$\langle H \rangle$ (MeV)	E (MeV)
20	31.8837	-39.4068	-1.3393	-8.8622	-8.8714
30	31.8838	-39.4069	-1.3392	-8.8623	-8.8715
40	31.8838	-39.4069	-1.3392	-8.8623	-8.8715
50	31.8838	-39.4069	-1.3392	-8.8623	-8.8715

Table 4.6: The calculated eigenvalue E from the the solution of the Faddeev equation and the expectation values of the kinetic energy $\langle H_0 \rangle$, the two-body potential $\langle V_{II} \rangle$, the three-body potential energy $\langle V_{III} \rangle$ and the total Hamiltonian $\langle H \rangle$ as functions of the number of grid points NX for the x and x'' grid with the other grid sizes fixed as NP = 44, NQ = 44 and NPHIINT = 20. The calculations are based on the two-body and three-body forces of MT2-II+MT3-I.

NP = M + N	$\langle H_0 \rangle$ (MeV)	$\langle V_{II} \rangle$ (MeV)	$\langle V_{III} \rangle$ (MeV)	$\langle H \rangle$ (MeV)	E (MeV)
32+12	31.8837	-39.4069	-1.3392	-8.8623	-8.8715
32+20	31.8838	-39.4069	-1.3392	-8.8623	-8.8715
32+28	31.8838	-39.4069	-1.3392	-8.8623	-8.8715
44+20	31.8846	-39.4073	-1.3396	-8.8623	-8.8711
54+20	31.8848	-39.4074	-1.3397	-8.8623	-8.8710
64+20	31.8848	-39.4074	-1.3397	-8.8623	-8.8710

Table 4.7: The calculated eigenvalue E from the the solution of the Faddeev equation and the expectation values of the kinetic energy $\langle H_0 \rangle$, the two-body potential $\langle V_{II} \rangle$, the three-body potential energy $\langle V_{III} \rangle$ and the total Hamiltonian $\langle H \rangle$ as functions of the number of grid points NP for the p and p'' grid with the other grid sizes fixed as NQ = 44, NX = 42, and NPHIINT = 20. The calculations are based on the two-body and three-body forces of MT2-II+MT3-I.

NQ = M + N	$\langle H_0 \rangle$ (MeV)	$\langle V_{II} \rangle$ (MeV)	$\langle V_{III} \rangle$ (MeV)	$\langle H \rangle$ (MeV)	E (MeV)
32+12	31.8847	-39.4074	-1.3397	-8.8623	-8.8710
32+20	31.8847	-39.4074	-1.3397	-8.8623	-8.8710
32+28	31.8847	-39.4074	-1.3397	-8.8623	-8.8710
44+20	31.8874	-39.4104	-1.3402	-8.8631	-8.8718
54+20	31.8900	-39.4132	-1.3406	-8.8639	-8.8726
64+20	31.8911	-39.4145	-1.3408	-8.8642	-8.8730

Table 4.8: The calculated eigenvalue E from the the solution of the Faddeev equation and the expectation values of the kinetic energy $\langle H_0 \rangle$, the two-body potential $\langle V_{II} \rangle$, the three-body potential energy $\langle V_{III} \rangle$ and the total Hamiltonian $\langle H \rangle$ as functions of the number of grid points NPHIINT for the ϕ'' grid with the other grid sizes fixed as NP = 74, NX = 42, and NPHIINT = 20. The calculations are based on the two-body and three-body forces of MT2-II+MT3-I.

NP=NQ	$\langle H_0 \rangle$ (MeV)	$\langle V_{II} \rangle$ (MeV)	$\langle V_{III} \rangle$ (MeV)	$\langle H \rangle$ (MeV)	E (MeV)
57+20	31.8915	-39.4149	-1.3409	-8.8643	-8.8731
67+20	31.8919	-39.4152	-1.3410	-8.8644	-8.8732
77+20	31.8920	-39.4154	-1.3410	-8.8644	-8.8732

Table 4.9: The calculated eigenvalue E from the the solution of the Faddeev equation and the expectation values of the kinetic energy $\langle H_0 \rangle$, the two-body potential $\langle V_{II} \rangle$, the three-body potential energy $\langle V_{III} \rangle$ and the total Hamiltonian $\langle H \rangle$ as functions of the number of grid points NP=NQ for the $p - q$ grid with NX = 42 NPHIINT = 20. The calculations are based on the two-body and three-body forces of MFT2NF-II+MFT3NF-I.

After a converged result is obtained, a further accuracy test is the insertion of solution from IOV iteration back into integral equation and compare the two results. We reinsert the calculated ψ back to Eq. (4.3) and get ψ' as

$$|\psi'\rangle = K(E)|\psi\rangle, \quad (4.40)$$

and evaluate the average relative error $\overline{\Delta}$ given as

$$\overline{\Delta} = \frac{\sum_{p,q,x} \left| \frac{\psi(p,q,x) - \psi'(p,q,x)}{\psi(p,q,x)} \right|}{N_p \cdot N_q \cdot N_x} \times 100. \quad (4.41)$$

where the $\sum_{p,q,x}$ means the summation over all grid points of p, q, x and the N_p , N_q and N_x are the number of grid points for each variable. If ψ is the solution of Eq. (4.3), the error $\overline{\Delta}$ should essentially vanish. Indeed this relative error can be evaluated over any specific (p, q) region so that we can determine which momentum region is the main source of error. This quantity is calculated with different grid size and (p, q) region and listed in Table 4.10. We find that the solution of Faddeev components $\psi(p, q, x)$ by IOV iteration in whole space satisfy Eq. (4.3) with high accuracy.

We are convinced that the numerical solution is in general very accurate. However, we notice that there are two facts need further consideration. One is the difference between $\langle H \rangle$ and E in Table 4.9, which is around 0.088 MeV. Of course this difference can be attributed to the numerical error, but the question is why this difference can not be improved by increasing the number of grid points. This is also the case for

p, q region fm^{-1}	< 2	< 5	< 10	< 15	entire integration region
NP=NQ=57, $\bar{\Delta} \cdot 10^{-7}\%$	24.7	24.8	25.1	26.9	36.1
NP=NQ=77, $\bar{\Delta} \cdot 10^{-7}\%$	24.6	25.2	25.4	26.4	32.8
NP=NQ=97, $\bar{\Delta} \cdot 10^{-7}\%$	24.6	26.5	26.1	26.9	32.2

Table 4.10: The results of average relative error $\bar{\Delta}$ calculated on different (p, q) region with different grid sizes.

NP=NQ	$\langle H_0 \rangle$ (MeV)	$\langle V_{II} \rangle$ (MeV)	$\langle H \rangle$ (MeV)	E (MeV)	$ \langle H \rangle - E $
57+20	28.640784	-36.338991	-7.698207	-7.698439	0.000231
67+20	28.640788	-36.339072	-7.698284	-7.698408	0.000124
77+20	28.640790	-36.339111	-7.698320	-7.698385	0.000064

Table 4.11: The same as Table 4.9 but calculations are based on MT2-II two-body force alone.

$\bar{\Delta}$ in Table 4.10 in which the relative error $\bar{\Delta}$ can not be improved by increasing the number of grid points either. In Table 4.11 we repeat the calculations of Table 4.9 with the two-body force MT2-II. We find that the difference between $\langle H \rangle$ and E is around 10^{-4} MeV and can be improved by increasing the number of (p, q) grid points. Furthermore, we repeat the calculations of Table 4.10 but using the two-body force MT2-II alone and show results in Table 4.12. We find that the $\bar{\Delta}$ evaluated over the entire integration region for MT2-II alone is smaller than that with the inclusion of MT3-I and can be improved somehow by increasing the number of (p, q) grid.

p, q region fm^{-1}	< 2	< 5	< 10	< 15	entire integration region
NP=NQ=57, $\bar{\Delta} \cdot 10^{-7}\%$	2.63	2.71	2.75	3.00	13.4
NP=NQ=77, $\bar{\Delta} \cdot 10^{-7}\%$	2.65	4.63	3.95	4.02	11.4
NP=NQ=97, $\bar{\Delta} \cdot 10^{-7}\%$	2.65	2.68	2.78	2.92	8.89

Table 4.12: The same as Table 4.10 but calculations are based on MT2-II two-body force alone.

Combining these facts we realize that the inclusion of three-body force induces a certain systematic errors. Let's look at the terms and calculations associated with three-body forces. First, we construct total wave function Ψ by Faddeev component ψ in Eq. (4.27). Second, we transform F_3 to F_{32} in Eq. (4.16) and from F_2 to the three-body force matrix elements in Eq. (4.18). All these calculations associated with three-body forces involve three-dimensional interpolation. The values of the functions at the points corresponding to $|\pm \frac{3}{4}\mathbf{q} - \frac{1}{2}\mathbf{p}|$ on the p -grid and those on the points corresponding to $|\pm \mathbf{p} - \frac{1}{2}\mathbf{q}|$ on the q -grid need to be evaluated by interpolation. At the large (p, q) region, when $x = \pm 1$, those magnitudes are very surely beyond the boundaries of the (p, q) grid no matter how large the boundaries are. At this case, we apply a natural boundary condition, i.e, set the function values of Faddeev component $\psi(p, q, x)$ to zero beyond the boundaries of the (p, q) grids. This condition is fairly reasonable. However, numerically this causes an artificial discontinuity on the (p, q) grid boundaries. The calculation with two-body force alone has no such issues. It can be concluded that the main difference between two-body and three-body force calculation is that the three-body force calculation needs some additional three-dimensional interpolations and the interpolated points are not part of the (p, q) grid. This leads to a discontinuity at the (p, q) boundaries when natural boundary conditions are applied. This is the main reason for the difference in accuracy between the two-body and three-body force calculations.

All these analysis are based on the two-body force MT2-II and three-body force MT3-I. It is necessary to check if the method presented here is good for other types of three-body forces. We consider the case of the two-body force MT2-II and three-body force MT3-II. The Table 4.13 is the same as the Table 4.9 but the calculation results are obtained using MT2-II and MT3-II rather than MT3-I. It is found that the calculated energy results of MT3-II also exhibit very regular convergence properties as those of MT3-I. This means that the proven numerical method for MT3-I calculation is equally good to the calculation for MT3-II.

Conclusively, the permutation based method suggested in Eq. (4.13) for three-body force calculation is formulated and implemented with satisfying accuracy and efficiency. The numerical results show that the convergence of binding energy calcu-

NP	NQ	NX	$\langle H_0 \rangle$ (MeV)	$\langle V_{II} \rangle$ (MeV)	$\langle V_{III} \rangle$ (MeV)	$\langle H \rangle$ (MeV)	E (MeV)
45	45	42	31.1745	-38.7859	-1.0404	-8.6518	-8.6454
61	45	42	31.1767	-38.7878	-1.0409	-8.6520	-8.6456
77	45	42	31.1773	-38.7881	-1.0413	-8.6521	-8.6466
77	61	42	31.1825	-38.7880	-1.0478	-8.6533	-8.6477
77	77	42	31.1837	-38.7886	-1.0481	-8.6530	-8.6480
87	87	42	31.1842	-38.7887	-1.0481	-8.6526	-8.6478
97	97	42	31.1847	-38.7892	-1.0481	-8.6526	-8.6478

Table 4.13: The same as Table 4.9 but the calculations are based on the MT2-II + MT3-II.

lation at 5th digit is achieved if p, q, x sizes are $97 \times 97 \times 42$, the calculated Faddeev component fulfills Faddeev equation with satisfying accuracy.

4.4 Three-Body Bound State Properties

The binding energy describes the bound state by a number, as do all the expectation values of physical operators. The distribution and correlation functions can be introduced to describe the bound state properties at a more microscopic level. The probability of finding a single particle with momentum q is given as

$$n(q) = 2\pi q^2 \int_0^\infty dp p^2 \int_{-1}^{+1} dx \Psi^2(p, q, x), \quad (4.42)$$

where the $n(q)$ is called the single particle momentum distribution. The so called two-body correlation function $c(r)$ is given as

$$c(r) = 2\pi r^2 \int_0^\infty dR R^2 \int_{-1}^{+1} dx_R \Psi^2(r, R, x_R), \quad (4.43)$$

which is the probability to find two particles with relative distance r . The calculation of $c(r)$ requires the total wave function in coordinate space,

$$\Psi(\mathbf{r}, \mathbf{R}) = \int d^3p d^3q \Psi(\mathbf{p}, \mathbf{q}) \exp(i\mathbf{p} \cdot \mathbf{r}) \exp(i\mathbf{q} \cdot \mathbf{R}). \quad (4.44)$$

The variables \mathbf{r} and \mathbf{R} are conjugate to the Jacobi momenta \mathbf{p} , \mathbf{q} and given as

$$\begin{aligned}\mathbf{r} &= \mathbf{x}_2 - \mathbf{x}_3, \\ \mathbf{R} &= \mathbf{x}_1 - \frac{1}{2}(\mathbf{x}_2 + \mathbf{x}_3).\end{aligned}\quad (4.45)$$

where \mathbf{x}_1 , \mathbf{x}_2 and \mathbf{x}_3 are the coordinates of three particles in configuration space. For the explicit calculation we first consider the \mathbf{q} -integration in Eq. (4.44)

$$\int d^3q \exp(i\mathbf{q} \cdot \mathbf{R}) \Psi(\mathbf{p}, \mathbf{q}) = \int_0^\infty q^2 dq \int_{-1}^{+1} dx_q \int_0^{2\pi} d\phi_q \exp(i\mathbf{q} \cdot \mathbf{R}) \Psi(\mathbf{p}, \mathbf{q}). \quad (4.46)$$

We choose the vector \mathbf{p} parallel to the z -axis and define the angles $\hat{\mathbf{q}} \cdot \hat{\mathbf{z}} = x_q$ and $\hat{\mathbf{R}} \cdot \hat{\mathbf{z}} = x_R$. Since the integration is carried out over all space, we can set $\phi_R = 0$, and obtain

$$\begin{aligned}& \int d^3q \exp(i\mathbf{q} \cdot \mathbf{R}) \Psi(\mathbf{p}, \mathbf{q}) \\ &= \int_0^\infty q^2 dq \int_{-1}^{+1} dx_q \int_0^{2\pi} d\phi_q \exp(iqR\hat{\mathbf{R}} \cdot \hat{\mathbf{q}}) \Psi(p, q, x_q),\end{aligned}\quad (4.47)$$

where

$$\hat{\mathbf{R}} \cdot \hat{\mathbf{q}} = x_q x_R + \sqrt{1 - x_q^2} \sqrt{1 - x_R^2} \cos \phi_q. \quad (4.48)$$

Thus, the integration over ϕ_q can be carried out separately

$$\begin{aligned}& \int_0^{2\pi} d\phi_q \exp(iqR\sqrt{1 - x_q^2} \sqrt{1 - x_R^2} \cos \phi_q) \\ &= 2\pi J_0(qR\sqrt{1 - x_q^2} \sqrt{1 - x_R^2} \cos \phi_q),\end{aligned}\quad (4.49)$$

where J_0 is Bessel function. Summarizing the above leads to the intermediate result

$$\begin{aligned}& \int d^3q \exp(i\mathbf{q} \cdot \mathbf{R}) \Psi(\mathbf{p}, \mathbf{q}) \\ &= 2\pi \int_0^\infty q^2 dq \int_{-1}^{+1} dx_q J_0(qR\sqrt{1 - x_q^2} \sqrt{1 - x_R^2} \cos \phi_q) \exp(iqR x_q x_R) \Psi(p, q, x_q) \\ &\equiv 2\pi \Psi_p(p, R, x_R).\end{aligned}\quad (4.50)$$

Next, we consider the integration over \mathbf{p} , where it is convenient to choose the vector \mathbf{r} parallel to the z -axis. Thus, the following angle, $\hat{\mathbf{R}} \cdot \hat{\mathbf{z}} \equiv \hat{\mathbf{R}} \cdot \hat{\mathbf{r}} \equiv x_R$, needs to be considered, and the integration over x_p and ϕ_p can be carried out separately as

$$\int_{-1}^{+1} dx_p \int_0^{2\pi} d\phi_p \exp(ipr x_p) = 4\pi \frac{\sin(pr)}{pr} \quad (4.51)$$

Finally, the Fourier transformation of $\Psi(p, q, \hat{\mathbf{p}} \cdot \hat{\mathbf{q}})$ can be calculated as

$$\Psi(r, R, x_R) = \frac{8\pi^2}{r} \int_0^\infty dp [\sin(pr) p \Psi_p(p, R, x_R)], \quad (4.52)$$

where

$$\Psi_p(p, R, x_R) = \int_0^\infty q^2 dq \int_{-1}^{+1} dx_q J_0 \left(qR \sqrt{1-x_q^2} \sqrt{1-x_R^2} \right) \cos(qR x_q x_R) \Psi(p, q, x_q). \quad (4.53)$$

Since the system consists of three identical bosons acting on each other by scalar forces, the most probable positions of the bosons in the ground state has the shape of an equilateral triangle. The expectation values of the r and R in Eq. (4.45) can be calculated as

$$\begin{aligned} \langle r \rangle &= \int_0^\infty R^2 dR \int_0^\infty r^2 dr \int_{-1}^{+1} dx_R r \Psi^2(r, R, x_R), \\ \langle R \rangle &= \int_0^\infty R^2 dR \int_0^\infty r^2 dr \int_{-1}^{+1} dx_R R \Psi^2(r, R, x_R). \end{aligned} \quad (4.54)$$

Here the values $\langle r \rangle$ and $\langle R \rangle$ are the length and height of the equilateral triangle. The geometrical relation between the length and height of an equilateral triangle is given by

$$\langle r \rangle : \langle R \rangle = 2 : \sqrt{3}. \quad (4.55)$$

We also define a deviation δ by

$$\delta = \frac{\langle r \rangle / \langle R \rangle - 2/\sqrt{3}}{2/\sqrt{3}} \times 100. \quad (4.56)$$

to specify the deviation of our calculation from an ideal geometric triangle. This is another good test of the quality of our calculation. In Table 4.14, this δ is calculated together with the $\langle r \rangle$, $\langle R \rangle$ and E for the MT2-II, MT2-II + MT3-I and MT2-II + MT3-II cases. It is found the δ for all these cases are below 2%, which further confirms the numerical accuracy of the three-body force calculation and the quality of total wave function in coordinate space. We also find that the three-body force MT3-I has slightly overall attractive contribution, so the $\langle r \rangle$ of MT2-II + MT3-I is slightly smaller than that of MT2-II, which means the purely attractive MT3-I makes

	MT2-II	MT2-II + MT3-I	MT2-II + MT3-II
E (MeV)	-7.6983	-8.8732	-8.6478
$\langle r \rangle$ (fm)	2.521	2.382	2.9401
$\langle R \rangle$ (fm)	2.221	2.096	2.5945
δ (%)	1.7	1.6	1.9

Table 4.14: The binding energy E , the expectation values $\langle r \rangle$, $\langle R \rangle$ and deviation δ characterizes the deviation from the shape of an equilateral triangle and is defined in Eq. (4.56) calculated with the MT2-II two-body force alone and with the addition of the two different three-body forces.

the whole system slightly tighter bound. However, the $\langle r \rangle$ of MT2-II + MT3-II is slightly less than that of MT2-II even though the overall contribution of MT3-II is also attractive like MT3-I. This can be understood by the repulsive core of MT3-II. So it is interesting to investigate the influences of three-body forces on the properties of three-body bound state in detail. The single particle momentum distribution and two-body correlation function corresponding the cases in Table 4.14 are shown in Fig. 4.2. The shoulder of the momentum distribution around $2\text{-}4\text{ fm}^{-1}$ is qualitatively similar to the case when using realistic forces [63]. There is hardly any big change with and without three-body forces because the contribution of the three-body force to the total binding energy is small, a fact which also has been noticed before in the context of realistic nuclear forces [63]. In addition, the three-body forces of two different types leads to essentially the same momentum distribution. Compared to the momentum distribution given by the two-body force alone, the minimum is shifted to a slightly higher momentum. The two-body correlations $c(r)$ displayed in Fig. 4.2 are similar to the ones obtained with realistic forces [63]. We see that the maximum of $c(r)$ is shifted slightly to smaller value of r once a three-body force is included, which is self-consistent with the minimum of $n(q)$ being shifted to a slightly higher momentum. The position of the maximum of $c(r)$ does not depend on the type of three-body force, however the actual shape of the function does. In order to have an idea about the typical momentum scale in the three-body bound state, we have the contour slices on the total wave function $\Psi(p, q, x = 1)$ shown in Fig. 4.3. The slices are at the

values 10^0 , 10^{-1} , 10^{-2} and 10^{-3} fm^3 . The shift of contour lines at each value due to the three-body force MT3-I is compatible to what we have seen in Fig. 4.2. The slice at 10^0 fm^3 encloses a p, q momentum region within 0.5 fm^{-1} , and around the p, q momentum region at 1.0 fm^{-1} the total wave function value falls down to 10^{-1} fm^3 . Together with the contour lines sliced at 10^{-2} and 10^{-3} fm^3 , it is found that the total wave function drops exponentially with the increasing p, q momentum, and only the momentum region at small p, q mainly contribute with the typical momentum scale around 1 fm^{-1} .

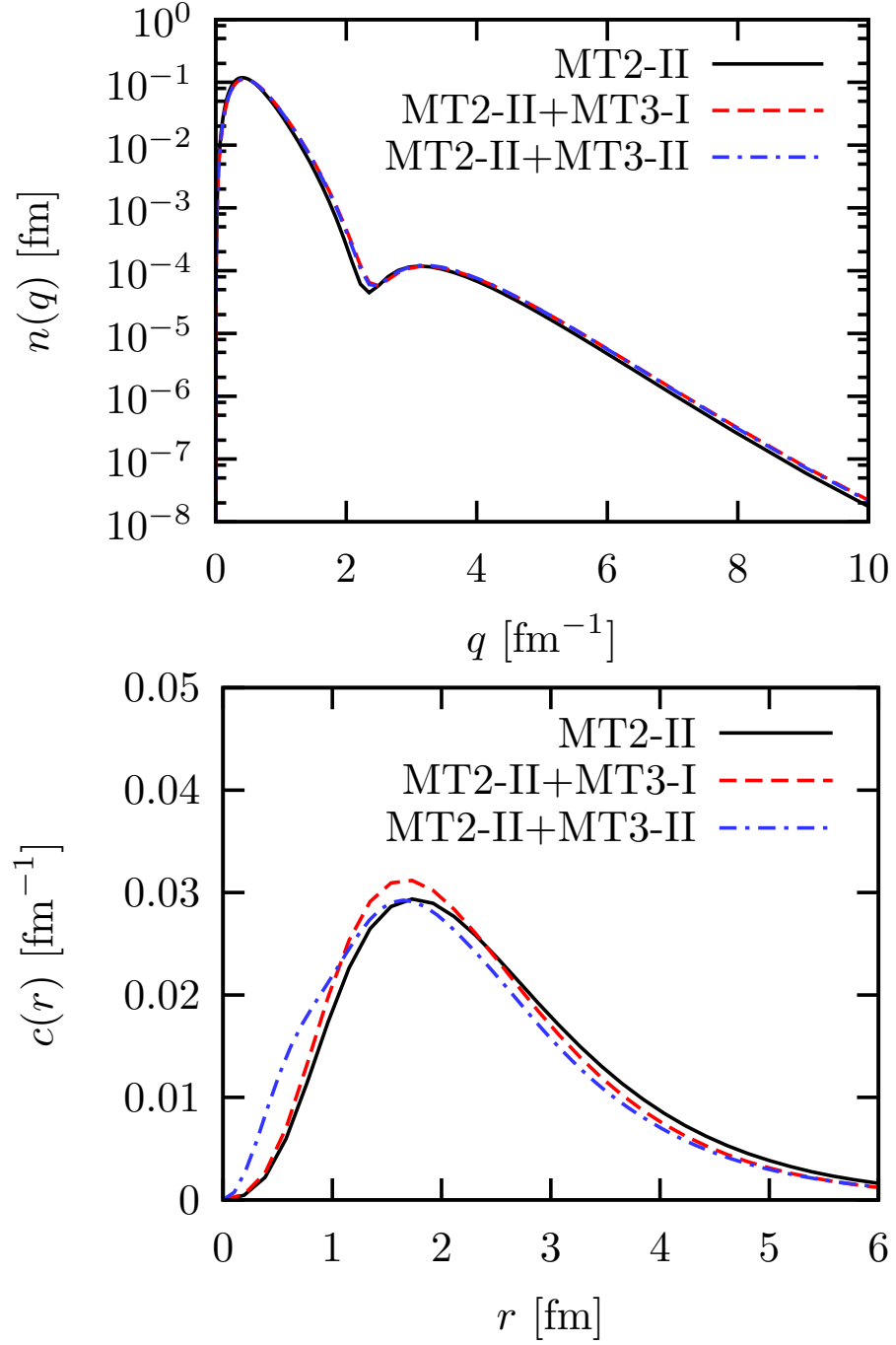


Figure 4.2: The calculated single particle momentum distribution $n(q)$ (upper panel) and two-body correlation function $c(r)$ (lower panel) for MT2-II two-body potential only, MT2-II+MT3-I two-body and three-body potential and MT2-II+MT3-II two-body and three-body potential.

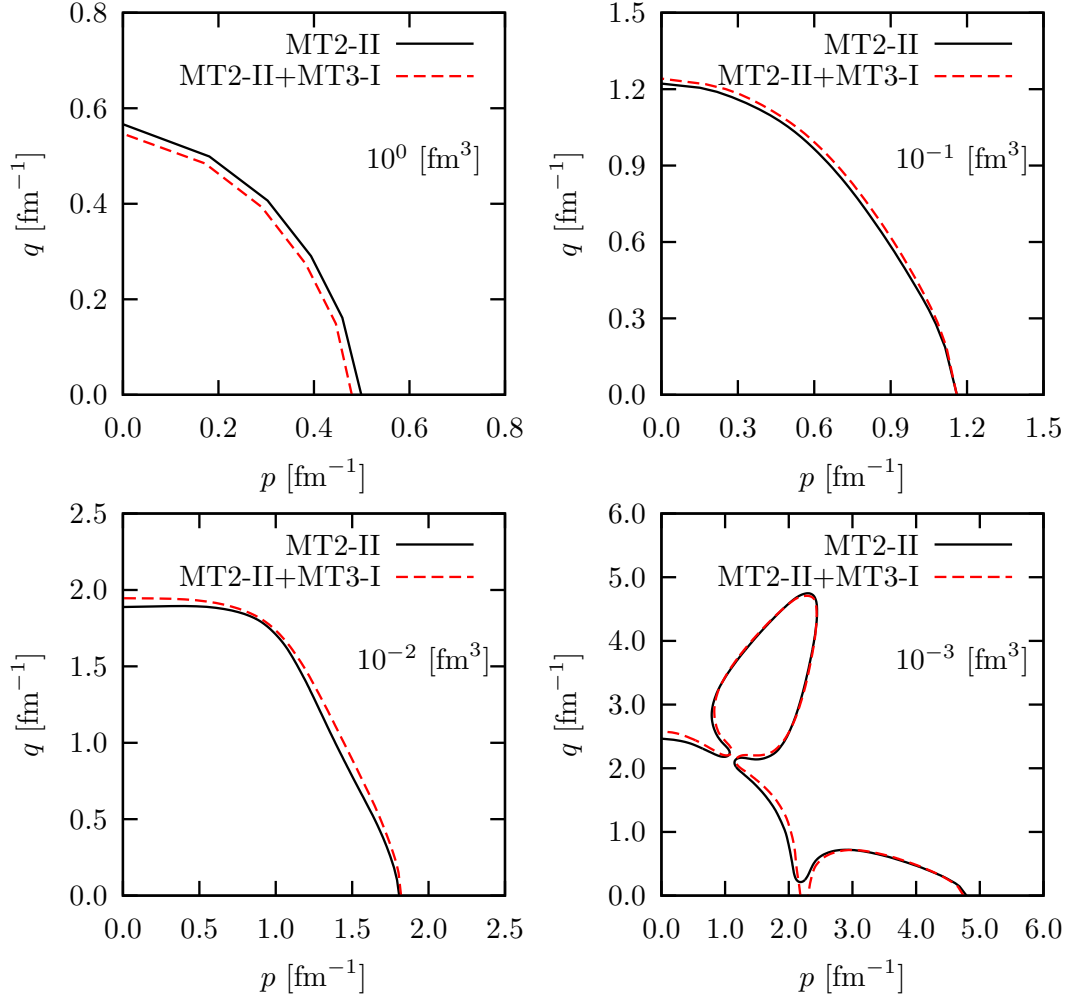


Figure 4.3: The contour slice when the calculated $\Psi(p, q, x = 1)$ is equal to 1.0, 10^{-1} , 10^{-2} and 10^{-3} in unit of fm^3 for MT2-II two-body potential only, and MT2-II+MT3-I two-body and three-body potential.

4.5 Model Studies of Three-Body Forces

A three-body force is specified by its meson-nucleon amplitude, exchanged meson mass and momentum cut-off parameter. In order to extract the three-body bound state properties as functions of three-body force characteristics, we take MT2-II + MT3-I as an example. We keep MT2-II unchanged and make a set of variations over the meson-nucleon amplitude, exchanged meson mass and cut-off parameter of MT3-I respectively, and see how the bound state properties are affected. This is done only for the attractive three-body force MT3-I since we have to vary only one meson-nucleon amplitude a_α , exchange meson mass m_α and cut-off parameter Λ_α in Eq. (4.32).

4.5.1 The Meson-Nucleon Amplitude

First, we check the effects of the meson-nucleon amplitude a_α . We calculate three-body bound state properties when a_α of MT3-I becomes $2a_\alpha$, $4a_\alpha$, $6a_\alpha$ and $8a_\alpha$ while all other parameters of MT2-II + MT3-I remain unchanged, as shown in Tables 4.2 and 4.3. The calculated expectation values of kinetic energy $\langle H_0 \rangle$, the two-body potential $\langle V_{II} \rangle$, the three-body potential energy $\langle V_{III} \rangle$ and the total hamiltonian $\langle H \rangle$ as functions of the different meson-nucleon coupling strengths a_α of MT3-I are shown in Table 4.15. Obviously with increasing a_α the three-body potential energy contribution $\langle V_{III} \rangle$ is increased. We notice that when a_α is linearly increased, the three-body potential energy $\langle V_{III} \rangle$ does not increase linearly. The stronger MT3-I becomes, the higher the binding energy becomes, the three-body bound state is more and more tightly bound. It is interesting to find that the contribution of two-body potential energy $\langle V_{II} \rangle$ from MT2-II increases when a_α becomes $2a_\alpha$ and $4a_\alpha$, but decreases when a_α becomes $6a_\alpha$ and $8a_\alpha$. Especially for the case of $8a_\alpha$, the corresponding $\langle V_{II} \rangle$ is almost zero, but the three-body potential energy is $\langle V_{III} \rangle = -219.3805$ MeV. This illustrates that MT3-I with a strength $8a_\alpha$ totally shifts the three-body bound state out of the region where the two-body force MT2-II is dominant. The larger and larger values of kinetic energy $\langle H_0 \rangle$ when a_α is increased indicate that the three-body force MT3-I mainly arises from the high momentum region. The details of such influences of MT3-I on the high momentum region can be found in Fig. 4.4 which shows the

	$\langle H_0 \rangle$ (MeV)	$\langle V_{II} \rangle$ (MeV)	$\langle V_{III} \rangle$ (MeV)	$\langle H \rangle$ (MeV)
a_α	31.8919	-39.4153	-1.3410	-8.8644
$2a_\alpha$	36.1500	-42.9119	-3.6314	-10.3933
$4a_\alpha$	50.2537	-50.4037	-15.2166	-15.3666
$6a_\alpha$	82.7022	-49.8850	-59.0747	-26.2575
$8a_\alpha$	158.3568	-0.4563	-219.3805	-61.4800

Table 4.15: The calculated expectation values of the kinetic energy $\langle H_0 \rangle$, the two-body potential $\langle V_{II} \rangle$, the three-body potential energy $\langle V_{III} \rangle$ and the total Hamiltonian $\langle H \rangle$ as functions of the different meson-nucleon coupling strength a_α of the three-body force MT3-I.

single particle momentum distribution $n(q)$ and two-body correlation function $c(r)$ as functions of a_α . The amplitude of $n(q)$ rises in the high momentum region when a_α is increased, while the peak of $c(r)$ shifts to smaller distances. This means that the force MT3-I is of short-range character. Compared with the original potential, the shoulder in $n(q)$ disappears and the maximum of $c(r)$ shifts from $r = 1.6$ fm to $r = 0.6$ fm when the strength becomes $8a_\alpha$. In order to see the effects of a_α more microscopically, the total wave functions $\Psi(p, q, x)$ at $x=1$ with different a_α are shown in Fig. 4.5. The reason for only showing $x = 1$ is that the $\Psi(p, q, x)$ does not have angular dependence for the pure scalar interactions we considered. It is found there are nodal lines determined by the zero points in potentials with both attractive and repulsive parts. Since the repulsive part of MT2-II is short-ranged, the position of potential zero points will be shifted when the strength of the short-ranged MT3-I gets changed, so we see the pattern of nodal lines in total wave function evolve with the increased a_α . For the $2a_\alpha$ case, the nodal line near $p, q = 0$ region looks like a neck shape. This neck shaped nodal line is broken when the a_α is further increased, relinked to other nodal lines at high p or high q regions and shifted further towards higher p, q momenta.

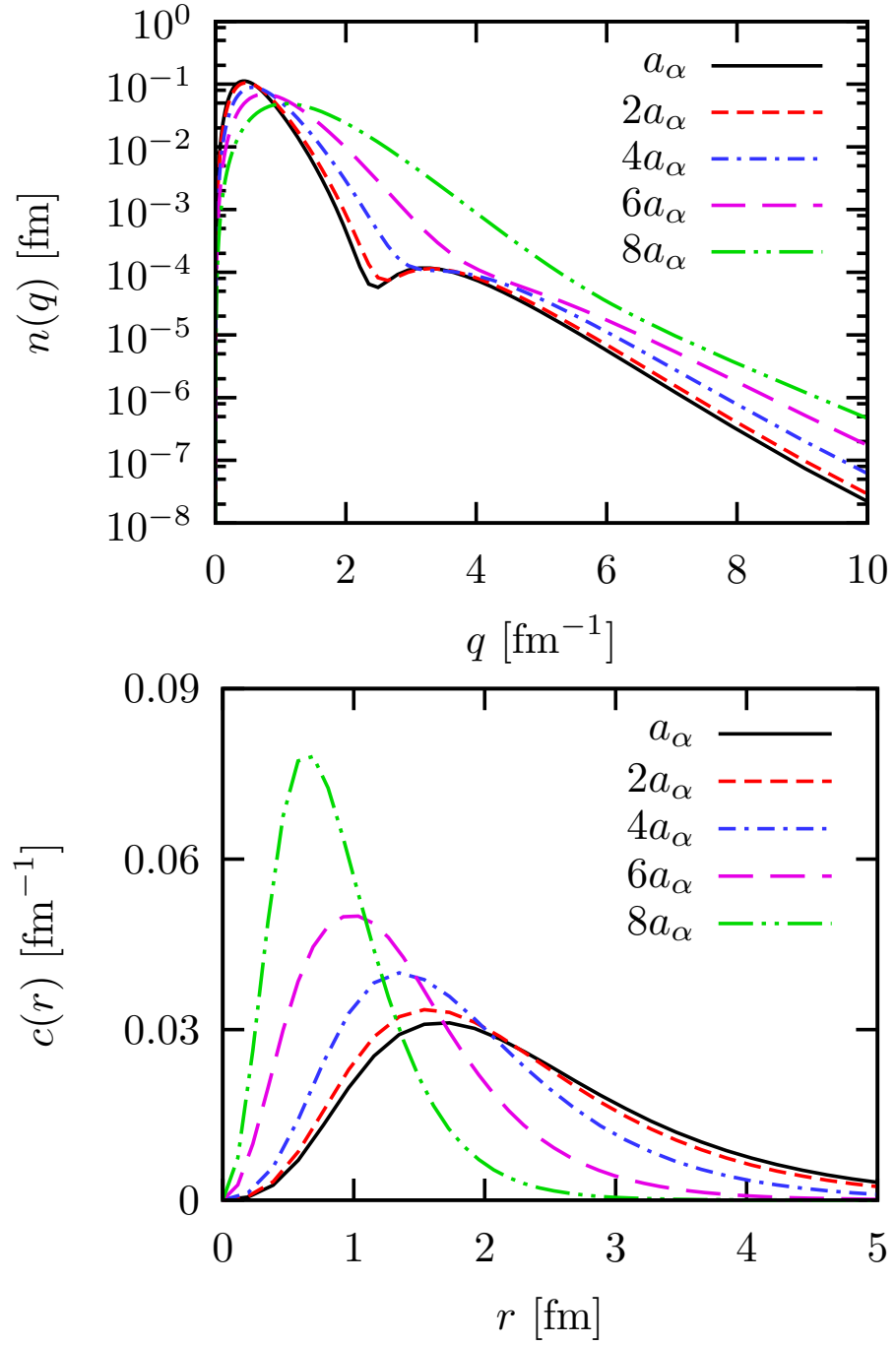


Figure 4.4: The calculated single particle momentum distribution $n(q)$ (upper panel) and two-body correlation function $c(r)$ (lower panel) as functions of the different meson-nucleon coupling strength a_α of the three-body force MT3-I with $a_\alpha = 1.73$.

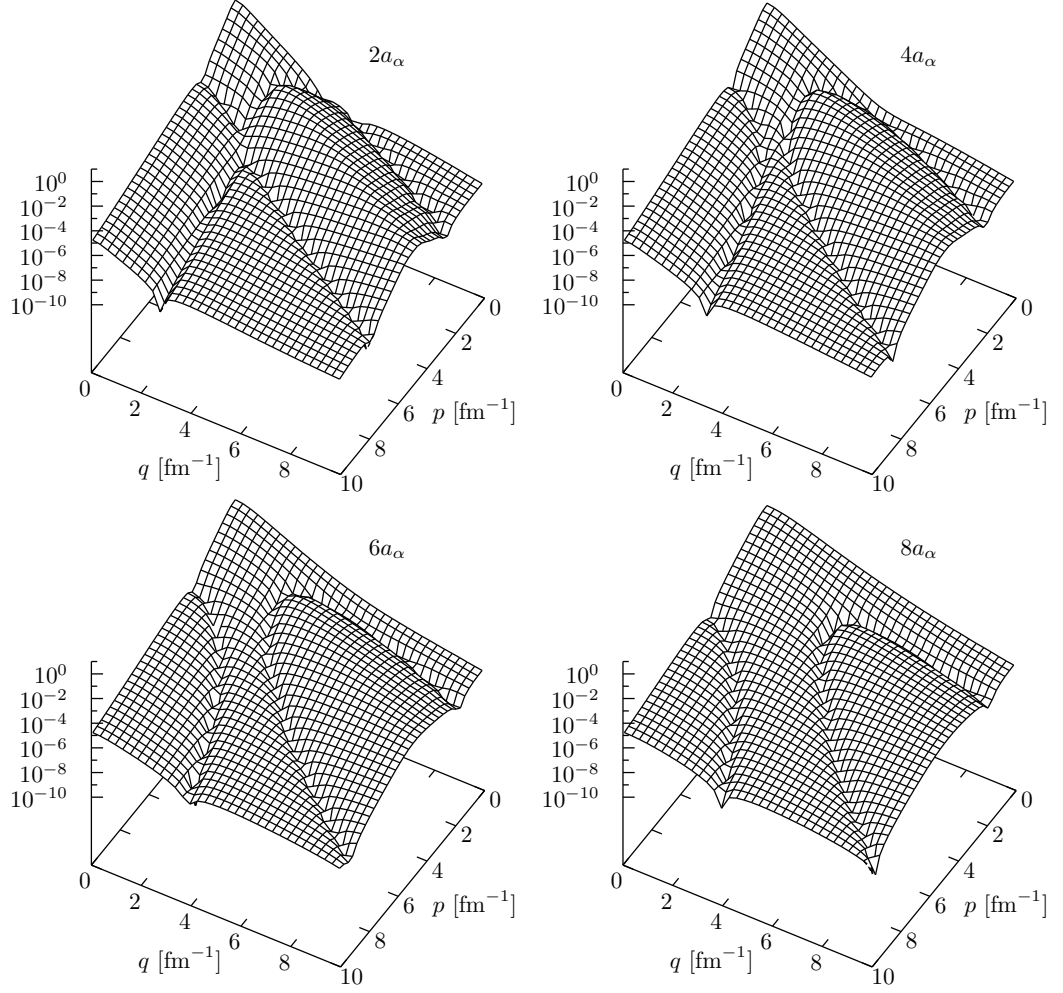


Figure 4.5: The calculated total wave function of three-body bound state $|\Psi(p, q, x)|$ in unit $[\text{fm}^3]$ at $x = 1$ as a function of the different meson-nucleon coupling strength a_α of the three-body force MT3-I. The upper left: $2a_\alpha$, the upper right: $4a_\alpha$, the lower left: $6a_\alpha$, the lower right: $8a_\alpha$.

4.5.2 The Exchanged Meson Mass

Now we return to the original two-body force MT2-II and three-body force MT3-I whose parameters are listed in Tables 4.2 and 4.3. We change the meson mass m_α in the two meson propagators but keep a_α/m_α of MT3-I in Eq. (4.32) unchanged. We want to see how the exchanged meson mass in the meson propagator of MT3-I influences the bound state properties. The calculated expectation values of kinetic energy $\langle H_0 \rangle$, the two-body potential $\langle V_{II} \rangle$, the three-body potential energy $\langle V_{III} \rangle$ and the total hamiltonian $\langle H \rangle$ as functions of the exchanged meson mass m_α of MT3-I are shown in Table 4.16. The corresponding momentum distribution and correlation are shown in Fig. 4.6. It is found that the three-body force effects gets enhanced when the exchanged meson mass m_α becomes lighter. This can be mathematically understood by the functional form of MT3-I in Eq. (4.32). The three-body force shows up in the bound state equation in Eq. (4.3) as the matrix elements of form $\langle \mathbf{pq} | V_4^{(1)} | \Psi \rangle$, so in the physics view point, the effects of m_α depends on the ratio between the mass m_α and the typical momentum scale in bound state wave function $|\Psi\rangle$. As we see from the profile of contour slices over $\Psi(p, q, x)$ in Fig. 4.3, the higher momentum effects in the matrix elements of three-body force would be strongly suppressed by the total wave function of bound state with the typical momentum scale at 1.0 fm^{-1} . When the meson mass is decreased down to $m_\alpha - 150 \approx 150 \text{ MeV}$ and $m_\alpha - 100 \approx 200 \text{ MeV}$ which are close to the typical momentum scale $\sim 1.0 \text{ fm}^{-1}$ in bound state, the meson propagator should be dynamically treated as we did in our calculation. On the other hand, when it gets heavier up to $m_\alpha \approx 300 \text{ MeV}$, $m_\alpha + 100 \approx 400 \text{ MeV}$ and $m_\alpha + 150 \approx 450 \text{ MeV}$ which is much larger than the typical momentum scale of bound state, the three-body force matrix elements might be approximated by

$$\left\langle \mathbf{pq} \left| \frac{F(Q^2)}{Q^2 + m_\alpha^2} \frac{F(Q^2)}{Q^2 + m_\alpha^2} \right| \Psi \right\rangle \approx \left\langle \mathbf{pq} \left| \frac{1}{m_\alpha^4} \right| \Psi \right\rangle. \quad (4.57)$$

In this heavier meson mass region, changing the mass m_α is equivalent to changing the coupling strength. Since we have

$$\begin{aligned} \left(\frac{m_\alpha}{m_\alpha + 100} \right)^4 &= 0.32 \approx \frac{1}{3}, \\ \left(\frac{m_\alpha}{m_\alpha + 150} \right)^4 &= 0.20 \approx \frac{1}{5}, \end{aligned} \quad (4.58)$$

$m_\alpha(\text{MeV})$	$\langle H_0 \rangle(\text{MeV})$	$\langle V_{II} \rangle(\text{MeV})$	$\langle V_{III} \rangle(\text{MeV})$	$\langle H \rangle(\text{MeV})$
$m_\alpha - 150$	55.2781	-54.4207	-21.3530	-20.4956
$m_\alpha - 100$	41.8976	-47.2189	-7.7968	-13.1181
m_α	31.8919	-39.4153	-1.3410	-8.8644
$m_\alpha + 100$	29.6684	-37.3463	-0.3740	-8.0519
$m_\alpha + 150$	29.2040	-36.8957	-0.1979	-7.8896

Table 4.16: The calculated expectation values of the kinetic energy $\langle H_0 \rangle$, the two-body potential $\langle V_{II} \rangle$, the three-body potential energy $\langle V_{III} \rangle$ and the total Hamiltonian $\langle H \rangle$ as functions of the exchanged meson mass m_α of the three-body force MT3-I with $m_\alpha = 305.8593$ MeV and ratio $\frac{a_\alpha}{m_\alpha}$ kept constant.

we repeat the calculations in Table. 4.15 but using the coupling strength $\frac{1}{5}a_\alpha$ and $\frac{1}{3}a_\alpha$ and list the results in Table. 4.17. Compared the results of the last two lines in Table. 4.16, it is found the the results for $\frac{1}{5}a_\alpha$ in Table 4.17 and the results for $m_\alpha + 150 \approx 450$ MeV in Table 4.16, the results for $\frac{1}{3}a_\alpha$ in Table 4.17 and the results for $m_\alpha + 100 \approx 400$ MeV Table 4.16 are almost the same. It should be pointed out that we do the full dynamic calculations of the meson propagator of the three-body force MT3-I as indicated at the left hand side of Eq. (4.57) for all cases. The almost equal results described above may be understood by the approximation at the left hand side of Eq. (4.57). The momentum distribution and correlation function for $\frac{1}{3}a_\alpha$ in Table 4.17 and $m_\alpha + 100 \approx 400$ MeV in Table. 4.16 are shown in Fig. 4.7. The resemblance between the two cases may further indicate the validity of the approximation in Eq. (4.57) when m_α is heavier. It turns out that $m_\alpha \geq 300$ MeV can be regarded as heavy enough in the context of the original two-body and three-body forces we considered.

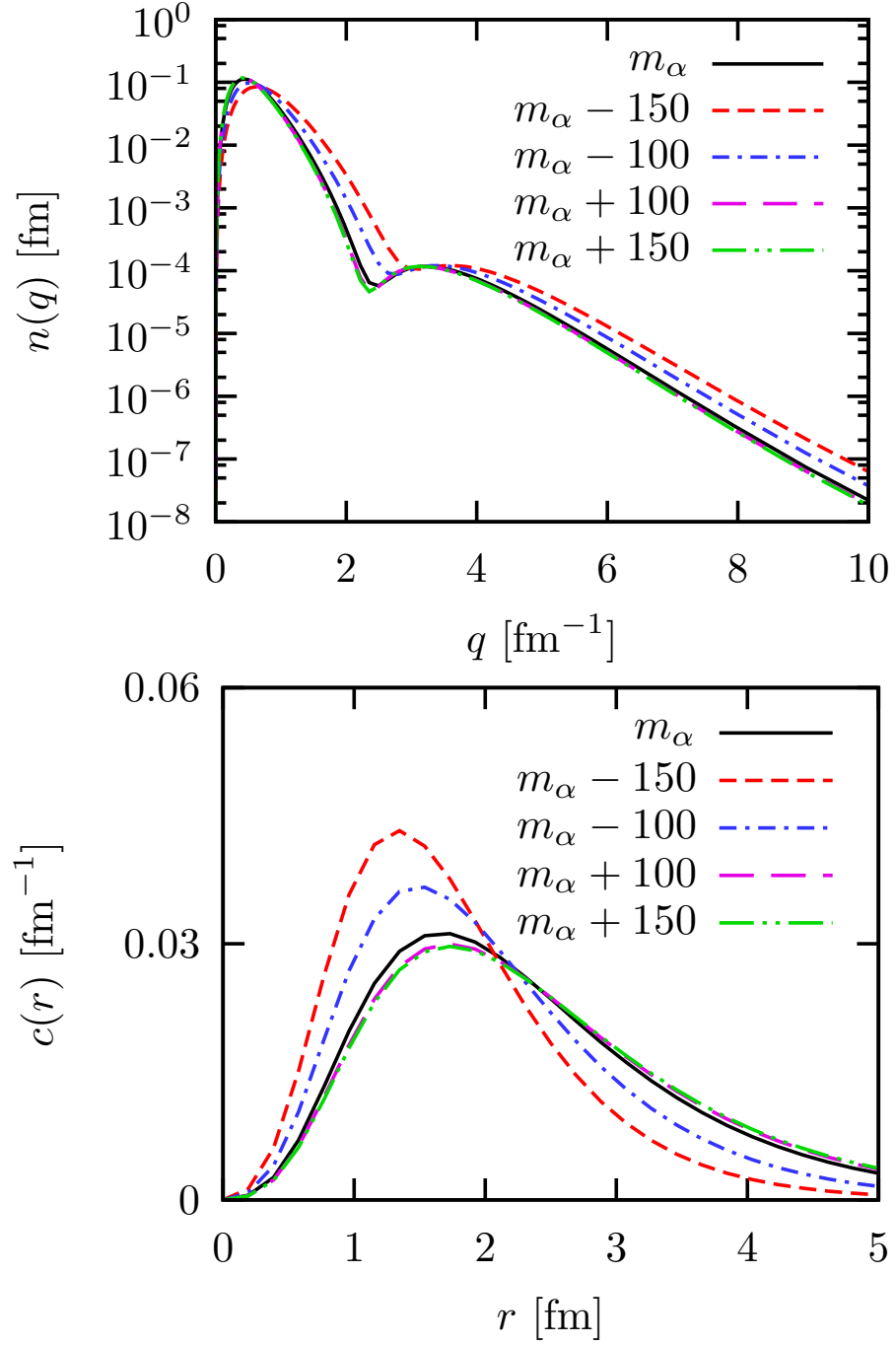


Figure 4.6: The calculated single particle momentum distribution $n(q)$ (upper panel) and two-body correlation function $c(r)$ (lower panel) as functions of the exchanged meson mass m_α of the three-body force MT3-I with $m_\alpha = 305.8593$ MeV and $\frac{a_\alpha}{m_\alpha} = \frac{-1.73}{305.8593}$ unchanged.

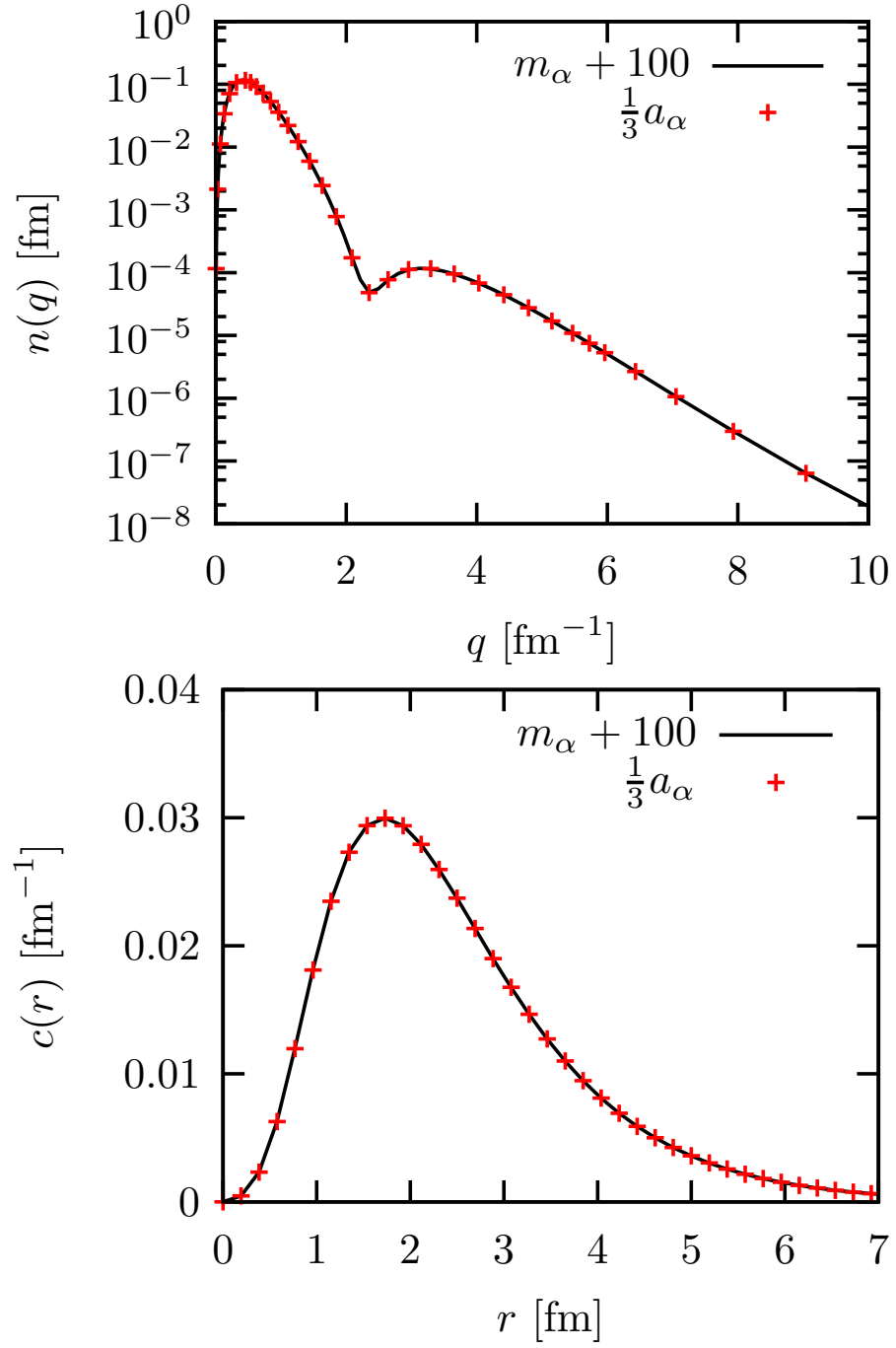


Figure 4.7: The The calculated single particle momentum distribution $n(q)$ (upper panel) and two-body correlation function $c(r)$ (lower panel) corresponding the cases of $\frac{1}{3}a_\alpha$ in Table 4.17 and $m_\alpha + 100 \approx 400$ MeV in Table 4.16.

	$\langle H_0 \rangle (\text{MeV})$	$\langle V_{II} \rangle (\text{MeV})$	$\langle V_{III} \rangle (\text{MeV})$	$\langle H \rangle (\text{MeV})$
$\frac{1}{5}a_\alpha$	29.2035	-36.8950	-0.1986	-7.8901
$\frac{1}{3}a_\alpha$	29.6352	-37.3173	-0.3723	-8.0543

Table 4.17: The same as Table 4.15 but with the meson-nucleon coupling strength a_α changed to $\frac{1}{5}a_\alpha$ and $\frac{1}{3}a_\alpha$.

4.5.3 The Momentum Cut-off Parameter

As it is shown in previous section, the three-body force in general is effectively short ranged because it affects mainly the high momentum region. The momentum cut-off function can be used to regulate the high momentum behavior by setting relevant momentum cut-off parameter Λ_α . We again return to the original two-body force MT2-II and three-body force MT3-I whose parameters are listed in Tables 4.2 and 4.3, and change the Λ_α to extract the dependence of bound state properties on it. The calculated expectation values of kinetic energy $\langle H_0 \rangle$, the two-body potential $\langle V_{II} \rangle$, the three-body potential energy $\langle V_{III} \rangle$ and the total hamiltonian $\langle H \rangle$ as functions of the momentum cut-off parameter Λ_α of MT3-I are shown in Table 4.18 and the corresponding momentum distribution and correlation function are shown in Fig. 4.8. From Table 4.18 it is found that there exists different cut-off parameter dependence with respect to different quantities. When $\Lambda_\alpha = 400$ MeV strongly suppresses the high momentum contribution, the three-body potential energy $\langle V_{III} \rangle$ is almost zero, but it gets larger and larger when Λ_α is increased, which means the three-body force we considered is really short ranged. This is self consistent to what we see from the a_α dependence. However, the overall bound state properties, like the expectation value of total energy $\langle H \rangle$ and the corresponding momentum distribution and correlation function shown in Fig. 4.8, do not have strong cut-off parameter dependence since, as we mentioned before, the typical momentum scale of bound state is within 1.0 fm^{-1} where the two-body force is dominant, and cut-off parameter is much larger than this scale.

$\Lambda_\alpha(\text{MeV})$	$\langle H_0 \rangle(\text{MeV})$	$\langle V_{II} \rangle(\text{MeV})$	$\langle V_{III} \rangle(\text{MeV})$	$\langle H \rangle(\text{MeV})$
$\Lambda_\alpha + 600$	33.6528	-40.8346	-2.2538	-9.4357
$\Lambda_\alpha + 300$	32.9699	-40.3181	-1.8720	-9.2203
Λ_α	31.8919	-39.4153	-1.3410	-8.8645
$\Lambda_\alpha - 300$	30.2397	-37.9018	-0.6290	-8.2911
$\Lambda_\alpha - 600$	28.6955	-36.3938	-0.0222	-7.7205

Table 4.18: The calculated expectation values of the kinetic energy $\langle H_0 \rangle$, the two-body potential $\langle V_{II} \rangle$, the three-body potential energy $\langle V_{III} \rangle$ and the total hamiltonian $\langle H \rangle$ as functions of the momentum cut-off parameter Λ_α of the three-body force MT3-I with $\Lambda_\alpha = 1000$ MeV.

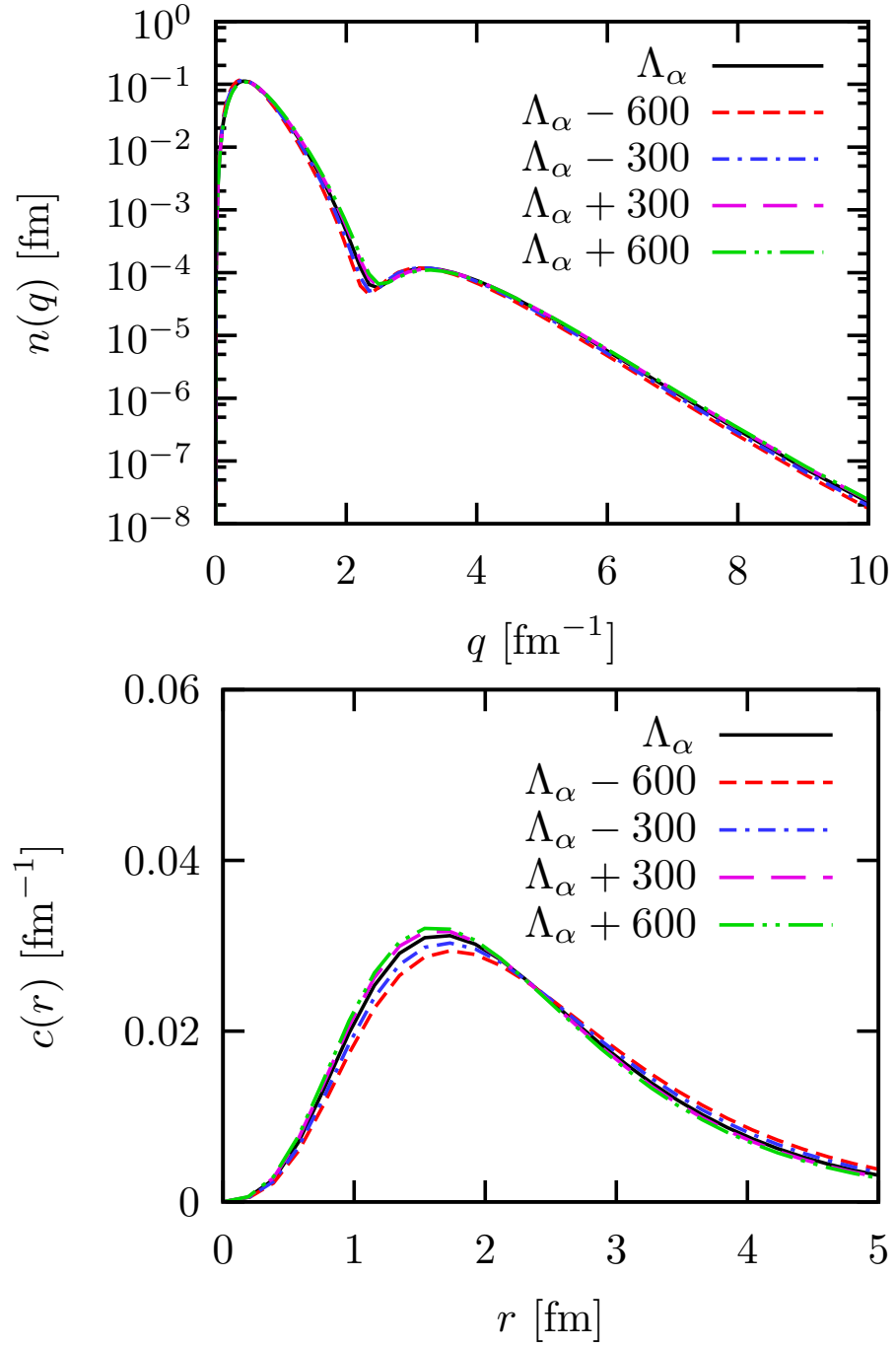


Figure 4.8: The calculated single particle momentum distribution $n(q)$ (upper panel) and two-body correlation function $c(r)$ (lower panel) as functions of the momentum cut-off parameter Λ_α of the three-body force MT3-I with $\Lambda_\alpha = 1000$ MeV.

	$\langle H_0 \rangle (\text{MeV})$	$\langle V_{II} \rangle (\text{MeV})$	$\langle V_{III} \rangle (\text{MeV})$	$\langle H \rangle (\text{MeV})$
$a_\alpha, a_{\alpha\rho}$	31.6662	-39.2386	-1.2581	-8.8305
$2a_\alpha, 2a_{\alpha\rho}$	34.1243	-41.4718	-2.4629	-9.8104
$4a_\alpha, 4a_{\alpha\rho}$	41.0706	-47.0688	-6.6947	-12.6929
$8a_\alpha, 8a_{\alpha\rho}$	59.5265	-58.1352	-23.0029	-21.6117
$16a_\alpha, 16a_{\alpha\rho}$	107.5586	-71.5472	-91.8266	-55.8151

Table 4.19: The calculated expectation values of the kinetic energy $\langle H_0 \rangle$, the two-body potential $\langle V_{II} \rangle$, the three-body potential energy $\langle V_{III} \rangle$ and the total hamiltonian $\langle H \rangle$ as functions of both the attractive and repulsive coupling strength a_α and $a_{\alpha\rho}$ of the three-body force MT3-II with $a_\alpha = -2.69$ and $a_{\alpha\rho} = 2.40$.

4.6 The Three-Body Force with Repulsive Core

The previous model studies are based on the three-body force MT3-I which is only attractive, we now consider the case of MT2-II + MT3-II, where the three-body force MT3-II has a repulsive part. Consider a special case for MT3-II: both the attractive coupling strength a_α and the repulsive coupling strength $a_{\alpha\rho}$ are increased by the same factor so that it produces similar $\langle H \rangle$ as MT3-I does in Table 4.15. The corresponding calculated expectation values of kinetic energy $\langle H_0 \rangle$, the two-body potential $\langle V_{II} \rangle$, the three-body potential energy $\langle V_{III} \rangle$ and the total hamiltonian $\langle H \rangle$ as functions of the attractive coupling strength a_α and the repulsive coupling strength $a_{\alpha\rho}$ of the three-body MT3-II are shown in Table 4.19. Compared to the Table 4.15 for MT3-I line by line, the $\langle H \rangle$ are close to each other. It is interesting to find that at the last line in both tables when the $\langle H \rangle$ is around $-50 \sim -60$ MeV, the only attractive MT3-I fully takes over the MT2-II whose potential energy contribution $\langle V_{II} \rangle$ is almost zero, whereas the MT3-II does not. This is because the simultaneously increased repulsive coupling strength keeps the whole bound state still within the region where the MT2-II can have considerable potential energy contribution $\langle V_{II} \rangle$. This mechanism of repulsive core in MT3-II can also be seen clearly in the momentum distribution and correlation function in Fig. 4.9. Compared to the Fig. 4.4, the shoulder structure in the momentum distribution in Fig. 4.9 shifts to higher momentum, but still remains when the strengths of MT3-II increased. The maximum of corresponding correlation

functions shifts to smaller distance, but has wider shape than those in Fig. 4.4. The corresponding total wave functions $\Psi(p, q, x)$ at $x = 1$ are shown in Fig 4.10. Contrary to the case for MT3-I in Fig. 4.5, where the ridge line near $p, q \sim 0$ is broken due to the increased coupling strength a_α of MT3-I. The stronger and stronger coupling strengths a_α and $a_{\alpha\rho}$ of MT3-II still keep that ridge line. The overall pattern of ridge lines does not change too much while they are shifted towards the higher momentum region. All these facts indicate that even though total binding energies are the same, the microscopic dynamics can be quite different with and without repulsive core. The repulsive core mainly plays the role to prevent the particles coming too close so that the shoulder structure in the momentum distribution remains, and the maximum in correlation function can not be shifted to a too small distance. Therefore the neck shaped nodal line near $p, q \sim 0$ region does not break.

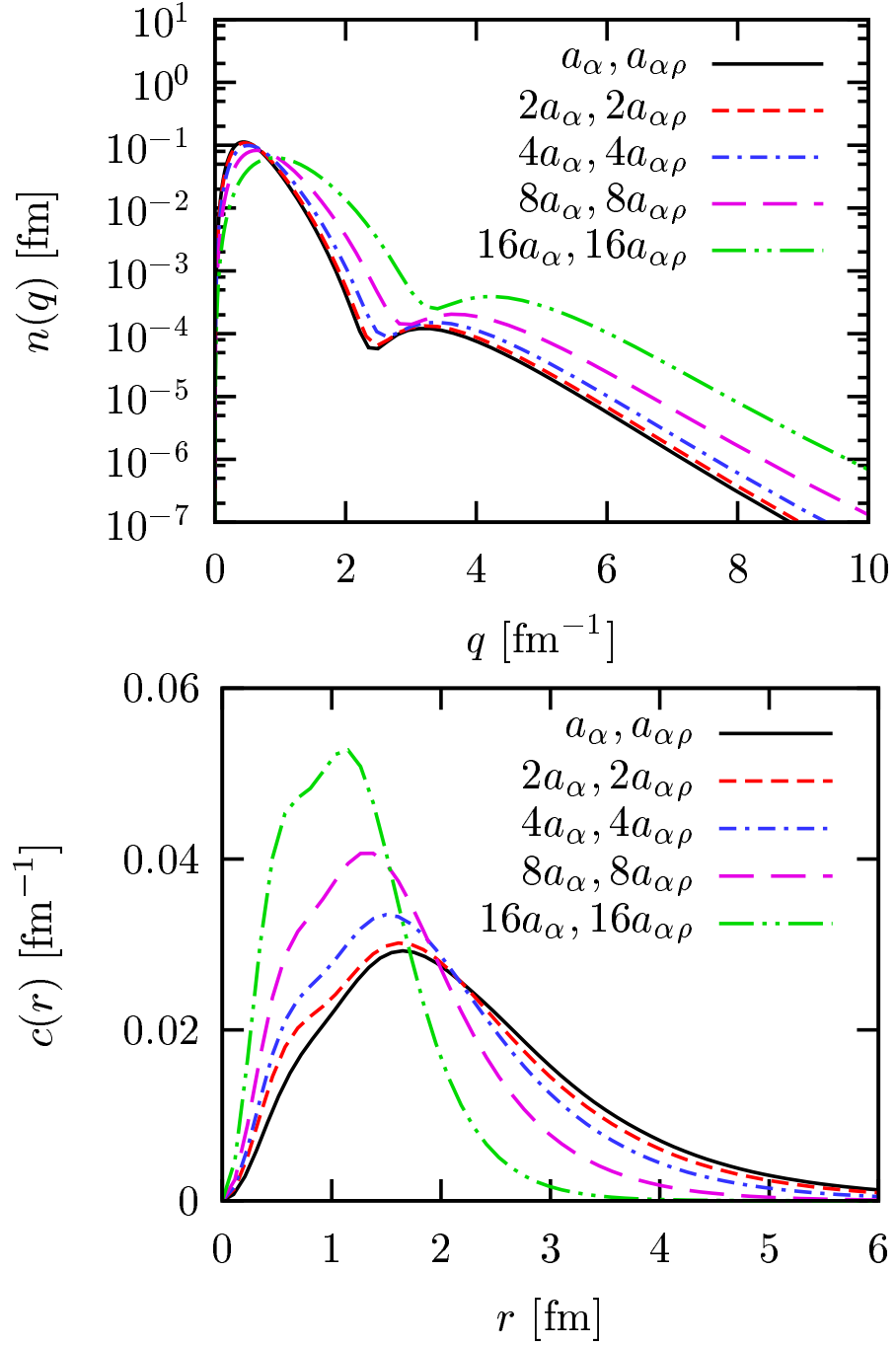


Figure 4.9: The calculated single particle momentum distribution $n(q)$ (upper panel) and two-body correlation function $c(r)$ (lower panel) as functions of the both attractive and repulsive coupling strength a_α and $a_{\alpha\rho}$ of the three-body force MT3-II with $a_\alpha = -2.69$ and $a_{\alpha\rho} = 2.40$.

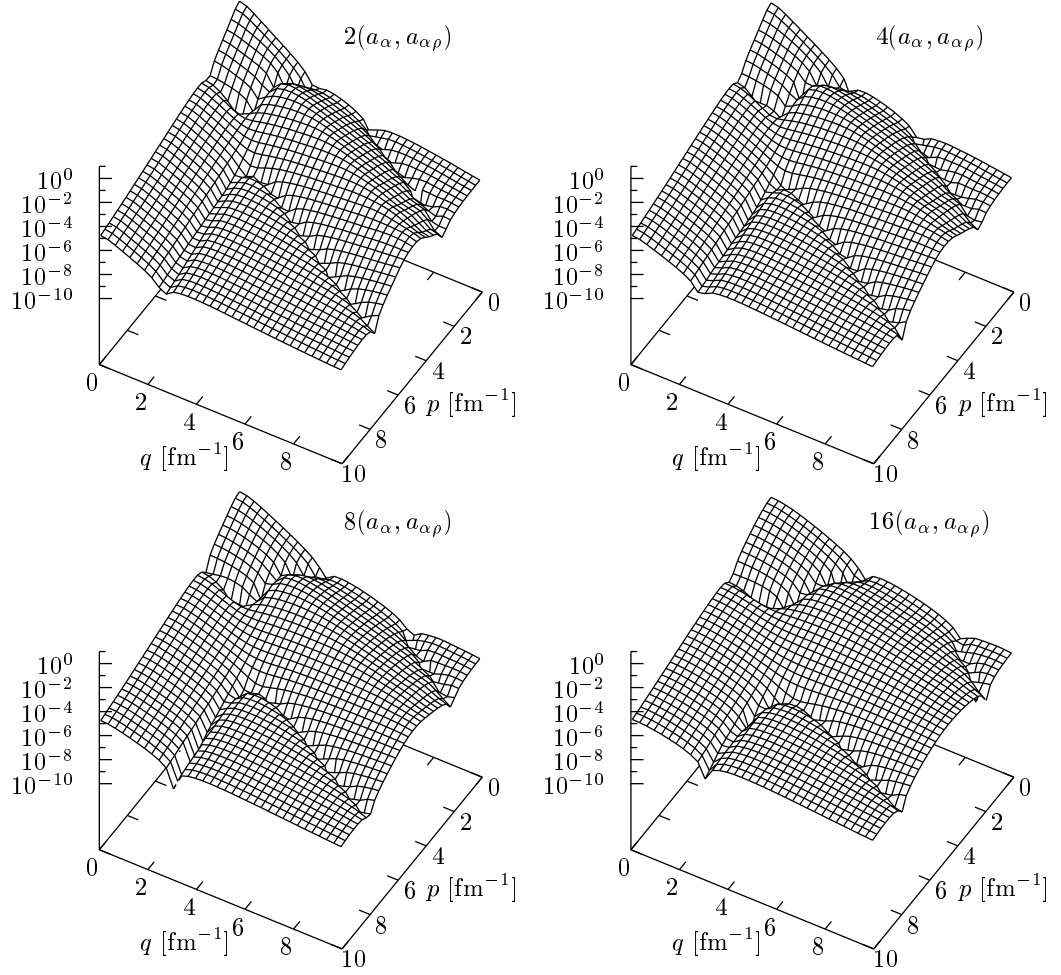


Figure 4.10: The calculated total wave function of three-body bound state $|\Psi(p, q, x)|$ in unit $[\text{fm}^3]$ at $x = 1$ as a function of the different meson-nucleon coupling strength a_α of the three-body force MT3-II. The upper left: $2a_\alpha, 2a_{\alpha\rho}$, the upper right: $4a_\alpha, 4a_{\alpha\rho}$, the lower left: $8a_\alpha, 8a_{\alpha\rho}$, the lower right: $16a_\alpha, 16a_{\alpha\rho}$.

	$g_\alpha^2/4\pi$	$m_\alpha[\text{MeV}]$	$\Lambda_\alpha[\text{MeV}]$	$a_\alpha[\text{MeV}^{-1}]$
MT3M-I	5.0000	305.8593	1000.0	-9.34

Table 4.20: The MT3M-I parameters.

$g_\alpha^2/4\pi$	$m_\alpha[\text{MeV}]$	$\Lambda_\alpha[\text{MeV}]$	a_α
5.0000	305.8593	1000.0	-26.96
$g_\rho^2/4\pi$	$m_\rho[\text{MeV}]$	$\Lambda_\rho[\text{MeV}]$	$a_{\alpha\rho}$
9.0000	650.0000	1900.0	23.30

Table 4.21: The MT3M-II parameters.

4.7 The Bound State with Three-Body Force Only

In previous sections the three-body forces MT3-I and MT3-II are studied together with two-body force MT2-II through bound state properties. Close to the realistic case, the two-body force MT2-II gives dominant contributions to bound state properties and three-body forces MT3-I and MT3-II give small corrections. An interesting question is that whether the short ranged three-body force of MT3-I or MT3-II type alone can generate a three-body bound state with the same binding energy of about -7.5 MeV as two-body force MT2-II does. Indeed this is possible. We consider four

Models	$\langle H_0 \rangle [\text{MeV}]$	$\langle V_{II} \rangle [\text{MeV}]$	$\langle V_{III} \rangle [\text{MeV}]$	$\langle H \rangle [\text{MeV}]$	$E [\text{MeV}]$
MT2-I	66.9672	-74.5475	-	-7.5803	-7.5801
MT2-II	28.6408	-36.3391	-	-7.6983	-7.6984
MT3M-I	280.6566	-	-288.2101	-7.5535	-7.5453
MT3M-II	135.3325	-	-142.9140	-7.5815	-7.5833

Table 4.22: The calculated expectation values of the kinetic energy $\langle H_0 \rangle$, the two-body potential $\langle V_{II} \rangle$, the three-body potential energy $\langle V_{III} \rangle$, the total hamiltonian $\langle H \rangle$ and the binding energy E as functions of different models.

different force models: two-body forces MT2-I without repulsive part and MT2-II with repulsive part, three-body forces MT3M-I without repulsive part and MT3M-II with repulsive part. The MT2-I and MT2-II is given in Eq. (4.31) and has parameters in Tables 4.1 and 4.2. Similarly, the three-body forces MT3M-I and MT3M-II have the same functional form and parameters as those of MT3-I and MT3-II respectively except that the coupling strength a_α and $a_{\alpha\rho}$ are readjusted as shown in Tables 4.20 and 4.21 to give three-body bound state with a binding energy around -7.5 MeV. Within this scenario all force models give same overall binding energy. We have an opportunity to distinguish the force characteristics more clearly through bound state properties, such as the distinctions between two-body and three-body forces, with and without repulsive core, etc. The calculated expectation values of the kinetic energy $\langle H_0 \rangle$, the two-body potential energy $\langle V_{II} \rangle$, the three-body potential energy $\langle V_{III} \rangle$, the total hamiltonian $\langle H \rangle$ and the total energy E as functions of different models are listed in Table 4.22, the momentum distributions and correlation functions calculated by the different force models are shown in Fig. 4.11. Clearly we see the major difference between two-body and three-body forces. In Table 4.22, it is found that three-body forces give much larger kinetic energies than two-body forces do. This is due to the short range character of the three-body forces. This is consistent with the larger amplitude at higher momenta in the momentum distribution and the peak position of correlation function shifts to smaller distance for three-body forces MT3M-I and MT3M-II, as shown in Fig 4.11. Another special feature of three-body forces is that the shape of the correlation functions is much narrower than that one obtained by two-body forces. Concerning the effects of the repulsive core, we find in Table 4.22 that MT2-II gives less kinetic energy than MT2-I. This is similar to the difference between MT3M-II and MT3M-I. The interpretation is that the repulsive core prevents particles coming too close to each other so that the peak positions in the correlation functions for forces with repulsive core is larger than the one from those obtained by the purely attractive forces. Consequently the amplitude in the higher momentum region obtained from the forces with repulsive core is a bit lower than the one obtained from attractive forces, as shown in Fig 4.11. The features of the repulsive core in bound state is more visible in the total wave function. The corresponding total

wave functions $\Psi(p, q, x)$ at $x = 1$ obtained from different force models are shown in Fig 4.12. It is found that only the forces with repulsive core lead to nodal lines in the total wave function. The pattern of these nodal lines is determined by the zero points in the forces with repulsive core. This is the reason why only forces with repulsive core generate a shoulder structures in the momentum distribution as shown in Fig. 4.11. Comparing the total wave functions given by MT2-II and by MT3M-II, we find the different nodal line style. This different styles also illustrate the distinction between two-body and three-body forces.

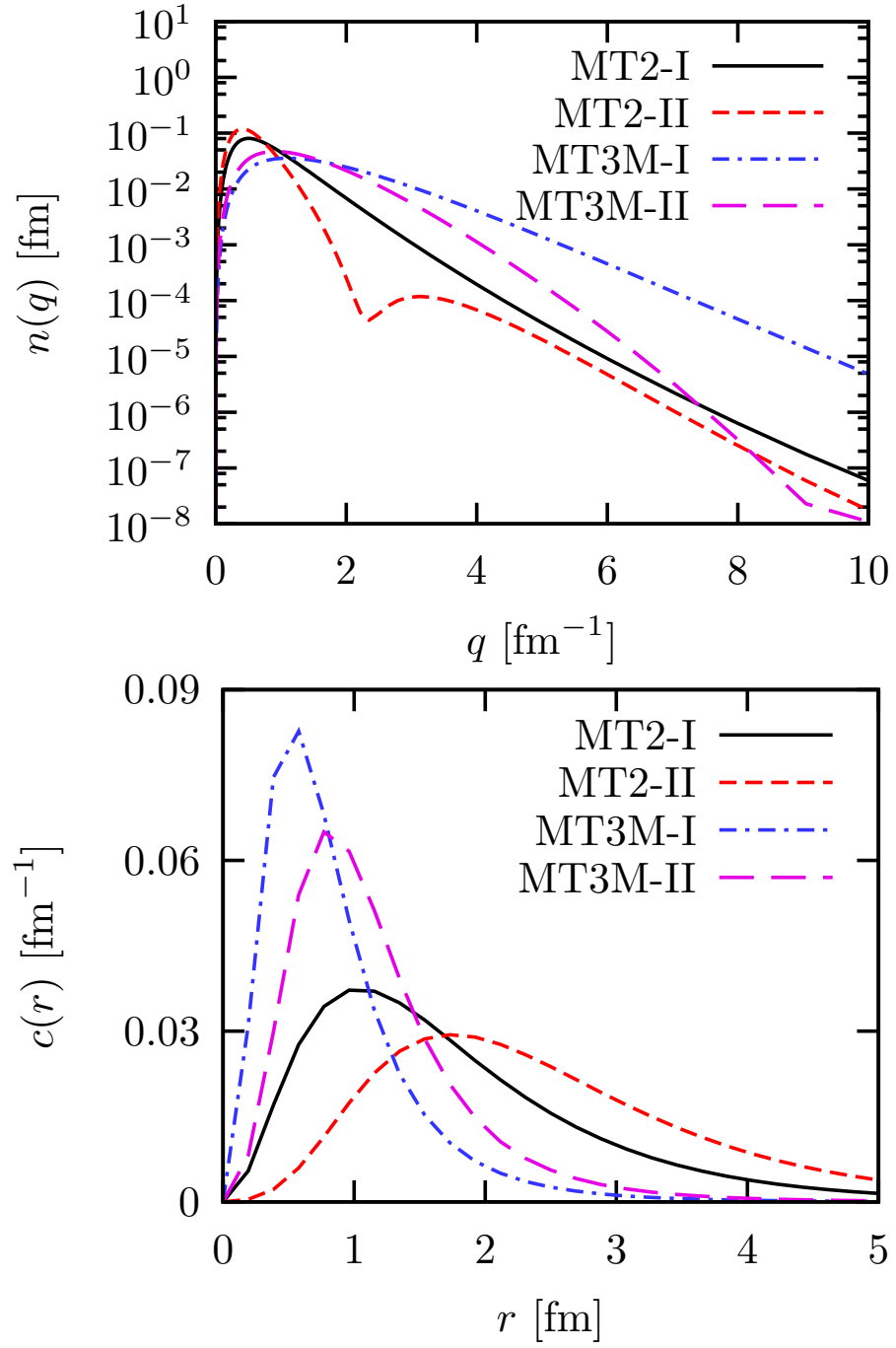


Figure 4.11: The calculated single particle momentum distribution $n(q)$ (upper panel) and two-body correlation function $c(r)$ (lower panel) as functions of different force models.

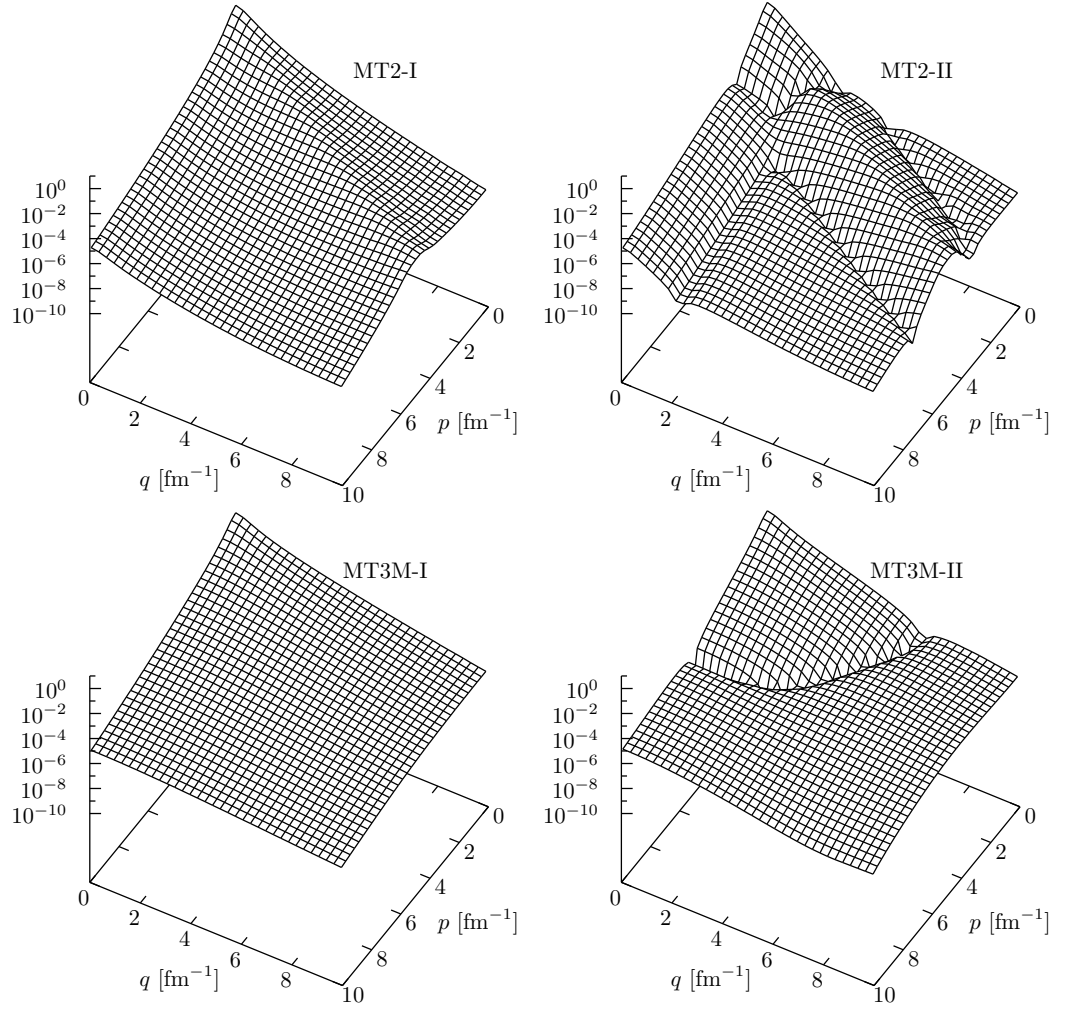


Figure 4.12: The calculated total wave function of three-body bound state $|\Psi(p, q, x)|$ in unit $[\text{fm}^3]$ at $x = 1$ as a function of the different force models.

$g_\alpha^2/4\pi$	$m_\alpha[\text{MeV}]$	$\Lambda_\alpha[\text{MeV}]$	a_α
5.0000	60.0	660	-1.90015

Table 4.23: The parameters of the purely attractive three-body force MMT3-I.

Model	$\langle H_0 \rangle$ (MeV)	$\langle V \rangle$ (MeV)	$\langle R \rangle$ (fm)	$\langle r \rangle$ (fm)	E (MeV)
MT2-I	66.967	-74.547	1.592	1.783	-7.5803
MMT3-I	67.306	-74.895	1.521	1.698	-7.5504

Table 4.24: The calculated eigenvalue E from the the solution of the Faddeev equation, the expectation values of the kinetic energy $\langle H_0 \rangle$, and the potential energy $\langle V \rangle$ for the two-body force MT2-I and the three-body force MMT3-I. Both forces give similar binding energies. The expectation values of $\langle R \rangle$ and $\langle r \rangle$ are also given for both cases.

4.8 The Interplay Between Two-Body and Three-Body Forces

Up to now we showed the difference between two-body and three-body forces. These differences are based on the fact that we took the exchanged meson masses and momentum cut-off parameters of MT3M-I and MT3M-II to be the same as those in MT3-I and MT3-II and readjusted the meson-nucleon coupling strength in MT3-I and MT3-II. We already showed in our model studies that the three-body force characteristics depend on the exchanged meson masses as well as the momentum cut-off parameters, the question is if it is possible to generate a three-body bound state by three-body force alone not only with the same binding energy as two-body force gives, but also with similar kinetic and potential energy to the ones given by two-body forces. For simplicity, we consider only attractive forces. Indeed this is possible if we use a pure attractive three-body force, called MMT3-I, with the same functional form as that of MT3-I and MT3M-I but the parameters in Table 4.23. This force MMT3-I alone can generate a three-body bound state with almost the same

kinetic and potential energy as those generated by MT2-I as shown in Table 4.24. The momentum distributions and correlation functions given by MMT3-I and MT2-I looks quite similar as shown in Fig. 4.13. From this we conclude that bound state properties are not enough to distinguish the mechanisms of two-body and three-body forces if no further physical restrictions are imposed on the exchanged meson mass and momentum cut-off parameters of the three-body forces. This implies the bound state properties alone can not distinguish potentials.

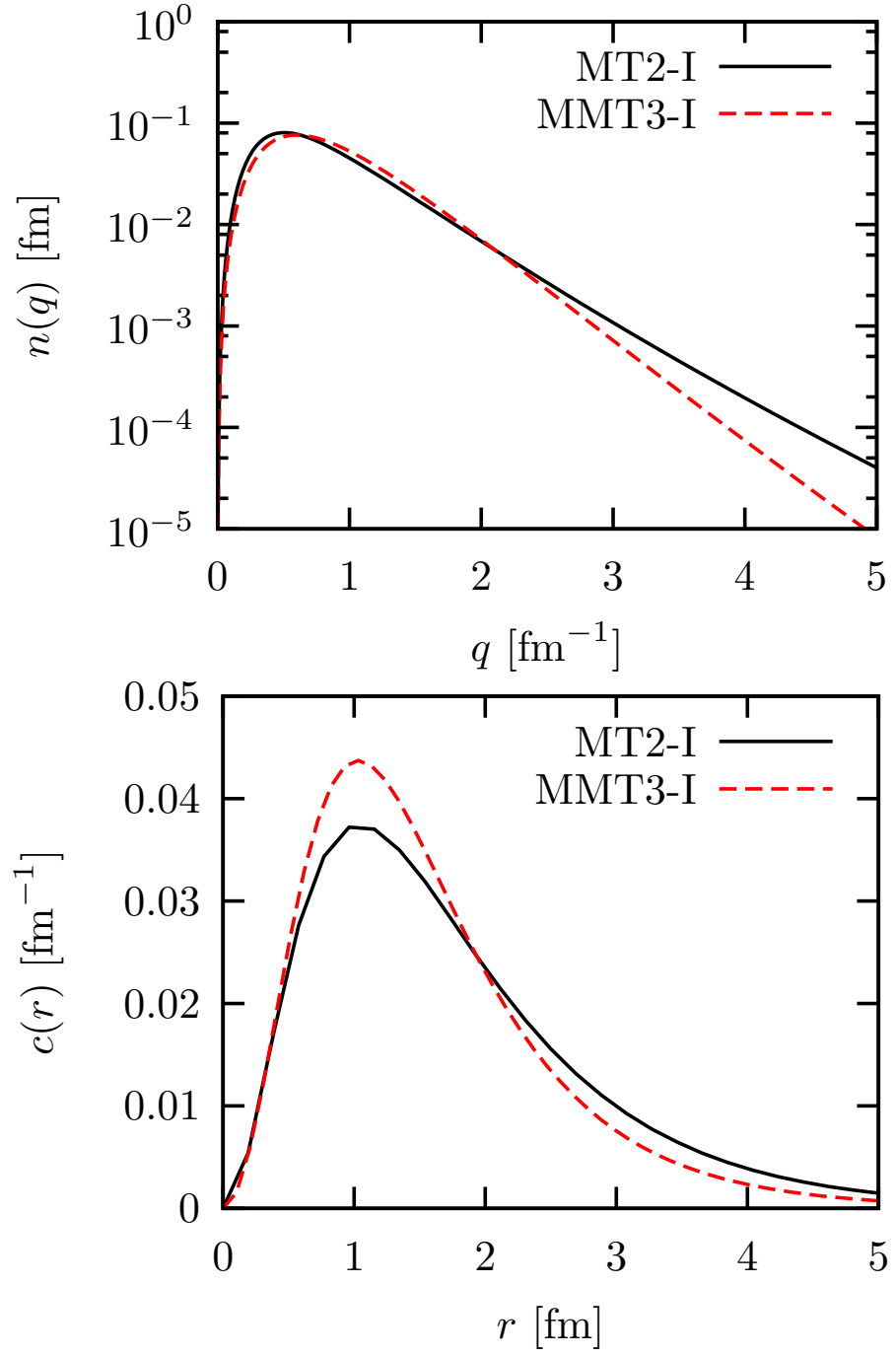


Figure 4.13: The calculated single particle momentum distribution $n(q)$ (upper panel) and two-body correlation function $c(r)$ (lower panel) as functions of different force models: MT2-I and MMT3-I.

4.9 Summary

In this chapter, we derived and calculated the Faddeev equation for three identical bosons interacting by two-body and three-body forces. The equation is formulated in momentum space directly in terms of momentum vectors, i.e. without angular momentum decomposition. The Faddeev equation is solved by iteration using a Lanczo's type method. An accuracy of 5 digits in the energy eigenvalue can easily be achieved. This approach avoids the very involved angular momentum algebra which is usually inherent in the partial wave decomposition of three-body forces.

All two-body and three-body forces we employ are scalar and of meson-exchange type, either purely attractive or attractive and repulsive. The two-body force is of a modified Malfliet-Tjon type, the three-body force is of a Fujita-Miyazawa type. For these forces we evaluated the single nucleon momentum distributions and the two-body correlation functions. These quantities turn out to be qualitatively very similar to those obtained with realistic spin dependent forces. We also evaluated the expectation values $\langle r \rangle$ for a pair distance and $\langle R \rangle$ for the distance of a third particle to the c.m. of the corresponding pair. In the case of an equilateral triangle the ratio of these two quantities is $2/\sqrt{3}$. Since we have three identical bosons the position of the three particles in the ground state should be at the corners of an equilateral triangle. Indeed the corresponding ratio for the expectation values $\langle r \rangle$ and $\langle R \rangle$ turned out to be $2/\sqrt{3}$ with a numerical error of about 1-2%.

We also do an excursion into a playground with forces by changing the three-body force parameters, and extract the information about how the three-body bound state properties depend on three-body forces. We find that the three-body force we considered is of short range and it mainly influences the high momentum components in three-body bound state. We also study how the three-body bound state with three-body force only behaves and how the two-body and three-body force interplay in this scenario.

Chapter 5

Analytical and Numerical Techniques

In this chapter the necessary analytical and numerical techniques used in this work are described. The cubic spline based interpolation method for multi-dimensional interpolations is briefly reviewed. The spline based integration methods are introduced, especially the one for treating the integration with logarithmic singularity. The Padé method for solving the inhomogeneous equation of the three-body scattering amplitude and the iterative method of Lanczos type for solving the homogeneous eigenvalue equation of the three-body bound state are presented with numerical demonstration.

5.1 Spline Based Interpolation and Integration

5.1.1 The Cubic Splines Interpolation

The cubic spline interpolation was introduced in Ref. [61]. For completeness the essential steps are explicitly given here, since we need these expressions to introduce the spline based integration later on.

Consider a function $f(x)$ given at certain grid points x_i , $i = 1, \dots, n$. Assume the x is in the interval $[x_i, x_{i+1}]$. For the sake of simple notation we use $x_i \equiv x_1$ and

$x_{i+1} \equiv x_2$. A unique cubic polynomial $f_i(x)$ for $x \in [x_1, x_2]$ can be defined as

$$f_i(x) = f(x_1)\phi_1(x) + f(x_2)\phi_2(x) + f'(x_1)\phi_3(x) + f'(x_2)\phi_4(x). \quad (5.1)$$

In terms of the spline functions, one obtains

$$\begin{aligned} \phi_1(x) &= \frac{(x_2 - x)^2}{(x_2 - x_1)^3} [(x_2 - x_1) + 2(x - x_1)], \\ \phi_2(x) &= \frac{(x_1 - x)^2}{(x_2 - x_1)^3} [(x_2 - x_1) + 2(x_2 - x)], \\ \phi_3(x) &= \frac{(x - x_1)(x_2 - x)^2}{(x_2 - x_1)^2}, \\ \phi_4(x) &= \frac{(x - x_1)^2(x - x_2)}{(x_2 - x_1)^2} \end{aligned} \quad (5.2)$$

with following constraints:

$$\begin{aligned} f_i(x_1) &= f(x_1), \\ f_i(x_2) &= f(x_2), \\ f'_i(x_1) &= f'(x_1), \\ f'_i(x_2) &= f'(x_2). \end{aligned} \quad (5.3)$$

Therefore the interpolating function $f_i(x)$ and their derivatives $f'_i(x)$ are continuous at the grid points x_i . We approximate the derivatives $f'(x_1)$ and $f'(x_2)$ with the help of quadratic polynomial, which is uniquely defined by the function values at a grid point and its two neighbors. Using $x_{i-1} \equiv x_0$ and $x_{i+2} \equiv x_3$, one has

$$\begin{aligned} f'(x_1) &\approx f(x_2) \frac{x_1 - x_0}{x_2 - x_1} \frac{1}{x_2 - x_0} - f(x_0) \frac{x_2 - x_1}{x_1 - x_0} \frac{1}{x_2 - x_0} \\ &\quad + f(x_1) \left(\frac{x_2 - x_1}{x_1 - x_0} - \frac{x_1 - x_0}{x_2 - x_1} \right) \frac{1}{x_2 - x_0}, \\ f'(x_2) &\approx f(x_3) \frac{x_2 - x_1}{x_3 - x_2} \frac{1}{x_3 - x_1} - f(x_1) \frac{x_3 - x_2}{x_2 - x_1} \frac{1}{x_3 - x_1} \\ &\quad + f(x_2) \left(\frac{x_3 - x_2}{x_2 - x_1} - \frac{x_2 - x_1}{x_3 - x_2} \right) \frac{1}{x_3 - x_1}. \end{aligned} \quad (5.4)$$

At the end points x_1 and x_n we define the quadratic polynomial by $f(x_1)$, $f(x_2)$ and $f(x_3)$ and by $f(x_{n-2})$, $f(x_{n-1})$ and $f(x_n)$ respectively. This is done by putting

$x_0 = x_3$ in the first case and $x_3 = x_{n-2}$ in the second case. Then the interpolating function in the i -th interval of the grid can be written as

$$f_i(x) = \sum_{j=0}^3 S_j(x) f(x_j) \quad (5.5)$$

where the $S_j(x)$ are the modified spline functions

$$\begin{aligned} S_0(x) &= -\phi_3(x) \frac{x_2 - x_1}{x_1 - x_0} \frac{1}{x_2 - x_0}, \\ S_1(x) &= \phi_1(x) + \phi_3 \left(\frac{x_2 - x_1}{x_1 - x_0} - \frac{x_1 - x_0}{x_2 - x_1} \right) \frac{1}{x_2 - x_0} - \phi_4(x) \frac{x_3 - x_2}{x_2 - x_1} \frac{1}{x_3 - x_1}, \\ S_2(x) &= \phi_2(x) + \phi_3 \frac{x_1 - x_0}{x_2 - x_1} \frac{1}{x_2 - x_0} + \phi_4(x) \left(\frac{x_3 - x_2}{x_2 - x_1} - \frac{x_2 - x_1}{x_3 - x_2} \right) \frac{1}{x_3 - x_1}, \\ S_3(x) &= \phi_4(x) \frac{x_2 - x_1}{x_3 - x_2} \frac{1}{x_3 - x_1}. \end{aligned} \quad (5.6)$$

The Eq. (5.5) is the cubic spline interpolation for one variable function, it can be naturally extended to an interpolation for multi-variable function. In our work we need to do two, three and five dimensional interpolations. For the two-dimensional case, one has

$$f_{ij}(x, y) = \sum_{i=0}^3 \sum_{j=0}^3 S_i(x) S_j(y) f(x_i, y_j), \quad (5.7)$$

for the three-dimensional case, one has

$$f_{ijk}(x, y, z) = \sum_{i=0}^3 \sum_{j=0}^3 \sum_{k=0}^3 S_i(x) S_j(y) S_k(z) f(x_i, y_j, z_k), \quad (5.8)$$

and for the five-dimensional case, one has

$$\begin{aligned} f_{ijklm}(x, y, z, u, v) = \\ \sum_{i=0}^3 \sum_{j=0}^3 \sum_{k=0}^3 \sum_{l=0}^3 \sum_{m=0}^3 S_i(x) S_j(y) S_k(z) S_l(u) S_m(v) f(x_i, y_j, z_k, u_l, v_m). \end{aligned} \quad (5.9)$$

For Eqs. (5.5), (5.7), (5.8) and (5.9), the r.h.s are already known function values and the modified spline functions on a given grid, the l.h.s are their approximate function values obtained by the cubic spline interpolation.

5.1.2 The Integration with Logarithmic Singularity

We consider the integration of $\int_b^a f(x) \ln |x-q| dx$ for $a < q < b$. The integrand has logarithmic singularity at $x = q$. Since a function $f(x)$ can be approximated by cubic splines piece by piece and each piece is a cubic polynomial $S_i(x)$ in Eq. (5.6), we want to evaluate this integration based on the spline function because $\int_b^a S_i(x) \ln |x-q| dx$ can be carried out analytically on each piece of cubic splines. In addition we also consider the integration of $\int_b^a dx f(x)$ type, because this will be useful for the cases when Gaussian quadrature is not applicable.

For $f(x)$, one can approximate it by cubic splines. Thus for $\int_b^a dx f(x)$ one has

$$\begin{aligned}
 I &= \int_b^a f(x) dx = \left(\int_{x_1}^{x_2} + \int_{x_2}^{x_3} + \dots + \int_{x_{n-1}}^{x_n} \right) f(x) dx \\
 &= \sum_{i=1}^{n-1} \int_{x_i}^{x_{i+1}} f(x) dx = \sum_{i=1}^{n-1} \int_{x_i}^{x_{i+1}} \left(\sum_{j=0}^3 S_j(x) f(x_j) \right) dx \\
 &= \sum_{i=1}^{n-1} \left(\sum_{j=0}^3 f(x_j) \int_{x_i}^{x_{i+1}} S_j(x) dx \right). \tag{5.10}
 \end{aligned}$$

if the function $f(x)$ is given on the grid point x_i , $i = 1, \dots, n$. So the integration on each interval indeed is over the spline functions in Eq. (5.2). On the i -th interval $[x_i, x_{i+1}]$, straightforwardly one has

$$\begin{aligned}
 \bar{\phi}_1 &= \int_{x_i}^{x_{i+1}} \phi_1(x) dx = \frac{x_{i+1} - x_i}{2}, \\
 \bar{\phi}_2 &= \int_{x_i}^{x_{i+1}} \phi_2(x) dx = \frac{x_{i+1} - x_i}{2}, \\
 \bar{\phi}_3 &= \int_{x_i}^{x_{i+1}} \phi_3(x) dx = \frac{(x_{i+1} - x_i)^2}{12}, \\
 \bar{\phi}_4 &= \int_{x_i}^{x_{i+1}} \phi_4(x) dx = -\frac{(x_{i+1} - x_i)^2}{12}. \tag{5.11}
 \end{aligned}$$

Then the integrations of modified spline functions S 's in Eq. (5.6) on the i -th interval $[x_{i+1}, x_i]$ are

$$\begin{aligned}
 \bar{S}_0 &= \int_{x_i}^{x_{i+1}} S_0(x) dx = -\bar{\phi}_3 \frac{x_{i+1} - x_i}{x_i - x_{i-1}} \frac{1}{x_{i+1} - x_{i-1}}, \\
 \bar{S}_1 &= \int_{x_i}^{x_{i+1}} S_1(x) dx = \bar{\phi}_1
 \end{aligned}$$

$$\begin{aligned}
& + \bar{\phi}_3 \left(\frac{x_{i+1} - x_i}{x_i - x_{i-1}} - \frac{x_i - x_{i-1}}{x_{i+1} - x_i} \right) \frac{1}{x_{i+1} - x_{i-1}} \\
& - \bar{\phi}_4 \frac{x_{i+2} - x_{i+1}}{x_{i+1} - x_i} \frac{1}{x_{i+2} - x_i}, \\
\bar{S}_2 = \int_{x_i}^{x_{i+1}} S_2(x) dx &= \bar{\phi}_2 \\
& + \bar{\phi}_3 \frac{x_i - x_{i-1}}{x_{i+1} - x_i} \frac{1}{x_{i+1} - x_{i-1}} \\
& + \bar{\phi}_4 \left(\frac{x_{i+2} - x_{i+1}}{x_{i+1} - x_i} - \frac{x_{i+1} - x_i}{x_{i+2} - x_{i+1}} \right) \frac{1}{x_{i+2} - x_i}, \\
\bar{S}_3 = \int_{x_i}^{x_{i+1}} S_3(x) dx &= \bar{\phi}_4 \frac{x_{i+1} - x_i}{x_{i+2} - x_{i+1}} \frac{1}{x_{i+2} - x_i}.
\end{aligned} \tag{5.12}$$

The integration $\int_b^a f(x)dx$ is thus given as

$$I = \int_b^a f(x)dx = \sum_{i=1}^{n-1} \left(\sum_{j=0}^3 f(x_j) \bar{S}_j \right). \tag{5.13}$$

The integration method in Eq. (5.13) is an important alternative way when the Gaussian quadrature and other methods are not applicable if the integrand is very rapidly varying. For example, the Fourier transformation which involves in the integration like $\int f(r, q) \sin(rq)$, where the Gaussian quadrature does not work since the integrand is a periodic function. Indeed the so called Filon methods used to calculate the Fourier transform stands on the same idea but using Lagrangian polynomials to replace the cubic splines [64].

Now consider the integration $I = \int_a^b f(x) \ln|x - q|dx$ when $f(x)$ is given on a set of grid points. The $f(x)$ can be reconstructed by cubic splines, then the whole integration I can be evaluated piece by piece. We need the following integral:

$$\begin{aligned}
\bar{\phi}_1 &= \int_{x_i}^{x_{i+1}} \phi_1 \ln|x - q|dx, \\
\bar{\phi}_2 &= \int_{x_i}^{x_{i+1}} \phi_2 \ln|x - q|dx, \\
\bar{\phi}_3 &= \int_{x_i}^{x_{i+1}} \phi_3 \ln|x - q|dx, \\
\bar{\phi}_4 &= \int_{x_i}^{x_{i+1}} \phi_4 \ln|x - q|dx.
\end{aligned} \tag{5.14}$$

Because the spline functions are polynomials of third order in x , we start out from the analytical results of following integration [65]

$$\begin{aligned}
\int \ln(a + bx) &= \left(x + \frac{a}{b}\right) \ln(a + bx) - x, \\
\int x \ln(a + bx) &= \frac{1}{2} \left(x^2 - \frac{a^2}{b^2}\right) \ln(a + bx) - \frac{1}{2} \left(\frac{x^2}{2} - \frac{ax}{b}\right), \\
\int x^2 \ln(a + bx) &= \frac{1}{3} \left(x^3 + \frac{a^3}{b^3}\right) \ln(a + bx) - \frac{1}{3} \left(\frac{x^3}{3} - \frac{ax^2}{2b} + \frac{a^2x}{b^2}\right), \\
\int x^3 \ln(a + bx) &= \frac{1}{4} \left(x^4 - \frac{a^4}{b^4}\right) \ln(a + bx) - \frac{1}{4} \left(\frac{x^4}{4} - \frac{ax^3}{3b} + \frac{a^2x^2}{2b^2} - \frac{a^3x}{b^3}\right).
\end{aligned} \tag{5.15}$$

There are five different cases for the integration on each interval, determined by the position of q , i.e. $q < x_i < x_{i+1}$, $q = x_i < x_{i+1}$, $x_i < q < x_{i+1}$, $x_i < q = x_{i+1}$ and $x_i < x_{i+1} < q$. For $\bar{\phi}_1$, one has

- When $q < x_i < x_{i+1}$

$$\begin{aligned}
\bar{\phi}_1 &= \bar{\phi}_1^{(0)} = \int_{x_i}^{x_{i+1}} \left(1 - \frac{3(x - x_i)^2}{(x_{i+1} - x_i)^2} + \frac{2(x - x_i)^3}{(x_{i+1} - x_i)^3}\right) \ln|x - q| dx \\
&= \int_{x_i}^{x_{i+1}} \left(1 - \frac{3(x - x_i)^2}{(x_{i+1} - x_i)^2} + \frac{2(x - x_i)^3}{(x_{i+1} - x_i)^3}\right) \ln(x - q) dx \\
&= C_1 + C_2 \ln(x_i - q) + C_3 \ln(x_{i+1} - q)
\end{aligned} \tag{5.16}$$

with

$$\begin{aligned}
C_1 &= \frac{1}{24(x_{i+1} - x_i)^2} [-12q^3 + 18q^2(x_{i+1} + x_i) + 4q(2x_i^2 - 13x_{i+1}x_i + 2x_{i+1}^2) \\
&\quad + 5x_i^3 - 23x_i^2x_{i+1} + 49x_ix_{i+1}^2 - 19x_{i+1}^3] \\
C_2 &= \frac{-(x_i - q)}{2(x_{i+1} - x_i)^3} [q^3 - q^2(2x_{i+1} + x_i) + qx_i(4x_{i+1} - x_i) \\
&\quad + (-x_i^3 + 4x_i^2x_{i+1} - 6x_ix_{i+1}^2 + 2x_{i+1}^3)] \\
C_3 &= \frac{(x_{i+1} - q)^3}{2(x_{i+1} - x_i)^3} [q - 2x_i + x_{i+1}]
\end{aligned} \tag{5.17}$$

- When $q = x_i < x_{i+1}$

$$\bar{\phi}_1 = \bar{\phi}_1^{(1)} = \int_q^{x_{i+1}} \left(1 - \frac{3(x - x_i)^2}{(x_{i+1} - x_i)^2} + \frac{2(x - x_i)^3}{(x_{i+1} - x_i)^3}\right) \ln|x - q| dx$$

$$= \lim_{x_i \rightarrow q} \bar{\phi}_1^{(0)} = \frac{1}{24}(x_{i+1} - q)(-19 + 12 \ln(x_{i+1} - q)) \quad (5.18)$$

- When $x_i < q < x_{i+1}$

$$\begin{aligned} \bar{\phi}_1 &= \bar{\phi}_1^{(2)} = \int_{x_i}^{x_{i+1}} \left(1 - \frac{3(x - x_i)^2}{(x_{i+1} - x_i)^2} + \frac{2(x - x_i)^3}{(x_{i+1} - x_i)^3} \right) \ln |x - q| dx \\ &= \int_{x_i}^{q-\varepsilon} \left(1 - \frac{3(x - x_i)^2}{(x_{i+1} - x_i)^2} + \frac{2(x - x_i)^3}{(x_{i+1} - x_i)^3} \right) \ln(q - x) dx \\ &\quad + \int_{q+\varepsilon}^{x_{i+1}} \left(1 - \frac{3(x - x_i)^2}{(x_{i+1} - x_i)^2} + \frac{2(x - x_i)^3}{(x_{i+1} - x_i)^3} \right) \ln(x - q) dx \\ &= C_1 + C_2 \ln(q - x_i) + C_3 \ln(x_{i+1} - q) \end{aligned} \quad (5.19)$$

where the C_1 , C_2 and C_3 here are the same as those in Eq. (5.17).

- When $x_i < q = x_{i+1}$

$$\begin{aligned} \bar{\phi}_1 &= \bar{\phi}_1^{(3)} = \int_{x_i}^q \left(1 - \frac{3(x - x_i)^2}{(x_{i+1} - x_i)^2} + \frac{2(x - x_i)^3}{(x_{i+1} - x_i)^3} \right) \ln |x - q| dx \\ &= \lim_{x_{i+1} \rightarrow q} \bar{\phi}_1^{(2)} = \frac{1}{24}(q - x_i)(-5 + 12 \ln(q - x_i)) \end{aligned} \quad (5.20)$$

- When $x_i < x_{i+1} < q$

$$\begin{aligned} \bar{\phi}_1 &= \bar{\phi}_1^{(4)} = \int_{x_i}^{x_{i+1}} \left(1 - \frac{3(x - x_i)^2}{(x_{i+1} - x_i)^2} + \frac{2(x - x_i)^3}{(x_{i+1} - x_i)^3} \right) \ln |x - q| dx \\ &= \int_{x_i}^{x_{i+1}} \left(1 - \frac{3(x - x_i)^2}{(x_{i+1} - x_i)^2} + \frac{2(x - x_i)^3}{(x_{i+1} - x_i)^3} \right) \ln(q - x) dx \\ &= C_1 + C_2 \ln(q - x_i) + C_3 \ln(q - x_{i+1}) \end{aligned} \quad (5.21)$$

where the C_1 , C_2 and C_3 here are the same as those in Eq. (5.17).

For $\bar{\phi}_2$, in general one can reformulate it as

$$\bar{\phi}_2 = \int_{x_i}^{x_{i+1}} \ln |x - q| - \bar{\phi}_1 \quad (5.22)$$

Thus for the different cases we have

- When $q < x_i < x_{i+1}$

$$\begin{aligned}\bar{\phi}_2 &= \bar{\phi}_2^{(0)} \\ &= (x_{i+1} - q) \ln(x_{i+1} - q) - (x_i - q) \ln(x_i - q) - (x_{i+1} - x_i) - \phi_1^{(0)}\end{aligned}\quad (5.23)$$

- When $q = x_i < x_{i+1}$

$$\begin{aligned}\bar{\phi}_2 &= \bar{\phi}_2^{(1)} = (x_{i+1} - q)(\ln(x_{i+1} - q) - 1) - \phi_1^{(1)} \\ &= \frac{1}{24}(x_{i+1} - q)(-5 + 12 \ln(x_{i+1} - q))\end{aligned}\quad (5.24)$$

- When $x_i < q < x_{i+1}$

$$\begin{aligned}\bar{\phi}_2 &= \bar{\phi}_2^{(2)} \\ &= (x_{i+1} - q) \ln(x_{i+1} - q) - (x_i - q) \ln(q - x_i) - (x_{i+1} - x_i) - \phi_1^{(2)}\end{aligned}\quad (5.25)$$

- When $x_i < q = x_{i+1}$

$$\begin{aligned}\bar{\phi}_2 &= \bar{\phi}_2^{(3)} = -(x_i - q)(\ln(q - x_i) - 1) - \phi_1^{(3)} \\ &= -\frac{1}{24}(x_i - q)(-19 + 12 \ln(q - x_i))\end{aligned}\quad (5.26)$$

- When $x_i < x_{i+1} < q$

$$\begin{aligned}\bar{\phi}_2 &= \bar{\phi}_2^{(4)} \\ &= (x_{i+1} - q) \ln(q - x_{i+1}) - (x_i - q) \ln(q - x_i) - (x_{i+1} - x_i) - \phi_1^{(4)}\end{aligned}\quad (5.27)$$

For $\bar{\phi}_3$, we have

- When $q < x_i < x_{i+1}$

$$\begin{aligned}\bar{\phi}_3 &= \bar{\phi}_3^{(0)} = \int_{x_i}^{x_{i+1}} \left((x - x_i) - \frac{2(x - x_i)^2}{(x_{i+1} - x_i)} + \frac{(x - x_i)^3}{(x_{i+1} - x_i)^2} \right) \ln |x - q| dx \\ &= \int_{x_i}^{x_{i+1}} \left((x - x_i) - \frac{2(x - x_i)^2}{(x_{i+1} - x_i)} + \frac{(x - x_i)^3}{(x_{i+1} - x_i)^2} \right) \ln(x - q) dx \\ &= C_1 + C_2 \ln(x_i - q) + C_3 \ln(x_{i+1} - q)\end{aligned}\quad (5.28)$$

with

$$\begin{aligned}
C_1 &= \frac{1}{144(x_{i+1} - x_i)} [-36q^3 + 6q^2(13x_{i+1} + 5x_i) + 12q(x_i^2 - 7x_{i+1}x_i - 3x_{i+1}^2) \\
&\quad + 7x_i^3 - 33x_i^2x_{i+1} + 75x_ix_{i+1}^2 - 13x_{i+1}^3], \\
C_2 &= \frac{(x_i - q)^2}{12(x_{i+1} - x_i)} [3q^2 + x_i^2 + 2q(-4x_{i+1} + x_i) - 4x_ix_{i+1} + 6x_{i+1}^2], \\
C_3 &= \frac{(x_{i+1} - q)^3}{12(x_{i+1} - x_i)} [3q - 4x_i + x_{i+1}]
\end{aligned} \tag{5.29}$$

- When $q = x_i < x_{i+1}$

$$\begin{aligned}
\bar{\phi}_3 &= \bar{\phi}_3^{(1)} = \int_q^{x_{i+1}} \left((x - x_i) - \frac{2(x - x_i)^2}{(x_{i+1} - x_i)} + \frac{(x - x_i)^3}{(x_{i+1} - x_i)^2} \right) \ln |x - q| dx \\
&= \lim_{x_i \rightarrow q} \bar{\phi}_3^{(0)} = \frac{1}{144} (x_{i+1} - q)^2 (-13 + 12 \ln(x_{i+1} - q))
\end{aligned} \tag{5.30}$$

- When $x_i < q < x_{i+1}$

$$\begin{aligned}
\bar{\phi}_3 &= \bar{\phi}_3^{(2)} = \int_{x_i}^{x_{i+1}} \left((x - x_i) - \frac{2(x - x_i)^2}{(x_{i+1} - x_i)} + \frac{(x - x_i)^3}{(x_{i+1} - x_i)^2} \right) \ln |x - q| dx \\
&= \int_{x_i}^{q-\varepsilon} \left((x - x_i) - \frac{2(x - x_i)^2}{(x_{i+1} - x_i)} + \frac{(x - x_i)^3}{(x_{i+1} - x_i)^2} \right) \ln(q - x) dx \\
&\quad + \int_{q+\varepsilon}^{x_{i+1}} \left((x - x_i) - \frac{2(x - x_i)^2}{(x_{i+1} - x_i)} + \frac{(x - x_i)^3}{(x_{i+1} - x_i)^2} \right) \ln(x - q) dx \\
&= C_1 + C_2 \ln(q - x_i) + C_3 \ln(x_{i+1} - q)
\end{aligned} \tag{5.31}$$

where the C_1 , C_2 and C_3 here are the same as those in Eq. (5.29).

- When $x_i < q = x_{i+1}$

$$\begin{aligned}
\bar{\phi}_3 &= \bar{\phi}_3^{(3)} = \int_{x_i}^q \left((x - x_i) - \frac{2(x - x_i)^2}{(x_{i+1} - x_i)} + \frac{(x - x_i)^3}{(x_{i+1} - x_i)^2} \right) \ln |x - q| dx \\
&= \lim_{x_{i+1} \rightarrow q} \bar{\phi}_3^{(2)} = \frac{1}{144} (x_i - q)^2 (-7 + 12 \ln(q - x_i))
\end{aligned} \tag{5.32}$$

- When $x_i < x_{i+1} < q$

$$\begin{aligned}
\bar{\phi}_3 &= \bar{\phi}_3^{(4)} = \int_{x_i}^{x_{i+1}} \left((x - x_i) - \frac{2(x - x_i)^2}{(x_{i+1} - x_i)} + \frac{(x - x_i)^3}{(x_{i+1} - x_i)^2} \right) \ln |x - q| dx \\
&= \int_{x_i}^{x_{i+1}} \left((x - x_i) - \frac{2(x - x_i)^2}{(x_{i+1} - x_i)} + \frac{(x - x_i)^3}{(x_{i+1} - x_i)^2} \right) \ln(q - x) dx \\
&= C_1 + C_2 \ln(q - x_i) + C_3 \ln(q - x_{i+1})
\end{aligned} \tag{5.33}$$

where the C_1 , C_2 and C_3 here are the same as those in Eq. (5.29).

For $\bar{\phi}_4$, we have

- When $q < x_i < x_{i+1}$

$$\begin{aligned}
\bar{\phi}_4 &= \bar{\phi}_4^{(0)} = \int_{x_i}^{x_{i+1}} \left(-\frac{(x - x_i)^2}{(x_{i+1} - x_i)} + \frac{(x - x_i)^3}{(x_{i+1} - x_i)^2} \right) \ln |x - q| dx \\
&= \int_{x_i}^{x_{i+1}} \left(-\frac{(x - x_i)^2}{(x_{i+1} - x_i)} + \frac{(x - x_i)^3}{(x_{i+1} - x_i)^2} \right) \ln(x - q) dx \\
&= C_1 + C_2 \ln(x_i - q) + C_3 \ln(x_{i+1} - q)
\end{aligned} \tag{5.34}$$

with

$$\begin{aligned}
C_1 &= -\frac{1}{144(x_{i+1} - x_i)} \\
&\quad [36q^3 + 13x_i^3 - 6q^2(13x_i + 5x_{i+1})12q(3x_i^2 + 7x_i x_{i+1} - x_{i+1}^2) \\
&\quad - 75x_i^2 x_{i+1} + 33x_i x_{i+1}^2 - 7x_{i+1}^3 +], \\
C_2 &= -\frac{(x_{i+1} - q)^2}{12(x_{i+1} - x_i)^2} [3q^2 + 2q(-4x_i + x_{i+1}) + 6x_i^2 - 4x_i x_{i+1} + x_{i+1}^2], \\
C_3 &= -\frac{(x_i - q)^3}{12(x_{i+1} - x_i)^2} [3q - 4x_{i+1} + x_i].
\end{aligned} \tag{5.35}$$

- When $x_i = q < x_{i+1}$

$$\begin{aligned}
\bar{\phi}_4 &= \bar{\phi}_4^{(1)} = \int_q^{x_{i+1}} \left(-\frac{(x - x_i)^2}{(x_{i+1} - x_i)} + \frac{(x - x_i)^3}{(x_{i+1} - x_i)^2} \right) \ln |x - q| dx \\
&= \lim_{x_i \rightarrow q} \bar{\phi}_4^{(0)} = -\frac{1}{144} (x_{i+1} - q)^2 (-7 + 12 \ln(x_{i+1} - q))
\end{aligned} \tag{5.36}$$

- When $q < x_i < x_{i+1}$

$$\begin{aligned}
\bar{\phi}_4 &= \bar{\phi}_4^{(2)} = \int_{x_i}^{x_{i+1}} \left(-\frac{(x-x_i)^2}{(x_{i+1}-x_i)} + \frac{(x-x_i)^3}{(x_{i+1}-x_i)^2} \right) \ln|x-q|dx \\
&= \int_{x_i}^{q-\varepsilon} \left(-\frac{(x-x_i)^2}{(x_{i+1}-x_i)} + \frac{(x-x_i)^3}{(x_{i+1}-x_i)^2} \right) \ln(q-x)dx \\
&\quad + \int_{q+\varepsilon}^{x_{i+1}} \left(-\frac{(x-x_i)^2}{(x_{i+1}-x_i)} + \frac{(x-x_i)^3}{(x_{i+1}-x_i)^2} \right) \ln(x-q)dx \\
&= C_1 + C_2 \ln(q-x_i) + C_3 \ln(x_{i+1}-q)
\end{aligned} \tag{5.37}$$

where the C_1 , C_2 and C_3 here are the same as those in Eq. (5.35).

- When $x_i < q = x_{i+1}$

$$\begin{aligned}
\bar{\phi}_4 &= \bar{\phi}_4^{(3)} = \int_q^{x_{i+1}} \left(-\frac{(x-x_i)^2}{(x_{i+1}-x_i)} + \frac{(x-x_i)^3}{(x_{i+1}-x_i)^2} \right) \ln|x-q|dx \\
&= \lim_{x_{i+1} \rightarrow q} \bar{\phi}_4^{(2)} = -\frac{1}{144}(x_i-q)^2(-13+12\ln(q-x_i))
\end{aligned} \tag{5.38}$$

- When $x_i < x_{i+1}, q$

$$\begin{aligned}
\bar{\phi}_4 &= \bar{\phi}_4^{(4)} = \int_{x_i}^{x_{i+1}} \left(-\frac{(x-x_i)^2}{(x_{i+1}-x_i)} + \frac{(x-x_i)^3}{(x_{i+1}-x_i)^2} \right) \ln|x-q|dx \\
&= \int_{x_i}^{x_{i+1}} \left(-\frac{(x-x_i)^2}{(x_{i+1}-x_i)} + \frac{(x-x_i)^3}{(x_{i+1}-x_i)^2} \right) \ln(q-x)dx \\
&= C_1 + C_2 \ln(q-x_i) + C_3 \ln(q-x_{i+1})
\end{aligned} \tag{5.39}$$

where the C_1 , C_2 and C_3 here are the same as those in Eq. (5.35).

Then, the integrations of modified spline functions S 's over i -th interval $[x_{i+1}, x_i]$ are

$$\begin{aligned}
\bar{S}_0 &= \int_{x_i}^{x_{i+1}} S_0(x)dx = -\bar{\phi}_3 \frac{x_{i+1}-x_i}{x_i-x_{i-1}} \frac{1}{x_{i+1}-x_{i-1}}, \\
\bar{S}_1 &= \int_{x_i}^{x_{i+1}} S_1(x)dx = \bar{\phi}_1 \\
&\quad + \bar{\phi}_3 \left(\frac{x_{i+1}-x_i}{x_i-x_{i-1}} - \frac{x_i-x_{i-1}}{x_{i+1}-x_i} \right) \frac{1}{x_{i+1}-x_{i-1}} \\
&\quad - \bar{\phi}_4 \frac{x_{i+2}-x_{i+1}}{x_{i+1}-x_i} \frac{1}{x_{i+2}-x_i},
\end{aligned}$$

$$\begin{aligned}
\bar{S}_2 = \int_{x_i}^{x_{i+1}} S_2(x) dx &= \bar{\phi}_2 \\
&+ \bar{\phi}_3 \frac{x_i - x_{i-1}}{x_{i+1} - x_i} \frac{1}{x_{i+1} - x_{i-1}} \\
&+ \bar{\phi}_4 \left(\frac{x_{i+2} - x_{i+1}}{x_{i+1} - x_i} - \frac{x_{i+1} - x_i}{x_{i+2} - x_{i+1}} \right) \frac{1}{x_{i+2} - x_i}, \\
\bar{S}_3 = \int_{x_i}^{x_{i+1}} S_3(x) dx &= \bar{\phi}_4 \frac{x_{i+1} - x_i}{x_{i+2} - x_{i+1}} \frac{1}{x_{i+2} - x_i}.
\end{aligned} \tag{5.40}$$

Finally, the integration with logarithmic singularity $\int_b^a f(x) \ln |x - q| dx$ can be evaluated as

$$I = \int_b^a f(x) \ln |x - q| dx = \sum_{i=1}^{n-1} \left(\sum_{j=0}^3 f(x_j) \bar{S}_j \right). \tag{5.41}$$

The advantage of this method is that the integration over the singular $\ln |x - q|$ is treated analytically and therefore it yields better numerical accuracy. Another method is the usual Gaussian quadrature with subtraction method. Now we can have an accuracy test for both methods. Assume we have an integral

$$\int_b^a f(x) \ln |x - q| dx \tag{5.42}$$

which is singular at $x = q$ if $q \in [a, b]$. We take three integrand functions $f(x)$ as

$$\begin{aligned}
f(x) &= \sqrt{x}, \\
f(x) &= x^2, \\
f(x) &= x^4.
\end{aligned} \tag{5.43}$$

with $a = 100$, $b = 0$, $q = 50$, and $f(x)$ is given on a set of grid points with number of points NP = 30, 60, 90. Because the integration for every $f(x)$ has analytic solution, the accuracy of numerical method is measured by percentage error

$$\delta = \frac{|I - I'|}{I} \times 100 \tag{5.44}$$

where I is the analytic answer and I' is the numerical one. The results for each integrand are listed in Tables 5.1 to 5.3.

We find that in general the spline based method gives accurate results. We notice that the accuracy of spline based method shows strong dependence on the integrand

the grid structure. For $f(x) = \sqrt{x}$, the results by Gaussian quadrature is more accurate than those by spline based method, but the accuracy can be improved by increasing the number of grid points as we see in the Table. 5.1 . This is because all spline functions are smooth but \sqrt{x} has infinite derivative at $x = 0$, so it is hard for spline functions to capture the structure of \sqrt{x} near $x = 0$. This is important for our application of spline based integration in the three-body scattering calculation. As pointed out in Ref. [26], the transition operator \hat{T} for three-body scattering has such square root behavior when $q \rightarrow q_{max}$ from below at low energies. We have dense grid points of Gaussian type grid there to ensure accuracy.

For $f(x) = x^2$, spline based method gives results with much better accuracy than those given by Gaussian quadrature. This is because the integrand are the native terms in the spline polynomials and the logarithmic singularity is treated analytically. But from Table 5.2, we find that higher accuracy is obtained by less grid points for spline based method. This indicates an important fact that more grid points does not necessarily lead to more accurate results for the spline-based method when treating an integral with logarithmic singularity. This can be understood by the limited machine rounding error when evaluating the $\ln|x - q|$ if the grid points are too dense so that $(x - q)$ is too small. In the case of $(x - q)$ too small, it causes a big value and a small value to be operated arithmetically together. In the computer calculation, the small value can be rounded off and only the big value remaining is taken into account. When $(x - q)$ gets smaller and smaller due to more grid points, there are more operations involved. The increased number of operations might amplify the effects of such machine roundoff error [66]. This unwanted case should be avoided in the numerical calculation by setting up balanced accuracy considerations for each piece of the whole calculation. Because the Gaussian grid generated by our code takes the middle point of the integration interval as the important point and aggregates more grid points around it, so in our case more and more grid points are put around $\frac{b-a}{2} = 50$ with increased grid points. As shown in Table 5.2, the spline-based integration calculated on equal spacing grid gives much higher accuracy which is several magnitude better than that obtained on Gaussian grid.

In Table 5.3 for $f(x) = x^4$, the accuracy behaves very regularly. The spline based method on both Gaussian grid and equal spacing grid give a better accuracy than Gaussian quadrature does. The accuracy by all methods can be improved by having more grid points.

The issue here is that we should be careful and keep in mind that both the integrand property and the finite machine error should be taken into account when we evaluate the overall accuracy of the integration. The systematic test like those shown in the Tables 5.1 to 5.3 should be done if necessary. Indeed we did a lot of trials to determine the proper grid structure for spline-based integration in our three-body scattering calculation in order to get reasonable systematics of the accuracy as illustrated in Fig. 3.3.

NP	Gaussian	Spline(Gaussian grid)	Spline(equal spacing grid)
30	6.71×10^{-4}	1.01×10^{-2}	1.20×10^{-2}
60	8.84×10^{-5}	1.32×10^{-3}	4.40×10^{-3}
90	2.91×10^{-5}	3.92×10^{-4}	2.40×10^{-3}

Table 5.1: The percentage error of Gaussian quadrature and spline based method for the integration $\int_b^a f(x) \ln |x - q| dx$ when $f(x) = \sqrt{x}$ at different number of grid points. The calculations of spline based method are performed on both the Gaussian grid and usual equal spacing grid.

NP	Gaussian	Spline(Gaussian grid)	Spline(equal spacing grid)
30	9.50×10^{-4}	7.91×10^{-10}	4.54×10^{-11}
60	1.33×10^{-4}	7.72×10^{-8}	5.73×10^{-10}
90	4.74×10^{-5}	3.38×10^{-6}	1.80×10^{-9}

Table 5.2: The percentage error of Gaussian quadrature and spline based method for the integration $\int_b^a f(x) \ln |x - q| dx$ when $f(x) = x^2$ at different number of grid points. The calculations of spline based method are performed on both the Gaussian grid and usual equal spacing grid.

NP	Gaussian	Spline(Gaussian grid)	Spline(equal spacing grid)
30	2.08×10^{-3}	2.46×10^{-4}	4.78×10^{-4}
60	2.67×10^{-4}	1.49×10^{-5}	3.08×10^{-5}
90	8.47×10^{-5}	7.42×10^{-6}	6.15×10^{-6}

Table 5.3: The percentage error of Gaussian quadrature and spline based method for the integration $\int_b^a f(x) \ln |x - q| dx$ when $f(x) = x^4$ at different number of grid points. The calculations of spline based method are performed on both the Gaussian grid and usual equal spacing grid.

5.2 Padé Method and The Solution of The Inhomogeneous Equation for Scattering Operator

Assume $f(z)$ is a meromorphic function near $z = 0$, and has a power series expansion

$$f(z) = a_0 + a_1z + a_2z^2 + \cdots + a_kz^k + \cdots \quad (5.45)$$

This power series converges within the radius which excludes the pole nearest to $z = 0$. However, $f(z)$ can be represented everywhere by the quotient of two polynomials $P_N(z)$ and $Q_M(z)$ of degrees N and M , respectively. We use the notation $R_{N,M}(z)$ to denote this quotient as

$$R_{N,M}(z) = \frac{P_N(z)}{Q_M(z)}. \quad (5.46)$$

The polynomials used in Eq. (5.46) are

$$\begin{aligned} P_N(z) &= p_0 + p_1z + p_2z^2 + \cdots + p_Nz^N, \\ Q_M(z) &= 1 + q_1z + q_2z^2 + \cdots + q_Mz^M. \end{aligned} \quad (5.47)$$

The difference of $f(z)$ and $R_{N,M}(z)$ can be written in the form of $f(z)Q_M(z) - P_N(z)$:

$$\left\{ \sum_{j=0}^{\infty} a_j z^j \right\} \left\{ \sum_{j=0}^M q_j z^j \right\} - \left\{ \sum_{j=0}^N p_j z^j \right\} \quad (5.48)$$

Since the polynomials in Eq. (5.47) are constructed so that $f(z)$ and $R_{N,M}(z)$ agree at $z = 0$ and their derivatives up to $(N + M)$ order also agree at $z = 0$, one has

$$\left\{ \sum_{j=0}^{\infty} a_j z^j \right\} \left\{ \sum_{j=0}^M q_j z^j \right\} - \left\{ \sum_{j=0}^N p_j z^j \right\} = \sum_{j=N+M+1}^{\infty} c_j z^j \sim O(z^{M+N+1}). \quad (5.49)$$

So $R_{M,N}(z)$ approximates $f(z)$ near $z = 0$ up to $O(z^{M+N+1})$ and the rational function $R_{N,M}(z)$ has $N + M + 1$ unknown coefficients which need to be determined [67]. In the special case of $Q_0(z) = 1$, the approximation is reduced to the power series expansion for $f(z)$ as in Eq. (5.45). For a fixed value of $N + M$ the error is smallest when $P_N(z)$ and $Q_M(z)$ have the same degree or when $P_N(z)$ has degree one higher than $Q_M(z)$.

When the l.h.s of Eq. (5.49) is set equal to zero, consequently the coefficients of the powers of z^j are set equal to zero for $j = 0, 1, \dots, N + M$. This yields a system of $N + M + 1$ linear equations:

$$\begin{aligned}
 a_0 - p_0 &= 0 \\
 q_1 a_0 + a_1 - p_1 &= 0 \\
 q_2 a_0 + q_1 a_1 + a_2 - p_2 &= 0 \\
 q_3 a_0 + q_2 a_1 + q_1 a_2 + a_3 - p_3 &= 0 \\
 &\dots \\
 q_M a_{N-M} + q_{M-1} a_{N-M+1} + \dots + a_N - p_N &= 0
 \end{aligned} \tag{5.50}$$

and

$$\begin{aligned}
 q_M a_{N-M+1} + q_{M-1} a_{N-M+2} + \dots + q_1 a_N + a_{N+1} &= 0 \\
 q_M a_{N-M+2} + q_{M-1} a_{N-M+3} + \dots + q_1 a_{N+1} + a_{N+2} &= 0 \\
 &\dots \\
 q_M a_N + q_{M-1} a_{N+1} + \dots + q_1 a_{N+M-1} + a_{N+M} &= 0.
 \end{aligned} \tag{5.51}$$

The M equations in Eq. (5.51) contain only the unknowns q_1, q_2, \dots, q_M and should be solved first. Then the substitution of the solutions for q_1, q_2, \dots, q_M back into the $N + 1$ equations of Eq. (5.50) gives the solution for $p_0, p_1, p_2, \dots, p_N$. In practice, it is more convenient to construct a special Padé approximation from a continued fraction expansion [68]. This is defined by

$$f(z) = \alpha_0 + \frac{\alpha_1 z}{1 + \frac{\alpha_2 z}{1 + \frac{\alpha_3 z}{1 + \dots}}} \tag{5.52}$$

Truncated at $\alpha_n = 0$, Eq. (5.52) leads to a ratio of finite polynomials, which has to be a certain type of Padé approximation because of the theorem of uniqueness. One can write this special type of Padé approximation as

$$f(z) \approx \tilde{R}(z) = \frac{A(z)}{B(z)} \tag{5.53}$$

where the $A(z)$ and $B(z)$ are polynomials up to certain order. Looking at the first few terms in Eq. (5.53), one has

$$\frac{A_0(z)}{B_0(z)} = \frac{\alpha_0}{1},$$

$$\begin{aligned}
\frac{A_1(z)}{B_1(z)} &= \frac{\alpha_0 + \alpha_1 z}{1}, \\
\frac{A_2(z)}{B_2(z)} &= \frac{\alpha_0 + \alpha_1 z + \alpha_0 \alpha_1 z}{1 + \alpha_2 z}, \\
&\dots,
\end{aligned} \tag{5.54}$$

In general by induction one has

$$\begin{aligned}
A_{n+1}(z) &= A_n(z) + \alpha_{n+1} z A_{n-1}(z) \\
B_{n+1}(z) &= B_n(z) + \alpha_{n+1} z B_{n-1}(z).
\end{aligned} \tag{5.55}$$

By the successive application of the recursion in Eq. (5.55) with the initial values of Eq. (5.54), one has the degrees of $A_n(z)$ and $B_n(z)$ in z as

$$\begin{aligned}
\text{degree}[A_{2n}(z)] &= \text{degree}[B_{2n}(z)] = \text{degree}[B_{2n+1}(z)] = n, \\
\text{degree}[A_{2n+1}(z)] &= n + 1,
\end{aligned} \tag{5.56}$$

A nice feature of this special Padé approximation induced by the continued fraction expansion is that the resulting $\tilde{R}(z)$ in Eq. (5.53) is always of the type $R_{N,N}(z)$ or $R_{N+1,N}$. This form has the smallest error as mentioned before. In order to carry out a Padé approximation of this specific type, we need to have the continued fractions related to the power series, i.e. we need to determine the coefficients $\{\alpha_i\}$ in the continued fraction expansion by using the coefficients $\{a_i\}$ of the power series expansion. With the initial values $\alpha_0 = a_0$ and $\alpha_1 = a_1$, this is given by the following recursion relation

$$\begin{aligned}
\alpha_{2n} &= -\frac{C(n+1/n)C(n-1/n-1)}{C(n/n-1)C(n/n)}, \\
\alpha_{2n+1} &= -\frac{C(n+1/n+1)C(n/n-1)}{C(n/n)C(n+1/n)}, \quad n \geq 1
\end{aligned} \tag{5.57}$$

with the definition of $C(r/s)$ as

$$C(r/s) = \det |\mathbf{C}| = \det \begin{vmatrix} a_{r-s+1} & a_{r-s+2} & \cdots & a_r \\ \cdot & \cdot & \cdot & \cdot \\ \cdot & \cdot & \cdot & \cdot \\ \cdot & \cdot & \cdot & \cdot \\ a_r & a_{r+1} & \cdots & a_{r+s-1} \end{vmatrix}. \tag{5.58}$$

The matrix \mathbf{C} has the dimension $s \times s$. When $s = 0$, $C(r/s)$ should be set equal to 1 [69]. We calculate the first two nontrivial results of α_i by Eq. (5.57) and get

$$\begin{aligned}\alpha_2 &= -\frac{C(2/1)C(0/0)}{C(1/0)C(1/1)} = -\frac{a_2}{a_1}, \\ \alpha_3 &= -\frac{C(2/2)C(1/0)}{C(1/1)C(2/1)} = -\frac{\det \begin{vmatrix} a_1 & a_2 \\ a_2 & a_3 \end{vmatrix}}{a_1 a_2} = \frac{a_2}{a_1} - \frac{a_3}{a_2},\end{aligned}\quad (5.59)$$

which are exactly the same as the results given in [45] by an alternative recursion method. Indeed the table of the nonzero $C(r/s)$ can be prepared separately as long as the coefficients of the power expansion $\{a_i\}$ are known, and therefore the evaluation of $\{\alpha_i\}$ is straightforward. Obviously the Padé approximation based on the continued fraction expansion is suitable for numerical calculation. Since this kind of Padé has the form $R_{N,N}(z)$ and $R_{N+1,N}$, Eq. (5.53) can be written as

$$\tilde{R}_n(z) = \frac{\tilde{P}_n(z)}{\tilde{Q}_n(z)}. \quad (5.60)$$

The corresponding Padé polynomials determined recursively in Eq. (5.55) are then written as

$$\begin{aligned}\tilde{P}_{n+1}(z) &= \tilde{P}_n(z) + \alpha_n z \tilde{P}_{n-1}(z) \\ \tilde{Q}_{n+1}(z) &= \tilde{Q}_n(z) + \alpha_n z \tilde{Q}_{n-1}(z)\end{aligned}\quad (5.61)$$

with the initial values $\tilde{P}_0 = 1$, $\tilde{Q}_0 = 0$ and $\tilde{P}_1 = \tilde{Q}_1 = 1$. Eq. (5.45) for determining the power series expansion coefficients $\{a_i\}$, Eqs. (5.57) and (5.58) for determining the continued fraction expansion coefficients, and Eq. (5.61) for determining the polynomials recursively are the basic equations to approximate $f(z)$ by the special Padé approximation of Eq. (5.60).

For the three-body scattering problem the equation for the three-body transition operator T in Eq. (2.41) can be rewritten as

$$T = [1 - K]^{-1} t P \quad (5.62)$$

where $K = G_0 t P$. Due to the large dimensionality (see e.g. Eq. (3.69)), it is impossible to do a direct inversion. Once the kernel K is prepared explicitly as in Eq. (3.69),

Eq. (5.62) can be expanded in power series as

$$T = tP[1 + K + K^2 + K^3 + \dots], \quad (5.63)$$

which is called the Neumann series. It is known that the Neumann series converges very slowly and diverges in the channel where there is a bound state. In order to get the full solution of T by this finite series expansion, we have to apply the special Padé approximation described in Eq. (5.60).

In practice we successively apply the kernel K to generate the finite Neumann series up to the $(i - 1)$ -th order in K , then we sum all terms up by the Padé approximation in Eq. (5.60) and get $T_{Pade}^{(i-1)}$. With one more application of K we get the Neumann series up to the i -th order. We do the same Padé approximation procedure and get $T_{Pade}^{(i)}$. Now we defined a distance between $T_{Pade}^{(i)}$ and $T_{Pade}^{(i-1)}$ as

$$\Delta_{Pade}^i(T) = \frac{\sum \left| T_{Pade}^{(i)} - T_{Pade}^{(i-1)} \right| \left| T_{Pade}^{(i)} \right|}{\sum \left| T_{Pade}^{(i)} \right|^2}. \quad (5.64)$$

Since in our numerical approach the $T^{(i)}$ is represented on a given 5-dimensional grid in Eq. (3.69), the summation in Eq. (5.64) runs over all grid points on which the T^i are represented. Notice that the defined distance between the $T^{(i)}$ at consecutive orders is weighted by the associated value of T^i on each grid point, therefore the grid points with large values of $T^{(i)}$ gives the largest contribution to the distance defined in Eq (5.64). Due to the existence and uniqueness of T , the Padé summation converges if

$$\lim_{i \rightarrow \infty} \Delta_{Pade}^i(T) = 0. \quad (5.65)$$

In practice, we stop the further application of K for higher order Neumann series and Padé approximation, and take the $T_{Pade}^{(n)}$ as the solution of T if

$$\Delta_{Pade}^n(T) < \epsilon. \quad (5.66)$$

where ϵ is a small number determined by the desired accuracy, We use typical values $\epsilon = 10^{-4}$.

Indeed T up to i -th order can also be evaluated by the direct sum of Neumann series, and one gets the corresponding partial sum $T_{Neu}^{(i)}$. The corresponding distance between $T_{Neu}^{(i)}$ at consecutive orders can be similarly evaluated by Eq. (5.64) as $\Delta_{Neu}^{(i)}(T)$. Thus one can compare the convergence property of the Padé method and that of the Neumann series. In Table 5.4 we show $\Delta_{Pade}^n(T)$ and $\Delta_{Neu}^n(T)$ according to Eq. (3.69) at $E_{lab} = 10$ MeV. It is found that for Padé approximation $\Delta_{Pade}^i(T)$ gets smaller and smaller with increased order, decreasing to 10^{-4} when $i = 12$. This means the Padé approximation sums the Neumann series in a convergent manner. Meanwhile, the $\Delta_{Neu}^i(T)$ does not converge with the increased order which means the direct sum of Neumann series is not convergent. Since the existence of a bound state leads to the corresponding pole in the transition amplitude, Neumann series is in general an asymptotic expansion rather than a convergent expansion. $E_{lab} = 10$ MeV is not far away from the pole dictated by the deuteron bound state with binding energy $E_d = -2.2236$ MeV. That is why the $\Delta T_{Neu}^{(i)}$ is saturated around 0.686, neither converges down nor diverges up. In Table 5.5 we show the results for $E_{lab} = 500$ MeV. The Padé approximation converges steadily as we see in Table 5.4. Because for this case, the energy is high and far away from deuteron pole, the $\Delta_{Neu}^n(T)$ also gets smaller and smaller. It turns out that the direct sum of Neumann series converges, even though it converges more slowly than the Padé approximation.

i	$\Delta_{Pade}^{(i)}$	$\Delta_{Neu}^{(i)}$
1	0.138×10^1	0.138×10^1
2	0.189×10^1	0.929×10^0
3	0.235×10^1	0.854×10^0
4	0.731×10^0	0.863×10^0
5	0.359×10^0	0.861×10^0
6	0.104×10^0	0.867×10^0
7	0.177×10^{-1}	0.869×10^0
8	0.211×10^{-1}	0.868×10^0
9	0.561×10^{-2}	0.867×10^0
10	0.224×10^{-2}	0.868×10^0
11	0.100×10^{-2}	0.868×10^0
12	0.907×10^{-4}	0.868×10^0

Table 5.4: Convergence property of Padé approximation and direct sum of Neumann series at different orders for the solution of T . The results are based on the calculation at $E_{lab} = 10$ MeV.

i	$\Delta_{Pade}^{(i)}$	$\Delta_{Neu}^{(i)}$
1	0.583×10^{-1}	0.583×10^{-1}
2	0.612×10^{-1}	0.277×10^0
3	0.295×10^0	0.492×10^{-1}
4	0.105×10^0	0.102×10^0
5	0.239×10^{-1}	0.192×10^{-1}
6	0.117×10^{-1}	0.388×10^{-1}
7	0.140×10^{-1}	0.138×10^{-1}
8	0.843×10^{-2}	0.106×10^{-1}
9	0.185×10^{-2}	0.686×10^{-2}
10	0.170×10^{-2}	0.631×10^{-2}
11	0.178×10^{-2}	0.331×10^{-2}
12	0.476×10^{-3}	0.224×10^{-2}
13	0.164×10^{-3}	0.260×10^{-2}
14	0.748×10^{-4}	0.184×10^{-2}

Table 5.5: Convergence property of Padé approximation and direct sum of Neumann series at different orders for the solution of T . The results are based on the calculation at $E_{lab} = 500$ MeV.

5.3 Iterated Ortho-normalized Vector Method and the Solution of The Homogeneous Equation for a Three-Body Bound State

The eigenvalue and eigenvector equation of the three-body bound state in Eq. (2.16) has following form

$$|\psi\rangle = K(E)|\psi\rangle. \quad (5.67)$$

It is convenient to consider a more general equation first

$$K(E)|\psi\rangle = \lambda(E)|\psi\rangle. \quad (5.68)$$

Here $K(E)$ is the integral kernel as a function of E , and $\lambda(E)$ is its eigenvalue with the corresponding eigenvector $|\psi\rangle$. The solution of Eq. (5.67) is given for $\lambda(E) = 1$. Due to the large dimensionality of $K(E)$ (as shown in Eq. (4.3)) which is up to $97 \times 97 \times 42 \times 97 \times 42$, directly solving the homogeneous equation

$$(K(E) - \lambda(E))|\psi\rangle = 0 \quad (5.69)$$

by standard routines based on the an LU decomposition algorithm is not efficient. Here we treat it by an iterative method of Lanzocs type, called the Iterated Ortho-normalized Vector (IOV) method [19, 70].

With the arbitrary initial trial vector $|\psi_0\rangle$, the sequential application of the kernel $K(E)$ generate a sequence of vectors

$$|\psi_i\rangle = K(E)|\psi_{i-1}\rangle, \quad (5.70)$$

so that

$$|\psi_i\rangle = K^i(E)|\psi_0\rangle. \quad (5.71)$$

The iteration is performed N times. Then with the set of vectors $\{|\psi_i\rangle\}$, the ortho-normal basis $\{|\bar{\psi}_i\rangle\}$ can be constructed through Schmidt orthogonalization

$$|\bar{\psi}_i\rangle = N_i \left\{ |\psi_i\rangle - \sum_{j=0}^{i-1} \langle \bar{\psi}_j | \psi_i \rangle |\bar{\psi}_j\rangle \right\}. \quad (5.72)$$

More explicitly,

$$\begin{aligned}
|\bar{\psi}_0\rangle &= N_0|\psi_0\rangle, \\
|\bar{\psi}_1\rangle &= N_1(|\psi_1\rangle - |\bar{\psi}_0\rangle\langle\bar{\psi}_0|\psi_1\rangle), \\
|\bar{\psi}_2\rangle &= N_2(|\psi_2\rangle - |\bar{\psi}_1\rangle\langle\bar{\psi}_1|\psi_2\rangle - |\bar{\psi}_0\rangle\langle\bar{\psi}_0|\psi_2\rangle), \\
&\dots, \\
|\bar{\psi}_i\rangle &= N_i\left(|\psi_i\rangle - \sum_{j=0}^{i-1} |\bar{\psi}_j\rangle\langle\bar{\psi}_j|\psi_i\rangle\right).
\end{aligned} \tag{5.73}$$

where the N_i is introduced as the normalization factor to guarantee that

$$\langle\bar{\psi}_i|\bar{\psi}_j\rangle = \delta_{ij}. \tag{5.74}$$

The transformations between the ortho-normalized and the original basis are

$$\begin{aligned}
|\psi_i\rangle &= \sum_{j=0}^i a_{ij}|\bar{\psi}_j\rangle, \\
|\bar{\psi}_i\rangle &= \sum_{j=0}^i b_{ij}|\psi_j\rangle.
\end{aligned} \tag{5.75}$$

Obviously the coefficients a_{ij} and b_{ij} can be determined by

$$\begin{aligned}
a_{ij} &= \langle\bar{\psi}_j|\psi_i\rangle, \\
\delta_{ij} &= \sum_{k=0}^i b_{ik}a_{kj}.
\end{aligned} \tag{5.76}$$

The unknown solution of Eq. (5.68) can be expanded in the ortho-normalized set $\{|\bar{\psi}_i\rangle\}$ as

$$|\psi\rangle = \sum_{i=0}^N c_i|\bar{\psi}_i\rangle \tag{5.77}$$

Substituting Eq. (5.77) into Eq. (5.68) yields

$$\begin{aligned}
\lambda \sum_{i=0}^N c_i|\bar{\psi}_i\rangle &= K(E) \sum_{i=0}^N c_i|\bar{\psi}_i\rangle \\
&= \sum_{i=0}^N c_i K(E) \sum_{j=1}^i b_{ij}|\psi_j\rangle = \sum_{i=0}^N c_i \sum_{j=0}^i b_{ij} K(E) |\psi_j\rangle \\
&= \sum_{i=0}^N c_i \sum_{j=0}^i b_{ij} |\psi_{j+1}\rangle = \sum_{i=0}^N c_i \sum_{j=0}^i b_{ij} \sum_{k=0}^{j+1} a_{j+1,k} |\bar{\psi}_k\rangle.
\end{aligned} \tag{5.78}$$

Since the $\{|\bar{\psi}_i\rangle\}$ are orthonormal, multiplying Eq. (5.78) with $\langle\bar{\psi}_k|$ gives

$$\begin{aligned}\lambda c_k &= \sum_{i=0}^N \sum_{j=0}^i c_i b_{ij} a_{j+1,k} \\ &= \sum_{i=0}^N c_i M_{ik}\end{aligned}\tag{5.79}$$

with

$$M_{ik} = \sum_{j=0}^i b_{ij} a_{j+1,k}, \quad 0 < k < N.\tag{5.80}$$

The eigenvalues of matrix \mathbf{M} are approximations of the eigenvalues $\lambda(E)$ of $K(E)$. The largest eigenvalue $\lambda(E)$ is the physical solution we want. It is well known that for all iterative methods, the largest eigenvalues dominate the iteration, so the corresponding eigenvectors have a large relative weight in the iterated basis $\{|\psi_i\rangle\}$. This makes for fast convergence of the largest eigenvalues with respect to the size of the basis N . For our case, $N = 8$. The largest eigenvalues and the corresponding eigenvectors of \mathbf{M} can be easily found by a standard algorithm, such as LU decomposition. The $\{c_i\}$ give the expansion coefficients for the solution of $|\psi\rangle$ in terms of $\{|\bar{\psi}_i\rangle\}$.

In order to obtain the solution of Eq. (5.67) with $\lambda(E) = 1$, we need to do a zero searching procedure to determine the corresponding E . Close to the E for $\lambda(E) = 1$, the dependence of $\lambda(E)$ on E is almost linear, so a Newton-Raphson linear zero searching algorithm is sufficient. First we take E_1 and E_2 which are near the physical values for $K(E) = 1$. Second we solve Eq. (5.68) and obtain the corresponding $\lambda(E_1)$ and $\lambda(E_2)$. Then the next trial energy E_3 can be determined by

$$E_3 = E_2 - (\lambda(E_2) - 1) \frac{(E_2 - E_1)}{\lambda(E_2) - \lambda(E_1)}.\tag{5.81}$$

The zero searching in Eq. (5.81) can be repeated until the E is found to fulfill $\lambda(E) = 1$. The zero searching procedure stops when

$$|\lambda(E) - 1| < \epsilon\tag{5.82}$$

where the ϵ is a small number determined by the desired accuracy. Usually we set $\epsilon = 10^{-6}$. In Table 5.6 we show a real example for the application of this IOV method

Iteration	Trial Energy E (MeV)	Calculated Eigenvalue $\lambda(E)$
1	-8.0000000000000000	1.0384960953702884
2	-9.0000000000000000	0.9947731374290576
3	-8.8804549642325679	0.9996991053714217
4	-8.8731527528587844	1.0000024570781632

Table 5.6: The sequence of the trial energy E and the corresponding largest eigenvalue $\lambda(E)$ in IOV method. The results is based on the real calculation of three-body bound state according to Eq. (4.3).

in our three-body bound state calculation. After the kernel $K(E)$ is prepared with a given two-body and three-body force, we set the initial vector as

$$|\psi_0(p, q, x)\rangle = \frac{1}{p^2 + q^2}. \quad (5.83)$$

because this is close to the asymptotic behavior of the solution. Then we take the first two trial energy values as $E_1 = -8.0$ MeV and $E_2 = -9.0$ MeV. Following the IOV procedure described above with the size of the basis $N = 8$, we get the iterative series of trail energies E and the calculated largest eigenvalues $\lambda(E)$ as shown in Table 5.6. In this case, four energy iterations are sufficient to obtain the binding energy up to the accuracy of $(\lambda(E) - 1) \sim 10^{-6}$.

Chapter 6

Summary and Outlook

In this work we developed a technique to solve the Faddeev equations for three identical bosons. This technique is directly based on momentum vectors and does not use the traditional partial wave decomposition usually employed in three-nucleon scattering. The numerical realization of this technique was attested to be feasible and efficient when applied to calculate three-body scattering observables. This demonstrates that this is a reliable alternative to the traditional partial wave decomposition which is only successful for the calculation of the three-body scattering below $E_{lab} = 300$ MeV. More important, this vector based technique is at present the only way to extend exact Faddeev calculations to energies higher than 300MeV.

To solve the Faddeev equation for three-body scattering, we need to set up the equation for the three-body transition operator explicitly in terms of Jacobi momentum vectors. There are three distinct momentum vectors involved, the momentum of the incident projectile \mathbf{q}_0 , and the momenta \mathbf{p} and \mathbf{q} of the three particles in the final state. The key point here is to select five independent and rotationally invariant variables to uniquely specify the geometry of the three momentum vectors. Besides the two magnitudes of the two relative Jacobi momenta \mathbf{p} and \mathbf{q} , we choose the angles between the vectors \mathbf{p} and \mathbf{q}_0 , and between \mathbf{q} and \mathbf{q}_0 . The fifth variable is the angle between the two planes spanned by \mathbf{p} , \mathbf{q}_0 and \mathbf{q} , \mathbf{q}_0 . In order to set up the Faddeev equation explicitly, we need to fix the orientation of the coordinate system in such a

way that the singularities in the free three-body propagator have a simple form. This can be achieved by choosing the vector \mathbf{q} parallel to the z -axis, i.e. the q -system.

Because we want to obtain the full solution of the three-body transition operator which accounts for all rescattering effects, we need to regularize the singularities in the free three-body propagator to solve the integral equation. This is done by using a subtraction method over an extended region so that the integration with the residual logarithmic singularities at the border of the singular region can be carried out by a spline-based integration technique we developed in this work. With this the kernel of the Faddeev integral equation is numerical tractable.

Next we generate the Neumann series of the Faddeev integral equation, which is in general divergent. The converged full solution of the three-body scattering operator is obtained by re-summing the divergent Neumann series by a Padé summation.

Due to the high complexity of the numerics involved, we performed thorough self-consistency and accuracy tests to ensure that the converged solution obtained by the Padé summation is indeed the solution of the Faddeev equation, and that this solution fulfills the built-in constraints of rotational invariance as well as unitarity.

After solving the Faddeev equation for the three-body transition amplitude, we calculated three-boson scattering observables at intermediate energies from $E_{lab} = 0.2$ GeV to $E_{lab} = 1.0$ GeV. We studied elastic scattering, semi-exclusive and exclusive breakup processes in this energy regime. Even though we considered bosons in a non-relativistic framework, we nevertheless can provide first qualitative insights to generic reaction mechanisms which are independent of the details of the spin-isospin structure of a three-body system. Since older calculations of three-body reactions at higher energies are often based on only the Born term, we focused on the question if the Born approximation is valid and if not, how many orders of rescattering are needed to come close to the full Faddeev result when considering specific scattering observables. We find that in nearly all cases studied, the Born approximation is insufficient and at least second and third order rescattering terms in the two-body t -matrix are required. In kinematic configurations where the final state interaction is enhanced, approximations which already include the rescattering terms of the two-body t -matrix up to fourth order are still not sufficient. Especially in the exclusive

breakup process in the so called star configurations, we find that the contributions of the first few rescattering terms oscillate around the full result of the transition amplitude and do not show the convergence to the full result. It turns out that any approximation at finite order of the two-body t -matrix is not capable of describing the reaction correctly for these cases, and the full Faddeev result is required. The research paper about this analysis is prepared and submitted to Physical Review C.

In the second part of this work, we solved the Faddeev equation for the bound state of three bosons with both, two- and three-body forces. We have implemented a method directly based on the momentum vectors for three-body force calculation, taking advantage of its permutation symmetry. The relative algebraic and computational ease of the momentum vector based method for the three-body force calculation is demonstrated [71]. We calculated bound state energies as well as properties of the three-boson system using two- and three-body forces [72]. We also did an excursion into a playground with forces, and extracted the information about how the three-body bound state properties depend on three-body forces. We find that the three-body force of Fujita-Miyazawa type we considered is of short range and it mainly influences the high momentum components in three-body bound state. We also studied how a system of three bosons behaves when bound by three-body force alone. We further studied the interplay of two- and three-body forces on the properties of the bound state.

Looking into the future, there are several interesting extensions based on our newly developed technique for solving the Faddeev equations for the three-body system. First we want to do a detailed study of exclusive breakup processes at higher energies up to GeV scale in the laboratory frame. This is a unique testing ground to analyze the reaction mechanism of three particles at higher energies. We want to scan the whole phase space of breakup final states because different reaction mechanisms can be disentangled by selecting specific configurations. This work is in progress.

We are also in a position to test the accuracy of approximations previously developed to consider three-body reaction at GeV energies. One example is the Glauber approximation, which currently has a renaissance in analyzing reactions of high energy electron- ^3He (^3H) scattering at energies achieved in Thomas Jefferson National

Accelerator Facility. A first analytic study has been carried out in [73] for the total cross section, where only the term of first order in the two-body t -matrix was considered. Now we are in a position to do a full test of the accuracy of the Glauber approximation for the total cross section at different energies.

Second, the inclusion of three-body force in the three-body scattering calculation is important. Since we have already implemented an efficient algorithm for calculating the three-body forces in momentum vector space for the bound state, the inclusion of a three-body force into a scattering calculation should be straightforward due to the formal equivalence of the Faddeev equations for bound state and scattering transition operator. It will be interesting to explore, if at high energies the relative importance between two- and three-body forces (which is always fixed at the bound state) changes, or if there are kinematic configurations where the three-body force even in first order as strong as the two-body force.

Including spin (and isospin) degrees of freedom of course is an additional task for the future. This will increase the space of states and will lead to coupled equations, however only a strictly finite number of equations. A first step in this direction was made in Ref. [40], where the pd charge exchange reaction (semi-exclusive breakup) has been studied in the first order of two-body t -matrix. Another important issue is the consideration of relativity since this will definitely be important at higher energies. Our treatment with momentum vectors and avoiding angular momentum decomposition will hopefully turn out to be rewarding when considering relativistic Faddeev calculations.

Appendix A

High Performance Computing and Its Application to The Faddeev Calculations for The Nuclear Three-Body System

Since Faddeev calculations for a three-body system are very CPU time and memory intensive, it is essential to decompose the whole calculation into independent pieces so that they can be mapped to multi-computing nodes and be worked out individually. This addresses the issue of parallel processing. All our calculations are carried out on massively parallel systems. After the whole calculation is successfully distributed, performance tuning for each task on a node is necessary so that the computation takes advantage of a computing facility and is executed with sufficient speed. This raises the issue of high performance tuning techniques. In this appendix we explain some important aspects of our three-body system calculations which are related to high performance computing techniques.

A.1 The Overview of Parallel High Performance Computing

High performance computing (HPC) refers to the technology for solving computational problems that need significant processing power and resources. The primary goal of HPC is to reduce the execution time and accommodate larger and more complex problems. There are two main aspects. One is the parallel processing at the programming level, which enables the access of more power and resources on well designed supercomputers. The other one is the high performance execution which makes work efficiently done on each processor node.

A.1.1 The Parallel Processing

In order to solve large computational problem such as the three dimensional Faddeev calculation for a three-body system, we need to access more computing resources, including CPU time and memory, which are not available on single node computer. Then we decompose the problem into tasks which can be worked out independently of each others. The supercomputer architectures we can access are basically two types. One is the multi symmetric processing (SMP) system and the other is the massively parallel processing (MPP) system.

The SMP system is a shared-memory model and distributes tasks among CPUs using a load-sharing methodology. Every processor is functionally identical and has equal status, i.e. has equal access to operating system (OS) services such as interrupts or Input/Output. Usually a SMP system is called tightly coupled system. The applications have to be multi threaded to take advantage of SMP system. The industrial standard of the application programming interfaces on SMP system are Open specifications for Multi Processing (OpenMP) and POSIX Threads programming (Pthreads). We use OpenMP [74].

The MPP system is a distributed-memory model and distributes tasks among CPUs using a messaging interface. Every processor has its own status and OS services. Usually a MPP system is called loosely coupled system. The applications must be

multi processed to take advantage of MPP. The standard application programming interfaces on a MPP system is Message Passing Interface (MPI) [75].

The most popular system available now is a combination of SMP and MPP, which is a distributed-shared memory model, and distributes tasks among CPUs using a both load-sharing and messaging interface. Applications should be multi processed and multi threaded for each process to take advantage of such a cluster system. This kind of architecture suggests potentially higher performance. Our three dimensional Faddeev calculation for three-body system is carried out on a cluster architecture.

It should be emphasized that the decomposition of the whole work and mapping them to a parallel system just enables the access of more computing resources. It does not directly contribute to the computation. So we have to minimize the overhead of the multi message communication and the multi thread management.

A.1.2 The High Performance Execution

The high performance execution means using computing resources most efficient. The most important aspects for this issue are the microprocessor architectures and the hierarchical memory and caching, i.e. how data are loaded, stored, accessed and operated [76]. High performance execution is achieved by tuning the applications to take the advantages of the microprocessor architecture and the hierarchical memory and caching.

The microprocessor architectures are quite complicated and different from machine to machine. The most common important feature at user level is the multi pipelined functional units. Pipelined operation means that an operation can be decomposed into stages like instruction fetch, instruction decoding, operand fetch, execution and write back. Different stages of multiple operations can be done concurrently, which is a kind of parallel processing at instruction level. Not all operations can be pipelined because their length is determined at run time. Of course the pipelined operations are faster than unpipelined ones. The frequently used unpipelined float point operations include division, square root, log, etc. For most modern supercomputers there are multi pipelined functional units on chip. So we should find a way to organize the operations pipelined and feed them to all units concurrently.

The data operated in a computation are loaded, stored and accessed in memory. The whole memory is organized in a hierarchical structure, leveled as register, level one cache (L1), level two cache (L2), translational lookaside buffer (TLB) and main memory storage. Data in the register are ready to be operated, data in the L1 and L2 cache can be moved to the register much quicker than from the main memory. Mapping the virtual logic memory address used in OS to the physical memory address used by the hardware needs a specific buffer, the TLB. The hierarchical structure is specified by the access time, including the latency and bandwidth. The lower the level in which the data are stored, the more time the system needed to pick them up and load them in CPU. So we should organize the data access pattern in such a way that it will be used effectively once they are loaded in. This is the most important principle for tuning performance.

A.1.3 Performance Tuning Techniques.

After the entire calculation is distributed as described above, we can do some performance tuning. The purpose of the performance tuning is to organize and re-organize the numerical implementation so that the calculation is executed at high performance.

First we need to profile the entire calculation at the module level or statement level to find which part is most time consuming. Then we isolate the most time consuming part alone and measure its performance quantitatively, determine the reasons for poor performance. Usually we measure following quantities to evaluate the performance

- Floating Point Operations:
 - Measure the total number of the operations, determine whether there are redundant operations and the possibility to reduce the number of operations.
 - Measure the number of operations in each functional unit, determine whether all functional units on the computing facility are busy. If not, it means something can be done to make all units busy so that higher performance is expected.

- Measure the number of operations executed per cycle, determine whether this rate is satisfactory.
- Memory Access Patterns:
 - Measure the number of loads per TLB miss. This quantity means how many data are loaded in CUP per flushing of the memory. The larger this number, the more execution of CPU and the better performance. If this number is small, the execution is slow because load/store takes a lot of time.
 - Measure TLB misses per cycle. This quantity means how many flushing of memory per cycle. If this number is large, it indicates that the pattern of memory access is bad, and a lot of time is wasted in store/load operation.

When this measure is done and we have some ideas about the reasons for poor performance, we can do the following performance tuning work focused on those aspects.

- Use the best algorithm to minimize the number of operations. This is the most important tuning !
- Unroll loops at outermost level to feed functional unit evenly and keep all of them busy.
- Access memory according to stride-one manner. This can reduce the TLB misses per cycle and increase the number of loads per TLB miss. This is also a very important tuning. We program using Fortran90 language, which is column majored.
- If necessary, block the memory access beyond with the size larger then that of TLB cache, so that all operands are in TLB. This can minimize the TLB and cache missing by reusing the data which have already been loaded. This is very important to the transpose operation for a matrix. Since we do not have transpose operation for large matrix, we do not use this techniques.

- Use compiler optimization options. We use the options recommended by the National Energy Research Scientific Computing Center(NERSC).
- Use highly tuned libraries. We using the highly tuned Lapack routines to solve the linear equation for two-body t -matrix.

We iterate this procedure several times until all parts in the whole calculation are execute efficiently.

A.2 The Application of HPC in Faddeev Calculation for Three-Body System

Now we briefly describe how the HPC techniques described in previous section are applied in our Faddeev calculation for the three-body system. Our computing works are developed on Seaborg, an IBM SP RS/6000 cluster architecture, administered by National Energy Research Scientific Computing Center (NERSC). It is a distributed memory MPP computer with 6,080 processors, and the processors are distributed among 380 compute nodes with 16 processors per node. Each SP node is a shared memory SMP computer. Every SP CPU has the microprocessor structure shown in Fig A.1 [77]. There are two Floating Point Units (FPU), two Load/Stores Units, two Single-Cycle Integer Units, one Multi-Cycle Integer Unit, one Branching Unit. The processor speed is 375 MHz. Each FPU can execute a floating point (FP) instruction per clock cycle. A FP instruction can be $*$, $+$, $-$, $(a * x + b)$ FMA. The two units FPU0, FPU1 can work in parallel. A FP division takes 18 cycles because it can not be pipelined. The theoretical peak FP performance is

$$(375 \text{ M cycles/s}) * (2\text{FMA/cycle}) * (2\text{Flops/FMA}) = 1500\text{MFlops/s.} \quad (\text{A.1})$$

To approach the peak, the computation loops must be operated in L1 and TLB only, and should not have division, square root, log, etc., but use FMAs ($a*x+b$) only. This could not be realistic except in very specialized circumstances. NERSC recommends following criterion,

- 0- 100 Mflip/s (code needs optimization)
- 100- 400 Mflip/s (code may need some optimization)
- 400- 800 Mflip/s (well optimized code)
- 800-1500 Mflip/s (very well optimized code or IBM library)

For the memory structure of seaborg, the levels and corresponding sizes access times are

- L1 cache: 64KB, 1 cycle
- L2 Cache: 8MB, 6-7 cycles
- TLB: 1MB
 - If data in L2 cache: 25 cycles
 - If in Main Memory: 100 cycles
- main memory: 16-64GB, 100 cycles

Notice the large L2 cache size on seaborg, this is very supportive for the shared memory computing.

A.2.1 Load Balanced Domain Decomposition and Data Distribution

In the Faddeev formalism for three-body system, both the equation for scattering transition operator and the equation for bound state in our approach are three-dimensional integral equations. Numerically the application of the kernel on a state is matrix multiplication. So the most natural distribution scheme is data domain decomposition, which makes the load on each piece balanced, i.e. the operations executed on each node are roughly equal. We notice that for both scattering and bound state Faddeev calculation in our approach we need to prepare the two-body t -matrix $t_s(p, p', x; E - \frac{3}{4m}q^2)$ as input. After the equations have been discretized, the t_s needs

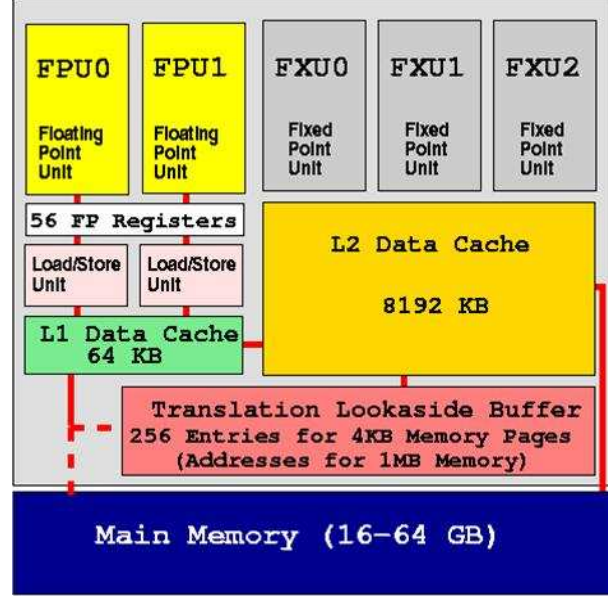


Figure A.1: The microprocessor architecture of SP CPU on Seaborg.

to be calculated for each energy $E - \frac{3}{4m}q^2$ corresponding the value of q at a grid point. The two-body t -matrix is solved as a linear equation of $Ax = b$ type

$$(1 - G_0V)t = V. \quad (\text{A.2})$$

A set of library routines, called LAPACK, for doing this job is available on almost all computing facilities, and is usually highly tuned and optimized according to the specific architecture of the facility. In order to take this advantage, we distribute our job according to the variable q , i.e. all calculation and data relevant to a specific value of q will be mapped to the same node, and the linear equation for t in Eq. (A.2) at energy $E - \frac{3}{4m}q^2$ is solved by using the library routines very efficiently. This distribution scheme automatically archives load balance with minimal communication overhead. The parallel computing in Refs. [36, 37, 38] applies this scheme. Our work follows this tradition.

A.2.2 The Scalable Multi-Leveled Computing Model for Three-Body Scattering Calculation

After we distribute the whole calculation according to the q variable using MPI, we check its message communication overhead. In the following table we show the statics about this distributive parallelism on one node. We find that the total time used for this calculation is 60652.560 seconds, in which the MPI communication time for distributing data is just 383.291 seconds. This means that most of the time is used in computation itself, the communication overhead caused by the parallelism is very small. All other nodes have almost the same statics. This indicates that we achieved a load balanced decomposition of the whole calculation.

-----Times-----			
0	Wall 5784.034	Usr 60652.560	Sys 26.420 MPI 383.291

MPI Routine	#calls	avg. bytes	time(sec)
-----Aggregate-----			
MPI_Comm_size	1	0.0	0.000
MPI_Comm_rank	1	0.0	0.000
MPI_Bcast	53	50.6	0.239
MPI_Gather	19	9953664.0	173.598
MPI_Allgather	35	5983939.3	87.575
MPI_Reduce	6	8.0	0.000
MPI_Allreduce	18	4.0	121.878

After the MPI distribution on each node which has 16 CPUs, we invoke multiple threads and map a partial domain of x_q grid to each CPU, which scales the calculation further on each node. This computing model is called multi-leveled. Each thread holds the same q of course, but just a partial domain of x_q grid, so the x_q variable is operated in parallel via a shared memory manner. After careful tuning work we achieve an ideal speed up, which is shown in Table A.1. We find that when the number of threads linearly increased, the run time linearly decreases. This means the memory layout of our implementation is well organized so that the overhead of multi-thread management is very small.

run time (Second)	138.4	69.8	35.1	17.9	12.1	9.1
number of threads	1	2	4	8	12	16

Table A.1: The run time of one Padé iteration with the different number of threads on each node.

In the following table we show the performance we obtained. The first two lines are the number of operations in the two floating point functional units respectively. These two number are almost equal. This means that all units are evenly busy. We also achieve a very low TLB missing shown at the third line by organizing the multi-nested loops in such a way that the memory is accessed via a stride one manner. Thus we have 4 operations per load/store which is shown on the third line. This means we use and reuse the data loaded in memory very efficiently. The last line tells us that the calculation is operated at the rate of 271941.911 Mflip/sec, i.e there are 271941.911 mega floating point operations executed in one wall clock time (WCT) second, namely each CPU operates at 550 mega floating point operation per second, which is well tuned according to the NERSC criterion. On the typical size $50 \times 20 \times 20 \times 20 \times 50 \times 50 \times 20 \times 20$ of the Gaussian grid for Padé iteration, converged results are obtained in two hours on Seaborg.

```

PM_FPU0_CMPL (FPU 0 instructions) : 747046644526592
PM_FPU1_CMPL (FPU 1 instructions) : 615201916466663
% TLB misses per cycle           :          0.018 %
number of loads per TLB miss     :          2102.381
Instructions per load/store       :           4.192
Flip rate (flips / WCT)          : 271941.911 Mflip/sec

```

A.2.3 The High Performance Demonstration of Three-Body Force Calculation

Our three-body force calculation was carried out on CRAY T3E at the Ohio Supercomputing center (OSC) and Neumann Institute of Computing (NIC). The

Methods	ops(M)	miss(M)	ops(M)/sec	wtime(Sec)
Direct(Eq. (4.14))	257764.86	131061.79	40.40	6497.48
Permutation(Eq. (4.11))	39326.69	14067.98	209.37	178.21

Table A.2: Performance Counting of direct and permutation methods for calculating three-body force.

CRAY T3E is a pure MPP system. Here we compare the performance of the three-body force calculations based on the direct method in Eq. (4.14) and the permutation method in Eq. (4.11). Their performance counting of one IOV iteration in solving the three-body bound state eigenvalue equation is shown in Table A.2. The second column shows the total number of operations in units of mega floating point operations. We find the algorithm based on the permutation in Eq. (4.11) has a much smaller number of operations than the direct method in Eq. (4.14) does. Due to the complicated memory layout of the direct method based on Eq. (4.14), it leads to high rate of TLB missing and low rate of operations, as shown in the third and fourth columns in Table A.2. In the fifth column, we find that one needs almost two hours to do one IOV iteration using the direct method. For the permutation method, one just needs three minutes. This indicates that the permutation based method in Eq. (4.11) is a very efficient way to calculate three-body force in three-dimensional manner.

Bibliography

- [1] L. D. Faddeev, Sov. Phys, JETP **12** 1014(1961).
- [2] L.D. Faddeev, *Mathematical Aspects of The Three-Body Problem in Quantum Scattering Theory* (Davey, New York, 1965).
- [3] L. D. Faddeev and S. P. Merkuriev, *Quantum Scattering Theory for Several Particle Ststems* (Kluwer Academic Publisher, Dordrecht, 1993).
- [4] E. O. Alt, P. Grassberger and W. Sandhas, Nucl. Phys. *B2*, 167(1967).
- [5] W. Glökle, Nucl. Phys. **A141**, 620(1970).
- [6] B. A. Lippmann and J. Schwinger, Phys. Rev. **79**, 469(1950).
- [7] R. Aaron and R. D. Amado, Y. Y. Yam, Phys. Rev. **140**, B1291(1965).
- [8] R. Aaron and R. D. Amado, Phys. Rev. **150**, 857(1966).
- [9] Y. Yamaguchi, Phys. Rev. **95**, 1628(1954).
- [10] R.A. Malfliet and A.J. Tjon, Nucl. Phys. **A127**, 161 (1969).
- [11] M. M. Nagels, T. A. Rijken and J. J. de Swart, Phys. Rev. **D17**, 768(1978).
- [12] R. Machleidt, Phys. Rev. **C63**, 024001(2001).
- [13] R. B. Wiringa, V. G. J. Stoks and R. Schiavilla, Phys. Rev. **C51**, 38(1995).
- [14] J. L. Friar, G. L. Payne, W. Glöckle, D. Hüber and H. Witala, Phys. Rev. **C51**, 2356(1995).

- [15] H. Witala, Th. Cornelius and W. Glöckle, *Few-Body Systems* **3**, 123(1988).
- [16] A. Kievsky, M. Viviani and S. Rosati, *Phys. Rev.* **C64**, 024002(2001).
- [17] M. Viviani, A. Kievsky and S. Rosati, *Few-Body Systems* **30**, 39(2001).
- [18] A. Picklesimer, R. A. Rice and R. Brandenburg, *Phys. Rev* **C45**, 2045(1992),
ibid, 547(1992), *Phys. Rev.* **C44**, 1359(1991).
- [19] A. Stadler, W. Glöckle and P. U. Sauer, *Phys. Rev.* **C44**, 2319(1991).
- [20] A. Stadler and P. U. Sauer, *Phys. Rev.* **C46**, 64(1992).
- [21] A. Nogga, D. Hüber, H. Kamada and W. Glöckle, *Phys. Lett.* **B409**, 19(1997).
- [22] A. Laverne and C. Gignoux, *Nucl. Phys.* **A203**, 597(1973).
- [23] J. L. Friar, B. F. Gibson and G. L. Payne, *Z. Phys.* **A301**, 309(1981), C. R. Chen, G.L. Payne, J.L. Friar and B.F. Gibson, *Phys. Rev.* **C31**, 2266(1985).
- [24] N. W. Schellingerhout, L. P. Kok and G. D. Bosveld, *Phys. Rev.* **A40**, 5568(1989); N. W. Schellingerhout, J. J. Schut and L.P. Kok, *Phys. Rev.* **C46**, 1192(1992).
- [25] Y. Wu, S. Ishikawa and T. Sasakawa, *Few-Body Systems* **15**, 145(1993).
- [26] W. Glöckle, H. Witala, D. Hüber, H. Kamada and J. Golak, *Phys. Rep.* **274**, 107(1996).
- [27] W. Glöckle, ‘Scattering, Scattering and Inverse Scattering in Pure and Applied Science’, Eds. R. Pike and P. Sabatier, Academic Press, p. 1339-1359 (2002).
- [28] J. Kuros-Zolnericzuk, H. Witala, J. Golak, H. Kamada, A. Nogga, R. Skibinski and W. Glöckle, *Phys. Rev.* **C66**, 024004(2002).
- [29] H. Witala, W. Glöckle, J. Golak, A. Nogga, H. Kamada, R. Skibinski and J. Kuros-Zolnierzuk, *Phys. Rev.* **C63**, 024007(2001).

- [30] K. Chmielewski, A. Deltuva, A.C. Fonseca, S. Nemoto and P.U. Sauer, Phys. Rev. **C67**, 014002(2003).
- [31] A. Arriaga, V. R. Pandharipande and R. B. Wiringa, Phys. Rev. **C52**, 2362(1995).
- [32] J. Carlson, Phys. Rev. **C36**, 2026(1987).
- [33] J. Carlson, Phys. Rev. **C38**, 1879(1988).
- [34] J. G. Zabolitzki, K. E. Schmidt and M. H. Kalos, Phys. Rev. **C25**, 1111(1982).
- [35] J. Carlson and R. Schiavilla, Rev. Mod. Phys. **70**, 743(1998).
- [36] Ch. Elster, J.H. Thomas and W. Glöckle, Few-Body Systems, **24**, 55(1998).
- [37] Ch. Elster, W. Schadow, A. Nogga and W. Glöckle, Few-Body System, **27**, 83 (1998).
- [38] W. Schadow, Ch. Elster, and W. Glöckle, Few-Body Systems **28**, 15 (2000).
- [39] I. Fachruddin, Ch. Elster and W. Glöckle, Phys. Rev. **C62**, 044002(2000).
- [40] I. Fachruddin, Ch. Elster and W. Glöckle, Phys. Rev. **C68**, 054003(2003).
- [41] S. A. Coon, M. D. Scadron, P. C. McNamee, B. R. Barrett, D. W. E. Blatt and B. J. H. McKellar, Nucl. Phys. **A317**, 242(1979).
- [42] J. Fujita and H. Miyazawa, Prog. Theor. Phys. **17**, 360(1957).
- [43] D. Hüber, H. Kamada, H. Witala and W. Glöckle, Acta Phys. Pol. **B28**, 1677(1997).
- [44] J. Haidenbauer and Y.N. Uzikov, Phys. Lett. **B 562**, 227 (2003).
- [45] W. Glöckle, *The Quantum Mechanical Few-Body Problem* (Springer-Verlag, Berlin-Heidelberg, 1983).
- [46] S. Weppner, PhD Thesis, Ohio University, 1998.

- [47] C. J. Joachain, *Quantum Collision Theory* (North-Holland, Third Version, 1987).
- [48] Private communication with T.-S. H. Lee.
- [49] L. Ray and G.W. Hoffmann, Phys. Rev. **C31**, 538 (1985); R. Crespo, R.C. Johnson and J.A. Tostevin, Phys. Rev. **C44**, R1735 (1991); Ch. Elster, T. Cheon, E.F. Redish and P.C. Tandy, Phys. Rev. **C41**, 814 (1990).
- [50] R. Machleidt, Adv. Nucl. Phys. **19**, 189(1989).
- [51] V. Komarov, *et al.*, Phys. Lett. **B 553**, 179 (2003).
- [52] G. G. Ohlsen, *Lecture Notes in Physics* **87**, 295(1978).
- [53] H. Witala, Th. Cornelius and W. Glöckle, Few-Body Systems **5**, 89(1988).
- [54] H. Witala, W. Glöckle and H. Kamada, Phys. Rev. **C43**, 1619(1991).
- [55] W. M. Kloet and J. A. Tjon, Nucl. Phys. **A210**, 380(1973).
- [56] H. T. Coelho, T. K. Das and M. R. Robilotta, Phys. Rev. **C28**, 1812(1983).
- [57] S. A. Coon and W. Glöckle, Phys. Rev. **C23**, 1790(1981).
- [58] C. R. Chen, G. L. Payne, J. L. Friar and B. F. Gibson, Phys. Rev. Lett. **55**, 374(1985).
- [59] D. Hüber, H. Witala, H. Kamada, A. Nogga, and W. Glöckle, Nucl. Phys. **A631**, 663c(1998).
- [60] V. A. Roudnev, S. L. Yakovlev and S. A. Sofianos, arXiv: physics/0204025 v2 9 April 2002.
- [61] D. Hüber, H. Witala, A. Nogga, W. Glöckle and H. Kamada, Few-Body System, **22**, 107 (1997).
- [62] Ch. Elster, E.E. Evans, H. Kamada and W. Glöckle, Few-Body Systems **21**, 25(1996).

- [63] A. Nogga, PhD Thesis, Ruhr-University Bochum, 2001.
- [64] E. A. Flinn, J. ACM **7**, 181(1960).
- [65] I. S. Gradshteyn and I. M. Ryzhik, *Table of Integrals, Series and Products* (Academic Press, Fourth Edition, 1965).
- [66] R. H. Landau, M. J. Páez, *Computational Physics, Problems Solving with Computers* (John Wiley & Sons Inc., 1997).
- [67] G. A. Baker and J. L. Gammel, ed., *The Padé Approximation in Theoretical Physics* (Academic Press, New York, 1970).
- [68] D. Hüber, Ph.D. thesis, Bochum University, Bochum, Germany, 1996.
- [69] G. A. Baker, Jr. *Essentials of Padé Approximation* (Academic Press, 1975).
- [70] Saake, Diploma Thesis, Bochum University, Bochum, Germany, 1992.
- [71] H. Liu, Ch. Elster and W. Glöckle, Computer Physics Communication **147**, 170(2002).
- [72] H. Liu, Ch. Elster and W. Glöckle, Few-Body System **33**, 241(2003).
- [73] Ch. Elster, W. Schadow, H. Kamada and W. Glöckle, Phys.Rev. **C58**, 3109(1998).
- [74] R. Chandra, R. Menon, L. Dagum, D. Hohl, D. Maydan and J. McDonald, *Parallel Programming in OpenMP* (Academic Press, 2001).
- [75] M. Snir, S. Otto, S. H. Lederman, D. Walker and J. Dongarra, *MPI, The Complete Reference* Vol.1 and Vol.2, (The MIT Press, Second Edition, 1998).
- [76] K. Dowd and C. Severance, *High performance Computing* (O'Reilly, Second Edition, 1998).
- [77] The information of IBM SP seaborg can be found at <http://www.nersc.gov/nusers/resources/SP/>